UNIVERSIDAD COMPLUTENSE DE MADRID
FACULTAD DE CIENCIAS FÍSICAS

TESIS DOCTORAL

From glassy bulk systems to spin-glass films: simulations meet experiments

Vidrios de espín en diversas geometrías (desde películas delgadas hasta sistemas cúbicos): un punto de encuentro entre las simulaciones y los experimentos

Spin-glass in diverse geometrie (da sottili film a sistemi cubici) :simulazioni incontrano esperimenti

MEMORIA PARA OPTAR AL GRADO DE DOCTOR

PRESENTADA POR

Ilaria Paga

Directores

Víctor Martín Mayor
Enzo Marinari

Madrid

© Ilaria Paga, 2021

From glassy bulk systems to spin-glass films: simulations meet experiments.

Vidrios de espín en diversas geometras (desde películas delgadas hasta sistemas cúbicos): un punto de encuentro entre las simulaciones y los experimentos.

Spin-glass in diverse geometrie (da sottili film a sistemi cubici): simulazioni incontrano esperimenti

PhD Thesis

Tesis doctoral en idioma inglés Tesi di dottorato in lingua inglese

Candidate:

Ilaria Paga

Supervisors:

Víctor Martín Mayor

Universidad Complutense de Madrid
Facultad de Ciencias Físicas
Departamento de Física Teórica I

Enzo Marinari

Sapienza, Università di Roma
Facoltà di Scienze MM.FF.NN.
Dipartimento di Fìsica

MMXX

Alle mie guide,
e alla mia tribú.

Contents

Foreword

A first acknowledgment

This dissertation is the result of a Ph.D. thesis in co-tutorship between the two universities *La Sapienza, Università di Roma*, Rome, Italy and *Universidad Complutense de Madrid*, Madrid, Spain. My supervisors were Enzo Marinari (Italian side) and Víctor Martín Mayor (Spanish side). I am very grateful for the time spent with both, and for the unquantifiable amount of things I learned from them during these years. I must acknowledge also Luis Antonio Fernández Pérez who is a master of optimization. He introduced me to his complicated codes and always shares useful computer or graphical tricks, without speaking about his research experience.

During my thesis, I have also had the opportunity of working with Prof. Ray Orbach and Qiang Zhai whose experiments inspire my whole dissertation. I am very grateful for their availability and their incredible works. Without their collaboration, my Ph.D. thesis could have not achieved the same results. I also wish to mention Federico Ricci-Tersenghi, Juan Jesus Ruiz-Lorenzo, and Gabriele Sicuro for supporting me and for helpful discussion allover my Ph.D.

I acknowledge also Javier Moreno-Gordo and Isidoro Gonzalez-Adalid Pemartin, who were Ph.D. students in the UCM group, and received me in the group; and Rafael Díaz Hernández Roja, Angelo Cavalieri, and Paolo Baldan, who were Ph.D. students of the Italian group of "chimera", and supported me when I needed it.

I also acknowledge that my thesis was funded by the European Research Council (ERC) under the European Unions Horizon 2020 research and innovation program (Grant No. 694925-LotglasSy), by the Italian Ministery for Education, University and Research (MIUR) through the FARE project *Structural Disorder and Out-of-Equilibrium Slow Dynamics in Interdisciplinary Applications*, and partially by Spains Ministerio de Economa, Industria y Competitividad (MINECO) through Grants No. FIS2015-65078-C2, No. FIS2016-76359-P (also partly funded by the EU through the FEDER program), by Agencia Estatal de Investigacin (AEI) through Grant No. PGC2018-094684-B-C21 (also partly funded by FEDER), by the Junta de Extremadura (Spain) through Grant No. GRU10158 and IB16013 (both partially funded by FEDER).

I am also grateful to the BIFI [1] for letting me use their CPU resources, and to its very professional staff.

High-performance computing in this thesis

Our main results are related to numerical simulations of a spin glass system at or above the critical temperature. The sluggish dynamics of spin glasses in the cold phase, $T \leq T_{\rm g}$, forces us to use powerful numerical resources to spot interesting phenomena. Being a physical thesis, we will mainly present the physical results, relegating to background or Appendices the engineering and computational details.

For [Zha20b, Pag21]: I enjoyed the chance of being part of the Janus Collaboration, a partnership of physicists and engineers that work with the FPGA-based machine *Janus II* [BJ14b], [2] devised expressly for Monte Carlo simulations of spin glasses. The Janus computer has been able to thermalize much larger lattices than conventional computers, at lower temperatures, and it can reach times comparable with those of experiments [Bel08b, AB10a, AB10b, Bn12a]. Moreover, for these projects, I had the opportunity to create a fruitful collaboration with the Austin experimental group of Prof. Orbach. The synergy between experiments, numerical simulations, and theory was impressive and allow us to solve a three-decade controversy on the spin-glass system in presence of an external magnetic field.

Besides, I had the chance to use the small cluster of my group in Madrid, clusters of my group in Rome, and *Cierzo* clusters from BIFI.

[1] The Institute for Biocomputation and Physics of Complex Systems of the University of Zaragoza.
[2] http://www.janus-computer.com/

List of publications

To help the panel of judges we include a list of the publications done by the candidate during her thesis.

Articles

- Fernandez, L. A. and Marinari, E. and Martin-Mayor, V. and Paga, I. and Ruiz-Lorenzo, J. J., "Dimensional crossover in the aging dynamics of spin glasses in a film geometry", Phys. Rev. B **100**, 184412, (2019) [Fer19a].
- Q. Zhai *et al.*, "Scaling Law Describes the Spin-Glass Response in Theory, Experiments, and Simulations", Phys. Rev. Lett. **125**, 237202 (2020) [Zha20b].
- M. Baity-Jesi *et al.*, "Temperature chaos is present in off-equilibrium spin-glass dynamics ", (2020) [BJ20].
- I. Paga *et al.*, "Spin-glass dynamics in the presence of a magnetic field: exploration of microscopic properties", *Journal of Statistical Mechanics: theory and Experiment*, 033301 (2021) [Pag21].

Abstracts in other languages

Scope and organization of this dissertation

During my Ph.D., we made small progress in the secular question on the nature of the spin-glass system. However, we demonstrated the unique and powerful combination of experiments, theory, and simulations addressing complex dynamics. On one hand, the experimental progress on the sample preparation and the increased precision on the measurements of key physical observables have opened new prospects in the spin-glass investigation. On the other hand, the Janus II special-purpose supercomputer, in combination with theory, is sufficient to extend simulation time and length scales to values explored experimentally. The text is organized into four parts. In the following paragraphs, we introduce briefly each of them.

Part I of this thesis provides an introduction to the physics of spin-glass systems. In chapter 1 we take a historical view on the study of spin glasses. Only the main theories on spin glasses will be discussed. In chapter 2 we detail the main observables that will be analyzed in the rest of this dissertation. Next, in chapter 3 we recall the application to spin glasses of important, general ideas from statistical physics (namely universality and the renormalization group).

Part II is dedicated to the numerical investigation of thin glassy film covering all the relevant time regimes, from picoseconds to equilibrium, at temperatures at and below the $3D$ critical point. Before addressing our results, in chapter 4 we recall few crucial facts about the very different dynamical behaviors of spin-glasses in spatial dimensions $D = 2$ and $D = 3$. In addition, we remark on the experimental success achieved in the investigation of glassy film. In chapter 5 we investigate through Parallel Tempering simulations the equilibrium properties expressed by a glassy film at the critical bulk temperature. The chapter contains unpublished results and unveils the landscape of a glassy film at the bulk temperature. In chapter 6, that comes from [Fer19b] and some unpublished results, we investigate, through Monte Carlo simulations, the dimensional crossover that happens as soon as the correlation length is compatible with the thickness, $\xi \propto L_z$. We discover dynamics characterized by four aging regimes and through a Renormalization group approach, we find a non-trivial temperature mapping between a film and a $2D$ system.

Part III examines in detail the dynamics of spin-glasses in the vicinity of and below their condensation temperature $T_{\rm g}$ in the presence of an external magnetic field. The synergy between experimental and numerical simulations, combined with theory, opens up a new vista for spin-glass dynamics. A direct outgrowth is the introduction of a new magnetization scaling law, which encompasses the full range of magnetic fields for temperatures in the vicinity of the condensation temperature, $T_{\rm g}$.

Part III is based on [Zha20b, Pag21]. Given the entangled nature of the experimental and numerical investigations in these papers, we shall cover both aspects in this thesis.

In part IV we give our conclusions, resuming the main results chapter by chapter.

We also include several appendices. Appendix A is on Monte Carlo algorithms and on parallel computing for spin-glass simulations, *i.e.* the Multispin coding technique. Appendix B explains our estimation of errors. Appendix C provides details about the measurement of connected propagators in a field. This is a heavy computation that we accelerated using multispin coding techniques. Appendix D provides details about the different techniques used overall Part III.

Resumen en castellano

Esta tesis presenta nuestra modesta contribución a la comprensión y modelización de los vidrios de espín. En particular, hemos mostrado que la combinación resultados teóricos, numéricos y experimentales permite revolucionar la comprensión de la dinámica de estos sistemas complejos. Desde el punto de vista experimental, los progresos en la preparación de muestras se alían con la alta precisión de las medidas para abrir nuevas perspectivas previamente insospechadas. Por otro lado, el uso combinado del superordenador Janus II y el análisis teórico ha permitido obtener (e interpretar) simulaciones en una escala temporal comparable a la de los experimentos. Para explicar de manera coherente estos avances, hemos dividido el texto en cuatro partes cuyo contenido describimos a continuación.

La Parte I de esta tesis contiene una introducción a la física de los vidrios de espín. En el capítulo 1 daremos una perspectiva histórica del estudio de los vidrios de espín, tomando en cuenta sólo las teoría más importantes. En el capítulo 2 defininimos y discutimos las principales cantidades físicas que consideraremos en esta tesis. La Parte I concluye con el cap. 3 donde adoptamos una perspectiva más amplia que cubre desde las aplicaciones más importantes de la física de los vidríos de espín hasta las peculiaridades de la física estadística de los sistemas de vitreos.

En la Parte II de la tesis abordaremos la investigación numéricas de los sistemas vitreos en geometría de película delgada. Explicaremos cómo hemos estudiado la dinámica en una escala temporal que abarca desde los picosegundos hasta el equilibrio, para varias temperaturas cercanas al punto crítico del sistema tridimensional. Antes de presentar nuestros resultados, en el capítulo 4 explicamos algunos factores cruciales sobre la dinámica de un sistema en $D = 2$ y $D = 3$. En el mismo capítulo se comentan los logros experimentales obtenidos en el estudio de vidrios de espn en geometría de película delgada. A continuación, en el capítulo 5 estudiamos las propiedades de equilibrio de este tipo de sistemas por medio de simulaciones de *parallel tempering* que alcanzan la temperatura crítica del sistema tridimensional. Este capítulo contiene resultados inéditos y muestra las características del *paisaje de energía libre* característico de la temperatura crítica del sistema $3D$. El capítulo 6, que se basa en referencia la Ref. [Fer19b] aunque contiene también algunos resultados más recientes, presenta nuestra investigación mediante simulaciones Montecarlo del *crossover* dimensional que se produce cuando la longitud de correlación crece hasta hacerse comparable con el espesor de la película, $\xi \propto L_{\mathrm{z}}$. Hemos descubierto que la dinámica está caracterizada por cuatro regímenes de *aging*. Utilizando la teoría del grupo de renormalizacíon hemos encontrado una correspondencia inusual entre la temperatura de un sistema de película delgada y un sistema $2D$.

La Parte III examina en detalle la dinámica de un sistema de espínes vidriosos cerca y por debajo de la temperatura de condensación T_{g} en presencia de un campo magnético externo. El uso combinado de un enfoque experimental, de las simulaciones numéricas y el análisis teórico abre nuevas posibilidades para la comprensión de la

dinámica de los vidrios de espín. Una demostración directa es la introducción de una nueva ley de escala para la magnetización del sistema que es válida en todo el régimen de campos magnéticos, al menos para temperaturas cercanas a T_{g}. Esta parte de la tesis se basa en [Zha20b, Pag21]. Debido a la complejidad de las investigaciones experimentales y numéricas presentadas en estos artículos, ambos aspectos serán analizados detalladamente en esta tesis.

La tesis termina en la Parte IV donde presentamos nuestras conclusiones y resumimos los principales resultados de cada capítulo. También se han incluido varios apéndices. El Apéndice A trata sobre el algoritmo de Monte Carlo y las optimización numéricas que hemos empleado (principalmente, *multispin coding*). El Apéndice B describe nuestro método de estimación de errores. En el Apéndice C se explica en detalle el cálculo del propagador conexo en presencia de un campo magnético. También en este caso un novedoso algoritmo *multispin coding* ha permitido reducir notablemente el esfuerzo computacional. Finalmente, el Apéndice D presenta detalles técnicos relevantes para la parte III.

Part I

Introduction

CHAPTER I

Background

This chapter is dedicated to the presentation of the birth and evolution of the spin-glass theory. This is a difficult goal given the bibliography and the scientific contributions that are the pilasters of such a complex theory. We try to present the evolution of the spin-glass knowledge historically; however, we insert an exhaustive bibliography for the interested reader [1].

We remark that this introduction has the only purpose to present the origin of spin-glass and we will only touch on those aspects of spin-glass theory that are useful to expose the results of this thesis. Since it aims to get into the topic and set the bases for further discussion, the introduction on spin-glass is left open, and recent developments are left to the introduction of each chapter.

1.1 The glass transition

If one cools a liquid quickly enough and the sudden increase of the relaxation times and viscosity is not followed by a proportional increase of the temperature, one can form a glass. This implies that the liquid stops flowing and appears as solid, even if apparently no phase transition takes place and no symmetry is broken. The famous plot by Angell in Fig. 1.1, displays how the viscosity and the relaxation times grow in a very short range of temperatures in a set of glass formers. With a factor 2 change in temperature, the viscosity grows 8-11 orders of magnitude. This behavior explains why, if we cool a liquid quickly enough, the sudden lack of thermal vibrations could arrest its dynamics before crystallizing. On the other hand, the very fast increase in the relaxation time suggests that somewhere a phase transition should exist. Unfortunately, a satisfying theory is still missing. Many different scenario and approaches have been developed,

[1] A great historical introduction on magnetism could be found in Ref.[Mat81]. Instead, for spin glass system we advised Ref.[Myd93, Méz84b, You98, Nis01, Bin11, Dom06] for historical comments, Ref. [She07] for the perspective and Ref. [Cas05] for the mathematical details.

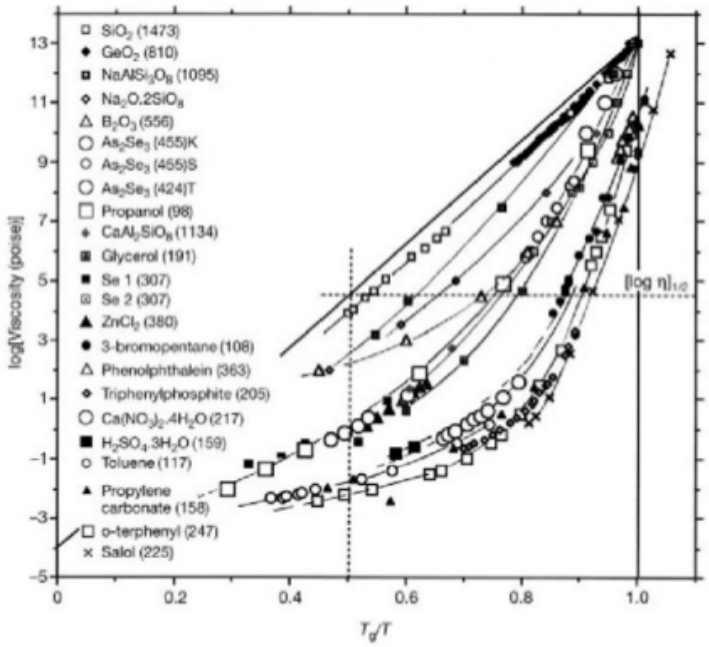

Figure 1.1: Plot is in log-scale and displays the viscosity η against the inverse of the temperature T, normalized to a constant T_{g}. At T_{g} the viscosity is 10^{13} poise. Fig from [Mar01].

but no one could explain this phenomenon.

The potentiality of amorphous solid states[2] is given by the several applications that glasses have in disparate systems. The most commonly known glasses are silica compounds. They are fused at temperature where the viscosity is low and they are malleable. The glassy phase is obtained by quickly taking them back to room temperature. Their main properties are manufacturability, transparency, uncorrosiveness, and low dilatancy. They can be found in many objects of our everyday life, such as windows, bottles, optical fibers, beakers and touchscreens.

Next, we can mention the metallic glasses whose, thanks to their magnetic properties, are mainly used for high-efficiency transformers or alternative to silicon to make molds for nanocomponets [Gre95]. Another example is the fiberglass which is the main component in automobile bodies. The fiberglass is obtained by embedding extremely fine fibers of glass in an organic polymer plastic, trapping air in order to make it a good thermal insulator [May93, Mar06]. Still, one can exploit the glassy model for describing the preservation of insect life under extreme conditions of cold or dehydration [Cro98], and in the protein folding [Web13]. Moreover, the glassy investigation is a useful tool for optimization and combinatorial problems [Méz87]. On one hand, there exist exact polynomial-time algorithms for ground-state calculations of $2D$ systems. On the other hand, the ground state calculation on a three-dimensional spin-glass is

[2]In literature, the amorphous solid states are called structural glasses

an NP-hard problem [3] for classical computers. A problem is called *NP-hard* if the existence of a polynomial algorithm for its solution implies the existence of such an algorithm for all the NP-complete problems [Bar82]. In conclusion, spin-glasses play a very important role outside physics, *e.g.* for neural networks, optimization problems, machine learning, social science and econophysics [Nis01, Har06, Méz09].

Spin glasses are characterized by an amorphous magnetic low-temperature state and a very peculiar phenomenology [Nag79, Myd93, Vin97, Jon98, Hér02]. The spin glasses have a very simple Hamiltonian. Their study gets an insight on the study of the glass phase in a more general sense and on complexity, since

- experimental measurements are easier through the use of very sensitive magnetometers called SQUIDs (Superconducting QUantum Interference Devices). See e.g. [Dru07, Kum14].

- The spin-glasses are a toy model which allows developing very advanced theoretical tools that can be reused in other contexts [Méz87, Bia12, Cha14].

- The basic spin-flip Monte Carlo algorithm is easy to simulate. Interactions between first neighbors are fixed by a *quenched disorder* that does not change with time.

- It is possible to construct dedicated hardware for more effective numerical studies [Bel06, Bel08a, BJ12, BJ14b, BJ17a, BJ18, Zha20b].

The list could continue, but we will refer principally to the above ones. The main topic of this dissertation is the comparison and the synergy between the numerical and experimental results. In Part II, we numerically evaluate the equilibrium properties and the dimensional crossover of a thin glassy film. Next, Part III is a synergy between experiments, simulations, and theory. We and our experimental co-authors were been able to draw out the physical scenario expressed by a spin glass system in presence of an external magnetic field in finite dimensions.

1.2 The origins of spin glass theory

The peculiar properties of solutions of Mn in copper Cu have started puzzling the condensed-matter community [Owe56, Nob59, Zim60] since the beginning of 1950s. These systems have a cusp in the susceptibility at a temperature T_c roughly proportional to the concentration of Mn. This temperature is the crossover between two different phases. For temperature above this critical one, the system is in the paramagnetic phase; instead, for temperature below it, no order was identified.

[3] The acronym NP stands for *Non-deterministic polynomial-time*.

On one hand, the investigation of the low-temperature phase, $T \leq T_c$, through the application of a very large external magnetic field and the recovering of the magnetization, unveils memory effects, *i.e.* the thermoremanent magnetization. On the other hand, they observed that a solution of Mn in copper Cu was not described by the Curie law:

- in the paramagnetic phase, the susceptibility, χ, was practically constant instead of being inversely proportional to the temperature, $\chi^{\text{Curie}} \propto 1/T$;
- in the low-temperature phase, the specific heat was linear in the temperature T instead of being proportional to $1/T^2$.

The peculiarity of the low-temperature phase was attributed to the $s-d$ interaction [Mar60], that couples electrons of unfilled inner shells and conduction electrons. This interaction can lead to ferromagnetism or antiferromagnetism, depending on the metal. It was supposed to be the dominant one in the low-temperature. Zener in 1951 was the first to formalize this interaction $s-d$ though a phenomenological model that did not involve the possibility of antiferromagnetism [Zen51a, Zen51b, Zen51c]. A few years later, Kasuya [Kas56] found that the $s-d$ interaction can imply antiferromagnetism. Next, the intuition of Yosida [Yos57] to relate the model from Ruderman and Kittel [Rud54] to the $s-d$ interaction, brought a great step forward in the description of solution of Mn in copper Cu. Yosida noticed that the $s-d$ interaction could be explained through a coupling between two magnetic moments through their hyperfine interaction with the conduction electrons.

This description is called RKKY and is characterized by a coupling $J_{\mathbf{xy}}^{(\text{RKKY})}$ between two Mn ions separated by $\mathbf{r}$ as

$$J_{\mathbf{xy}}^{(\text{RKKY})} \sim \cos\left(\frac{\mathbf{k}\cdot\mathbf{r}}{|\mathbf{r}|^3}\right). \tag{1.1}$$

Let us make some considerations:

- since the $\mathbf{k}$ is of the order of the Fermi vector, the oscillations of the cosine are very quick.
- The cosine function, depending on the distance between two ions, can have positive (ferromagnetic) or negative (antiferromagnetic) couplings.
- Since the interactions of Cu substrate were negligible, the cusp of the susceptibility was entirely attributed to the RKKY interaction between the Mn ions [Mar60].
- The coupling $J_{\mathbf{xy}}^{(\text{RKKY})}$ was treaded as a random variable since the positions in the alloy of these ions are random [Bro59].
- The distance between ions, $\mathbf{r_{xy}}$, depends on the single realization of the alloy and of its disorder.

The birth of spin glass theory. Anderson in 1970, for the first time, used the term *spin glass* in analogy with structural glasses. Assuming that the dominant interactions were between the Mn ions [4], he introduced a very simple Hamiltonian [And70]

$$\mathcal{H} = \frac{1}{2} \sum_{\mathbf{x} \neq \mathbf{y}} \vec{s}_{\mathbf{x}} \cdot J_{\mathbf{xy}} \cdot \vec{s}_{\mathbf{y}} \,, \tag{1.2}$$

where the $J_{\mathbf{xy}}$ is a random matrix.
Anderson's intuition was to replace the "experimental" coupling $J_{\mathbf{xy}}^{(\mathrm{RKKY})}$, Eq. (1.1), by the random variables $J_{\mathbf{xy}}$. Anderson treated the random matrix $J_{\mathbf{xy}}$ in the Hamiltonian as the disorder. Since the disorder does not change with time, we define it *quenched*. A single realization of the disorder identifies a *sample*.
The couplings $J_{\mathbf{xy}}$ are distributed through an unknown distribution that should reproduce roughly the RKKY interaction. Being the couplings $J_{\mathbf{xy}}$ both negative and positive, the energy along all the bonds can not be satisfied. When it happens, we call the system *frustated* [Tou77]. An illustrative example of *frustration* is shown in Fig. 1.2. Let us consider a $2D$ Edward-Anderson Ising model on a square lattice with nearest-neighbor coupling $J_{\mathbf{xy}} = \pm 1$. An elementary unit of a lattice is called *plaquette*. If the number of negative bonds in a *plaquette* is odd, it will be impossible to satisfy all the bonds simultaneously.

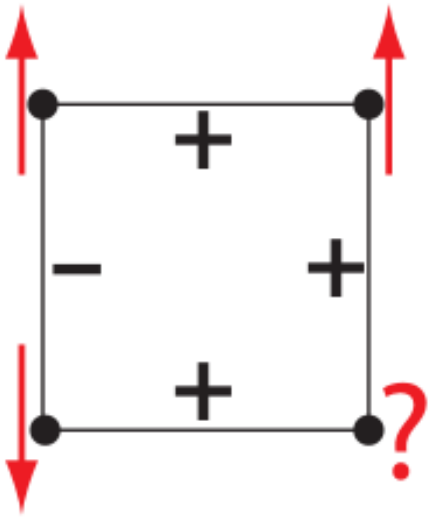

Figure 1.2: An elementary unit of a $2D$ Edward-Anderson Ising spin-glass characterized by an odd number of negative bonds. With the arrangement shown in the figure, there is no way of orienting the spins so that all of the bonds are satisfied.

However, Anderson did not average over the disorder and he only tried a mean-field approach.

[4] The electrons transmit the interaction, but not influence significantly it

The Edwards-Anderson model. The paternity of the SG as a branch of theoretical physics is attributed to Edwards and Anderson. In 1975, they introduced a simple model which qualitatively described the experimental observations [Edw75, Edw76].

In order to investigate the low-temperature phase and detect the random preferred directions exhibited by the spins, they defined the local order parameter

$$q = \lim_{t\to\infty} \frac{1}{N} \sum_{\mathbf{x}}^{N} \langle \vec{s}_{\mathbf{x}}(0) \cdot \vec{s}_{\mathbf{x}}(t) \rangle_t \ , \tag{1.3}$$

where $\langle \mathcal{O}(t) \rangle$ is the time average of a generic observable $\mathcal{O}$, $\langle \mathcal{O}(t) \rangle_t \equiv \frac{1}{t} \int_0^t dt' \mathcal{O}(t')$.

They call the local order parameter in Eq. (1.3) *overlap*. The overlap measures whether an alignment is taking place by examining if after a time t the single spins $s_{\mathbf{x}}(t)$ tend of pointing in the same direction or not.
If the system, at the equilibrium, is ergodic, one can rewrite Eq. (1.3) as

$$q = \frac{1}{N} \sum_{\mathbf{x}}^{N} \langle \vec{s}_{\mathbf{x}} \rangle^2 \ , \tag{1.4}$$

where we replace the time average $\langle \ldots \rangle_t$ with an ensemble average $\langle \ldots \rangle$. If the overlap $q = 0$, it means that there is no favored direction and the system is in the paramagnetic phase. On the other side, in the low-temperature phase, which we can call it now *spin glass* phase, each spin will align along a privileged direction and $q \neq 0$.

In Ref. [Edw75], Anderson and Edward defined an Hamiltonian with nearest neighbor interactions on a regular lattice:

$$\mathcal{H}_{\mathrm{EA}} = \frac{1}{2} \sum_{|\mathbf{x}-\mathbf{y}|=1} \vec{s}_{\mathbf{x}} \cdot J_{\mathbf{xy}} \cdot \vec{s}_{\mathbf{y}} \ , \tag{1.5}$$

assuming a unitary distance between nearest neighbors and a Gaussian distribution $P(J)$ for the coupling matrix $J_{\mathbf{xy}}$.

This model is called the *Edward-Anderson model* (EA) and, exploiting a mean-field approach, predicts both a phase transition with q as order parameter and the cusp of the susceptibility at the critical temperature T_{c}.

Each realization, *i.e. sample*, is characterized by a different coupling matrix, $J_{\mathbf{xy}}$; however, if one averages over the coupling distribution, $P(J)$, each sample must exhibit the same behavior in the thermodynamical limit. This assumption is called *self averageness*.

Let us take into account the free energy, $\mathcal{F}_J$, and the partition function, $\mathcal{Z}_J$, of a sample with a set J of couplings:

$$\mathcal{F} = \int \mathcal{F}_J P(J) dJ = -k_{\mathrm{B}} T \int P(J) \log \mathcal{Z}_J dJ \, . \tag{1.6}$$

Let us average the free energy over the disorder

$$\mathcal{F} = -k_{\mathrm{B}} T \, \overline{\log \mathcal{Z}_J} \tag{1.7}$$

where $\overline{(\dots)}$ is the average over the disorder.

The average in Eq. (1.7) is called:

- *quenched average* if one has to handle with $\overline{\log(\mathcal{Z}_J)}$;
- *annealed average* if one can directly take the average of the partition function, $\mathcal{Z}_J$:

$$\mathcal{F}_{\text{Ann}} = -k_{\text{B}}T \, \log \overline{\mathcal{Z}_J} \tag{1.8}$$

where $\mathcal{F}_{\text{Ann}}$ is the *annealed free-energy*. However, the *annealed average* brings uncorrected results at low temperature (see e.g. [Méz87]).

In this dissertation, the average over the disorder is always a *quenched average*.

For solving Eq. (1.5), Edwards and Anderson proposed the *replica trick*, that consists in using

$$\log(x) = \lim_{n\to 0} \frac{x^n - 1}{n} \tag{1.9}$$

to transform the annoying logarithm in a power law. The identity comes trivially from a first order expansion of the exponential function: $x^n = \mathrm{e}^{n\log(x)} = 1 + n\log(x) + o(n^2)$. Substituting Eq. (1.9) in Eq. (1.7), one obtains

$$\mathcal{F} = -k_{\text{B}}T \, \overline{\log \mathcal{Z}_J} = -k_{\text{B}}T \lim_{n\to 0} \frac{\overline{\mathcal{Z}^n} - 1}{n} \, . \tag{1.10}$$

Assuming that n is an integer, one could treat $\overline{\mathcal{Z}^n}$ as the partition function of n independent *replicas* of the same system, that share the same coupling matrix (*disorder*) but are independent one from the other.

Let us define the order parameter, see Eq. (1.3), exploiting the replicas formalism [Par83]

$$q^{\text{ab}} = \left\langle \vec{s}_{\mathbf{x}}^{\,(\text{a})} \cdot \vec{s}_{\mathbf{x}}^{\,(\text{b})} \right\rangle \, , \tag{1.11}$$

where (a) and (b) indicate different replicas. The replica trick, Eq. (1.9), was a huge simplification, but the limit $n \to 0$ with $n \in \mathbb{N}$ introduced some mathematical forcings that only nowadays were solved.

The Sherrington-Kirkpatrick model. Also in 1975, Sherrington and Kirkpatrick proposed a mean-field approach to the EA model. They modified Eq. (1.5) by imposing fully-connected interactions and Ising spins $s_{\mathbf{x}} = \pm 1$ [She75]

$$\mathcal{H}_{\text{SK}} = \frac{1}{2} \sum_{\mathbf{x},\mathbf{y}} \vec{s}_{\mathbf{x}} \cdot J_{\mathbf{xy}} \cdot \vec{s}_{\mathbf{y}} \, , \tag{1.12}$$

where the couplings $J_{\mathbf{xy}}$ are distributed as a normalized Gaussian [5].

Let us remark the difference between the defined Hamiltonians:

[5] A normalized Gaussian has zero mean, $\overline{J_{\mathbf{xy}}} = 0$, and the variance is such that the energy is extensive, $\overline{J^2} = 1/N$

- Anderson Hamiltonian: $\sum_{\mathbf{x}\neq\mathbf{y}}$ is a sum over all the $\mathbf{x}$ and $\mathbf{y}$, except $\mathbf{x} = \mathbf{y}$, see Eq. (1.2);
- Edward-Anderson Hamiltonian: $\sum_{|\mathbf{x}-\mathbf{y}|=1}$ is a sum over all the nearest neighbor $\mathbf{x}$ and $\mathbf{y}$, see Eq. (1.5);
- Sherrington-Kirkpatrick Hamiltonian: $\sum_{\mathbf{x},\mathbf{y}}$ is a sum over all the choices of $\mathbf{x}$ and $\mathbf{y}$, see Eq. (1.12) .

For solving the *quenched average* of the free energy, Eq. (1.7), Sherrington and Kirkpatrick used the *replica trick*, Eq. (1.9), and hypothesized that the system has a *replica symmetry* (RS). This implies that the overlap defined in Eq. (1.11) is always the same no matter which two replicas are chosen:

$$q^{\mathrm{ab}} = q(1 - \delta^{\mathrm{ab}}) \,. \tag{1.13}$$

This approach is called *replica symmetry ansazt*.

In 1978, de Almeda and Thouless, [Alm78b], demonstrated that the RS solution of the SK model [She75] is stable only at high temperature and they generalized the results to spins with any finite number m of components [Alm78a]. The instability of the paramagnetic phase, at a temperature below a certain temperature (T_{c}), is due to massless modes in the overlap correlation functions (replicon modes) [Bra79]. The RS solution was shown to be unstable in presence of an external applied magnetic field at low temperature and, so, at least in the SK modeling, there exists a spin glass phase in a field, see Fig. 1.3. The critical line where the RS phase becomes unstable is called

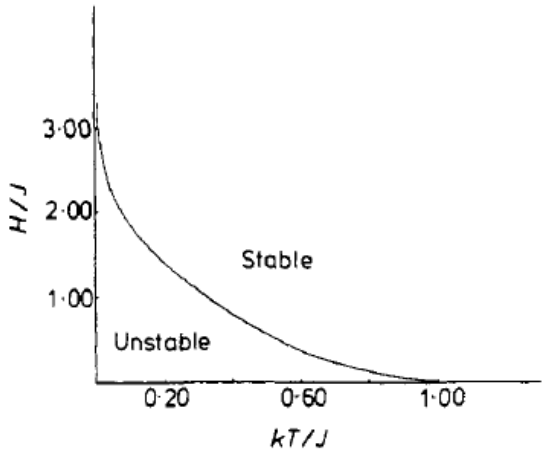

Figure 1.3: Stability of the *replica symmetry* solution of the SK model. The dAT line separates the zone of the phase diagram where the RS phase is stable from the one where magnetic ordering appears. Figure from [Alm78b].

the dAT line and we will marginally investigate it in Part. III.

Sherrington and Kirkpatrick hypothesized that the unphysical features were due by the violation of the commutativity between the limit $n \to 0$ (see Eq. (1.9)) and

the thermodynamical limit $N \to \infty$ (N is the number of spins). Otherwise, in the 1978 it was demonstrated that the commutativity of the two limits holds [Hem79], and so, the unphysical features, as the negative entropy, was due by the *replica symmetry* ansatz [Alm78b, Bra78]. However, no theory could predict how to break the symmetry between replicas to obtain a physically reasonable solution.

Given the initial failures of the replica approach, different theories were developed. In particular, we want to mention the mean-field formulation based on expansions in $6 - \epsilon$ dimension of space [Har76, You76, Che77, Sou77] and the Thouless-Anderson-Palmer (TAP) approach . The main difference between the replica method and the TAP one is that the replica method constructs a mean-field theory after having averaged over the disorder, instead the TAP approach formed a mean-field theory first [Tho77]. Unfortunately, even the TAP was shown to be useful only at high-temperature [Méz87, Kir78] without any validity in the *spin glass* phase.

Another instructive model for understanding the nature of the spin-glass phase and the influence of an external magnetic field at finite temperature is the long-range $1D$ spin glass [Kot83, Bra86, Kat03a, Kat03b, Kat05b, Kat05a, Kat05c, Leu08, Leu09]. Let us define the Hamiltonian:

$$H = \sum_{i>j} \frac{\epsilon_{ij} S_i S_j}{a|i-j|^{\sigma}} \ , \tag{1.14}$$

where S_i are Ising spins, $S_i = \pm 1$, a is the lattice spacing, ϵ_{ij} are identically distributed Gaussian random variables, and σ is the interaction-range parameter. This model exhibits an interaction-range parameter, σ, such that the model can be turned between no-phase, simple phase and complex phase behavior, see Fig. 1.4.

The Parisi solution. The solution of the SK model could be found only relaxing the replica symmetry ansatz. It was an hard task since the overlap, q^{ab}, is an $n \times n$ matrix, where $n \to 0$, according to the replica trick, see Eq. (1.9). This implies that the overlap matrix could be parametrized in infinite ways. The breakthrough was done by Parisi in 1979 when he showed that adding new order parameters to the SK model shifted the negative zero-temperature entropy [Par79b]. In this way, each new order parameter is equivalent to a breaking of the replica symmetry (RSB) and it unveils, for the first time, the complexity of the *spin glass* phase. Parisi hypothesized that the spin-glass phase, in the SK modeling, is characterized by *infinite steps of Replica Symmetry Breaking*, (∞-RSBS) [Par79a].

The Parisi ansatz for the matrix q^{ab} consisted in an iterative process starting from the RS ansatz $q^{\mathrm{ab}} = q_0(1 - \delta^{\mathrm{ab}})$, see Fig. 1.5 [Par80b, Par80c, Par80a].

The first step of *replica symmetry breaking* (RSB) consists in divided the $n \times n$ matrix in n/m_1 blocks of size $m_1 \times m_1$, see the second matrix in Fig. 1.5. The off-diagonal blocks remain unchanged, instead the off-diagonal terms of the diagonal blocks now assume the overlap value q_1. The second step of RSB works in the same way, look at the third matrix in Fig. 1.5. It iterates the symmetry breaking in each of the n/m_1 diagonal blocks and, exactly as the 1-RSB, we subdivided each block in m_1/m_2 sub-blocks of size $m_2 \times m_2$. The off-diagonal sub-blocks remain unchanged, instead, the

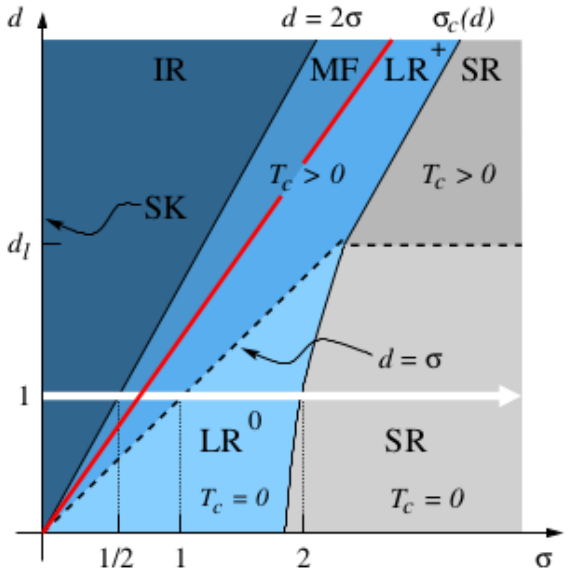

Figure 1.4: Sketch of the phase diagram in the $d-\sigma$ plane of the long-range spin glass with power-law interactions. The horizontal white arrow corresponds to $d = 1$ and we focus only on it. By tuning the power-law exponent σ different universality classes can be probed. For $\sigma \leq 1/2$ the system is in the infinite-range SK universality class. For $1 < \sigma \leq 2/3$ the model exhibits a mean-field behavior corresponding to an effective space dimension $d_{\text{eff}} \geq 6$, where $d_{\text{eff}} \sim 2/(2\sigma - 1)$ for $1/2 \leq \sigma \leq 1$. The thick (red) line separates mean-field from non-mean-field behavior. For $2/3 < \sigma < 1$ the model is a long-range spin glass with a finite ordering temperature T_{c}, whereas for $1 \leq \sigma < 2$ the long-range spin glass has $T_{\text{c}} = 0$. When $\sigma \geq 2\,[\sigma_c(d)]$ the model is short-ranged with zero transition temperature. Figure taken from Ref. [Kat08].

off-diagonal terms of the diagonal sub-blocks now assume the overlap value q_2. One can obtain the full RSB solution iterating this technique infinite times.

The overlap matrix constructed following the Parisi ansatz or the RS ansatz is replica equivalent. As the reader can note in Fig. 1.5, the overlap matrix has any two rows (or columns) identical up to permutations.

The paramagnetic phase, or equivalently the RS phase, is characterized by $q^{\text{ab}} = 0 \ \forall \text{a}, \text{b}$, so the probability distribution of the order parameter is simply

$$P(q) = \delta(0)\,. \tag{1.17}$$

On the other hand, the full RSB ansatz (solution of the SK model), implies that the spin-glass phase has a not trivial probability distribution of the order parameter. The order parameter, q^{ab}, can assume $n(n-1)$ off-diagonal values and so its associated

$$\left(\begin{array}{cccccc} 0 & & & & & \\ & 0 & & & & \\ & & 0 & & & q_0 \\ & & & 0 & & \\ & & & & 0 & \\ & q_0 & & & & 0 \end{array}\right) \longrightarrow \left(\begin{array}{ccc|ccc} 0 & & q_1 & & & \\ & 0 & & & q_0 & \\ q_1 & & 0 & & & \\ \hline & & & 0 & & q_1 \\ & q_0 & & & 0 & \\ & & & q_1 & & 0 \end{array}\right) \longrightarrow \tag{1.15}$$

$$\left(\begin{array}{cc|cc|cc} 0 & q_2 & & q_1 & & \\ q_2 & 0 & & & & \\ \hline & q_1 & 0 & q_2 & & \\ & & q_2 & 0 & & q_0 \\ \hline & & & & 0 & q_2 \\ & q_0 & & & q_2 & 0 \\ \hline & & & & & \\ & & q_1 & & 0 & q_2 \\ & & & & q_2 & 0 \end{array}\right) \longrightarrow \cdots \tag{1.16}$$

Figure 1.5: Sketch the first two steps of replica symmetry breaking. The first $n \times n$ matrix corresponds to the RS ansatz. The matrix is completely symmetric under replica exchange. The second matrix represents the first step of RSB. As we explain in the main text, the matrix is divided into blocks, and the overlap q^{ab} can now assume two no-zero values. The third matrix shows the 2-step RSB: each inner block is subsequently divided into smaller blocks and the overlap q^{ab} can now assume three no-zero values. The SK solution is obtained through infinite RSB steps.

distribution behaves as:

$$\begin{aligned} P(q) &= \frac{1}{n(n-1)} \sum_{\mathrm{a}\neq\mathrm{b}} \delta\left(q - q^{\mathrm{ab}}\right) = \\ &= \frac{n}{n(n-1)} \left[(n-m_1)\delta(q-q_0) + (m_1-m_2)\delta(q-q_1) + \right. \\ &\left. +(m_2-m_3)\delta(q-q_2) + \ldots\right] . \end{aligned} \tag{1.18}$$

According to the replica trick, see Eq. (1.9), one has to take the $n \to 0$ limit, so

$$P(q) = m_1\delta(q-q_0) + (m_2-m_1)\delta(q-q_1) + (m_3-m_2)\delta(q-q_2) + \ldots \ . \tag{1.19}$$

Being a distribution positive, Eq. (1.19) implies the constrain $0 < m_1 < m_2 < \ldots < 1$.

Let us define the function $q(x)$ such that

$$q(x) = q_i \quad \text{if} \ \ m_i < x < m_{i+1} \,, \tag{1.20}$$

where we are supposing that the q_i constitute an increasing sequence which is infinite in the full RSB case. After a k-step RSB, $q(x)$ is a piecewise function that takes at

most $k+1$ different values. In the limit of full RSB, $k \to \infty$, $q(x)$ becomes a continuous function in the interval [0,1] [Par80b].
Parisi also shows that

$$q(x) = q_{\mathrm{m}} \quad \text{for } x \leq x_{\mathrm{m}}\,, \tag{1.21}$$

$$q(x) = q_{\mathrm{M}} \quad \text{for } x \geq x_{\mathrm{M}}\,. \tag{1.22}$$

This means that the $P(q)$ function can be rewritten as the sum of two delta functions connected by a smooth function $\tilde{P}(q)$ which is no-zero only in the interval $x_{\mathrm{m}} < x < x_{\mathrm{M}}$ [see Fig. 1.6]

$$P(q) = x_{\mathrm{m}}\delta(q - q_{\mathrm{m}}) + \tilde{P}(q) + x_{\mathrm{M}}\delta(q - q_{\mathrm{M}})\,. \tag{1.23}$$

In Fig. 1.6, we show the behavior of the overlap distribution in different cases for reader simplicity.

Let us take two random states α and β, both with a $P(q)$ distribution, with mutual overlap $q^{\alpha\beta}$. If the two states α and β have maximal overlap $q^{\alpha\beta} = q_{\mathrm{M}}$, with probability x_{M} the two states are identical. If $q^{\alpha\beta} = q_{\mathrm{m}}$, with probability x_{m} the two states are as different as it is possible. With probability $1 - x_{\mathrm{m}} - x_{\mathrm{M}}$ the situation will be something in between. The q_{m} and x_{m} depend on an external magnetic field as $H^{2/3}$ [Asp04], in contra position to $q(x)$ and x_{M} which are weakly depend on the field. When one approaches the critical field from the SG phase, the distance between the two peaks in the $P(q)$ decreases until the $P(q)$ becomes trivial $\delta(q - q_{\mathrm{EA}})$ above the dAT line.

The Parisi ansatz implies that there is a hierarchical structure in the organization of the states in the SG phase, see Eq. (1.19)[Méz84a, Méz85b, Ram86]. Let us explain the ultrametricity of the overlap space exploiting a tree representation, see Fig. 1.7

The root of the "tree" corresponds to the RS solution, where all the states have the same overlap q_0, see Eq. (1.13). The one-step symmetry breaking, 1-RSB, corresponds to the first branches of our "tree". Replicas within the same group have the same overlap q_1 and it holds the overlap relation $q_0 < q_1$, see Eq. (1.19).
The reader can easily iterate this process for further steps of RSB. The overlap between two replicas α and β can be identified by returning towards the root until the two states belong to the same group. For example, the overlap between states α and β in Fig. 1.7 is $q^{\alpha\beta} = q_1$. The ultrametricity condition is easily verified by picking three generic states.

The RSB ansatz implies that the spin-glass phase has a complex energy landscape characterized by an infinitely large number of metastable states. Parisi himself [Par83] explained such landscape in a very figurative way comparing the metastable states to valleys separated by high mountains whose height goes to infinity in the infinite-volume limit. The number of valleys is exponential in the number of spins N [Bra80, Dom80, You81], and the dynamics in the spin-glass phase is so sluggish that, in the thermodynamical limit, the ergodicity is broken [Mac82].

The Parisi solution of the SK model and his RSB ansatz were physically consistent; however, more than 20 years were needed to confirm rigorously his solution [Gue02, Gue03, Tal06].

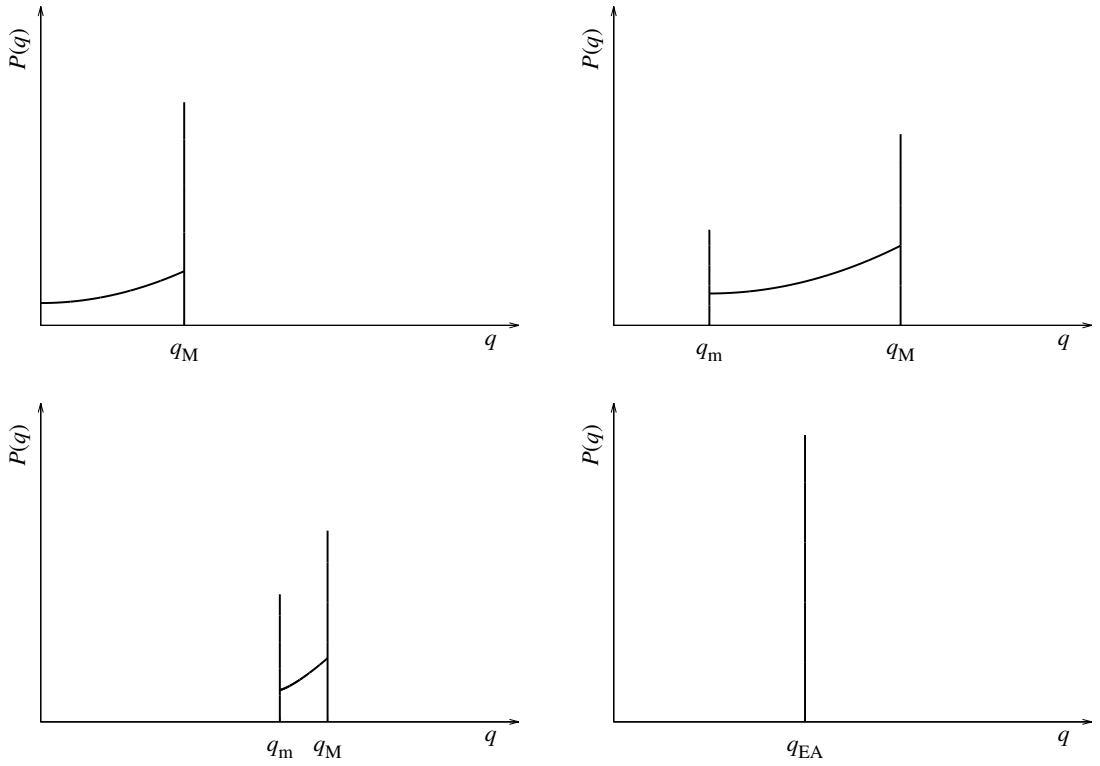

Figure 1.6: Different instances of $P(q)$ in the SK model. **Top left**: at zero field, close to T_c. **Top right**: at small magnetic field H in the spin-glass phase. **Bottom left**: approaching the dAT line from the spin-glass phase, the difference $q_M - q_m$ shrinks. **Bottom right**: in the RS phase the $P(q)$ is a delta function centered in q_{EA}.

A still open question is to understand if and how the Parisi solution of the SK model, is valid in infinite dimensions, is suitable or not for describing the EA model in finite dimension.

The droplet picture. We conclude this short introduction by reporting the main idea of the *droplet model*. This theory was proposed by Fisher and Huse in 1987 [Fis86] and proves a new picture of the ordered phase in spin-glasses [Fis87, Hus87, Fis88b, Fis88a]. The *droplet model* is exact in one dimension and describes the SG phase of low-dimensional as a "ferromagnet in disguise" with only two pure states, with an order parameter $q = \pm q_{EA}$. The theory derives from a Migdal-Kadanoff approximation [Mig75, Kad76] on the EA model [And78].

A pure state is formed by the coexistence of low energy *droplet* of spins. The disorder affects the stability of the boundaries of these domains. Each domain tries, exploiting unsatisfied links, to increase its size. The droplet boundaries scales as

$$L^{d_s} \quad \text{with} \quad d - 1 \leq d_s < d \,. \tag{1.24}$$

The *droplet ansatz* hypothesizes that the free-energy cost of the lowest-energy ex-

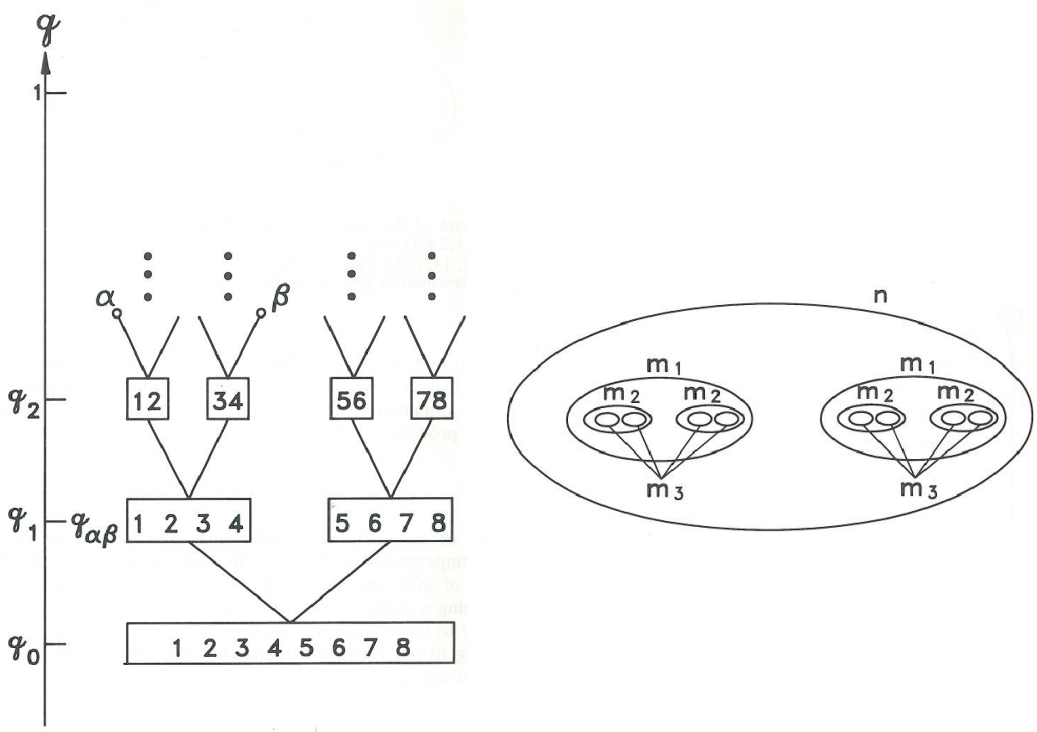

Figure 1.7: The RSB ansatz as a branching process. The overlap between two states α and β can be treated as the first common level of RSB between the state α and β (**left**). Another way to visualize this is to represent the RSB process as an iterative subdivision in subsets (**right**), then the overlap between two states α and β is given by the smallest set containing both α and β. Figure from [Myd93].

citations of linear size ℓ is

$$F_\ell \sim \gamma(T)\ell^\theta \,, \tag{1.25}$$

where θ is the stiffness coefficient, $0 < \theta < (d-1)/2$ and γ is the stiffness modulus. Note that the direct implication of Eq. (1.25) is that there are possible only small excitations[6]. For $D = 3$ the situation concerning the spin-glass behavior is unclear. However, for $D = 2$ the droplet pictures is well established, in particular by the application of exact ground-state algorithms to obtain droplets for large system sizes [Har03].

In the *droplet scenario*, the correlation function decays as

$$C(|\mathbf{x}-\mathbf{y}|) = \overline{\langle s_\mathbf{x} s_\mathbf{y}\rangle^2} - \overline{\langle s_\mathbf{x}\rangle^2 \langle s_\mathbf{y}\rangle^2} \sim \frac{1}{|\mathbf{x}-\mathbf{y}|^\theta} \,, \tag{1.26}$$

where θ is the stiffness coefficient.
Still, the system can express only two pure states, so the overlap distribution is a delta function,

$$P(q) = \delta(q - q_{\mathrm{EA}}) \,. \tag{1.27}$$

[6] According to Eq. (1.25), a finite fraction, ℓ, of the total number of spins needs infinite energy to be excited.

Let us brevity explain which is the prescription of the *droplet model* in presence of an external magnetic field. The presence of an external magnetic field H modifies the boundary scaling of Eq. (1.24) as:

$$L^{\theta} - HL^{d/2}\,. \tag{1.28}$$

Because of the bound $\theta < (d-1)/2$, the spin-glass phase is unstable to the presence of any magnetic field.

CHAPTER II

Observable quantities in numerical simulations

In the last decades, numerical simulations have taken a central role in the investigation of physics supporting analytic work and experiments. This success is motivated by the advantage to measure directly the microscopical properties of systems only through the Hamiltonian knowledge. This approach has opened new perspective in the physical investigation since the analytic predictions are often not useful for the experimentalist. In spin-glasses, the analytics tools are exact only in infinite dimension, a limit that, of course, is not achievable in real samples. In this chapter we will introduce the main observable quantities in numerical simulations and analyses.

Some notation. Numerical simulations are the core of the results presented in this work. We carried on massive simulations on systems of N spins, both in regular d-dimensional cubic lattices of size $L^d = N$ (Part III), and in a film geometry, where $N = L^2 L_z$ and the thickness $L_z \ll L$ (Part II).
Each spin $\vec{s}_{\mathbf{x}}$ occupies a position $\mathbf{x}$ on the nodes of the lattice and has m components, $\vec{s}_{\mathbf{x}} = (s_{\mathbf{x},1}, s_{\mathbf{x},2}, \ldots, s_{\mathbf{x},m})$. If $m = 1$ we call them *Ising spins* and remove the vector symbol, $s_{\mathbf{x}}$. If $m = 3$ they are *Heisenberg spins*. A *configuration* is constituted by the set of all the spins $\vec{s}_{\mathbf{x}}$, which we denoted with a ket, $|\vec{s}\rangle$.

A thermalized configuration, at the working temperature T, follows the Boltzmann distribution

$$P(|s\rangle) \sim \mathrm{e}^{-\beta \mathcal{H}(|s\rangle)}\,, \tag{2.1}$$

where $\mathcal{H}$ is the model's Hamiltonian and $\beta = 1/k_{\mathrm{B}}T = 1/T$ is the inverse temperature, as we set to one the Boltzmann constant, $k_{\mathrm{B}} = 1$.

Once the system is thermalized, one can take thermal averages of any measurable observable $\mathcal{O}$ and we denote it with $\langle \mathcal{O} \rangle$. The averages over the disorder, instead, are indicated with an overline $\overline{\mathcal{O}}$.

Let us define the scalar product between two configurations $|s\rangle$ and $|s'\rangle$ through a

Dirac's notation:

$$\langle s|s'\rangle = \sum_{\mathbf{x}}^{N} \vec{s}_{\mathbf{x}} \cdot \vec{s}'_{\mathbf{x}} \ . \tag{2.2}$$

Now that the notation is established, we proceed describing the set of observables $\mathcal{O}$ that we measured in our simulations. Since in this dissertation we will present both equilibrium and dynamical results, in the following of this Section, we do not indicate the time dependence of the observable $\mathcal{O}$.

2.1 Overlaps

A spin glass, in the cold phase, is characterized by a broken phase space, where a configuration is constituted by a mixture of *pure states* [Cas05]:

$$|\cdot\rangle = \sum_{\alpha} w_\alpha \langle\cdot\rangle_\alpha \ , \tag{2.3}$$

where α is an index running over all the states, and w_α is the statistical (Gibbs) weight of state α.
For historical reason, we can identify these pure states as replicas of the system. We indicate different replicas using the superscripts $^{(a)}$,$^{(b)}$,$^{(c)}$ and $^{(d)}$.

In a disordered system the order parameter is the overlap. This quantity can measure the similarity between *states* and it has a gauge-invariance [Méz87].
The definition of overlap depends on the model we consider and on its symmetries.

Ising overlap For Ising spins $s_{\mathbf{x}} = \pm 1$ the local overlap is defined as

$$q_{\mathbf{x}} = s^{(a)}_{\mathbf{x}} s^{(b)}_{\mathbf{x}} \, , \tag{2.4}$$

and we can create the global overlap

$$q = \frac{1}{N} \sum_{\mathbf{x}}^{N} q_{\mathbf{x}} = \frac{1}{N} \langle s^{(a)} | s^{(b)} \rangle \ , \tag{2.5}$$

where we used notation (2.2).

Scalar overlap If the Hamiltonian is not invariant under a rotational transformation, the overlap can be expressed straightforwardly through the scalar product between the vector spins of different replicas. The site overlap would be

$$q_{\mathbf{x}} = \vec{s}^{\,a}_{\mathbf{x}} \cdot \vec{s}^{\,b}_{\mathbf{x}} \, , \tag{2.6}$$

and the global overlap

$$q = \frac{1}{N} \sum_{\mathbf{x}}^{N} q_{\mathbf{x}} \, . \tag{2.7}$$

2.2

Scalar correlators

The two-point correlation function $C(\mathbf{x},\mathbf{y}) = \langle q_{\mathbf{x}} q_{\mathbf{y}} \rangle$ has a central role in the simulation analysis. If it holds the translational invariance, one can express the two-point correlation function as a function of the separation $\mathbf{r} = \mathbf{y} - \mathbf{x}$:

$$C(\mathbf{x},\mathbf{y}) \to C(\mathbf{r}) = \frac{1}{N}\sum_{\mathbf{x}}^{N} q_{\mathbf{x}} q_{\mathbf{x}+\mathbf{r}} \ . \tag{2.8}$$

For any given wave vector $\boldsymbol{k}$ we can define the Fourier transformation of the correlation function $C(\mathbf{r})$ as

$$\hat{C}(\mathbf{k}) = \frac{1}{N}\sum_{\mathbf{r}} C(\mathbf{r}) \mathrm{e}^{\mathrm{i}\boldsymbol{k}\cdot\mathbf{r}} \,, \tag{2.9}$$

and $C(\mathbf{r})$ can be obtained back as its anti Fourier transformation

$$C(\mathbf{r}) = \frac{1}{L}\sum_{\mathbf{k}}^{L} \hat{C}(\mathbf{k}) e^{-ik\cdot\mathbf{r}} \,. \tag{2.10}$$

Let us calculate the wave-vector dependent susceptibilities:

$$\chi(\boldsymbol{k}) = N\left[\hat{q}(\boldsymbol{k})\hat{q}(\boldsymbol{k})^*\right] , \tag{2.11}$$

where, the Fourier transform of the overlap field is:

$$\hat{q}(\mathbf{k}) = \frac{1}{N}\sum_{\mathbf{x}}^{N} q_{\mathbf{x}} e^{ik\cdot x} \,. \tag{2.12}$$

Substituting Eq. (2.12) in Eq. (2.11), one can relate the susceptibilities to the correlation function:

$$\chi(\boldsymbol{k}) = \frac{1}{N}\sum_{\mathbf{x}}^{N} q_{\mathbf{x}} \mathrm{e}^{\mathrm{i}\boldsymbol{k}\cdot\mathbf{x}} \sum_{\mathbf{y}}^{N} q_{\mathbf{y}} \mathrm{e}^{-\mathrm{i}\boldsymbol{k}\cdot\mathbf{y}} = \tag{2.13}$$

$$= \frac{1}{N}\sum_{\mathbf{x},\mathbf{y}}^{N} C(\mathbf{x},\mathbf{y}) \mathrm{e}^{\mathrm{i}\boldsymbol{k}\cdot(\mathbf{x}-\mathbf{y})} = \tag{2.14}$$

that in the presence of translational invariance and recalling equation ((2.9)) becomes

$$= \frac{1}{N}\sum_{\mathbf{x}}^{N}\sum_{\mathbf{r}}^{N} C(\mathbf{r}) \mathrm{e}^{\mathrm{i}\boldsymbol{k}\cdot(\mathbf{r})} = \hat{C}(\boldsymbol{k}) \,. \tag{2.15}$$

This implies that one can measure correlation functions both in the real and in the Fourier space.

The two-point correlation functions are computed from the Fourier transform of the fields,

$$C(r) \;=\; \frac{1}{L}\sum_{n=0}^{L-1} \mathrm{e}^{-\mathrm{i}\mathbf{r}\cdot\boldsymbol{k}n}\chi\big(\boldsymbol{k}n\big) \;\equiv\; \sum_{y,z} C(x=r,y,z)\,, \tag{2.16}$$

where r is the modulus of the distance. Of course, we can align the lattice displacement vector $\mathbf{r}$ along any of three coordinate axes, so we average over these three choices.

2.3

Four-replica Correlators

In part III we will present our investigation on a spin-glass system in presence of an external magnetic field for temperature close to the critical temperature, $T \backsimeq T_g$. An Ising spin glass in presence of an external magnetic field is characterized by a no-zero order parameter, $q_{\mathrm{EA}} \neq 0$ even in the paramagnetic phase. This implies that the two-point correlation function $C(\mathbf{r})$ decays to a non-zero value, and one can not extract the correlation length value, ξ (see below for details).

The most informative connected correlation function, that goes to zero at infinite distance in presence of an external magnetic field, is the replicon $G_{\mathrm{R}}(\mathbf{r})$ [Alm78b, Dom06]

$$G_{\mathrm{R}}(\mathbf{r}) = \frac{1}{N}\sum_{\mathbf{x}} \overline{\left(\langle s_{\mathbf{x}} s_{\mathbf{x}+\mathbf{r}}\rangle - \langle s_{\mathbf{x}}\rangle\langle s_{\mathbf{x}+\mathbf{r}}\rangle\right)^2}\,. \tag{2.17}$$

To compute G_{R} we calculate the 4-replica field

$$\Phi_x^{(\mathrm{ab;cd})} = \frac{1}{2}(s_{\mathbf{x}}^{(\mathrm{a})} - s_{\mathbf{x}}^{(\mathrm{b})})(s_{\mathbf{x}}^{(\mathrm{c})} - s_{\mathbf{x}}^{(\mathrm{d})})\,, \tag{2.18}$$

where the indexes $\mathrm{a},\mathrm{b},\mathrm{c},\mathrm{d}$ indicate strictly different replicas. Notice that

$$\left\langle \Phi_{\mathbf{x}}^{(\mathrm{ab;cd})}\Phi_{\mathbf{y}}^{(\mathrm{ab;cd})}\right\rangle = \left(\langle s_{\mathbf{x}} s_{\mathbf{x}+\mathbf{r}}\rangle - \langle s_{\mathbf{x}}\rangle\langle s_{\mathbf{x}+\mathbf{r}}\rangle\right)^2\,, \tag{2.19}$$

so we obtain G_{R} by taking also the average over the samples [1]

$$E(\Phi_{\mathbf{x}}^{(\mathrm{ab;cd})}\Phi_{\mathbf{y}}^{(\mathrm{ab;cd})}) = G_{\mathrm{R}}(\mathbf{x}-\mathbf{y})\,. \tag{2.20}$$

Here, and everywhere there is more than one possible permutation of the replica indices, we average over a third of all the possible permutations to gain statistics (see Appendix C for details). From this point on everything is formally like the two-replica construction, using $\Phi_{\mathbf{x}}$ instead of $q_{\mathbf{x}}$ to construct the susceptibilities $\chi(\mathbf{k})$. For example correlations in the Fourier space are defined by Fourier-transforming $\Phi_{\mathbf{x}}^{(\mathrm{ab;cd})}$, so the wave-vector dependent replicon susceptibility is expressed as

$$\chi_{\mathrm{R}}(\mathbf{k}) = \frac{1}{N}E(|\hat{\Phi}_{\mathbf{k}}^{(\mathrm{ab;cd})}|^2) \quad , \quad \hat{\Phi}_{\mathbf{k}}^{(\mathrm{ab;cd})} = \sum_{\mathbf{x}}^{N} \mathrm{e}^{\mathrm{i}\mathbf{k}\cdot\mathbf{x}}\Phi_{\mathbf{x}}^{(\mathrm{ab;cd})}\,. \tag{2.21}$$

[1] The average is over the disorder.

2.4

Integral method for evaluating the correlation length

Historically, the determination of characteristic length scales was based on the evaluation of a particular functional form in the limit of very large distance. However, this approach is limited by the precise knowledge of the functional form that describes the interested phenomenon, which is very difficult, for example in the out-equilibrium regime. A more convenient method to estimate the characteristic length is though the Integral method [Bel08a, Bel09a]:

$$I_k = \int_0^\infty \mathrm{d}r\, r^k C(r) \tag{2.22}$$

$$\xi_{k,k+1} = \frac{I_{k+1}(T, t_\mathrm{w})}{I_k(T, t_\mathrm{w})}\,. \tag{2.23}$$

This method introduces a huge simplification. However, as the reader can notice, Eq. (2.22) holds only if the correlation function $C(\mathbf{r})$ decays to zero. In Part II we will use the two-point correlation function, $C(\mathbf{r})$ in Eq. (2.22); instead in Part III, we will exploit the replicon propagator $G_\mathrm{R}(\mathbf{r})$, Eq. (2.17).

CHAPTER III

Phase transitions with a diverging length scale

In this Section, we address an introduction to the main successful topics used for describing phase transitions. Our goal is not to give an extended treatment of the consolidated analysis tools, that can be found elsewhere (see e.g. [Ma76, Bin86, Hua87, Car96, Ami05]), but only to explain some concepts that we will be using throughout this dissertation.

3.1 Second-order-like phase transitions

A spin glass system is characterized by a second-order phase transition given by a divergence in the second derivative of the free energy as approaching the critical point, T_c from above.

For simplicity, we will refer to Ising spins, but the treatment is analogous for m-component spins. At the critical temperature, the relevant observables have a power-law divergence. These exponents are called *critical exponents* and control the phase transition. We can evaluate six critical exponents, $\alpha, \beta, \gamma, \delta, \eta, \nu$. Each one identifies a Universal class (see below for details).

The correlation length ξ can be defined through the long-distance decay of the two-point correlation function,

$$\langle s_{\mathbf{x}+\mathbf{r}} s_{\mathbf{x}} \rangle \overset{|\mathbf{r}|\to\infty}{\sim} \mathrm{e}^{-|\mathbf{r}|/\xi}\,, \tag{3.1}$$

and it has a power law divergence as approaching the critical temperature

$$\xi \propto |\tau|^{-\nu}\,, \tag{3.2}$$

where τ is the reduced temperature $\tau = \frac{T-T_c}{T_c}$, and T_c is the critical temperature. The

specific heat diverges as

$$C_{\mathrm{h}}(\tau) \sim |\tau|^{\alpha} \,. \tag{3.3}$$

The case $\alpha = 0$ can indicate a discontinuity or a logarithmic divergence. The magnetization m vanishes as

$$\hat{m}(\tau) \sim (-\tau)^{\beta} \tag{3.4}$$

when we approach the critical temperature from below. The susceptibility, which is the system's response to a small external field H , diverges like

$$\chi(\tau) \sim |\tau|^{\gamma} \,. \tag{3.5}$$

At exactly the critical point $\tau = 0$, for small fields H the magnetization behaves as

$$m(\tau = 0, h) \sim |h|^{1/\delta} \,, \tag{3.6}$$

and the two point correlation function decays with a power-law

$$\langle s_{\mathbf{x}+\mathbf{r}} s_{\mathbf{x}} \rangle \overset{|\mathbf{r}|\to\infty}{\sim} |\mathbf{r}|^{-(d-2+\eta)} \,, \tag{3.7}$$

where η is the anomalous dimension.

These critical exponents are constrained by a set of four independent *scaling relations*,

$$\begin{aligned} 2\beta + \gamma &= 2 + \alpha \,, \\ 2\beta\delta - \gamma &= 2 + \alpha \,, \\ \gamma &= \nu(2 - \eta) \,, \\ \nu d &= 2 - \alpha \,. \end{aligned} \tag{3.8}$$

that reduce to two the number of independent exponents.

The four relations in Eq. (3.8) relate the exponents to the dimension of space and they define the so-called *hyperscaling* relation. They are valid only under the upper critical dimension d_u.
The universality class depends on the system dimension through the critical exponents, see Eq. (3.8).

3.2

Real-space coarse graining

The coherence length ξ is the characteristic length scale and represents the size of patches of correlated spins. If in ferromagnetic system this physical interpretation is straightforward [Ma76, Hua87, Ami05], in disordered ones there are still controversy [Har76, Dot87, Dot01, Ang13].

The microscopical interaction between correlated spins can be detected by performing a coarse-graining of size b on the system. To construct a block Hamiltonian, the

domain of correlated spins needs to sensible larger than the coarse-graining step b, $\xi \gg b$. Note that the block Hamiltonian is linked to the original one through the extensive ownership only in the thermodynamical limit. The block variables $\sigma_{\mathbf{x}}$ can be defined as the mean spin in the block

$$\sigma_{\mathbf{x}} = b^{-d} \sum_{\mathbf{y} \in \mathbf{x}}^{b^d} s_{\mathbf{y}} \,, \tag{3.9}$$

where the sum runs over all the spins $s_{\mathbf{y}}$ that belong to the block σ_x. Notice that there will be $L^d b^{-d}$ blocks, and each one includes exactly b^d spins. The probability distribution for the blocks of spins is

$$\begin{aligned} P'[\{\sigma\}] &= \left\langle \prod_{\mathbf{x}} \delta \left(\sigma_{\mathbf{x}} - b^{-d} \sum_{\mathbf{y} \in \mathbf{x}}^{b^d} s_{\mathbf{y}} \right) \right\rangle_P \propto \\ &\propto \int \mathrm{e}^{-\mathcal{H}[\{s\}]/T} \prod_{\mathbf{x}} \delta \left(\sigma_{\mathbf{x}} - b^{-d} \sum_{\mathbf{y} \in \mathbf{x}}^{b^d} s_{\mathbf{y}} \right) ds_1 ds_2 ... ds_N \equiv \\ &\equiv \mathrm{e}^{-\mathcal{H}_{\mathrm{block}}[\{\sigma\}]/T} \,, \end{aligned} \tag{3.10}$$

where with $\langle \ldots \rangle_P$ we indicate the average using the equilibrium distribution P of the spins $s_{\mathbf{y}}$:

$$P \propto \mathrm{e}^{-\mathcal{H}[\{s\}]/T} \tag{3.11}$$

and $\mathcal{H}_{\mathrm{block}}$ is the block Hamiltonian deriving from the coarsening we made. At the critical temperature T_{c} the correlation length diverges, so our Hamiltonians, $\mathcal{H}_{\mathrm{block}}$ and $\mathcal{H}$, are always equivalent.

3.3

Scaling hypothesis and Widom scaling

Widom was the first to conjecture the scaling hypothesis [Wid65]:
"at the critical temperature, T_{c}, the singular behavior of the correlation length is due to long-range interaction of spin fluctuations and ξ is the only relevant length."

Let us formalize this setting. We assume that the coarse-graining procedure does not change the free energy:

$$\mathcal{F} = \mathcal{F}_{\mathrm{coarse}} \tag{3.12}$$

in the thermodynamical limit, $L \to \infty$.
We remark as this approach focus only on the long-range correlations that arise from

being at criticality. Analogously to Eq. (3.9), we can write the renormalized temperature $\tilde{t}$ and field $\tilde{h}$ as

$$\begin{cases} \tilde{\tau} = \tau\, b^{y_\tau} \\ \tilde{h} = h\, b^{y_h}\,, \end{cases} \tag{3.13}$$

where y_τ and y_h are generic exponents that contains all the rescaling dependence. Using Eq. (3.13) and (3.12), the intensive free energy scales as

$$f(\tau, h) = b^{-d} f(\tilde{\tau}, \tilde{h}) = b^{-d} f(\tau\, b^{y_\tau}, h\, b^{y_h})\,. \tag{3.14}$$

In order to relate the y_τ and y_h to the critical exponents [see Eq. (3.8)], we study the behavior of the magnetization m [Par88]:

$$m(\tau, h) = \frac{\partial f(\tau, h)}{\partial h} = b^{-d} \frac{\partial f(\tau\, b^{y_\tau}, h\, b^{y_h})}{\partial h} = b^{y_h - d} m(\tau\, b^{y_\tau}, h\, b^{y_h})\,. \tag{3.15}$$

Since b is an arbitrary scaling parameter, we can set it to grow as any diverging function of $\tilde{\tau}$ or $\tilde{h}$. Let us take the zero-field limit $h = 0$ and choose $b = (-\tau)^{-1/y_\tau}$, so Eq. (3.15) becomes

$$m(\tau, 0) = (-\tau)^{(d - y_h)/y_\tau} m(-1, 0)\,. \tag{3.16}$$

Comparing Eq. (3.4) to Eq. (3.16), we can relate the rescaled temperature $\tilde{\tau}$ and field $\tilde{h}$ to the critical exponent β, as follows:

$$\beta = (d - y_h)/y_\tau\,. \tag{3.17}$$

On the other hand, if we study the behavior of the magnetization, see Eq. (3.15), along the critical curve $\tau = 0$ with a helpful choice of b, $b = h^{-1/y_h}$, we obtain:

$$m(0, h) = (h)^{(d - y_h)/y_h} m(0, 1)\,. \tag{3.18}$$

For a small h value, the behavior of the magnetization m along the critical line is:

$$m(0, h) \sim h^{1/\delta} \tag{3.19}$$

and so, exploiting Eq. (3.6), we obtain a second relation between the y_τ and y_h and the critical exponents:

$$\delta = y_h/(d - y_h)\,. \tag{3.20}$$

Using Eqs. (3.8) one can easily reconstruct all the other critical exponents.

3.4

Finite-size scaling

Finite-size scaling (FSS) is one of the most powerful technique for measuring the thermodynamical properties by using the lattice L as a scaling variable. The idea is the

same as the one we have explained in the previous section for the coarse-grained parameter b.

FSS was proposed by Nightingale [Nig76] and developed by Binder [Bin82]. Its success is visible to the amount of scientific papers whose exploited it to analyze second order phase transitions in the field of spin glasses (see e.g. [Bin86, Bal96b, Bal98, Bal00, Lee03, Cam06, Jör06, Leu08, Jör08, Has08, Fer09, Bn12b, BJ13, BJ14c, Lul16, Fer19b]).

For any observable $\mathcal{O}$ that has, approaching the critical temperature, a power-law divergence, $\mathcal{O} \propto |\tau|^{x_\mathcal{O}}$ [1], one can always express its thermal average close to the critical point through a Taylor expansion

$$\begin{aligned} \langle \mathcal{O}(L,T) \rangle &= L^{x_\mathcal{O}/\nu} \Big[f_\mathcal{O}(L^{1/\nu}(\tau)) + L^{-\omega} g_\mathcal{O}\big(L^{1/\nu}\tau\big) \\ &+ L^{-2\omega} h_\mathcal{O}\big(L^{1/\nu}\tau\big) + \dots \Big], \end{aligned} \tag{3.21}$$

where $f_\mathcal{O}, g_\mathcal{O}$ and $h_\mathcal{O}$ are analytic scaling functions for observable $\mathcal{O}$, while ν is the critical exponent defined in Eq. (3.2). The exponent $\omega > 0$ is universal, and it expresses the finite size corrections to the dominant scaling. The lower dots, ..., stand for subleading corrections to scaling.

These topics will be vital for the analysis that we will address in Chapter 5. There, we will construct several dimensionless quantities to evaluate the scaling behavior of a thin glassy film.

3.5 Universality and RG flow

The Renormalization Group (RG) method has these assumptions:

- in the thermodynamical limit and close to the critical point (for spin glass system the critical point is the critical temperature T_c), the coarse-graining transformation (Eq.(3.9)) does not significantly change the free energy [Eq. (3.12)].
- Since the rescaled parameter b is arbitrary, see Eq. (3.13), we can build a flow of rescaled trajectories that converges to a fixed point in the space of the rescaled parameters. In other words, a fixed point attracts the RG trajectories that start in a finite region around it. Geometrically, this region is a hypersurface in the space of the scaling variables.
- In the thermodynamical limit, the behavior of a system is controlled by its fixed point. This implies the concept of universality. Two systems characterized by different Hamiltonians, if they are dominated by the same fixed points, belong to the same universality class.

[1] For notation clarity, τ is the reduced temperature $\tau = (T - T_c)/T_c$.

Let us be more precise taking as example the Ising model [Hua87] with $d > 1$ spatial dimensions and a zero external magnetic field, $h = 0$. The system has a second-order phase transition at a temperature T_c and it has a single control parameter t (see Eq. (3.13)). This implies that the critical hypersurface of the rescaled trajectories is only a point. There are a zero-temperature and an infinite-temperature stable fixed point, respectively governing the behavior of the ferromagnetic and of the paramagnetic phases (see Fig. 3.1). The fixed points are classified as:

- stable if it is attractive: the RG trajectories, starting from a neighborhood of the hypersurface, converge to the considered fixed point.
- Otherwise, the fixed point is unstable: the RG trajectories, starting from a neighborhood of the hypersurface, go away from the considered fixed point.

The two fixed point of Fig. 3.1 are separated by a fixed point at T_c that represents the critical point. On one hand, if the system is close to the critical temperature, but

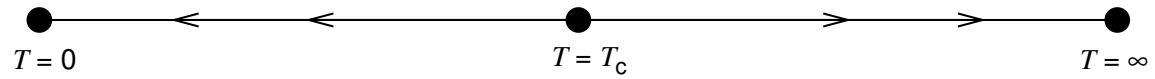

Figure 3.1: RG flow in the Ising model in absence of an external magnetic field, $h = 0$. The only control parameter is the temperature. There are two stable fixed points at zero and infinite temperature, and one unstable fixed point at the critical temperature T_c. The arrows represent the direction of the flow. Figure from [BJ15].

above it, $T > T_c$, the RG trajectory will converge to the $T = \infty$ fixed point after a large enough number of coarse-graining steps. On the other hand, if the system is close to the critical temperature, but below it, $T < T_c$, the system is described by the zero-temperature fixed point after a large enough number of coarse-graining steps. In Fig. 3.1, we represent the flow directions through arrows. Being the critical fixed point unstable implies that a trajectory can converge to it only if it starts exactly at $T = T_c$. As long as $t \simeq 0$, the behavior of a system will need a very large number of coarsening steps before acting as the stable infinite-temperature (or zero-temperature) fixed point prescribes.

This concept will be deeply developed in Chap. 6. Note that the fixed point depends on the geometry of the system. We will use this concept in Part II in order to demonstrate that a glassy film is governed by the $2D$ and $3D$ fixed points.

Part II

The Edward-Anderson model in film geometry

CHAPTER IV

Introduction

Historically, experiments and numerical simulations in the investigation of spin-glass systems have been developed separately. The numerical simulations were not able to approach experimental times, while the quality of experimental data was not yet high enough. Moreover, the crucial physical quantities that one can measure in experiments and simulations are not the same. In the simulations, one can easily access the microscopical configurations; instead, in the experiments, one can evaluate the response functions. Hence, a fruitful comparison between these two approaches was impossible.

In the last decades, the experimental data has sensible increased quality and the remarkable simulations of the dedicated supercomputer, Janus II, for the first time, can measure numerically spin-glass correlations that approach experimental time and length scales. The synergy between experiments and simulations have got several steps forwards in the comprehension of the $3D$ spin-glass dynamics [BJ18, BJ17a, Zha20b]. In the lab, spin-glass samples are permanently out of equilibrium when studied at temperatures below the critical one, $T_{\rm g}$, implying that the equilibrium theory is not always sufficient. A possible approach to overcome this difficulty is extracting from the non-equilibrium dynamics crucial information about the (so difficult to reach) equilibrium regime [Cug93, Fra99, AB10b, BJ17b]. However, custom-built computers [BJ14b] and other simulation advances [Man15a, Fer15] have made it possible to study theoretically [Bel08b, Bel09a, Man15b, BJ17a, BJ18, Fer19b, Fer18a] the simplest experimental protocol. In this protocol, see e.g. [Joh99], a spin-glass at some very high-temperature is fastly quenched to the working temperature $T < T_{\rm g}$ and the excruciatingly slow growth of the spin-glass correlation length ξ is afterward studied as a function of the time elapsed since the quench, t. Although simulations do not approach yet the experimental time and length scales ($t \sim 1$ hour and $\xi \sim 100\, a_0$, where a_0 is the average distance between magnetic moments), the range covered is already significant: from picoseconds to milliseconds [Man15a, Fer15] or even 0.1 seconds using dedicated computers [Bel08b, BJ18] (or conventional ones in the case of two-dimensional spin glasses [Fer19b, Fer18a]).

Yet, thanks to advances in sample preparation, a new and promising experimental

protocol has appeared in the last five years. Indeed, single-crystal spin-glass samples with a thin-film geometry (thickness of $4.5 - 20$ nm) have been investigated [Guc14, Guc17, Zha17b, Ken18]. These experiments are interpreted in terms of a correlation length ξ saturating at a constant value after reaching a characteristic length scale, namely the thickness of the film. The bounded growth of ξ along the longitudinal direction of the film is a direct experimental confirmation [Guc14] for a lower critical dimension $2 < D_\ell < 3$, in agreement with the theoretical expectation $D_\ell \sim 2.5$ [Bra86, Fra94, Mai18]. The film-geometry has allowed as well for extremely accurate measurements [Zha17b] of the aging rate

$$z(T, \xi) = \frac{\mathrm{d}\,\log t}{\mathrm{d}\,\log \xi}\,, \tag{4.1}$$

which gives access to the dominant free-energy barrier Δ, $t \sim \tau_0 \exp[\Delta/(k_{\rm B}T)]$ [1] [$\tau_0 = \hbar/(k_{\rm B}T_{\rm g})$ is a time scale]. The increased accuracy has shown that, contrary to previous expectations [Joh99, Bel08b, Bel09a, BJ17a], the aging rate depends on ξ (see also [Ber04, BJ18]). Besides, the dependency of the barrier Δ with the applied magnetic field has been clarified [2] [Guc17, Zha20b]. However, a theoretical study of these fascinating thin-film experiments was lacking.

This part is organized as follows. In Sec. 4.1 we summarize the spin-glass physics in $2D$ and $3D$. In Sec. 4.2, we formalize all the observables that we will take into account for evaluating glassy film systems. In Sec. 4.3, we report the numerical details of our massive computer simulations. Finally, in Chap. 5 , we will report our investigation of the equilibrium properties of a thin glass film at the critical $3D$ temperature. Next, in Chap. 6 we unveil the out-equilibrium properties that are characterized by four aging regimes and through the Renormalization Group (RG) approach we found a non-trivial temperature mapping between a film and a $2D$ system.

4.1

$2D$ and $3D$ spin-glass

Let us discuss a few crucial facts about the very different behavior of spin-glasses in spatial dimensions $D = 2$ [Fer18a, Fer19b] and $D = 3$ [BJ18]

4.1.1 Glassy bulk system

A $3D$ spin-glass system has a phase transition at $T = T_g$ that separates the high-temperature paramagnetic phase from the spin-glass phase [Gun91, Pal99, Bal00,

[1] At the critical temperature $T_{\rm g}$, the aging rate coincides with the so-called dynamic critical exponent

[2] In part III, we will report the experimental behavior of the free energy barrier Δ in presence of an external magnetic field in a mono-cristal of CuMn 6at%.

Har99a]. The correlation length, $\xi(T,t)$, diverges as a power-law:

$$\xi(T,t) \sim |\frac{T-T_g}{T_g}|^{-\nu_{3D}} \,, \tag{4.2}$$

where $\nu_{3D} = 2.56(4)$ and the critical temperature $T_g = 1.1019(2)$ [BJ13].

In the out-equilibrium regime, the size of the glassy domains is seen to grow as:

$$\xi(t,T) \propto t^{1/z(T)} \tag{4.3}$$

where the exponent $z(T)$ is the aging rate and t is the time. The aging rate is defined as:

$$z(T,\xi) = \frac{\mathrm{d}\,\log\, t}{\mathrm{d}\,\log \xi} \,, \tag{4.4}$$

which is expected to behaves, in first approximation, as [BJ18]:

$$z(T) \backsimeq z(T_g)\frac{T_g}{T} \,, \quad z(T_g) = 6.69(6) \,. \tag{4.5}$$

According to Ref. [BJ18], the aging rate, $z(T)$, is ξ-independent at exactly $T = T_g$. Otherwise it has subleading corrections depending on the correlation length itself. At $T < T_g$, but only once ξ grows large-enough [BJ18], the aging-rate grows with ξ. This implies that the dynamics has a slows-down, and a power-law description is no longer appropriate, see Eq. (4.3).

The aging rate, $z(T)$, is a key quantity since it is measurable both experimentally and numerically. In particular, it is connected to the dominant free-energy barrier Δ

$$t \sim \tau_0 \exp\left(\frac{\Delta}{k_{\mathrm{B}}T}\right) \tag{4.6}$$

where $\tau_0 = \hbar/(k_{\mathrm{B}}T_g)$ is a time scale.

A simplifying feature is that the renormalized aging-rage $z(T,\xi)T/T_g$ turns out to be roughly T-independent: when $T < T_g$, the dominant barrier $\Delta(\xi)$ depends little (or not at all) on temperature.

4.1.2 Spin-glasses in $D = 2$

A $2D$ spin-glass system has been deeply studied both experimentally and numerically [Har01, Amo03, Luk04, Luk06, J̈06, Fer16b, Fer16a] but for decades its dynamics has puzzled physicists.

On the experimental side, $2D$ spin-glasses were first analyzed in Ref. [Sch93] and the authors assumed *activated dynamics*. Activated dynamics involves a faster divergence of the characteristic time than a conventional power law. At low temperatures, the typical barrier height of the free-energy is:

$$\Delta \sim \xi^{\psi} \quad 0 \leq \psi \leq d-1 \,. \tag{4.7}$$

and, exploiting Eq. (4.6), one can connect the typical barrier height to the characteristic time τ, which means that τ grows with ξ faster than any power law (quite a severe dynamic slowdown, indeed).

On the other hand, pioneering simulations of the $2D$ Ising spin-glass dynamics could not solve whether behaves as critical or activated [Rie94, Bar01]. The controversy was solved recently in Ref. [Fer18a, Fer19b]. The authors clarified the dynamical behavior of a $2D$ spin-glass using a large-scale numerical simulation of the out-equilibrium dynamics of the $D = 2$ Ising spin-glass. They followed the microscopic spin-glass coherence length $\xi(t_{\rm w}, T)$ from *virtually* zero to its equilibrium value $\xi_{\rm eq}(T)$. In Ref. [Fer18a] the authors demonstrated that the $2D$ dynamics has different dynamical regimes and its dynamics could be classified as *critical* or *activated*.

A possible estimation for the lower critical dimension for spin-glass systems is $D_\ell = 2.5$. Evidences for the lower critical dimension D_ℓ value are supported by renormalization group studies [Fra94], by domain-wall calculations [Har99b, Boe05], and by experiments [Guc14]. From this point of view, spin-glass systems with dimension $D \geq D_\ell$ are characterized by a finite critical temperature [Gun91, Pal99, Bal00]. In $D = 2$ the Ising spin-glass remains paramagnetic for any temperature $T > 0$, but it has a critical limit at $T = 0$. Very good evidence for this fact was obtained through exact ground-state and domain-wall calculations for large systems sizes [Har01]. A good proof of this was achieved by exact ground-state and domain-wall calculations for large systems sizes [Har01]. In the $T \to 0$ the physics of the system is dictated by the low energy configurations and by the coupling interactions $J_{\mathbf{xy}}$. If the $J_{\mathbf{xy}}$ are discrete, binary coupling with 50% probability, an energy gap appears. Instead, the gap disappears if the couplings $J_{\mathbf{xy}}$ have associated a probability distribution that allows approaching with continuity the value $J = 0$ [Fer16b].

Depending on the nature of the coupling distribution, *i.e.* binary or gaussian, several Renormalization Group (RG) fixed points appear at $T = 0$. However, most of these fixed points are unstable even for the tiniest positive temperature [Amo03]. This implies that, for infinite system and $T > 0$, only one of those fixed points dominates and, so, the growth of the coherent correlation length $\xi(t)$ is ruled by a single scaling function [Fer18a].

Being in $2D$, the system is always in the paramagnetic phase, and $\xi(t, T)$ eventually reaches its equilibrium limit $\xi_{\rm eq}(T)$, which we expect to have a critical point at $T = 0$:

$$\xi_{\rm eq}(T) \sim T^{-\nu_{\rm 2D}} + ..., \tag{4.8}$$

where $\nu_{\rm 2D} = 3.580(4)$ [Kho18] and the dots stand for subleading corrections to scaling [Fer19b].

When $a_0 \ll \xi(t, T) \ll \xi_{\rm eq}(T)$ we have a power law:

$$\xi \propto t^{1/z_{\rm 2D}} \tag{4.9}$$

with $z_{\rm 2D} \approx 7.14$ irrespective of T [Fer19b]. This implies that the $2D$ dynamics may be much faster than $3D$ dynamics (aging rates $z \sim 15$ are not uncommon in 3D at low T). For times scale $t \gg \tau_{\rm eq}^{\rm 2D}(T)$, where $\tau_{\rm eq}^{\rm 2D}(T)$ is the equilibrium characteristic

autocorrelation time, equilibrium is approached. A super-Arrhenius behavior is found for

$$\tau_{\rm eq}^{\rm 2D}(T) \propto \exp[\Delta^{\rm 2D}(\xi_{\rm eq})/T] \,, \tag{4.10}$$

where the barrier $\Delta^{\rm 2D}(\xi_{\rm eq})$ grows very mildly with $\xi_{\rm eq}$ [Fer19b].

Let us conclude this Section defining the $2D$ asymptotic equilibrium behavior of the correlation function [Fer18a]:

$$C^{\rm eq}(r) \sim \frac{K_0(r/\xi_{\rm exp})}{\log(\xi_{\rm exp})} \,, \tag{4.11}$$

where $K_0(\cdot)$ is the zero order modified Bessel function of the second kind [Olv10] and $\xi_{\rm exp}$ is the "exponential" correlation length[3]

4.2

Observables in a thin glassy film

In Chap. 2, we have introduced the main observables that we will take into account in this dissertation. Here, we report the derivation of these observables in a film geometry. We will address them in the out-equilibrium formulation, but the equilibrium one can be obtained trivially by just dropping the time.

4.2.1 Longitudinal and transversal correlation length

The spatial autocorrelation function [Bel09b] is defined as:

$$C_4(T,\vec{r},t) = \overline{\langle q^{(a,b)}\left(\vec{x},t\right) q^{(a,b)}\left(\vec{x}+\vec{r},t\right)\rangle_T} \,. \tag{4.12}$$

The overlap between two replicas is

$$q^{(a,b)}\left(\vec{x},t\right) \equiv \sigma^{(a)}\left(\vec{x},t\right)\sigma^{(b)}\left(\vec{x},t\right) \tag{4.13}$$

where (a,b) are labels for different replicas, $\overline{(\cdots)}$ denotes the average over the disorder and $\langle\cdot\rangle_T$ stands for the average, over the thermal noise at temperature T.
The longitudinal correlation length $\xi_{12}^{\parallel}(t)$ is defined on the *longitudinal* lattice displacements $\vec{r}=(r,0,0)$ or $\vec{r}=(0,r,0)$ as:

$$C_4\left(T,\vec{r},t\right) \sim \frac{f(u,v)}{r^{\theta}} \,,\; u = \frac{r}{\xi^{\parallel}(T,t)} \,,\; v = \frac{\xi^{\parallel}(T,t)}{\xi_{\rm eq}^{\parallel}(T)} \,, \tag{4.14}$$

where $f(u,v)$ is an unknown scaling function.
In equilibrium, the $f(u,v=1)$ decays for large u as $\exp(-u)/\sqrt{u}$ [Fer18a]. Moreover $v=1$ is reachable in a film at $T<T_{\rm c}$ only thanks to the 3D-to-2D crossover [Guc14].

[3]The accurate definition of $\xi_{\rm exp}$ is discussed in Chapter 5

On the other hand, off-equilibrium, $f(u, v<1)$ decays super-exponentially in u [Fer18a] and a Renormalization Group (RG) argument implies that the scaling function $f(u, v)$ depends as well on the effective *two-dimensional* temperature $T_{\text{eff,2D}}$, [see Sec.6.3 for details]. Fortunately, we can study the dynamical growth of $\xi^{\parallel}$ without parameterizing $f(u, v)$ through the integral estimators [Bel08b, Bel09a]:

$$I_k(T,t) = \int_0^\infty \mathrm{d}r\, r^k C_4(T,r,t) \tag{4.15}$$

and so

$$\xi^{\parallel}_{k,k+1}(T,t) \equiv I_{k+1}(T,t)/I_k(T,t) \tag{4.16}$$

We shall specialize to $\xi^{\parallel}_{12}(T,t)$ which has been roughly studied [BJ18, Fer19b, Fer18a].

As for correlations along the short transverse direction, we defined the *transversal* correlation length $\xi^{\perp}_{12}$ through

$$\xi^{\perp}_{12}(T,t) = \sum_{r=0}^{L_z/2} r^2 C_4^{\perp}(T,r,t) / \sum_{r=0}^{L_z/2} r\, C_4^{\perp}(T,r,t)\ , \tag{4.17}$$

where, for open boundary condition (OBC), one can extend the sum over $L_{\mathrm{z}} - 1$.

4.2.2 Renormalization Group Transformation

Being at the critical temperature, T_{g}, we can study the system through a Renormalization Group (RG) perspective [Ami05]. We decompose our system in boxes of size L_z^3 and we rescale the overlap field as:

$$Q^{(\mathrm{a,b})}(\mathbf{X},t) = \frac{1}{L_z^3} \sum_{r_1,r_2,r_3=0}^{L_z-1} q^{(\mathrm{a,b})}(\mathbf{r} + L_z\mathbf{X}, t)\ , \tag{4.18}$$

and we define the correlation function in the 2D renormalized lattice as:

$$C_4^{\mathrm{RG}}(T;\mathbf{R},t) = \overline{\langle Q^{(\mathrm{a,b})}(\mathbf{X},t) Q^{(\mathrm{a,b})}(\mathbf{X}+\mathbf{R},t)\rangle_T} \tag{4.19}$$

We gain statistics by averaging over all the L_z^3 possible starting position of the boxes and all pairs of different replicas. Our analysis's program exploits the last chips extension SEE2 to minimize the computational effort [4].
The estimate of the correlation length was done as well through the integral estimators, see Eq. 4.16:

$$I_k^{\mathrm{RG}}(T,t) = \int_0^\infty \mathrm{dR}\, \mathrm{R}^k C_4^{\mathrm{RG}}(T,R,t)\ , \tag{4.20}$$

and we estimate the correlation length as

$$\xi^{\mathrm{RG}}_{k,k+1}(T,t) = I^{\mathrm{RG}}_{k+1}(T,t)/I^{\mathrm{RG}}_k(T,t)\ . \tag{4.21}$$

These RG-transformations will be used in the following for evaluating the dimensional crossover, $D = 3 \to 2$, that controls the dynamics of a spin-glass film.

[4] SEE2 stands for *Streaming SIMD Extensions*

4.3 Simulations

Metropolis dynamics belongs to the universality class of physical evolution and is straightforward to implement.
Our goal is to obtain data without finite-size effects and within the thermodynamic limit. Rather than restoring to special hardware, we employed synchronous multispin coding on standard CPUs. We implemented two multispin codings on a film geometry: the MUlti SAmple (MUSA) and the MUlti SIte (MUSI) multispin coding.

The MUSA algorithm is based on the representation of many sample systems in a single computer word (128 bits in our implementation), i.e. each bit represents a different sample; instead, the MUSI one represents many spins of the same replica in a single computer word (256 bits in our implementation). The code implementing MUSA is much simpler than the MUSI one, and thus, it was adequate for the equilibrium simulations and for the first set of the out-equilibrium ones [5]. In particular, we used it for carrying on the simulation with OBC along the Z direction. The MUSA efficiency does not depend on the choice of boundary conditions. On the Intel(R) Xeon(R) E5-2680v3 processors of the *Cierzo* cluster [6], our MUSA code simulates 24 replicas of the same sample at a rate of 12 picoseconds per spin flip. The optimal number for N_{R} is given by the memory-consuming coupling matrix which is shared by the N_{R} replica.

On the other hand, the MUSI code has longer development times but is significantly faster than MUSA. MUSI codes update $\sim \exp(4/T)$ spins with a single random number [Fer15] and it is faster as the decreasing of temperature.
At our highest temperature $T = 1.1$, on the E5-2680v3 processors, our MUSI code simulates 24 replicas at an overall rate of 8 picoseconds per spin flip. Unfortunately, the MUSI code is not completely general, it has some limitations:

- it supports only Periodic Boundary Condition (PBC). For open boundary conditions, spins on the top (or bottom) layer have only 5 neighbors, which implies that one can only update $\sim \exp(2/T)$ spins with a single random number.
- The lattice size can be only a multiple of 16 and the thickness can be pair. In Appendix A, we will explain in detail the MUSI implementation in a film geometry and how to manage the random number generator.

4.3.1 The optimal number of replica N_{R} and samples N_{S}

Our MUSA implementation simulates contemporaneity 128 *independent* samples and the optimal number of N_{R} is given by memory-sharing reason. On the other hand, the speed-up of the MUSI code[7] is given by the packing of the spins in the computer words. Hence, the choice of the optimal number of replica N_{R} and samples N_{S} was chosen in

[5] The first set of simulations is the one characterized by a short thickness, $L_z \leq 6$.
[6] The Cierzo cluster is at the BIFI supercomputing center
[7] The MUSI implementation was used only for the out-equilibrium simulations.

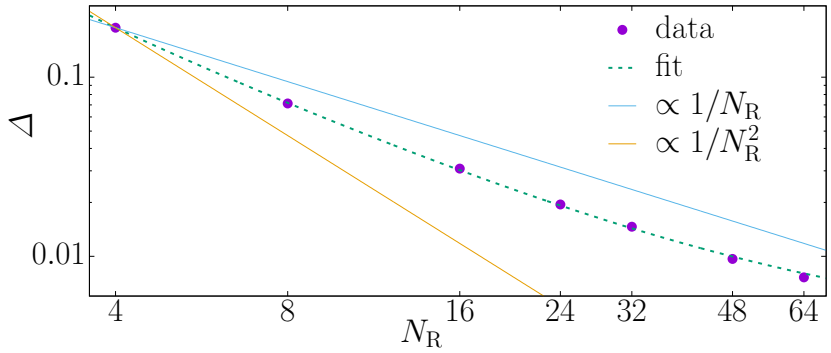

Figure 4.1: **Squared statistical error** for $\xi_{12}(T_c, t=2^{22}, L_z=4)$, as computed from a set of $N_S = 128$ samples and N_R replicas, versus N_R. The dashed line is a fit to Eq. (4.22). The relevant quantities extracted from the fit are $\sigma_R^2/\sigma_S^2 \approx 156$ and $x \approx 0.65$. For reference, we show with continuous lines the two extremal behaviors, namely $x = 1$ (with $\Delta \propto 1/N_R^2$) and $x = 0.5$ (with $\Delta \propto 1/N_R$). Because $\sigma_R^2 \gg \sigma_S^2$, Δ shows an intermediate behavior for small N_R. However, when $N_R > 30$ the contribution of thermal fluctuations to the final error becomes comparable to the sample contribution and there is little gain in further increasing N_R.

order to minimize the final errors of the correlation length $\xi_{12}^{\parallel}(t)$, [see Eq. (2.23)], given a fixed computer effort $E = N_S N_R$.
The variance, or the squared error, in ξ_{12} approximately follows this behavior in the off-equilibrium regime [BJ18]:

$$\Delta(N_S, N_R) = \left[\sigma_S^2 + \sigma_R^2 \left(\frac{2}{N_R(N_R-1)}\right)^x\right] \frac{1}{N_S}\,, \tag{4.22}$$

where the exponent x takes a value in the range $0.5 < x < 1$, σ_S^2 and σ_R^2 are (respectively) the sample and thermal contributions to the variance and $N_R(N_R-1)/2$ is the number of distinct pairs of replica indices for calculating $C_4(\vec{r}, t)$ [8].
Clearly, we are looking for a compromise by minimizing the (squared) error achievable for a fixed numerical effort $E = N_R N_S$, which results into an optimal value

$$N_R^* \approx \left[2^x (2x-1) \frac{\sigma_R^2}{\sigma_S^2}\right]^{1/(2x)}\,, \tag{4.23}$$

where for algebra's simplicity we approximate $N_R(N_R-1) \approx N_R^2$. Now, we need to estimate the ratio σ_R^2/σ_S^2 and the exponent x and we followed these steps.
We carried out short MUSI runs with $t = 2^{22}$ at T_c, for thickness $L_z = 4$, with $N_R^{tot} = 72$ and $N_S = 128$. We randomly extracted $N_R = 4, 8, 16, 24, 32, 48$ and 64 replicas out of the ensemble of N_R^{tot} possibilities, and computed ξ_{12} and its squared error $\Delta(N_S, N_R)$ with the jackknife method, see e.g. Ref. [Ami05] or Appendix B.1.
In order to stabilize the estimation of Δ we averaged over 20 random extractions of the N_R replicas. The obtained $\Delta(N_R, N_S)$ are shown in Fig. 4.1 with our fit to Eq. (4.22).

[8] The exponent x depends on the dimension of the system.

The resulting optimal value is $N_{\mathrm{R}}^{*} \approx 29.4$ which is compatible with the approximated value $N_{\mathrm{R}}^{*} \approx 27.3$ in Eq. (4.23).
However, by plugging $N_{\mathrm{S}} = E/N_{\mathrm{R}}$ in Eq. (4.22) and varying N_{R} while keeping E fixed, we observed that the minimum at N_{R}^{*} is quite broad, which is fortunate because the value that optimizes the performance of our MUSA code on the *Cierzo* processors is $N_{\mathrm{R}} = 24$.

CHAPTER V

Equilibrium properties of a thin glassy film at the bulk temperature

In this chapter, we study the equilibrium properties of a thin glassy film at the $3D$ critical temperature for several thickness and lattice values, Sec. 5.1. In Sec. 5.2 we evaluate the correlation function in the film geometry and in the rescaled lattice after a Renormalization Group (RG) transformation. Next, in Sec. 5.3 exploiting a Finite-Size Scaling (FSS) approach, we confirm the existence of glassy behavior in the film geometry as it was supposed in the experiments of the last generations, [Guc14, Guc17, Zha17b, Ken18]. In Sec. 5.4 we calculate the universal coefficient of some dimensionless observables.

5.1 Model and protocol

We considered the Edward-Anderson model [Edw75], defined on a three-dimensional film geometry characterized by a lattice $L_x = L_y = L$ and a width L_z on whose nodes we placed spin $\sigma = \pm 1$ that interact with their first neighbors through:

$$\boldsymbol{H} = -\sum_{\langle \mathbf{x},\mathbf{y} \rangle} J_{\mathbf{xy}} \sigma_{\mathbf{x}} \sigma_{\mathbf{x}} \ , \tag{5.1}$$

where the quenched disordered couplings are $\{J_{\vec{xy}}\} = \pm 1$ with 50% probability.
We imposed open boundary conditions (OBC) along all the three Cartesian directions [1] and we simulated our system for different thickness and lattice values through a Parallel Tempering (PT) algorithm. For each case reported in Tab. 5.1, we performed two independent replicas.
According to the PT prescription, we replicated each replica at N_T different temperatures, which are performed independently. In Appendix A.3 we discuss the details of

[1] We imposed open Boundary condition for evaluating the effect of the transversal saturation

L	L_z	N_T	ΔT	T_{min}	T_{max}
150	2	48	0.009	1.088	1.511
150	4	48	0.009	1.088	1.511
150	6	56	0.007	1.1019	1.506
150	8	66	0.006	1.1019	1.516
200	4	48	0.009	1.088	1.511
200	6	56	0.007	1.1019	1.506
200	8	66	0.006	1.1019	1.516

Table 5.1: Information about the Parallel Tempering parameters.

the PT algorithm.
The temperature increment ΔT and the number of temperature N_T were chosen for optimizing the acceptance ratio of the temperature swaps, and they are reported in Tab. 5.1. To check whether the samples were thermalized, we measured the exponential self-correlation time of the PT random walk in temperature τ [AB10a]. We required the simulations to last at least $10\,\tau$. Equilibrium measurements were taken off-line over the thermalized configurations. To speed up our algorithm we used the MUlti Samples (MUSA) multispin coding technique, see Sec. 4.3. In Appendix A we address the details of this packing technique.
The errors were estimated with the jackknife method [2].

5.2

Scaling function

The success of the experiments of Refs. [Guc14, Guc17] is based on the hypothesis that a glassy film, at or below the bulk critical temperature, $T \leq T_g$, acts as a bidimensional system as soon as its correlation length is compatible with the thickness, $\xi \sim L_z$. This implies that, at the equilibrium, a glassy film should be described by the $2D$ propagator. Recalling Eq. (4.11), in a $2D$ glassy system the asymptotic correlation function $C_4(\vec{r}, T)$ behaves as [Fer18a]:

$$C^{\text{eq}}_{2\text{D}}(r) = A(\xi_{\text{exp}})\text{K}_0(r/\xi_{\text{exp}})\,, \tag{5.2}$$

where $\text{K}_0(\cdot)$ is the zero order modified Bessel function of the second kind [Olv10], ξ_{exp} is the exponential correlation length, and $A(\xi_{\text{exp}})$ is an amplitude depending on the temperature through ξ_{exp}.

For each lattice value, we calculated the spacial autocorrelation function defined in Eq. (4.12). Being at the equilibrium, we can just drop the time from the $C_4(T, \vec{r})$

[2] The reader can found details in Appendix B.1 or in Ref.[You12] .

definition:

$$C_4(T,\vec{r}) = \overline{\langle q^{(a,b)}(\vec{x})\, q^{(a,b)}(\vec{x}+\vec{r},)\rangle_T}\ . \tag{5.3}$$

Since we simulated systems with OBC, the correlation function $C_4(\vec{r},T)$, Eq. (5.2), depends explicitly to the z-layer and the transversal invariance does not hold. We computed the longitudinal correlation function $C_4(\vec{r},T)$ for the top layers and the central ones, namely defined as:

$$C_4^{\rm Top}(\vec{r},T) = \frac{C_4(\vec{r},T,0) + C_4(\vec{r},T,L_{\rm z}-1)}{2} \tag{5.4}$$

$$C_4^{\rm Med}(\vec{r},T) = \frac{C_4(\vec{r},T,L_{\rm z}/2) + C_4(\vec{r},T,L_{\rm z}/2+1)}{2}\ . \tag{5.5}$$

To evaluate the effect or not of the z-dependence on the longitudinal correlation function, $C_4^{\rm Top}(\vec{r},T)$ and $C_4^{\rm Med}(\vec{r},T)$, we fitted them, in the $r >> \xi_{\rm exp}$, as

$$C_4^{\rm eq}(r,T) = A(\xi_{\rm exp})\left[{\rm K}_0\left(\frac{r}{\xi_{\rm exp}(T)}\right) + {\rm K}_0\left(\frac{L-r}{\xi_{\rm exp}(T)}\right)\right]\ , \tag{5.6}$$

where we have included the first-image term, ${\rm K}_0\left[\frac{(L-r)}{\xi_{\rm exp}(T)}\right]$ (we use open boundary conditions) as a further control of finite-size effects.
In Fig. 5.1 we report the comparison between $C_4^{\rm Top}(\vec{r},T)$ and $C_4^{\rm Med}(\vec{r},T)$ in the case $L_{\rm z}=8$ and $L=200$, as example. As one can observe, the z-dependence has no neg-

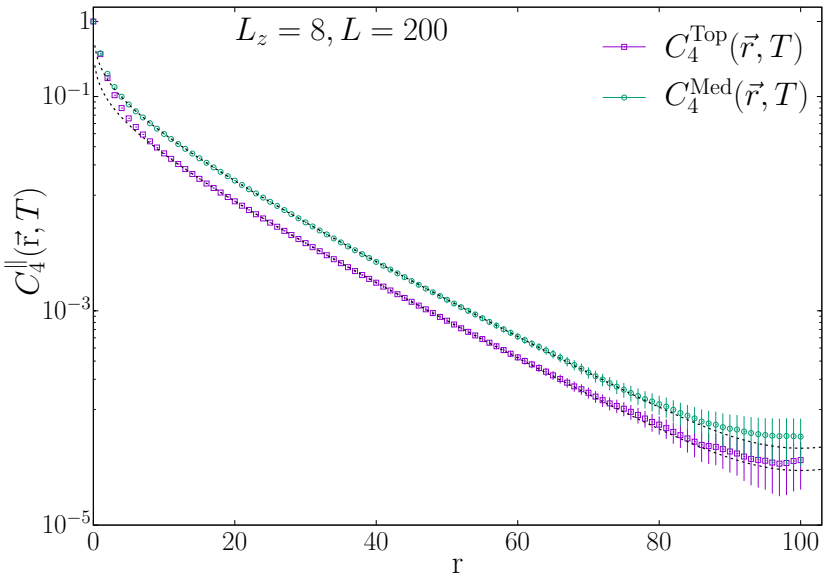

Figure 5.1: Comparison between the $C_4^{\rm Top}(\vec{r},T)$ and the $C_4^{\rm Top}(\vec{r},T)$. The plot is in semi-log scale and the dashed line are fits through the Bessel function of order zero [Olv10] with hyberbolic cosine corrections in the region $r >> \xi_{exp}$, $f(x) = A(\xi_{\rm exp}[K_0[x/\xi_{exp}] + {\rm K}_0[(L-x)/\xi_{exp}]]$ (see below for details).

ligible effect, the signal of $C_4^{\rm Top}(\vec{r},T)$ is smaller than the $C_4^{\rm Med}(\vec{r},T)$. Fortunately, the

decay is exactly the same for both the reported cases and, hence, the physical scenario emerges to be perfectly compatible. In the following of this chapter, we always refer to the central correlation function $C_4^{\parallel}(\vec{r},T) = C_4^{\mathrm{Med}}(\vec{r},T)$, where the boundary effects are minimized.

In Fig. 5.2 we report the behavior of the correlation function for different lattices and thickness at the bulk critical temperature, T_g. As one can observe in Fig. 5.2:

- the correlation function $C_4^{\parallel}(r)$ increases with film width L_z. According to the experimental hypothesis of a dynamical arrest when $\xi(t) \propto L_z$, the value of ξ depends on the thickness value. This implies that a spin-glass film has two characteristic lengths: the correlation length ξ and the thickness. In the next chapter 6, we will develop this concept through out-equilibrium simulations.
- The open boundary conditions (OPB) introduce non-negligible finite-size effects whose we took into account thanks to the first-image term of Eq. (5.6).
- For both lattices of size L, we are in the thermodynamical limit $L >> \xi_{\mathrm{exp}}$. The only discrepancy is given by the finite-size effects.
- The data are perfectly described by Eq. (5.6) in the large r region. In Tab. 5.2 we report the fitting parameters.

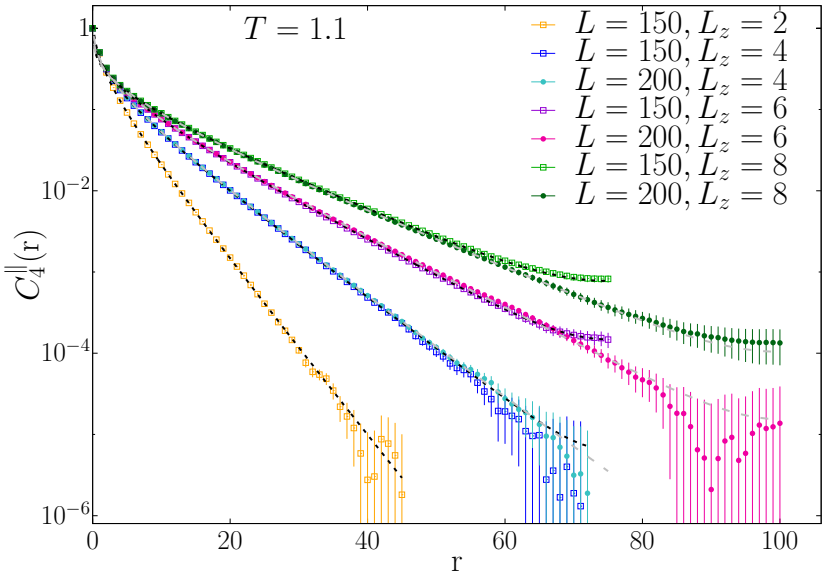

Figure 5.2: The longitudinal correlation function $C_4^{\parallel}(r)$ as a function of the distance r at the bulk critical temperature $T_g = 1.102(3)$ in semi-log scale. The dash lines, grey for lattice value $L = 200$ and black for $L = 150$, are fits through the Bessel function of order zero [Olv10] with hyberbolic cosine corrections in the region $r >> \xi_{exp}$, $f(x) = A[K_0[x/\xi_{exp}] + \mathrm{K}_0[(L-x)/\xi_{exp}]]$.

	L_z	$A(\xi_{exp})$	ξ_{exp}	χ^2/dof	x-range
$L = 150$	2	0.2756(21)	4.287(25)	14.239/29	[4:36]
	4	0.1998(22)	7.447(71)	19.649/49	[6:58]
	6	0.1619(26)	10.82(14)	24.640/64	[8:75]
	8	0.1350(25)	14.34(22)	21.899/61	[11:75]
$L = 200$	4	0.2001(15)	7.493(45)	20.553/51	[6:60]
	6	0.1570(19)	11.07(10)	25.636/61	[8:79]
	8	0.1380(26)	14.06(21)	25.480/70	[11:84]

Table 5.2: The fitting parameters of Eq. (5.6) for the longitudinal correlation function $C_4^{\parallel}(r, T_g)$.

	L_z	$A(\xi_{exp}^{RG})$	ξ_{exp}^{RG}	χ^2/dof	x-range
$L = 150$	2	0.5666(38)	2.154(11)	6.642/13	[2:18]
	4	0.6353(47)	1.902(17)	4.080/10	[1:14]
	6	0.693(13)	1.801(24)	2.849/7	[2:12]
	8	0.6853(85)	1.765(25)	1.945/5	[1:9]
$L = 200$	4	0.6621(55)	1.877(11)	4.17/10	[2:15]
	6	0.661(12)	1.862(23)	2.877/8	[2:12]
	8	0.6766(63)	1.787(19)	2.751/7	[1:11]

Table 5.3: The fitting parameters of Eq. (5.6) for the rescaled correlation function $C_4^{RG}(r)$.

5.2.1 Renormalization Group Trasformation

To study the equilibrium behavior of our film system, we performed a Renormalization Group transformation. We decomposed our system in boxes of size of L_z^3, and we rescaled the overlap field and the correlation function, $C_4^{RG}(r)$, according to Eq. (4.18)-(4.19).
Analogously to Fig. 5.2, we investigate the decay of the rescaled correlation function $C_4^{RG}(r)$. We guess that, after the coarse-graining of Eq. (4.18), the system has the same equilibrium propagator of a $2D$ system, see Eq. (4.11). In Fig. 5.3, we report the behavior of $C_4^{RG}(r)$. The fitting procedure is perfect for all the distance range and, in Tab. 5.3 we address the fitting parameters. As one can observe from Fig. 5.3, there emerges a scaling behavior for all the thickness except for the smallest one, $L_z = 2$.

Evaluating the $C_4^{RG}(r)$, at a given distance r^*, [see the insert of Fig. 5.3], we unveils a significant L_z-dependence. The analysis of this L_z-effect will be developed in the next Sections.

In conclusion, we analyzed the longitudinal correlation function, $C_4(r)$, and its rescaled one, $C_4^{RG}(r)$, according to a $2D$ description, see Eq. (4.11). Notice that the $2D$ propagator fits perfectly to the film description only after the Renormalization Group transformation, where the third dimension, namely the thickness, is absorbed.

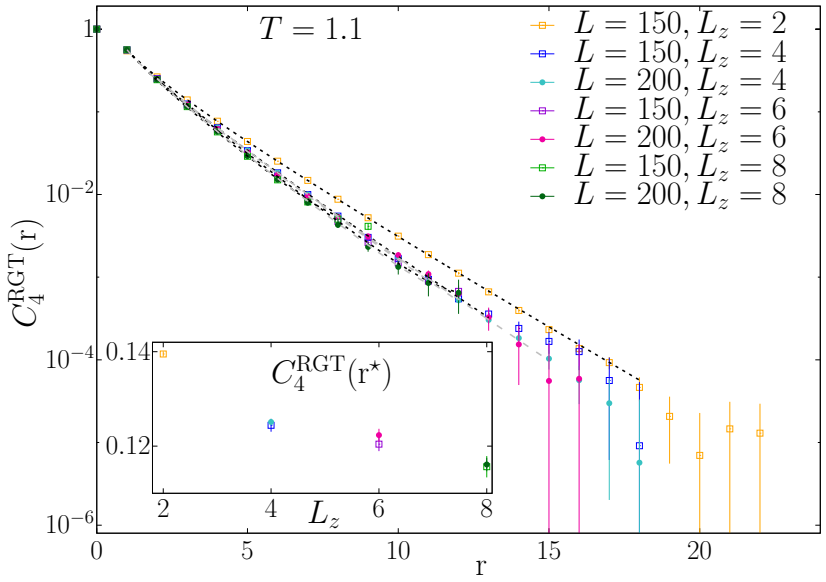

Figure 5.3: The renormalized correlation function $C_4^{\mathrm{RG}}(r)$ as a function of the distance r at the bulk critical temperature T_g in semi-log scale. The dash lines, grey for lattice value $L = 200$ and black for $L = 150$, are fits through the Bessel function of order zero [Olv10] with hyberbolic cosine corrections in the region $r > 1$, $f(x) = AK_0[x/\xi] + BK_0[(L-x)/\xi]$(**main**). The **insert** is a zoom of the C_4^{RG} at the fixed distance $r = 3$ as a function of the thickness L_z.

5.3

Finite-Size Scaling

At equilibrium, simulations near the bulk critical temperature T_g in a lattice of linear size L are usually far from the thermodynamic limit because of the extreme growth of the correlation length. In a glassy film, instead, the thermodynamical limit holds, see Fig. 5.2, since it achieves equilibrium with a finite correlation length. This section is focused on the investigation of thin glassy film through a finite-size scaling (FSS) approach, where the scaling variable is the thickness L_z and not the lattice L.

If an observable $\mathcal{O}$ diverges at the critical temperature as

$$\mathcal{O} \propto \left(\frac{T - T_g}{T_g}\right)^{-1/\nu} , \tag{5.7}$$

its thermal average close to the critical point can be expressed like:

$$\langle \mathcal{O} \rangle = F_{\mathcal{O}}\left[(T - T_g) \cdot L_z^{1/\nu}\right] + L_z^{-\omega} G_{\mathcal{O}}\left[(T - T_g) \cdot L_z^{1/\nu}\right] + \ldots \tag{5.8}$$

where ν and ω are the bulk universal exponents, [BJ13], and $F_{\mathcal{O}}[\cdot]$ and $G_{\mathcal{O}}[\cdot]$ are analytic scaling functions for observable $\mathcal{O}$.
Notice that the ω critical exponent expresses the finite-size corrections to the dominant

scaling. In first approximation, we neglected these second-order corrections. In this Section, we analyze the behavior of three dimensionless observables:

1. $A(\xi_{\rm exp})\xi_{\rm exp}^{D-2+\eta}$,
2. $\xi_{12}/L_{\rm z}$, where ξ_{12} is the 2nd moment of the integral estimator of Eq. (2.23),
3. and the Binder parameter:
$$B = \frac{\overline{\langle Q^4\rangle}}{\overline{\langle Q^2\rangle}^2} \tag{5.9}$$
where Q is the renormalized spin defined in Eq. 4.18.

Let us recall Eq. (4.14), the scaling function $f(u,v)$ has distinct behaviors in the large, $r >> \xi_{\rm exp}$, and in the small distance region, $r < \xi_{\rm exp}$:

$$\text{for } r >> \xi_{\rm exp} \quad C_4^{\parallel}(r) \sim A(\xi_{\rm exp}){\rm K}_0\left(\frac{r}{\xi_{\rm exp}}\right) ; \tag{5.10}$$

$$\text{for } r << \xi_{\rm exp} \quad C_4^{\parallel}(r) \sim \left(\frac{1}{r}\right)^{D-2+\eta} . \tag{5.11}$$

Since the correlation length $\xi_{\rm exp}$ is well-defined and finite in a glassy film, the correlation function $C_4^{\parallel}(r)$ defined in Eq. 4.14 should be continuous and smooth between the two asymptotic behaviors, $r << \xi_{\rm exp}$ and $r >> \xi_{\rm exp}$. This implies that, at a distance $r \sim \xi_{exp}$, through the correlation function, $C_4^{\parallel}(r)$, holds:

$$\left(\frac{1}{\xi_{\rm exp}}\right)^{(D-2+\eta)} \sim A(\xi_{\rm exp}) , \tag{5.12}$$

where the Bessel Function of order zero $\rm K_0$ at $\xi_{\rm exp}$ is a constant.
Let us rewrite Eq. (5.12) in a more convenient way:

$$A(\xi_{\rm exp})\xi_{\rm exp}^{D-2+\eta} \sim const . \tag{5.13}$$

According to Eq. (5.8), we study the behavior of the dimensionless observable in Eq. (5.13), wherein first approximation, we neglected the $L_{\rm z}$ finite-size effects. Let us explicitly write the numerical value of the exponent $D-2+\eta$:

$$D-2+\eta = 0.61 , \tag{5.14}$$

where $D=3$ and $\eta = -0.39$ [BJ13]. As one can observe from Fig. 5.4, there emerges a scaling behavior for all the $L_{\rm z}$ and L values; however, there are $L_{\rm z}$ finite-size effects.

Next, we calculated through the integral estimators of Eq. (2.23) the second-order momentum of the correlation length, ξ_{12}, and we evaluated the dimensionless quantities $\xi_{12}/L_{\rm z}$ according to the (FSS) technique, see Eq. (5.7). As one can observe in Fig. 5.5, a scaling behavior seems to emerge but this rescaled quantity, $\xi_{12}/L_{\rm z}$, is more sensitive

than $\xi_{\rm exp}/L_{\rm z}$ to the $L_{\rm z}$-effects. Data with $L_{\rm z}=2$ show a clear departure from the other thickness. This implies that a glassy film has at least two characteristic lengths: the correlation length, ξ, and the thickness $L_{\rm z}$.
If $L_{\rm z}$ is too small, a glassy film does not preserve the bulk critical landscape. This is perfectly understandable. Let us explain it qualitatively. For a very large thickness value, $L_{\rm z}=L\to\infty$, a glassy film is exactly a bulk system, which is characterized by the well-known second-order divergence of the correlation length, $\xi\sim|\tau|^{-\nu}$, where τ is the reduced temperature $\tau=(T-T_g)/T_g$. On the other hand, for a thickness $L_{\rm z}=1$ a film is a $2D$ system always in the paramagnetic phase. Hence, the thickness value, $L_{\rm z}$, needs to be large enough to preserve the bulk critical properties, as Fig. 5.5 indicates. The same conclusion can be explained as follows: if a glassy film has a too short thickness the dimensional crossover that happens as soon as the $\xi\sim L_{\rm z}$, is so fast that the landscape does not have enough time to express its complexity.

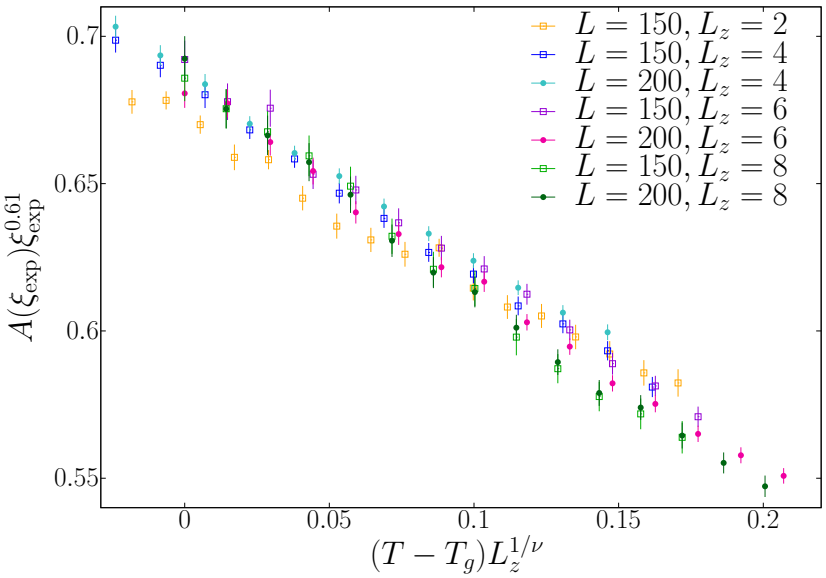

Figure 5.4: The product of the Zero-Bessel amplitude $A(\xi_{\rm exp})$ and the correlation length $\xi_{\rm exp}$ to the power $\mathrm{D}-2+\eta=0.61$ as a function of the scaling function $(T-T_g)L_{\rm z}^{\nu}$, where ν and η are the bulk critical exponents.

Finally, we studied the Binder parameter, see Eq. (5.9). In Fig. 5.6, we report the evaluation of the Binder parameter, B, through the (FSS) approach. The scenario is compatible with the one that emerges from the analogous analysis of the rescaled correlation length, $\xi_{12}/L_{\rm z}$, see Fig. 5.5. The bulk properties are preserved only for large enough thickness value. Moreover, the $L_{\rm z}$ finite-size effects are not negligible and we address in the next Section a more sophisticated analysis.

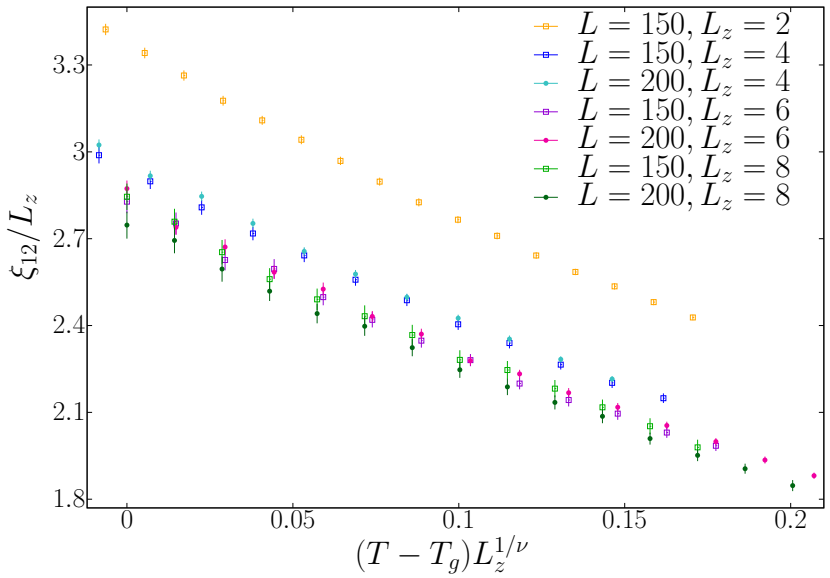

Figure 5.5: The correlation lengths ξ_{12} rescaled by the thickness L_z as a function of the scaling function $(T - T_g)L_z^{\nu}$.

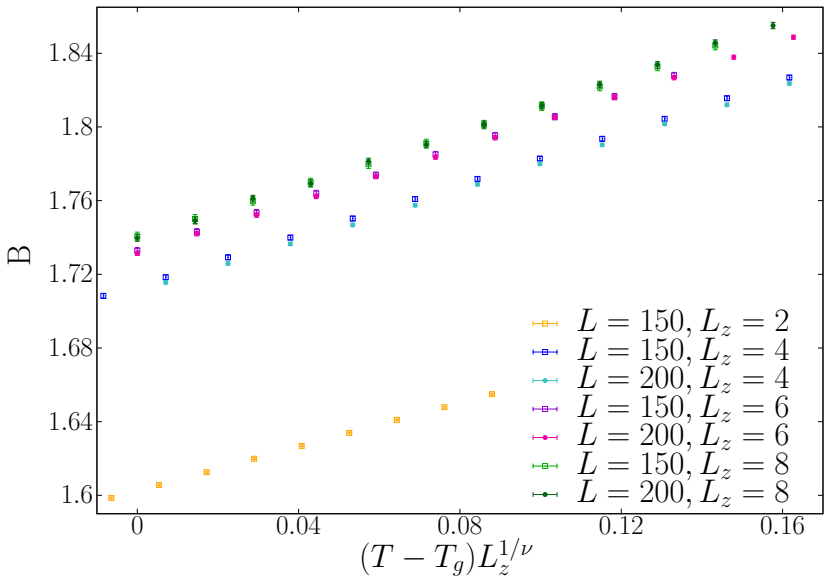

Figure 5.6: The Binder estimator as a function of the scaling function $(T - T_g)L_z^{1/\nu}$. We do not report all the $L_z = 2$ values because they do not add any information to the plot.

5.4

Universal parameters

Our (FSS) analysis, see Figs. 5.4-5.6, indicated that we can not neglect the second term of Eq. (5.8), which controls the finite-size effects. In this section, we will manipulate Eq. (5.8) to include more terms in the expansion and we will calculate some universal parameters of a thin glassy film.

Being at the critical point T_g, we expand Eq. (5.8) through a Taylor expansion:

$$\langle \mathcal{O} \rangle = F[0] + x\, F'[0] + \frac{x^2}{2} F''[0] + L_{\rm z}^{-\omega} \left(G[0] + x\, G'[0] + \frac{x^2}{2} G''[0] \right) \tag{5.15}$$

where, for notation simplicity, $x = (T - T_g) L_{\rm z}^{1/\nu}$.
Let us rewrite Eq. (5.15) as:

$$\begin{aligned} \langle \mathcal{O} \rangle = & \underbrace{F[0] + G[0] L_{\rm z}^{-\omega}}_{\mathcal{M}_0} + x \underbrace{\left(F'[0] + G'[0] L_{\rm z}^{-\omega} \right)}_{\mathcal{M}_1} \\ & + \frac{x^2}{2} \underbrace{\left(F''[0] + G''[0] L_{\rm z}^{-\omega} \right)}_{\mathcal{M}_2} \end{aligned} \tag{5.16}$$

where the quantities $F[0]$, $F'[0]$ and $F''[0]$ are universal parameters.
We study these parameters in the following way:

1. we calculate several dimensionless observable,*i.e* $\xi_{12}/L_{\rm z}$, $\xi_{\rm exp}/L_{\rm z}$, ξ^{RG} and the Binder parameter B.

2. We fitted each of these observables through the function

   $$\mathcal{O} = \mathcal{M}_0 + \mathcal{M}_1 x + \mathcal{M}_2 x^2 \tag{5.17}$$

   and we estimated the different $\mathcal{M}_i$ coefficients, see Eq. (5.16).

3. We fit each found coefficient $\mathcal{M}_i$ through the function

   $$g_i(\hat{x}) = A_i + B_i \hat{x}\,, \tag{5.18}$$

   where $\hat{x} \equiv L_{\rm z}^{-\omega}$ and the index i is referred to the coefficients $\mathcal{M}_i$.

4. We calculate the universal parameters $F^{(n)}[0]$ thanks to the zero-extrapolation of the fitted functions $g_i(\hat{x})$, namely the parameters A_i

According to Ref. [BJ13], the critical exponent ω is, $\omega = 1.12(10)$. We evaluate the scaling corrections $L_{\rm z}^{-\omega}$ for three different ω cases: $\omega = 1.12$, $\omega = 1.11$ and $\omega = 1.13$. In Tab. 5.4, we report the parameters A_i calculated for these three ω cases. We do not see any significant discrepancy in the determination of the zero-extrapolated values A_i using different ω values.
In Fig. 5.7 we show the behavior of the $\mathcal{M}_i$ as a function of $L_{\rm z}^{-\omega}$ and its fitting functions, in the central case $\omega = 1.12$. The inserts are enlargements of the zero extrapolations. Some interesting observations arise:

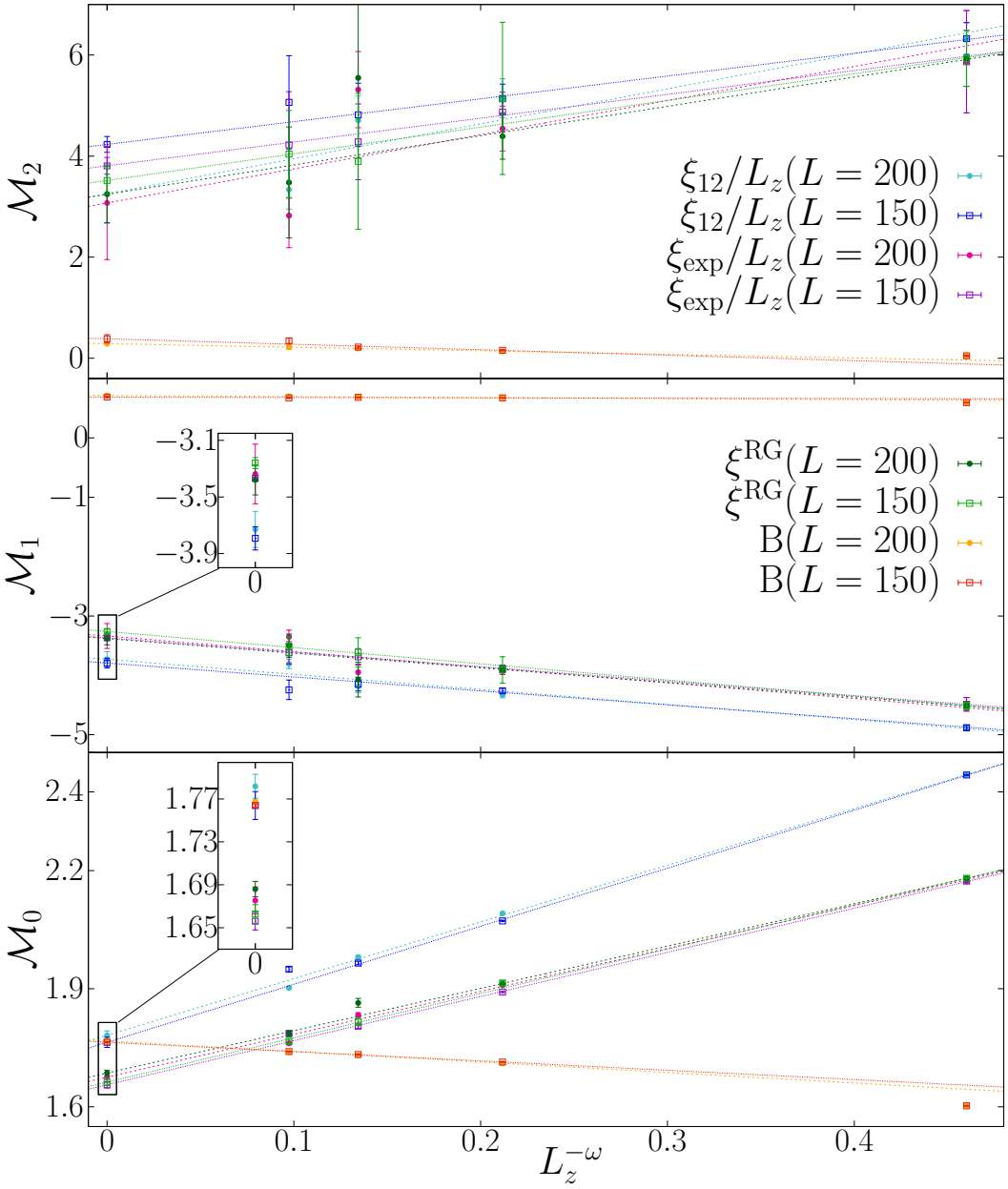

Figure 5.7: Behavior of the $\mathcal{M}_i$ parameters as a function of $L_z^{-\omega}$, as they are defined in Eq. (5.16) and with $\omega = 1.12$. The dash lines are the fitted function $g_i(x) = A_i + B_i x$ with $x \equiv L_z^{-\omega}$. For each dimensionless quantities we performed an independent fit and each fit is reported with the same color of its dimensionless quantities.(**Main**). In the **insert** we show the zoom of the zero-extrapolated values.

1. the universal factors A_i, see Eq. (5.18), clearly show that the dimensionless quantities $\xi_{\rm exp}/L_z$ is compatible to the one of $\xi^{\rm RG}$. This is consistent by construction and it is further proof that the film, at the equilibrium, is acting as a $2D$ system.

2. The universal factor A_0 is compatible in the errors for the ξ_{12}/L_z and the Binder

			A_0	A_1	A_2
$\omega = 1.11$	$L = 200$	ξ_{12}/L_z	1.788(11)	-3.62(12)	3.24(58)
		ξ_{exp}/L_z	1.672(12)	-3.33(21)	3.05(1.12)
		ξ^{RG}	1.683(7)	-3.37(10)	3.23(56)
		B	1.767(2)	0.714(4)	0.289(1)
	$L = 150$	ξ_{12}/L_z	1.760(13)	-3.78(1)	4.22(16)
		ξ_{exp}/L_z	1.653(8)	-3.36(8)	3.79(17)
		ξ^{RG}	1.660(8)	-3.25(3)	3.51(27)
		B	1.764(1)	0.68(1)	0.38(8)
$\omega = 1.12$	$L = 200$	ξ_{12}/L_z	1.782(11)	-3.73(12)	3.25(0.58)
		ξ_{exp}/L_z	1.675(12)	-3.34(21)	3.07(1.12)
		ξ^{RG}	1.686(7)	-3.38(10)	3.24(56)
		B	1.767(2)	0.714(4)	0.288(1)
	$L = 150$	ξ_{12}/L_z	1.764(13)	-3.79(8)	4.23(15)
		ξ_{exp}/L_z	1.663(8)	-3.368(8)	3.80(17)
		ξ^{RG}	1.764(8)	-3.26(4)	3.52(27)
		B	1.764(1)	0.68(1)	0.38(8)
$\omega = 1.13$	$L = 200$	ξ_{12}/L_z	1.785(11)	-3.73(13)	3.26(58)
		ξ_{exp}/L_z	1.677(13)	-3.34(21)	3.09(1.11)
		ξ^{RG}	1.688(7)	-3.38(10)	3.26(56)
		B	1.767(2)	0.713(4)	0.287(1)
	$L = 150$	ξ_{12}/L_z	1.767(12)	-3.79(8)	4.24(15)
		ξ_{exp}/L_z	1.658(7)	-3.37(7)	3.82(17)
		ξ^{RG}	1.665(8)	-3.26(4)	3.53(27)
		B	1.763(1)	0.687(12)	0.38(8)

Table 5.4: Values of the universal parameters for the dimensionless quantities and for three different ω values.

parameter, B. This implies that the microscopical structure of a glassy film preserves the critical bulk properties.

3. For the Binder parameter, the universal factors A_1 and A_2 are not correlated to the other analyzed dimensionless quantities.The higher-order universal coefficients A_i contains information about the geometry of the system.

5.5 Remark

In this Chapter, we investigated equilibrium properties of thin glassy films through massive Parallel Tempering simulations. Exploiting a Renormalization group approach,

we have shown that, at equilibrium, it is possible to map a glassy film through the $2D$ correlation propagator, see Fig.5.3. However, for large enough thickness value, $L_z > 4$, Figs.5.4-5.6 unveil a scaling behavior controlled by the bulk critical exponents.These results are important because they prove that, despite the shortness of the thickness $L_z << L$, a glassy film feels the critical behavior of the $3D$ spin-glass system. This is quantitatively described in the form of an avoided phase-transition, as specified by Finite-Size Scaling.

CHAPTER VI

The out-equilibrium regime of a thin glassy film

This chapter is dedicated to the out-equilibrium regime of a thin glassy film. We will report the results of Ref. [Fer19b] and some unpublished ones.
Motivated by recent experiments of exceptional accuracy, we study numerically the spin-glass dynamics in a film geometry. We cover all the relevant time regimes, from picoseconds to equilibrium, at temperatures at and below the 3D critical point. The dimensional crossover from $3D$ to $2D$ dynamics, which starts when the correlation length becomes comparable to the film thickness, consists of four dynamical regimes. Our analysis, based on a Renormalization Group transformation, finds that the overall physical picture employed by Orbach *et al.* is consistent with their interpretation of experiments [Guc14, Guc17, Zha17b, Ken18]. This chapter is organized as follows. In Sec. 6.1 we report the simulation details of our massive numerical simulations; in Sec. 6.2 we address the numerical evaluation of the growth of the correlation lengths, both in the longitudinal and transversal direction. Next, in Sec. 6.3, we unveil the scaling properties of a thin glassy film for several thickness and temperature in the out-equilibrium regime. Finally, in Sec. 6.4 we evaluate the dynamical inherent structure of the film state.

6.1 Model and simulations

We study numerically the Edward-Anderson model in a cubic lattice with a film geometry. Our films have two long sides of length $L_x = L_y = L$, and thickness $L_z << L$. We imposed periodic boundary conditions (PBC) along the two longitudinal directions X and Y.
We have simulated systems of lattice size $L_x = 256$ and different thickness $L_z = 4, 6, 8$ and 16. We choose the lattice value $L_x >> \xi$ such that the thermodynamic limit holds

T	L_z	Boundary condition
$T = 0.7$	4	PBC and OBC
	8	PBC and OBC
	16	PBC and OBC
$T = 0.98$	4	PBC and OBC
	8	PBC and OBC
	16	PBC and OBC
$T = 1.1$	4	PBC and OBC
	6	PBC
	8	PBC and OBC
	16	PBC and OBC

Table 6.1: Information about the simulations.

$L_x \to \infty$. We have considered both PBC and Open Boundary Condition (OBC) along the transversal direction Z. Our numerical protocol is an instantaneous temperature quenching. At the initial time $t = 0$, our spins are in a random configuration, that corresponds to a very high temperature $T = \infty$, and then, the system is abruptly quenched down to our working temperature T.
We have simulated the Metropolis dynamics and we have followed the evolution of the system as t increases. The time unit is the Monte Carlo step (a full lattice Metropolis sweep. A sweep roughly corresponds to 1 picosecond [Myd93]).
Our spins $\sigma_{\mathbf{x}} = \pm 1$ interact with their lattice nearest-neighbors through the Hamiltonian:

$$H_{\mathrm{EA}} = -\sum_{<\vec{x},\vec{y}>} J_{\vec{x}\vec{y}}\, \sigma_{\vec{x}}\, \sigma_{\vec{y}}\,, \tag{6.1}$$

where the quenched disordered couplings are $\{J_{\vec{x}\vec{y}}\} = \pm 1$ with 50% probability.
For each quenched realization of the coupling (a sample) we study N_{R} real replicas. We have already addressed all the numerical details in Sec. 4.3.

6.2

Longitudinal and transversal correlation length

In this section, we address the out-equilibrium analysis of the longitudinal and transversal correlation length.

We simulated our film system both with OBC and PBC for several thickness and for three different temperatures. We have listed all the cases in Tab. 6.1.

6.2.1 Longitudinal correlation length $\xi^{\parallel}_{12}$

According to Eq. (4.16), we evaluate the growth of the longitudinal correlation length $\xi^{\parallel}_{12}(t)$, see Fig. 6.1. All the main points can be assessed by looking at the data at $T = 0.98$; the data at the cold temperature $T = 0.7$ and at the critical temperature $T_{\rm g} = 1.1$. are useful to confirm the scenario that we will draw out.

We identified four different regimes in the time evolution of $\xi^{\parallel}_{12}(t)$.

In the first regime, for small times, the growth of $\xi^{\parallel}_{12}(t)$ is indistinguishable from what happens in a regular $3D$ system [1]. Eventually, the growth rate changes at a time depending on both the thickness value and the temperature. Let us call t_1 the time where the growth of $\xi^{\parallel}_{12}(t)$ is distinguishable from the bulk evolution. The time t_1 increases proportional to the thickness value and decreases as the temperature goes far from the critical one. This effect is completely expectable since the dynamics are slower as the temperature is colder.

Hence, the system enters in a second regime where $\xi^{\parallel}_{12}(t)$ grows faster than in a $D = 3$. All the curves, in Fig. 6.1, are above the grey dashed lines that indicate the bulk evolution. In this second regime, the aging rate $z_{\rm film}(T)$ of the growth of correlation length is neither that of a regular bidimensional system nor that of a bulk one. This regime is a transient between the bulk and the $2D$ dynamics.

Then, we identify a third regime where for a while the system grows exactly as bidimensional. In Fig. 6.1, we reported with black dashed lines the $2D$ growth correspondent for each case.

Finally, the fourth regime corresponds to the saturation of the $\xi^{\parallel}_{12}(t)$ to its equilibrium values. We could achieved the equilibrium for all the cases at $T = 1.1$, see Fig. 6.1, and for the shortest thickness $L_z = 4$ at $T = 0.98$, see Fig. 6.1; instead, at $T = 0.7$ the dynamics is so slow that we could only achieve the third regime, see Fig. 6.1.

Effects of the boundary conditions

We checked that the growth of $\xi^{\parallel}_{12}(t)$ does not have any significant dependence on the boundary condition.

The longitudinal correlation function is calculated layer by layer. In the PBC case, we averaged over all the layers, as it is holding the transversal translation invariance, and we calculated the $\xi^{\parallel}_{12}(t)$ through the integral estimation, see Eq. 4.16, where the correlation function $C_4(T, r, t) = \sum_{z=0}^{L_z} C_4^z(T, r, t)$.

On the other hand, for the OBC, the situation is more complex, since it does not hold the translation invariance anymore. We distinguished between two cases [2]

- the C_4 averaged between the external layers:

$$C_4^{\rm TOP} = \frac{C_4(z = 0) + C_4(z = L_z - 1)}{2}\,, \tag{6.2}$$

[1] The bulk data are taken from Ref. [BJ18]

[2] We are omitting the explicit dependence on time t, temperature T and distance r of the correlation function $C_4(T, r, t)$ for notation's simplicity. As the reader can notice, these are exactly the same cases considered in the equilibrium context.

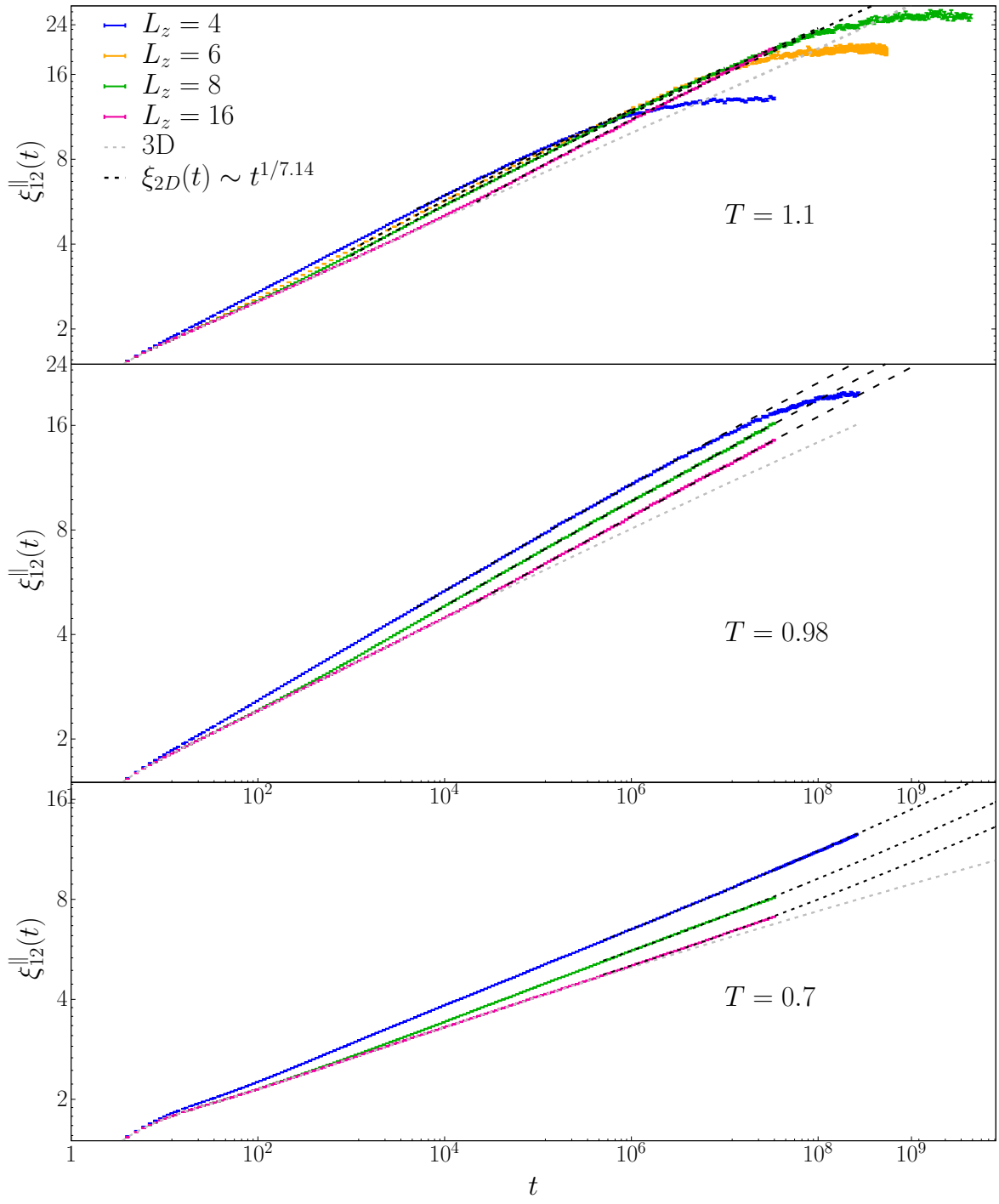

Figure 6.1: Plots show the time evolution of the correlation length $\xi^{\parallel}_{12}(t)$ at three different temperatures. The grey lines correspond to the regular $3D$ evolution [BJ18]; instead, the black dashed lines identify the $2D$ evolution. We fit $\xi^{\parallel}_{12}(t)$ as $f(x) = A\, x^{1/z_{2D}}$ in order to understand when the system start to grow exactly as a $2D$ system.

- and the C_4 averaged between the internal layers:

$$C_4^{\mathrm{ZMED}} = \frac{C_4(z = L_z/2) + C_4(z = L_z/2 - 1)}{2} \,. \tag{6.3}$$

Hence, for the OBC we built two different estimations of the correlation length $\xi_{12}^{\parallel}(t)$. In Fig. 6.2 we compared the growth of $\xi_{12}^{\parallel}(t)$ in PBC cases with the OBC ones. As one

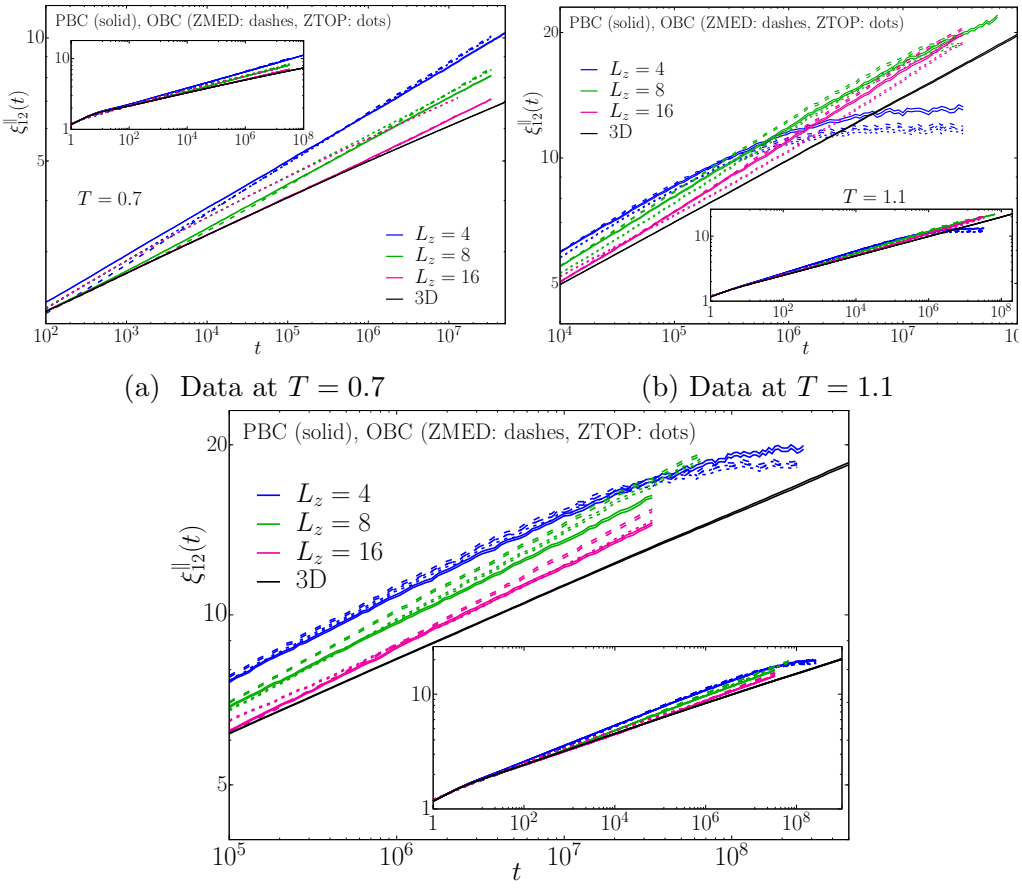

(a) Data at $T = 0.7$ (b) Data at $T = 1.1$

(c) Data at $T = 0.98$

Figure 6.2: Growth of the longitudinal correlation length $\xi_{12}^{\parallel}(T, t)$ as a function of the time t as computed with periodic boundary conditions (PBC) or with open boundary conditions (OBC) on the central layers (ZMED) or on the top layers (ZTOP). At each temperature, the **insert** shows the data from the **main** panel in the full time-range of our simulations.

can observe, the difference in the growth of $\xi_{12}^{\parallel}(t)$ are not significant and the overall scenario is not affected by the boundary conditions.

6.2.2 Transversal correlation length

The experimental approach on the film investigation is based on the hypothesis that the system has a dimensional crossover as soon as the transversal correlation length saturates to the thickness value. The sum estimator $\xi^{\perp}_{12}$ defined in Eq. 4.17, for OBC and computing the correlations from the bottom layer $z = 0$, we can extend the sum up to $L_z - 1$.
In Fig. 6.3 we reported both the behavior of $\xi^{\perp}_{12}$ performed with OBC and PBC. One can easily observe as $\xi^{\perp}_{12}$ converges to a constant value, and there are finite-size effects due to the periodic boundary conditions. In conclusion, we checked that the decision

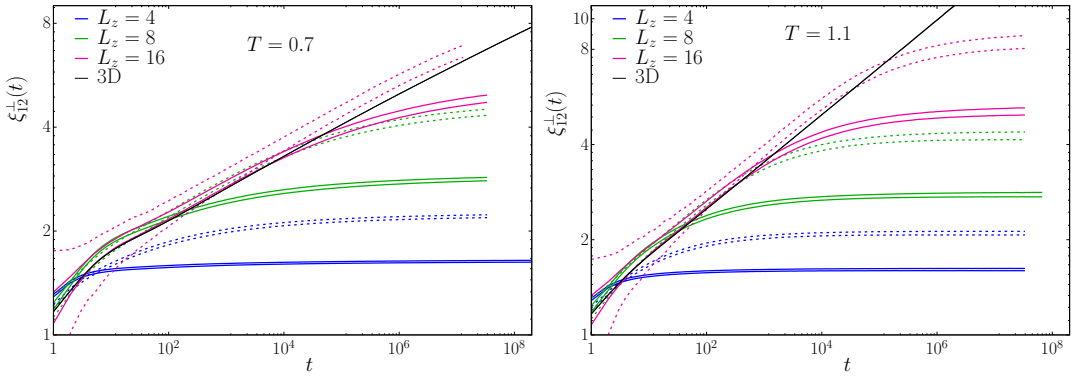

(a) Data $T = 0.7$. (b) Data at $T = 1.1$

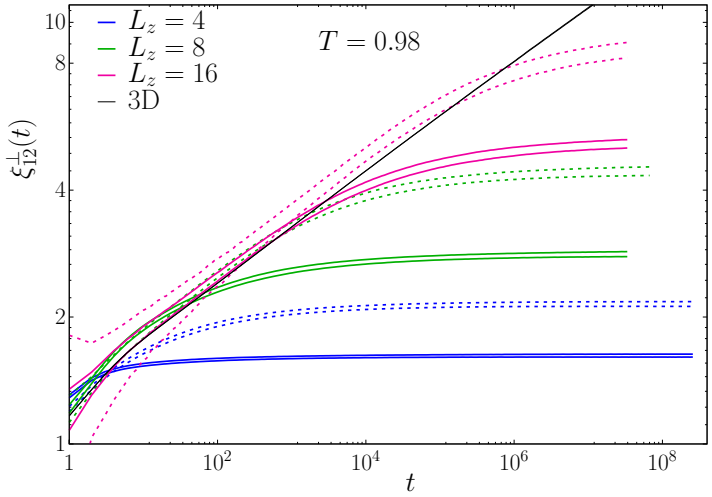

(c) Data at $T = 0.98$

Figure 6.3: Plots show the time evolution of the transversal correlation length $\xi^{\perp}_{12}$. The dashed lines are the behavior of $\xi^{\perp}_{12}$ for OBC condition; instead the continuous ones are for PBC ones. Moreover, for reader's simplicity, we reported the relative errors of $\xi^{\perp}_{12}$ through lines distance than the errorbars.

on using open or periodic boundary condition does not significantly affect the growth of the correlation lengths both along the longitudinal, $\xi^{\parallel}_{12}(t)$, and transversal direction, $\xi^{\perp}_{12}(t)$.

6.2.3 Comparison between the motions in the transversal plane and the longitudinal one.

We compared the $\xi^{\parallel}_{12}(t)$ and $\xi^{\perp}_{12}(t)$ in Fig. 6.4. The dynamical behaviors of these two quantities are very different.
As expected $\xi^{\perp}_{12}$ saturates. However, the $\xi^{\parallel}_{12}$ continues growing *after* $\xi^{\perp}_{12}$ saturates: in no way the time where $\xi^{\parallel}_{12}(t)$ and $\xi^{\perp}_{12}(t)$ stop growing is the same.
As one can see in Fig. 6.4, $\xi^{\parallel}_{12}$ needs time to respond to the saturation of $\xi^{\perp}_{12}$; and its dynamics is faster-than-$3D$ growth. Saturation of $\xi^{\parallel}_{12}$ eventually happens at later times. Although $\xi^{\parallel}_{12}$ saturates as well. These two-time scales are remarkably different.

Hence, the film dynamics is characterized by a fast motion (along the transversal plane) and four aging regimes in the longitudinal plane. Moreover, as Fig. 6.4 shows, the glassy film has more than one relevant scale variable. In a bulk system, the dynamics is controlled by the correlation length $\xi(t)$; instead, in a film geometry, the thickness has a central role in the process too. We will extend this concept in the next section thanks to a Finite-Size Scaling (FSS) approach.

6.3

Finite-Size Scaling approach

The dynamics in the longitudinal plane depends on the thickness value; however, we are going to identify a second characteristic length that controls the $3D$-to-$2D$ crossover: the bulk correlation length $\xi^{\mathrm{3D}}_{12}(t)$.
Hence, exploiting a Finite-Size Scaling approach, we have studied the behavior of the dimensionless $\xi^{\parallel}_{12}(t)/\xi^{\mathrm{3D}}_{12}(t)$ as a function of $\xi^{\mathrm{3D}}_{12}(t)/L_z$. These dimensionless quantities have the advantage to study the film dynamics as a function of $\xi^{\mathrm{3D}}_{12}(t)$ instead of time. As one can see in Fig. 6.5, a very good scaling behavior emerges. The ratio $\xi^{\mathrm{film}}_{12}(t)/\xi^{\mathrm{3D}}_{12}(t)$ grows beyond 1, thus signaling a faster-than-$3D$ dynamics as soon as $\xi^{\mathrm{3D}}_{12}(t) \approx L_z/4$. At the cold temperature $T = 0.7$, the ratio $\xi^{\mathrm{film}}_{12}(t)/\xi^{\mathrm{3D}}_{12}(t)$ confirms as the system is still very far from the equilibrium's achievement.

The saturation regime observed in Figs. 6.3, where data are shown as a function of the time, corresponds to the decrease behavior of Fig 6.5b-6.5c. When the system covers its fourth regime, see Sec. 6.2, its dynamics arrests and so the rescaled quantity $\xi^{\mathrm{film}}_{12}(t)/\xi^{\mathrm{3D}}_{12}(t)$ goes to zero in the limit $t \to \infty$.

Effects of the boundary conditions We have compared the behavior of the dimensionless $\xi^{\parallel}_{12}(t)/\xi^{\mathrm{3D}}_{12}(t)$ as a function of $\xi^{\mathrm{3D}}_{12}(t)/L_z$ for the OBC and the PBC cases, see Tab. 6.1. The layer-dependence with OBC makes slightly more complicated the analysis of scaling function, see Fig.6.6. Fortunately, the difference between the OBC and PBC is tiny and the physical scenario which emerges is compatible.

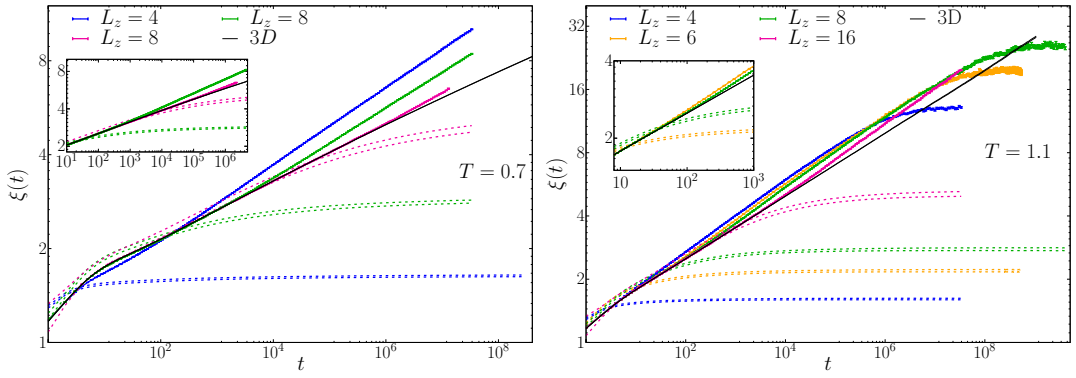

(a) Data at $T = 0.7$

(b) Data at $T = 1.1$

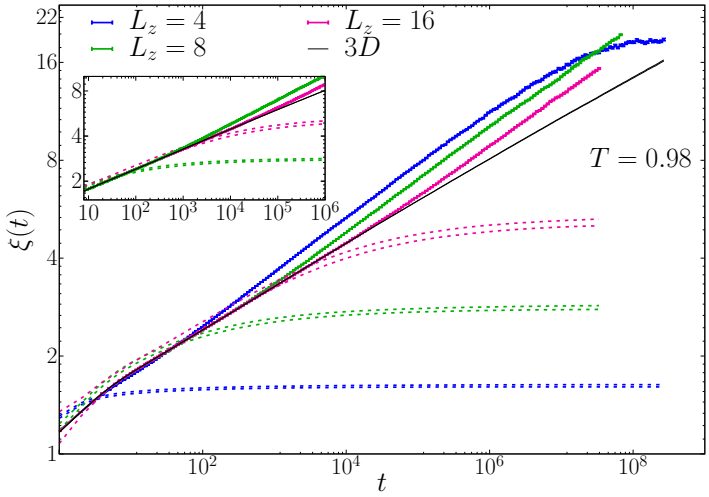

(c) Data at $T = 0.98$

Figure 6.4: Growth of the longitudinal $\xi_{12}^{\parallel}$ (solid lines) and of the transversal $\xi_{12}^{\perp}$ (dashes lines) correlation lengths with the waiting time t after a quench to temperature T. For each temperature, the **inset** is a zoom of the saturation of $\xi_{12}^{\perp}$ and of the separation between the $\xi_{12}^{\parallel}$ and the bulk correlation length.

6.3.1 Renormalization Group Transformation

The scale-invariance evinced in Fig. 6.5 prompts us to consider the film dynamics from the Renormalization-Group perspective (see e.g. [Ami05]). Indeed, in equilibrium, phenomenological renormalization [Nig76] maps our film at temperature T to a truly 2D spin glass at an effective temperature $T_{\text{eff,2D}}$:

$$\xi_{12}^{\parallel,\text{eq}}\left(T, L_z\right) = L_z\, \xi_{12}^{\text{eq,2D}}\left(T_{\text{eff,2D}}\right) , \tag{6.4}$$

where the equilibrium correlation length $\xi_{12}^{\text{eq,2D}}$ is a smooth function of $T_{\text{eff,2D}}$ (provided that $T_{\text{eff,2D}} > 0$). For any fixed $T > T_c$, $T_{\text{eff,2D}}$ increases with L_z ($T_{\text{eff,2D}} \to \infty$ when $L_z \to \infty$). On the other hand, holding fixed $T \leq T_c$ while L_z grows, $T_{\text{eff,2D}}$ reaches a limit. The limit is neither 0 nor ∞, because the whole spin-glass phase is critical in 3D [AB10b, Con09].

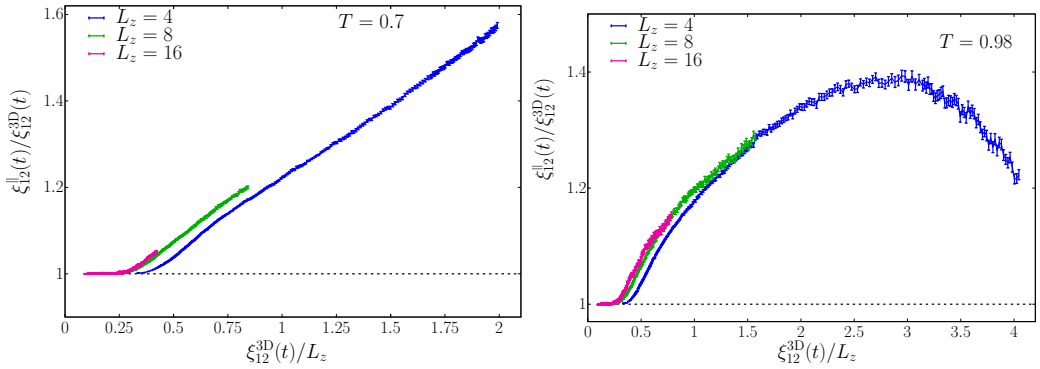

(a) Data at $T = 0.7$ (b) Data at $T = 0.98$

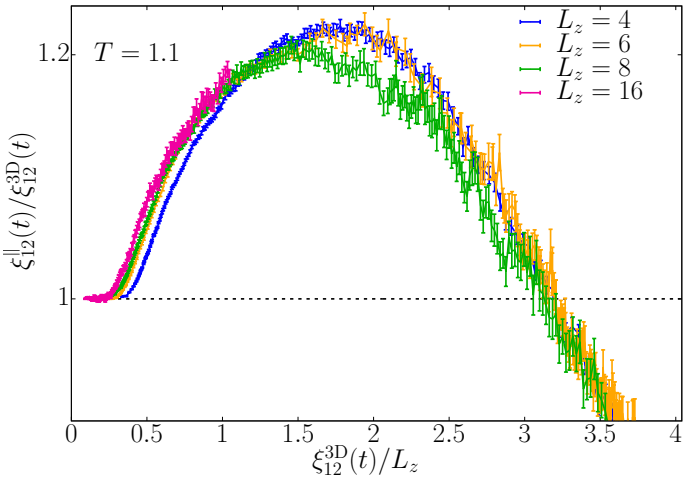

(c) Data at $T = 1.1$

Figure 6.5: Dynamical scale-invariance for the dimensionless quantity $\xi^{\rm film}_{12}(t)/\xi^{\rm 3D}_{12}(t)$ as a function of the rescaled bulk length $\xi^{\rm 3D}_{12}(t)/L_z$.

Two questions naturally appear:

1. *Is the equilibrium mapping* (6.4) *meaningful for an aging, off-equilibrium film?*
2. *Is it sensible to assume* $T_{eff,2D} \approx T$*?* (an assumption that, although not explictly, underlies the experimental analysis [Guc14, Guc17, Zha17b, Ken18]).

In order to address the above two questions, we perform on our aging films a linear Kadanoff-Wilson block spin transformation of size L_z [see (4.18)-(4.19)]: from L_z^3 of our original spins at time t, we obtain a single renormalized spin in the renormalized 2D system. The correlation functions computed for the *aging* renormalized spins can be compared with those of a truly 2D system at the temperature $T_{\rm eff,2D}$ obtained from Eq. (6.4). In particular, we have found it useful to compute the dimensionless ratio $\xi^{\rm RG}_{23}(t)/\xi^{\rm RG}_{12}(t)$ for both the renormalized spins and the truly 2D system [Eq. (4.14) tells us that $\xi^{\rm RG}_{23}(t)/\xi^{\rm RG}_{12}(t)$ is a smooth function of the ratio $\xi^{\rm RG}_{12}(t)/\xi^{\rm RG,eq}_{12}$] [3].

[3] We use $\xi_{12}(t)/\xi^{\rm eq}_{12}$ as a computable proxy for the unknown v in Eq. (4.14), see Fig. 6.7 and Ref. [Fer18a].

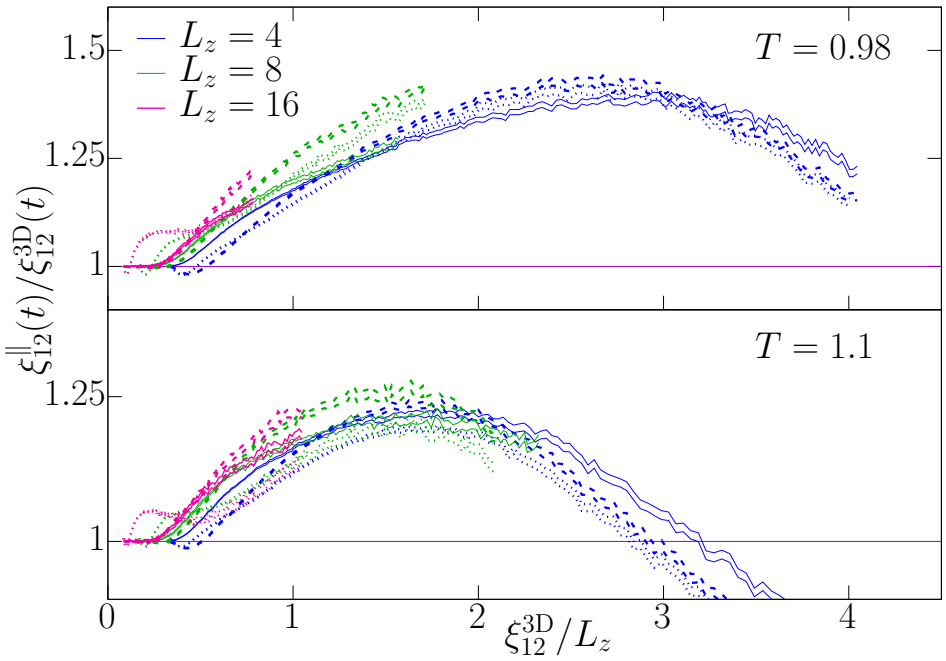

Figure 6.6: Dynamical scale-invariance for the dimensionless quantity $\xi^{\rm film}_{12}(t)/\xi^{\rm 3D}_{12}(t)$ as a function of the rescaled bulk length $\xi^{\rm 3D}_{12}(t)/L_z$ for the PBC case (solid) and for the OBC external-layer (dots) at temperatures $T = 0.98$ (**top**) and $T = 1.1$ (**bottom**).

As expected for a film at $T \leq T_{\rm c}$, the scaling function in Fig. 6.7 does not depends on L_z. To be precise, for $T = 0.98$ we did not reach equilibrium in the $L_z = 8$ film. However, by taking $\xi^{\rm eq}_{12}$ from the block-spins formed from the $L_z = 4$ film, we find an excellent scaling: corrections to scaling, if any, are not measurable within our statistical accuracy for the films.

Now, the very same scaling function can be computed in a regular two 2D system at temperature $T_{\rm 2D}$. If one takes $T_{\rm 2D} = T$ (T is the film's temperature), we find a clear discrepancy in Fig. 6.7. On the other hand, if we take $T_{\rm 2D} = T_{\rm eff,2D}$ the matching with the film's scaling function is much better, although corrections to scaling for the 2D system are suppressed only when $T_{\rm 2D} \to 0$. Hence, the answer to our first question above is *yes, Eq.* (6.4) *is meaningful in the off-equilibrium regime, as well.*

As for our second question, Finite Size Scaling (see e.g. [Ami05]) implies $\mathrm{d}T_{\rm eff,2D}/\mathrm{d}T \propto L_z^{1/\nu}$ at $T_{\rm c}$. Hence, when L_z grows, the mapping $T \to T_{\rm eff,2D}$ becomes singular at $T = T_{\rm c}$. On the other hand, we do not see questions of principle implying a singular mapping for $T < T_{\rm c}$. Accordingly, we find $T_{\rm eff,2D} \approx 1.11\,T$ at $T = T_{\rm c}$, but $T_{\rm eff,2D} \approx 1.04\,T$ at $T \approx 0.9\,T_{\rm c}$. In other words, *the assumption* $T_{eff,2D} \approx T$ *is sensible*, provided that $T < T_{\rm c}$.

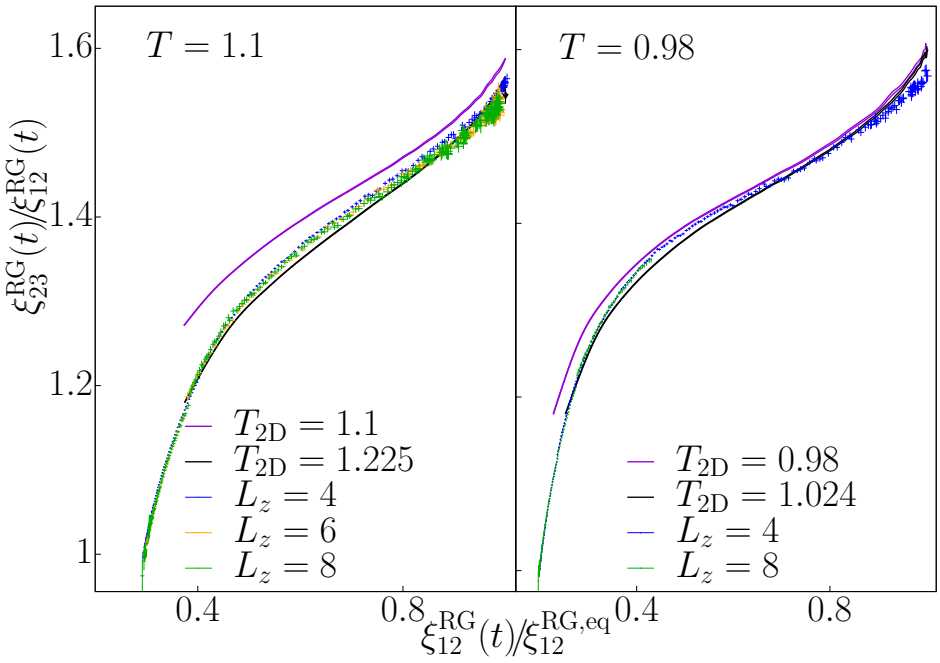

Figure 6.7: The scale-invariant ratio $\xi_{23}^{\rm RG}(T,t)/\xi_{12}^{\rm RG}(T,t)$, versus the ratio $\xi_{12}^{\rm RG}(t,T)/\xi_{12}^{\rm RG,eq}(T)$. In our direct-quench protocol, $\xi_{12}(t,T)$ grows monotonically to its equilibrium value $\xi_{12}^{\rm eq}(T)$. For $T = 1.1 \approx T_{\rm c}$ and $T = 0.98 \approx 0.9T_{\rm c}$, we compare the scaling function obtained from block-spins (as extracted from films of several thickness L_z), with two analogous functions computed in 2D systems. If the 2D system is considered at the film's temperature $T_{\rm 2D} = T$, the scaling function $\xi_{23}(T,t)/\xi_{12}(T,t)$ clearly differs from the block-spin result. On the other hand, the film and the 2D scaling function essentially coincide if the 2D system is considered at the effective temperature $T_{\rm eff,2D}$ defined by Eq. (6.4).

6.4

Equilibrium or *almost* equilibrium?

As we have shown in the previous sections, a glassy film has two motions: one in the transversal plane (**fast**) and another in the longitudinal one (**slow**). However, the equilibrium is achieved only if all the system is at equilibrium (both the fast and slow motions). This means that the complete saturation of $\xi_{12}^{\perp}$ could happen only when $\xi_{12}^{\parallel}$ does too.

In the transversal plane, the correlation length $\xi_{12}^{\perp}$ is really fast to achieve *almost* its equilibrium value, 99%, and, then, it needs *a life* to fill the last gap 1% (see below and Fig. 6.8). Hence, we hypothesized that: "*the saturation of* $\xi_{12}^{\perp}$ *happens as soon as it achieves the* 99% *of its equilibrium value*

$$\xi_{12}^{\perp}(t_{\rm saturation}) = 0.99\,\xi_{12}^{\perp}(t_{\infty})\,\text{"}. \tag{6.5}$$

In the following, we will show how this definition of the saturation time along the

transversal plane is consistent with the physical dynamics that we have explained in the previous sections.

Thermal noise

The errors of $\xi^{\perp}_{12}$ were calculated exploiting the jackknife technique, see Appendix B.1 for details. However, these estimations are dominated by sample-to-sample fluctuations. Hence, we did a delicate computational technique to isolate the thermal contribution to the error.

Being at the equilibrium, the time dependence in the overlap calculation of Eq. (4.13) can be dropped off and we can average over different times in order to gain statics and to have a very accurate measurement of the transversal correlation length $\xi^{\perp}_{\rm eq}$. This technique is called *Cauchy condensation* and we exploited it to average over the last $N_T = 20$ times, where we are certain to have achieved the equilibrium:

$$\xi^{\perp}_{\rm Cauchy}(i_{\rm sample}) = \frac{1}{N_T}\sum_{i_t=0}^{N_T-1} \xi^{\perp}_{12}(t_{i_t}, i_{\rm sample})\,; \tag{6.6}$$

where i_t is a time index, $i_{\rm samples}$ indicates an independent sample, and $\xi^{\perp}_{\rm Cauchy}(i_{\rm sample}) \equiv \xi^{\perp}_{\rm eq}(i_{\rm sample})$ [4].

The estimator $\xi^{\perp}_{\rm Cauchy}(i_{\rm sample})$ is very accurate. For each time t, let us define a new variable:

$$\xi^{\perp}_{\rm fluc}(t, i_{\rm sample}) = \left[\xi^{\perp}_{\rm Cauchy}(i_{\rm sample}) - \xi^{\perp}_{12}(t, i_{\rm sample})\right]\,. \tag{6.7}$$

Then, we calculated the error of this quantity as:

$$\overline{\xi^{\perp}_{\rm fluc}(t)} = \frac{1}{N_S}\sum_{i_{\rm sample}=0}^{N_S}\left(\frac{1}{N_T}\sum_{i_{\rm t}=0}^{N_T}\xi^{\perp}_{\rm fluc}(t_{i_{\rm t}}, i_{\rm sample})\right)$$

$$\overline{\left[\xi^{\perp}_{\rm fluc}(t)\right]^2} = \frac{1}{N_S}\sum_{i_{\rm sample}=0}^{N_S}\left(\frac{1}{N_T}\sum_{i_{\rm t}=0}^{N_T}\left[\xi^{\perp}_{\rm fluc}(t_{i_{\rm t}}, i_{\rm sample})\right]^2\right)$$

$$\sigma(t) = \sqrt{\frac{\overline{\left[\xi^{\perp}_{\rm fluc}(t)\right]^2} - \left[\overline{\xi^{\perp}_{\rm fluc}(t)}\right]^2}{N_T - 1}}\,. \tag{6.8}$$

This technique reduces drastically the errors of $\xi^{\perp}_{12}(t)$. The built quantity $\xi^{\perp}_{\rm fluc}(t)$ absorbs the sample-to-sample fluctuations and, hence, we obtained an error estimation of $\xi^{\perp}_{12}(t)$ that contains only thermal fluctuations. For the following analysis, we will use this error estimation.

Now, let us define a time window $\tau \in [t_1 : t_2]$ where the time t_1 and t_2 are defined as:

$$\xi^{\perp}(t_1) = 0.99\,\xi^{\perp}_{\rm eq} \quad \text{and} \quad \xi^{\perp}(t_2) \simeq \xi^{\perp}_{\rm eq}\,. \tag{6.9}$$

We focused on the case $L_z = 4$. In Fig. 6.8 we show the growth of both the correlation lengths $\xi^{\perp}_{12}(t)$ and $\xi^{\parallel}_{12}(t)$ in the time window τ at two different temperatures.

[4] In simulations, we have stored configurations at times t_n integer-part-of $2^{n/4}$.

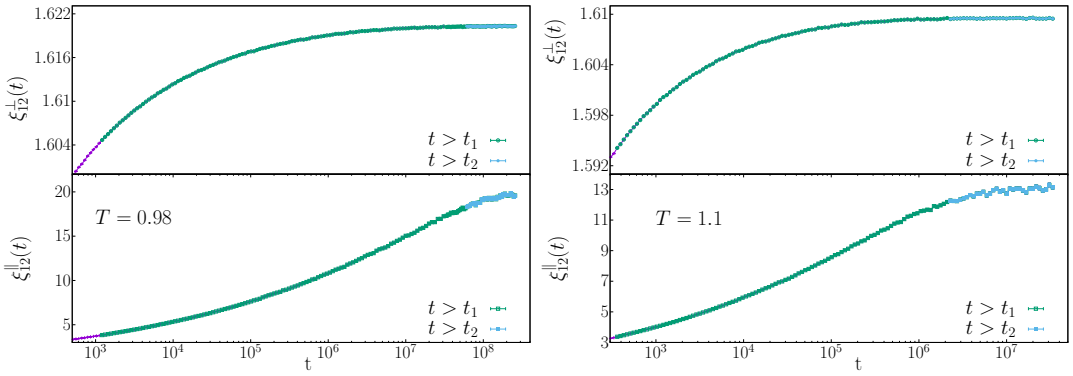

(a) Data at $T = 0.98$ (b) Data at $T = 1.1$.

Figure 6.8: Evaluation of the growth of the correlation lengths, $\xi^{\perp}(t)$ and $\xi^{\parallel}(t)$, in the time window, τ. **On the left** data at $T = 0.98$ and **on the right** data at $T = 1.1$.

As one can see from Fig. 6.8, when $\xi_{12}^{\perp}$ achieves *almost* its equilibrium values, its joined $\xi_{12}^{\parallel}$ is far away from its *equilibrium*:

$$\begin{aligned} T = 1.1 \qquad & \xi^{\parallel}(t_1) \sim 0.257\, \xi_{eq}^{\parallel} \\ T = 0.98 \qquad & \xi^{\parallel}(t_1) \sim 0.196\, \xi_{eq}^{\parallel}\,. \end{aligned} \tag{6.10}$$

Moreover, when $\xi_{12}^{\perp}$ achieves its *real* equilibrium at the time t_2, the longitudinal correlation length $\xi_{12}^{\parallel}(t_2)$ is:

$$\begin{aligned} T = 1.1 \qquad & \xi^{\parallel}(t_2) \sim 0.934\, \xi_{eq}^{\parallel} \\ T = 0.98 \qquad & \xi^{\parallel}(t_2) \sim 0.934\, \xi_{eq}^{\parallel}\,. \end{aligned} \tag{6.11}$$

or in other words, $\xi_{12}^{\parallel}$ achieves its *almost* equilibrium.

Hence, our numerical definition of *almost equilibrium* is consistent for both film motions.

6.5

The density distribution $P(q)$

According to Ref. [Guc14], they observed a saturation of the relaxation function, $S(t, t_w, T, H)$, as soon as the transversal correlation length is compatible with the thickness value $\xi_{12}^{\perp} \propto L_z$. One possible explanation for this behavior is that the occupancy of the states created when $\xi_{12}^{\perp} \propto L_z$ increases, as it must do because the number of correlated spins is increasing with increasing the waiting time t_w ($\xi_{12}^{\parallel}(t) > \xi_{12}^{\perp}$), but the structure of those created states does not. Hence, we have investigated the behavior of the density probability to infer the microscopical scenario.

6.5.1 Growth of $\langle Q^2_{\mathrm{a,b}}(t)\rangle$

We perform a Kadanoff-Wilson transformation over our system and we define spins over the renormalized system, see Eq. 4.18.
Then, we study the time evolution of the rescaled quantity:

$$\langle Q^2_{\mathrm{a,b}}(t)\rangle = \frac{1}{N_{\mathrm{box}}}\sum_{\{\mathrm{box}\}}^{N_{\mathrm{box}}}\frac{1}{\tilde{V}}\sum_{\mathbf{X}}^{\tilde{V}}\left[\frac{1}{L_z^3}\sum_{r_1,r_2,r_3=0}^{L_z-1} q^{(\mathrm{a,b})}(\mathbf{r}+L_z\mathbf{X},t)\right]^2 , \tag{6.12}$$

where we averaged over all the possible boxes, that we can build on our film system, and over the renormalized lattice $\tilde{V} = V/L_z^3$.
The rescaled quantity, $\langle\overline{Q^2_{\mathrm{a,b}}(t)}\rangle$, is an indicator of the microscopical structure of the states. In Fig. 6.9 we report the growth of $\langle\overline{Q^2_{\mathrm{a,b}}(t)}\rangle$ as a function of time.
Analogously to Fig. 6.8, we studied the evolution of $\langle\overline{Q^2_{\mathrm{a,b}}(t)}\rangle$ in the time window τ.

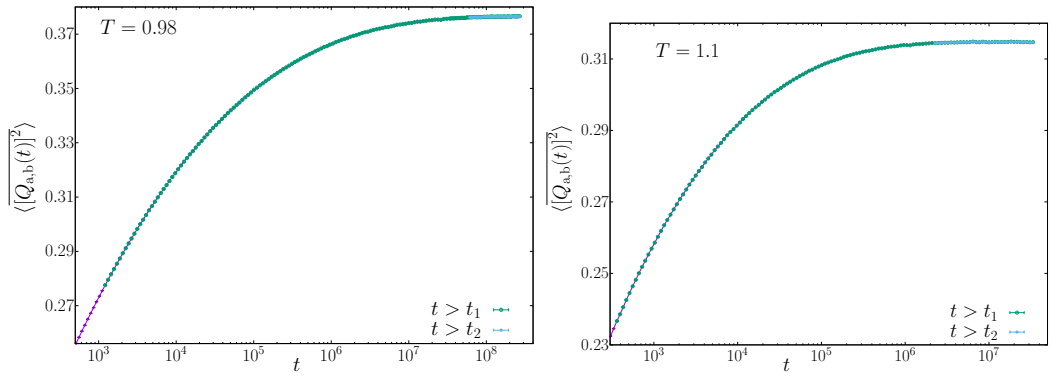

(a) Data at $T = 0.98$ (b) Data at $T = 1.1$.

Figure 6.9: Evaluation of the growth of the $\langle\overline{Q^2_{\mathrm{a,b}}(t)}\rangle$ in the time window, τ. **On the left** data at $T = 0.098$ and **on the right** data at $T = 1.1$.

At time t_1, when the transversal correlation length $\xi^{\perp}_{12}(t_1)$ achieves its *almost equilibrium*, we see that $\langle\overline{Q^2_{\mathrm{a,b}}(t)}\rangle$ is still far away from its equilibrium:

$$\begin{aligned} T = 1.1 \qquad & \langle\overline{[Q_{\mathrm{a,b}}(t_1)]^2}\rangle \sim 0.752\,\langle\overline{[Q_{\mathrm{a,b}}]^2}\rangle_{\mathrm{eq}} \\ T = 0.98 \qquad & \langle\overline{[Q_{\mathrm{a,b}}(t_1)]^2}\rangle \sim 0.737\,\langle\overline{[Q_{\mathrm{a,b}}]^2}\rangle_{\mathrm{eq}}\,. \end{aligned} \tag{6.13}$$

Instead, at time t_2, consistently to the previous results, the $\langle\overline{Q^2_{\mathrm{a,b}}(t)}\rangle$ is close to the *real* equilibrium:

$$\begin{aligned} T = 1.1 \qquad & \langle\overline{[Q_{\mathrm{a,b}}(t_2)]^2}\rangle \sim 0.999\,\langle\overline{[Q_{\mathrm{a,b}}]^2}\rangle_{\mathrm{eq}} \\ T = 0.98 \qquad & \langle\overline{[Q_{\mathrm{a,b}}(t_2)]^2}\rangle \sim 0.998\,\langle\overline{[Q_{\mathrm{a,b}}]^2}\rangle_{\mathrm{eq}}\,. \end{aligned} \tag{6.14}$$

Hence, the microscopical structure of the states does not arrest its evolution when $\xi^{\perp}$ saturates.

6.5.2 Behavior of the density probability $P(Q(t))$

Hence, we studied the properties of the density distribution $P(Q(t))$,where, for notation simplicity, $\langle Q^2_{\mathrm{a,b}}(t)\rangle = Q(t)$.

The $P(Q(t))$ is the average over the disorder distribution $P(J)$ [5]

$$P(Q(t)) = \overline{P_J(Q(t))}\ , \tag{6.15}$$

where, for each sample realization one can define the density distribution as

$$P_J(Q(t)) = \langle \frac{1}{V}\sum_{i=0}^{V} \delta(Q(t) - Q_i^J(t))\rangle\ . \tag{6.16}$$

The definition of Eq. 6.16 holds only in the thermodynamical limit. Instead, in a finite-size system the thermodynamical distribution $P(Q(t))$ is enlarged because the delta functions became distributions with no-zero widths.

A simple way to take into account the spreading of the delta functions due to finite-size effects is to introduce a symmetric convolution kernel

$$G_{\Delta}^{(k)}(h - h') \equiv C \exp\left[-(|h - h'|/\Delta)^k\right]\ , \tag{6.17}$$

where C is a normalizing constant, the spreading parameter $\Delta = 1/\sqrt{V}$ such that holds the thermodynamic limit $\lim_{L\to\infty} \Delta = 0$ and $k = 2$ for having the Gaussian convolution [Bn11]. As the time increases and, so, the correlation length $\xi(t)$, the $P(Q(t))$ curves have a spreading. This behavior is perfectly consistent with the increasing of the inherent state of the system.

According to Ref. [Guc14], the saturation of the transversal correlation length $\xi^{\perp}_{12}$ is followed by a dynamical arrest and, so , $\xi^{\perp}_{12}$ is the characteristic value proportional to the free-energy barrier $\Delta_{\max}$. Hence, we studied the behavior of $P(Q(t))$ in the time window $\tau \in [t_1 : t_2]$.

The behavior of $P(Q(t))$ clearly draws out a scenario where the system does not arrest its dynamics, and its state structure evolves.

[5] We focused only in the binary distribution $P(J) = \pm 1$.

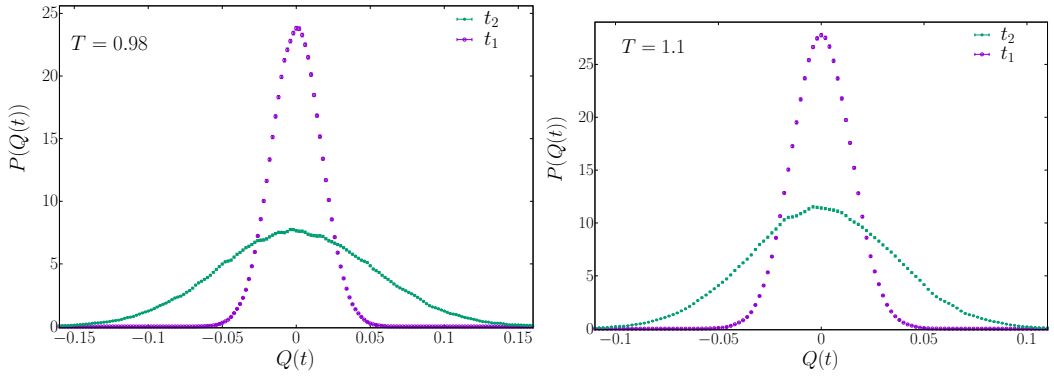

(a) Data at $T = 0.98$ (b) Data at $T = 1.1$.

Figure 6.10: Plots show the behavior of the density probability $P(Q(t))$ in the time window τ. **On the left** we report data at $T = 0.98$; **on the right** data at $T = 1.1$.

6.6

Remark

We have studied in detail, for the first time, the dimensional crossover in the aging dynamics of spin glasses in film geometry, uncovering rich and composed dynamics. Several very different regimes and scaling laws emerge, and we have succeeded to clarify with good precision the behavior of all of them. We hope and believe that our findings will be a sound basis for analyzing experimental results on such systems. Our analysis starts from the intuition about the presence of a dimensional crossover, linking $2D$ and $3D$ physics through films: we find that the intuition is correct but oversimplifies a reality that turns out to be more complex. Film physics is becoming very relevant from an experimental point of view, but it is also becoming clear that it can also become a powerful computational tool.

Part III

The Edward-Anderson model in presence of an external magnetic field

CHAPTER VII

The Ising spin-glass in presence of an external magnetic field

In this chapter, we will present the results that we have obtained in the evaluation of the spin-glass dynamics in presence of an external magnetic field [Zha20b, Pag21]. We examined in details the dynamics of the spin-glass system in the vicinity and below its transition temperature T_g. The advent of realistic time and length scales on the dedicated supercomputer, Janus II, enables a synergy between theory, experiment, and simulations that encompasses a relatively complete examination of the dynamical properties of spin-glass dynamics.
We believe that the experimental results are vital for a full comprehension of our numerical and theoretical ones. Hence, we are going to present them in this chapter. We want to underline that we carry out the numerical simulations and, in order to describe the behavior of both experimental and numerical results, we unveil a new powerful scaling law.

This chapter is organized as follows. Section 7.2 details the experimental measurements of the non-linear magnetization of the CuMn spin-glass. Section 7.3 describes the nature of the numerical simulations. Section 7.4 introduces the response function, $S(t, t_{\rm w}; H)$, and its extraction from experiment and simulations. Section 7.5 develops the new scaling law, and applies it to both experimental and simulation results. Next, in Sec. 7.6 we show how to connect the peak of the response function $S(t, t_{\rm w}; H)$ to a Hamming distance (HD). In addition, Section 7.7 exhibits the nature of the growth of the numerical correlation length ξ in the presence of a magnetic field at temperatures close to the critical temperature T_g. We observed interesting overshoot phenomena that we prove to be general, as they are observed even in ferromagnetic systems. Section 7.8 investigates the de Almeida-Thouless (dAT) phase boundary in D = 3. Important technical details are provided in the appendices. Finally, Section 7.9 summarizes our results, and point to future opportunities exhibited from the synergy between theory, experiment, and simulations.

7.1 Introduction

We present an analysis of the zero field cooling magnetization, $M_{\rm ZFC}(t, t_{\rm w}; H)$, as a function of $t, t_{\rm w}$ and magnetic field H at prescribed temperatures $T \leq T_g$. In this protocol the "sample" is quenched in zero magnetic field from a temperature $T > T_g$ to a measuring temperature $T \leq T_g$. The word *quench* means different things experimentally and in simulations. In the former, there is a finite *cooling rate* as the system is cooled from above T_g to the measurement temperature T. It is typically of the order of one to tens of second/degree of cooling. In the case of simulations, it can be instantaneous. Though on the surface this would seem a difficult issue, in fact temperature chaos [Bra87, Ban87] (that we now know to be present in non-equilibrium dynamics as well [BJ20]) makes the two approaches similar if not identical. Experimentally, though the cooling rate is finite, lowering the temperature sufficiently (larger δT than milli-Kelvins) creates new spin-glass states without knowledge of previous history (termed rejuvenation [Jon98]). This is the reason that the magnetic susceptibility is reproducible from one experiment to another without any dependence on the cooling rate. Thus, the *final* state reached upon a temperature quench experimentally is as *fresh* as the state arrived at in simulations upon an instantaneous temperature quench.

After the measurement temperature T is reached, the system is held for a time $t_{\rm w}$, the *waiting time*, after which a magnetic field H is turned on. The subsequent magnetization, $M_{\rm ZFC}(t, t_{\rm w}; H)$, is then measured over a time interval t. The response consists of two terms: an instantaneous increase in magnetization (the so-called *reversible magnetization*), and a slowly increasing magnetization, the *irreversible magnetization*. The latter is found to depend upon all of the factors, $t, t_{\rm w}, H$. The rise of the irreversible part is typically very slow, taking literally times of the order of the age of the universe to reach equilibrium. For this reason, a spin-glass, once perturbed from a quasi-equilibrium state, never reaches equilibrium, and one is always in a dynamical or non-equilibrium regime.

The "target" of the sum of the reversible and irreversible magnetizations is the so-called *field-cooled* magnetization, $M_{\rm FC}$, for which the measuring protocol is the reverse of the zero-field magnetization. Namely, at $T > T_g$, a magnetic field H is turned on, and then the temperature is quenched to $T \leq T_g$. Typically, $M_{\rm FC}$ is relatively constant, but not without its own dynamics. If the magnetic field is suddenly removed, the magnetization immediately decays by its reversible part (the same as in the zero-field case), followed by a slow decay termed the irreversible part or $M_{\rm TRM}(t, t_{\rm w}; H)$, the thermoremananet magnetization *dependent upon the waiting time* $t_{\rm w}$. In general, it is found that,

$$M_{\rm FC} = M_{\rm ZFC}(t, t_{\rm w}; H) + M_{\rm TRM}(t, t_{\rm w}; H) \quad , \tag{7.1}$$

the so-called extended principle of superposition [Nor97]. There is an immense literature covering both $M_{\rm ZCF}(t, t_{\rm w}; H)$ and $M_{\rm TRM}(t, t_{\rm w}; H)$ measurements, and the physical insights gained from them [Vin97, Nor97, Vin07].

Our approach is rather different, in that we choose to quantify the dynamics in terms of the spin-glass correlation length $\xi(t, t_{\rm w}; H)$. Experimentally, this approach was introduced first in the work of Joh et al. [Joh99] who developed the following protocol. They used the relaxation function, $S(t, t_{\rm w}; H)$ defined by,

$$S(t, t_{\rm w}; H) = d\Big[-M_{\rm TRM}(t, t_{\rm w}; H)\Big] \Big/ d\ln\, t \quad . \tag{7.2}$$

It is known that $S(t, t_{\rm w}; H)$ peaks at was is termed an effective waiting time, $t_H^{\rm eff}$ which is usually of the order of $t_{\rm w}$ [Nor86]. It is a time characteristic of the decay of $M_{\rm TRM}(t, t_{\rm w}; H)$, or though Eq. (7.1), of the increase of $M_{\rm ZFC}(t, t_{\rm w}; H)$ with time t. As noted by Hammann *et al.* [Led91, Ham92] for states distributed according to ultrametric symmetry, the dynamics are controlled by a largest free energy barrier height, $\Delta_{\rm max}$ associated with the state that has the smallest overlap with the initial state, $q_{\rm min}$. Thus, $t_H^{\rm eff}$ can be associated with $\Delta_{\rm max}$ through the usual Arrhenius law:

$$\Delta_{\rm max} = k_B T\big(\ln t_H^{\rm eff} - \ln \tau_0\big) \quad , \tag{7.3}$$

where τ_0 is a characteristic exchange time, $\tau_0 \sim \hbar/k_B T_g$.

In order to extract a correlation length, Joh et *al.* [Joh99] used the notion that the free energy barrier heights were reduced in the presence of a magnetic field by the Zeeman energy, E_Z, [Joh99, Guc14, Bou92, Vin95, BJ17a] and that, for small magnetic fields H,

$$E_Z = \big(V_{\rm corr}/a_0^3\big)\chi_{\rm FC} H^2 \quad , \tag{7.4}$$

where $\chi_{\rm FC}$ is the field-cooled magnetic susceptibility per spin, $V_{\rm corr}$ is the correlated volume, and a_0 the average spatial separation of the magnetic ions, so that the number of correlated spins $N_{\rm corr} = V_{\rm corr}/a_0$. They took [Zha19, Zha20a],

$$N_{\rm corr} = V_{\rm corr}/a_0^3 = \frac{4\pi}{3}\xi^{3-(\theta/2)} \equiv b\,\xi^{3-(\theta/2)} \quad , \tag{7.5}$$

where b is a geometrical factor, θ is the "replicon" exponent [1] [BJ17a], and ξ is in units of a_0. Using Eqs. (7.2) through (7.5), they exhibited the data shown in Fig. 7.1.
The data in the limit of small magnetic fields H were clearly linear in H^2, allowing Eqs. (7.4) through (7.5) to set a value for ξ. The deviation from linearity in H^2 was puzzling, leading to the authors stating: "*We do not have a satisfactory explanation for this change in slope. A different description predicts a linear dependence of E_Z upon H, which can be made to fit the data...but with a significant deviation at small field changes.*" It is the purpose of this work to analyze the entirety of the data in terms of non-linear terms in the spin-glass magnetization according to a new scaling law. In addition to our analysis of new magnetization data contained in this work, we shall also show that the data of Fig. 7.1, and subsequent experiments of Bert *et al.* [Ber04] on the Ising spin-glass $Fe_{0.5}Mn_{0.5}TiO_3$, fit the new scaling law well, obviating the need for questioning Eq. (7.4), and putting to rest the controversy over the nature of the

[1] See Appendix D.2 for details.

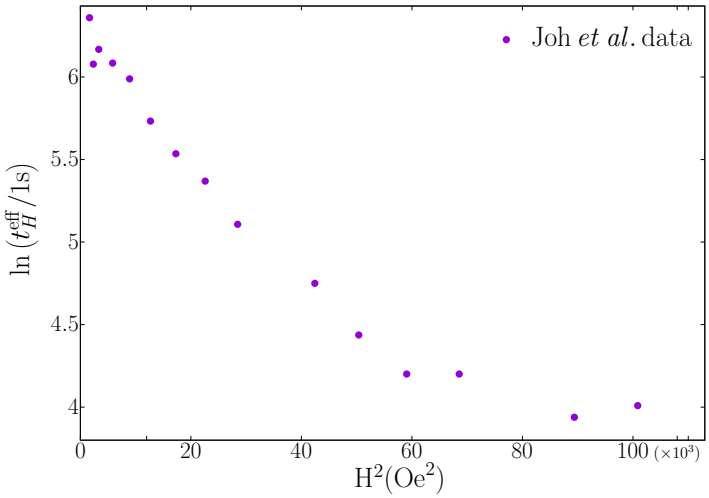

Figure 7.1: A plot of ln $t_H^{\rm eff}$ [equivalently E_Z from Eq. (7.4)] vs H^2 for Cu:Mn 6 at % ($T/T_g = 0.83, t_{\rm w} = 480$ sec) at fixed $t_{\rm w}$ and T. (Data taken from Ref. [Joh99])

Zeeman energy in spin-glasses. Our experimental co-workers bring together a complete set of magnetization measurements of a single crystal of the prototypical spin-glass, CuMn 6 at.%. As opposed to thin films where the correlated volume is of "pancake" geometry [Zha17a], the correlated volume is most certainly spherical and unlimited by finite size crystallites separated by grain boundaries [Rod04, Rod13]. Accompanying these experimental measurements are the simulations performed on the dedicated supercomputer, Janus II, that, for the first time, exhibit spin-glass correlations that approach experimental time and length scales.

A breakthrough for the comprehension of spin-glass system in the presence of a magnetic field is given by the range of the correlation lengths that we are able to achieve both experimentally and numerically. We were able to reports results up to $\xi \approx 23.6\, a_0$ (a_0 is the typical Mn-Mn distance), which represents a step forward by a factor of three than from previous work [BJ17a]. On the experimental side, we reach a correlation length four times larger than in Ref. [Joh99].

Although our simulations were designed to that end, we attempt a preliminary location of the dAT line in the phase diagram of the 3D spin-glass (sec. 7.8).

The synergy between these two approaches, combined with theory, opens up a new vista for spin-glass dynamics. A direct outgrowth of this collaboration is the introduction of the new magnetization scaling law that encompasses the full range of magnetic fields for temperatures in the vicinity of the condensation temperature T_g [Zha20b]. This scaling law successfully describes both experimental and simulation results, and as noted above, will resolve a nearly three-decade-old controversy concerning the nature of the magnetic state.

7.2

Experimental details

The experimental measurements were made with a CuMn $\sim$ 6 at.% single crystal sample, prepared using a Bridgman method. The Cu and Mn were arc melted several times in an argon environment, and cast in a copper mold. The ingot was them processed in a Bridgman furnace. Both x-ray fluorescence and optical observation showed that the beginning of the growth is a single phase. More details can be found in Appendix A of Ref. [Zha19]. The transition temperature, $T_g = 31.5$, was determined from the temperature at which $M_{\rm ZFC}(T)$ first began to depart from $M_{\rm FC}(T)$.

The magnetization measurements were made using a commercial DC SQUID. The sample was quenched from 40 K at 10 K/min to the measuring temperature T_m in zero magnetic field. After stabilization of the temperature, the system was aged for a waiting time $t_{\rm w}$ before a magnetic field was applied, and the magnetization $M_{\rm ZFC}(t, t_{\rm w}, T_m)$ recorded as a function of time t. The temperatures T_m were chosen as 28.5 K, 28.75 K, and 29 K, so that $T_m \geq 0.9 T_g$. The magnetic fields ranged from 16 Oe to 59 Oe. Table 7.1 displays the relevant experimental parameters, including the effective replicon exponent $\theta(\tilde{x})$.

Table 7.1: The values of the temperatures T_m and two waiting times $t_{\rm w}$ for the four experimental regimes, the respective correlation lengths at times $t_{\rm w}$ (in units of the average Mn-Mn spacing a_0), and the effective replicon exponent $\theta(\tilde{x})$ obtained from Eqs. (7.41) and (7.42) below (see also Appendix D.2).

	T_m (K)	$t_{\rm w}$ (s)	$\xi(t_{\rm w})/a_0$	$\theta(\tilde{x})$
Exp. 1	28.50	10000	320.36	0.337
Exp. 2	28.75	10000	341.76	0.344
Exp. 3	28.75	20000	359.18	0.342
Exp. 4	29.00	10000	391.27	0.349

7.3

Some details of the simulations

We carried out massive simulations on the supercomputer Janus II [BJ13] studying the Ising-Edwards-Anderson (IEA) model in a cubic lattice with periodic boundary conditions and size $L = 160\, a_0$, where a_0 is the average distance between magnetic moments, see Tab. 7.2 for the simulation details. The $N = L^D$ Ising spins, $s_{\mathbf{x}} = \pm 1$, interact with their lattice nearest neighbors though the Hamiltonian:

$$\boldsymbol{H} = -\sum_{\langle \mathbf{x},\mathbf{y} \rangle} J_{\mathbf{xy}} s_{\mathbf{x}} s_{\mathbf{x}} - H \sum_{\mathbf{x}} s_{\mathbf{x}} \,, \tag{7.6}$$

where the quenched disordered couplings are $J_{\mathbf{xy}} = \pm 1$ with 50% probability. We name a particular choice of the couplings a *sample*. In the absence of an external magnetic field $H = 0$, this model undergoes a spin-glass transition at the critical temperature $T_g = 1.102(3)$ [BJ13].

As we explained in the Sec. 7.1 in order to mimic the experimental protocol of the zero-field cooling (ZFC) in the simulation, we followed this procedure. The initial random spin configuration was placed instantaneously at the working temperature T, and left to relax for a time $t_{\rm w}$, at $H = 0$. At time $t_{\rm w}$, the external magnetic field was turned on and the magnetic density was recorded,

$$M_{\rm ZFC}(t, t_{\rm w}; H) = \frac{1}{160^3} \sum_{\mathbf{x}} s_{\mathbf{x}}(t + t_{\rm w}; H) \tag{7.7}$$

as well as the correlation function,

$$C(t, t_{\rm w}; H) = \frac{1}{160^3} \sum_{\mathbf{x}} s_{\mathbf{x}}(t_{\rm w}; H = 0)\, s_{\mathbf{x}}(t + t_{\rm w}; H)\,. \tag{7.8}$$

The non-equilibrium dynamics was simulated according to a Metropolis algorithm; the numerical time unit being the lattice sweep, roughly corresponding to one picosecond of physical time [Myd93]. For each temperature and waiting time, see Tab. 7.2, several magnetic fields were simulated. For computational reasons, one single independent sample was performed for each case. However, we checked the robustness and the sample-independence of our results in a single case, studied in detail in Appendix D.3.

According to Ref. [BJ17a], the value of the dimensionless magnetic field H used in the numerical simulation can be matched to the physical one. This relation was estimated from experimental $Fe_{0.5}Mn_{0.5}TiO_3$ data [AK94]. We found for $H = 1$ in the IEA model that it was corresponded to 5×10^4 Oe physically. Hence, our experimental range (16 Oe to 59 Oe) corresponds to magnetic field $0.0003 \lesssim H \lesssim 0.0012$ in the IEA model. However, the signal-to-noise ratio, which scales linearly in H for small fields, limited our simulation to $H \geq 0.005$ [Méz87], equivalent to a physical $H = 250\,\text{Oe}$.

In order to match the experimental and numerical scales, we exploited a dimensional analysis [Fis85] to relate H and the reduced temperature $\hat{t} = (T_g - T)/T_g$ through the scaling,

$$\hat{t}_{\rm num} \approx \hat{t}_{\rm exp} \left(\frac{H_{\rm num}}{H_{\rm exp}} \right)^{\frac{4}{\nu(5-\eta)}} , \tag{7.9}$$

where $\nu = 2.56(4)$ and $\eta = -0.39(4)$ are $H = 0$ critical exponents [BJ13], while the subscript exp and num stand for experiment and simulation respectively. According to Eq. (7.9), and signal-to-noise limitation, we can match the experimental and numerical scales by increasing $\hat{t}_{\rm num}$, resulting in $0.89 \lesssim T_{\rm num} \lesssim 0.99$. Given our pre-existing database of long simulations at $H = 0$ [BJ18], it has been convenient to work at temperatures $T_{\rm num} = 0.9$ and $T_{\rm num} = 1.0$. Table 7.2 displays the relevant numerical parameters, including the effective replicon exponent $\theta(\tilde{x})$ and the $C_{\rm peak}(t_{\rm w})$ values that will be introduced and explained in Sec. 7.4.2.

	T	$t_{\rm w}$	$\xi(t_{\rm w}; H=0)$	$t_{\rm max}$	$\theta(\tilde{x})$	$C_{\rm peak}$
Run 1	0.9	2^{22}	8.294(7)	2^{30}	0.455	0.533(3)
Run 2	0.9	$2^{26.5}$	11.72(2)	$2^{30.5}$	0.436	0.515(2)
Run 3	0.9	$2^{31.25}$	16.63(5)	2^{33}	0.415	0.493(3)
Run 4	1.0	$2^{23.75}$	11.79(2)	2^{28}	0.512	0.422(2)
Run 5	1.0	$2^{27.625}$	16.56(5)	2^{30}	0.498	0.400(1)
Run 6	1.0	$2^{31.75}$	23.63(14)	2^{35}	0.484	0.386(4)

Table 7.2: Main parameters for each of our numerical simulations: T, $t_{\rm w}$, $\xi(t_{\rm w})$, the longest simulation time $t_{\rm max}$, the replicon exponent θ (see Appendix D.2) and the value of $C_{\rm peak}(t_{\rm w})$ employed in Eq. (7.15).

7.4

Measurements and computations of the relaxation rate

We address the relaxation function $S(t, t_{\rm w}; H)$ in Sec. 7.4.1, and explain how $t_H^{\rm eff}$ is extracted from simulations in Sec. 7.4.2.

7.4.1 Extracting the relaxation function $\mathbf{S(t, t_w; H)}$

The main quantity used in the experiment of [Joh99] is the relaxation function $S(t, t_{\rm w}; H)$:

$$S(t, t_{\rm w}; H) = \frac{{\rm d}M_{\rm ZFC}(t, t_{\rm w}; H)}{{\rm d}\ln t} \tag{7.10}$$

that exhibits a local maximum at time $t_H^{\rm eff}$.
Experimentally, the magnetization measurements $M_{\rm ZFC}(t, t_{\rm w}; H)$ enable the evaluation of the relaxation function $S(t, t_{\rm w}; H)$ directly. A representative set of data for $T_m = 28.5$ K and $t_{\rm w} = 10^4$ sec is displayed in Fig. 7.2.

Numerically, the calculation of $S(t, t_{\rm w}; H)$ is sensitive to the relative errors of the magnetization density which increase as:

$$\frac{\delta M_{\rm ZFC}(t, t_{\rm w}; H)}{M_{\rm ZFC}} \propto 1/H\,. \tag{7.11}$$

We employ two tricks to extract the relaxation function $S(t, t_{\rm w}; H)$ from simulations. On the one hand, we perform a de-noising method to regularize the magnetization density $M_{\rm ZFC}(t, t_{\rm w}; H)$, exploiting the Fluctuation-Dissipation relations (FDR) [Cug93, Cru03, Fra94, Fra98, Fra99]

$$\frac{T}{H} M_{\rm ZFC}(t, t_{\rm w}; H) = \mathcal{F}(C; H)\,, \tag{7.12}$$

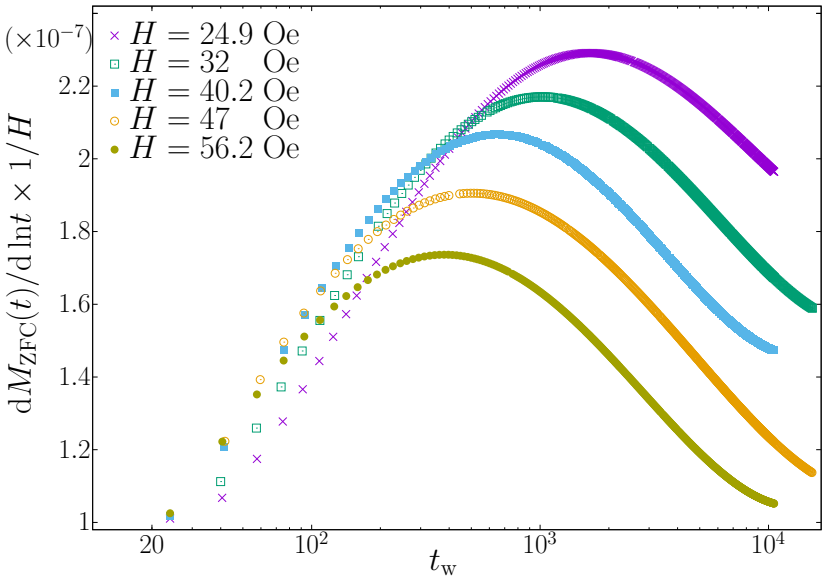

Figure 7.2: Example of $S(t, t_{\mathrm{w}}; H)$ measurements for different magnetic fields. The sample is a single crystal CuMn 6 at.%, and the measurements were taken at a waiting time of 10 000 s and at a temperature $T = 28.5$ K. The time at which $S(t, t_{\mathrm{w}}; H)$ peaks is taken as t_H^{eff}, the effective response time. The shift to shorter times as H increases is the measure of the reduction of $\Delta_{\max}$ with increasing Zeeman interaction, and is used to extract the linear and non-linear terms in the magnetic susceptibility.

where $\mathcal{F}(C; H)$ behaves at large $C(t, t_{\mathrm{w}}; H)$ as $\mathcal{F}(C; H) = 1 - C(t, t_{\mathrm{w}}; H)$. We report the details in Appendix D.1.1. On the other hand, we defined the $S(t, t_{\mathrm{w}}; H)$ as a finite time difference

$$S(t, t_{\mathrm{w}}, t'; H) = \frac{M_{\mathrm{ZFC}}(t', t_{\mathrm{w}}; H) - M_{\mathrm{ZFC}}(t, t_{\mathrm{w}}; H)}{\ln\left(\frac{t'}{t}\right)}\,, \tag{7.13}$$

In simulations, the time is discrete and we have stored configurations at times $t_n =$ integer-part-of $2^{n/4}$, with n an integer. Let us write explicitly the integer dependence of the time t and t' as:

$$t \equiv t_n \qquad t' \equiv t_{n+k} \tag{7.14}$$

where k is an integer time parameter. The reader will note that there is a tradeoff in the choice of k. On the one hand, the smaller k is the better the finite-difference in Eq. (7.13) represents the derivative. On the other hand, when k grows the statistical error in the evaluation of Eq. (7.13) decreases significantly. In this section we report only the case for $k = 8$ (more details about time discretization are provided in Appendix D.1.3). The numerical $S(t, t_{\mathrm{w}}, t'; H)$ are exhibited in Fig. 7.3. A local maximum in the long-time region can be seen.

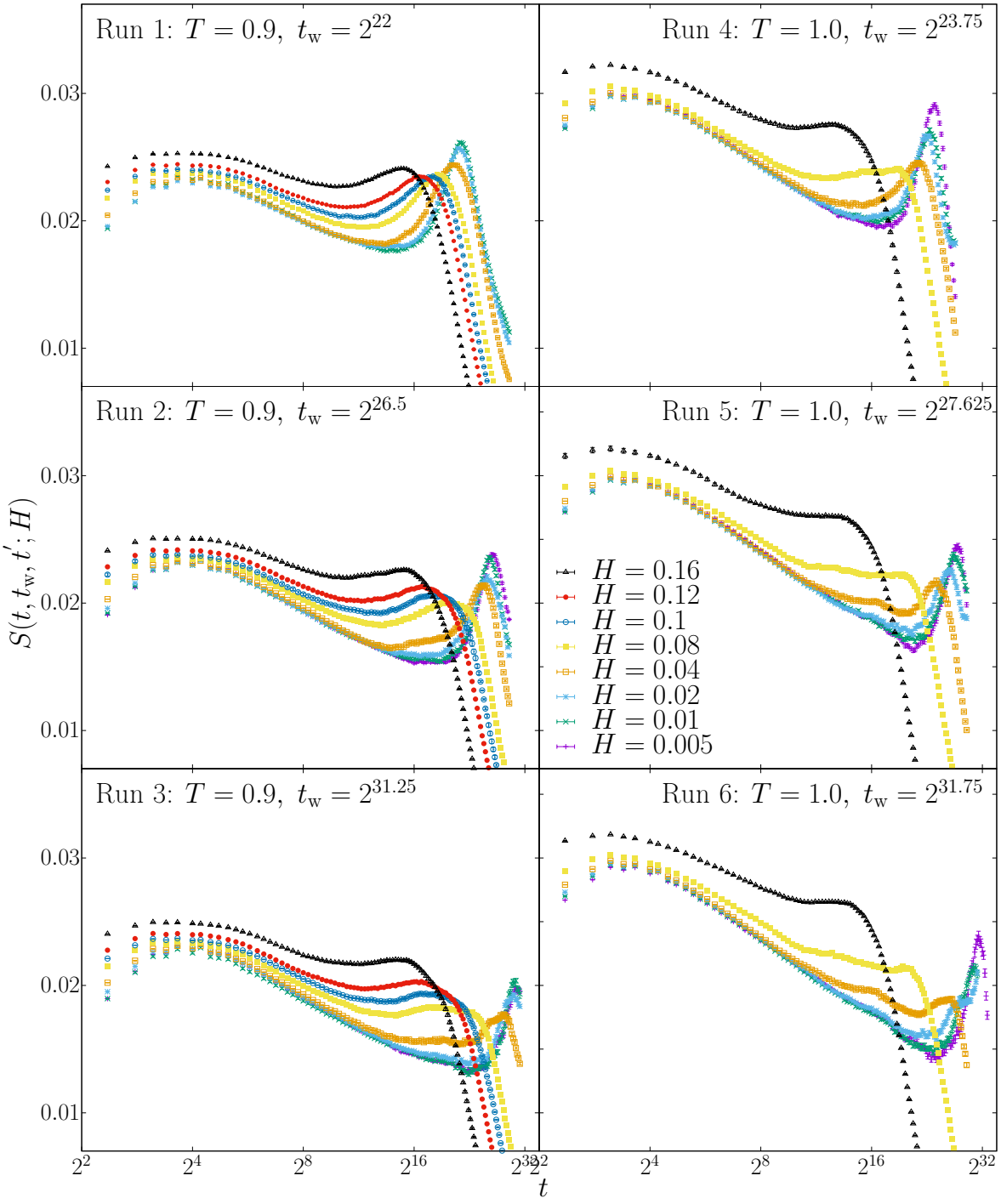

Figure 7.3: **Time evolution of the relaxation function** $S(t, t_w, t'; H)$ of Eq. (7.13) for the six runs of Table 7.2.
All the plots have the time parameter $k = 8$ in Eq. (7.14).

7.4.2 A different approach for the computation of t_H^{eff} in the simulations

As explained in Sec 7.1, we are interested in the evaluation of the time when the relaxation function $S(t, t_w, t'; H)$ peaks, namely t_H^{eff}. Two problems arise:

1. The reader will note two separate peaks in the $S(t, t_{\rm w}; H)$ curves in Fig. 7.3: namely the peak at microscopic times $t \sim 4$, and the peak we are interested in $t \sim t_{\rm w}$. Unfortunately, the distinction between the two peaks is only clear at small H. Previous numerical work [BJ17a] did not face this problem, probably because of their smaller correlation length, $\xi \approx 8$, (the nonlinear susceptibilities grow very fast with ξ: see the next Section).

2. We are most interested in the limit $H \to 0$, which is extremely noisy as we have explained above.

An interesting possibility emerges when plotting the relaxation function $S(t, t_{\rm w}, t'; H)$ in terms of the correlation function $C(t, t_{\rm w}; H)$, rather than as function of time, (see Fig. 7.4). The correlation function $C(t, t_{\rm w}; H)$ is a decreasing function of time, the long time region corresponding to small $C(t, t_{\rm w}; H)$, and vice versa. Hence, the *physical* peak in which we are interested is the peak that appears at small $C(t, t_{\rm w}; H)$,(see Fig. 7.4). Analogously to Fig. 7.3, we report only the case for $k = 8$ in Fig. 7.4.

The simulation data strongly suggest that, when $H \to 0$, the correlation function $C(t, t_{\rm w}; H)$ approaches a constant value $C_{\rm peak}(t_{\rm w})$ at the maximum of the relaxation function. Hence, our proposal is to *define* $t_H^{\rm eff}$ in the simulations as the time when $C(t, t_{\rm w}; H)$ reaches the value $C_{\rm peak}(t_{\rm w})$

$$C(t_H^{\rm eff}, t_{\rm w}; H) = C_{\rm peak}(t_{\rm w}) \ . \tag{7.15}$$

As the reader can see, Eq. (7.15) is solvable also at $H = 0$ [instead of a finite magnetic field as regained for magnetization data, Eq. (7.2)]. The crucial point for our *new* $t_H^{\rm eff}$ definition, see Eq. (7.15), is the determination of the values of $C_{\rm peak}(t_{\rm w})$. Two problems arise:

1. The constant value $C_{\rm peak}(t_{\rm w})$ is well defined only for small magnetic field H.

2. The relaxation function as a function of the correlation, $\mathcal{S}(C, H)$, is an implicit function of a re-parametrized time,

$$t_{\rm new} = \frac{1}{2} \ln \left(\frac{t_{n+k}}{t_n} \right) \ , \tag{7.16}$$

   (see Appendix D.1.3 for details).

Our strategy is to study, for each run, the behavior of $\mathcal{S}(C, H)$ for the two smallest magnetic fields H and for three different integer times k. We report in Fig. 7.5 an enlargement of the peaks for $\mathcal{S}(C, H)$ used for the evaluation of $C_{\rm peak}(t_{\rm w})$. We report our estimates for $C_{\rm peak}(t_{\rm w})$ in Tab. 7.2.

The relaxation function $S(t_{\rm new}, t_{\rm w}; H)$ depends on the correlation length $\xi(t_{\rm w})$, and on the applied magnetic field H, Eq. (7.2). We observe, however, that $S(t_{\rm new}, t_{\rm w}; H)$ has a temperature dependence, which we extract by comparing Runs 2 and 4 in Fig. 7.5. These two cases are characterized by

1. A similar starting correlation length $\xi(t_{\rm w}; H = 0) \approx 11.7$, (see Tab. 7.2);

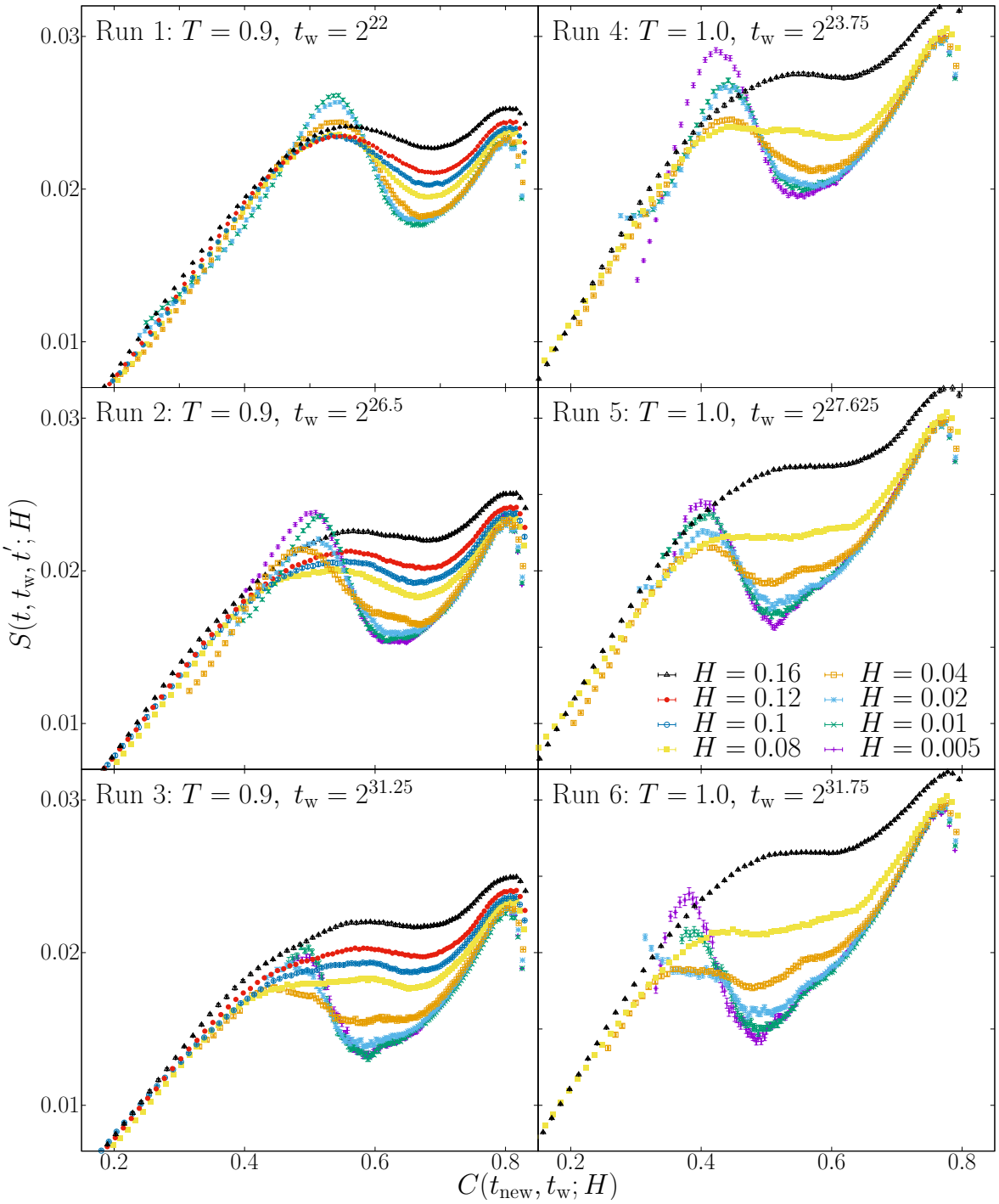

Figure 7.4: $S(t, t_w; H, k)$ **as a function of** $C(t, t_w; H)$.
The peak region is enlarged in Fig. 7.5. The physically relevant peak is the one for small C, corresponding to long times. We consider the reparametrized t_{new} with $k = 8$ in Eq. (7.16).

2. The same applied magnetic field in each subfigure, respectively, namely $H =$

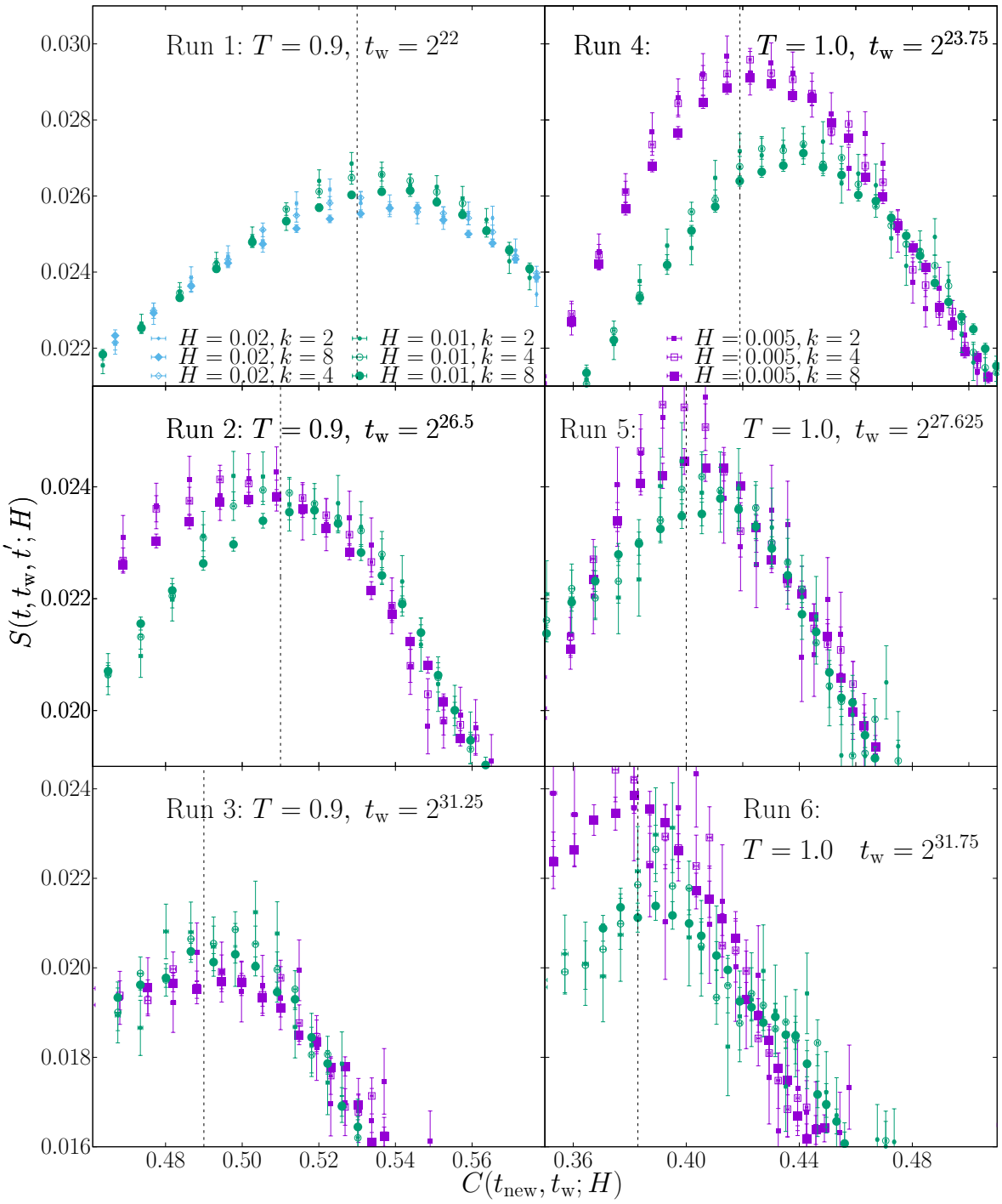

Figure 7.5: Enlargement of the peak region of $S(t, t_w, t'; H)$ as a function of $C(t, t_w; H)$ for several values of time parameter k in Eq. (7.14).
The dashed black lines indicate the $C_{peak}(t_w)$ positions.

0.005 and $H = 0.01$.

Yet, there appears to be two different scenarios in the data plotted in Fig. 7.5. In

Run 2, the peak of $\mathcal{S}(C, H)$ is almost the same for all the rescaled time curves. In Run 4, however, the peaks are separated for different k. As it will be explained in Section 7.5.5, this difference in behavior is caused by increasing nonlinear effects of the magnetization, $M_{\mathrm{ZFC}}(t, t_{\mathrm{w}}; H)$.

In conclusion, Eq. (7.15) solves our two problems at once. We no longer need to resolve the short-time and the long-time peaks in Fig. 7.3, and it bypasses the problem of the vanishing magnetization as H goes to zero.

7.5

Scaling law

We address here three different aspects of the scaling law. The assumptions that lead us to our scaling law are given in Sec. 7.5.1. Next, in Sec. 7.5.2, we use the scaling law in the analysis of our experimental data (previous data are also reanalyzed in Sec. 7.5.3), with the corresponding analysis for our simulations given in Sec. 7.5.4. Sec. 7.5.5 exhibits together our experimental and numerical results according to the new scaling law. Next, in Sec. 7.6 we show how to connect the peak of the response function $S(t, t_{\mathrm{w}}; H)$ to a Hamming distance (HD). In Sec. 7.7 we address the nature of the growth of the numerical correlation length $\xi(t_{\mathrm{w}})$ in presence of a magnetic field at temperatures close to the condensation temperature T_g.

7.5.1 Nonlinear scaling law

Scaling laws for the spin-glass susceptibility in the vicinity of the condensation temperature have been proposed and analyzed for decades. We first recall an important early approach, and then develop the scaling law that we have employed to analyze our experiments and simulations.

Nonlinear magnetization effects, and their scaling properties in spin-glasses were first introduced by Malozemoff, Barbara, and Imry [Mal82a, Mal82b, Cha93]. They introduced the relationship for the singular part of the magnetic susceptibility,

$$\chi_s = H^{2/\delta} f\left(t_r / H^{2/\phi}\right) \quad , \tag{7.17}$$

where $f(x)$ is a constant for $x \to 0$; $f(x) = x^{-\gamma}$, for $x \to \infty$; $\phi = \gamma\delta/(\delta - 1) \equiv \beta\delta$, and t_r is the reduced temperature T/T_g. This form was used by Lévy and Ogielski [LŐ86] and by Lévy [Lév88] who measured the ac nonlinear susceptibilities of very dilute AgMn alloys above and below T_g as a function of frequency, temperature, and magnetic field. The critical exponents of Eq. (7.17) were evaluated as $\beta = 0.9$, $\gamma = 2.3$, $\delta = 3.3$, $\nu = 1.3$, $z = 5.4$. They differ substantially from Monte Carlo simulations for short range Ising systems [BJ13] [*e.g.* $\beta = 0.782(10)$, $\gamma = 6.13(11)$, $\nu = 2.562(42)$]. The discrepancy for the value of γ is very large, and most probably arises from the lack of the knowledge of an exact value of T_g in the experiments. This illustrates the value and need of a different approach for scaling the nonlinear magnetization of spin-glasses in the vicinity of T_g.

Our approach is to express the non-linear components of the magnetic susceptibility in terms of $\xi(t, t_{\rm w})$ [2], the spin-glass correlation length in a magnetic filed H. This approach gives the nonlinear magnetization a direct connection to a measurable quantity, and obviates the need for an accurate value of T_g.

The argument goes as follows. Let $M(t, t_{\rm w}; H)$ be the magnetization per spin, where explicit attention is paid to the waiting (aging) time, $t_{\rm w}$, in the preparation of the spin-glass state. The generalized susceptibilities $\chi_1,\ \chi_3\ , \chi_5$ ... are defined through the Taylor expansion,

$$M(H) = \chi_1 H + \frac{\chi_3}{3!} H^3 + \frac{\chi_5}{5!} H^5 + \mathcal{O}(H^7) \quad . \tag{7.18}$$

where, for brevity sake, we omit the arguments t and $t_{\rm w}$.

Under equilibrium conditions, and for a large enough correlation length, ξ_{eq}, there is a scaling theory for the magnetic response to an external field H [Par88] [Ami05]. Our main hypothesis in this work is that this scaling theory holds not only at equilibrium, but even in the non-equilibrium regime for a spin-glass close to $T_{\rm g}$, and in the presence of a small external magnetic field H:

$$M(t, t_{\rm w}; H) = [\xi(t + t_{\rm w})]^{y_H - D} \mathcal{F}\left(H[\xi(t + t_{\rm w})]^{y_H}, \frac{\xi(t + t_{\rm w})}{\xi(t_{\rm w})} \right) \ . \tag{7.19}$$

Because of the full-aging spin-glass dynamics (see, e.g. [Rod03]), Eq. (7.19) tell us that $\xi(t + t_{\rm w})/\xi(t_{\rm w})$ will be approximately constant close to the maximum of the relaxation rate, (see Fig. 7.2), so that we shall omit this dependence. Hence, combining Eq. (7.18) and (7.19), one can express the generalized susceptibility $\chi_1,\ \chi_3\ , \chi_5$ ... in terms of the spin-glass correlation length $\xi(t, t_{\rm w}; H)$

$$\chi_{2n-1} \propto |\xi(t_{\rm w})|^{2n\, y_H - D} \quad , \tag{7.20}$$

where we have omitted the arguments t, H for simplicity, and

$$2y_H = D - \frac{\theta}{2} \quad , \tag{7.21}$$

with θ the "replicon" exponent [BJ17a].
As the reader can notice, Eq. (7.20) predicts the paradoxical result:

$$\chi_1 \propto \xi^{-\theta/2} \tag{7.22}$$

hence, χ_1 goes to zero when $\xi \to \infty$. In fact, Eq. (7.20) neglects the contribution of the regular part of the free-energy. A better description for χ_1 is [Zha20b]:

$$\chi_1 = \frac{\hat{S}}{T} + \frac{a_1(T)}{\xi^{\theta/2}} \quad , \tag{7.23}$$

[2] The correlation length, $\xi(t, t_{\rm w})$ is of course a function of the temperature T also, but here we are only interested in non-linearity of magnetization.

where $\hat{S}$ is the function appearing in the Fluctuation-Dissipation relations [BJ17b], and $a_1(T)$ is some unknown (hopefully smoothly varying with temperature) constant.

The free-energy variation *per spin* in presence of a magnetic field can be obtained by integrating the magnetic density, Eq.(7.18), with respect to the magnetic field:

$$\Delta F = -\left[\frac{\chi_1}{2}H^2 + \frac{\chi_3}{4!}H^4 + \frac{\chi_5}{6!}H^6 + \mathcal{O}\big(H^8\big)\right] \quad . \tag{7.24}$$

Substituting the scaling behavior from Eq. (7.20) and Eq. (7.23), the free-energy ΔF can be written as,

$$\Delta F = -\left[\frac{\hat{S}}{2T}H^2 + \frac{a_1(T)}{\xi^{\theta/2}}H^2 + a_3(T)\xi^{D-\theta}H^4 + a_5(T)\xi^{2D-(3\theta/2)}H^6 + \mathcal{O}\big(H^8\big)\right] \quad , \tag{7.25}$$

where again the $a_n(T)$ are unknowns and (again, hopefully) smoothly varying functions of temperature. We use the effective response time, t_H^{eff}, to reflect the total free energy change at magnetic field H and $H = 0^+$:

$$\ln\left[\frac{t_H^{\text{eff}}}{t_{H\to 0^+}^{\text{eff}}}\right] = N_{\text{corr}}\Delta F \quad , \tag{7.26}$$

where N_{corr} is the number of correlated spins, $N_{\text{corr}} = \frac{V_{\text{corr}}}{a_0^3}$, with V_{corr} the correlated spins volume, and a_0 the lattice constant or average distance between magnetic moments. Combining Eq. (7.26) with Eqs. (7.5) and (7.24) leads to,

$$\begin{aligned}\ln\left[\frac{t_H^{\text{eff}}}{t_{H\to 0^+}^{\text{eff}}}\right] = -b\Bigg[&\left(\frac{\hat{S}}{2\,T} + \frac{a_1(T)}{\xi^{\theta/2}}\right)\xi^{D-(\theta/2)}H^2 \\ &+ a_3(T)\xi^{2D-(3\theta/2)}H^4 + a_5(T)\xi^{3D-2\theta}H^6 + \mathcal{O}\big(H^8\big)\Bigg] \quad ,\end{aligned} \tag{7.27}$$

where the coefficient b is a geometrical factor, see Eq. (7.5), and we have absorbed the term k_BT in the $a_n(T)$ coefficients, see Eq. (7.3). The correction term $a_1(T)/\xi^{\theta/2}$ is small compared to $\hat{S}/T$, and so will be dropped in subsequent expressions. Eq. (7.27) shows that the higher order terms have the functional form,

$$\chi_{2n-1}\frac{H^{2n}}{(2n)!} = a_{2n-1}(T)\xi^{-\theta/2}\left[\xi^{2y_H}H^2\right]^n \quad , \tag{7.28}$$

where

$$2y_H = D - \frac{\theta}{2} \quad . \tag{7.29}$$

This leads to the new scaling relation,

$$\ln\left[\frac{t_H^{\text{eff}}}{t_{H\to 0^+}^{\text{eff}}}\right] = \frac{\hat{S}}{2T}\,\xi^{D-(\theta/2)}H^2 + \,\xi^{-\theta/2}\mathcal{G}\big(T, \xi^{D-(\theta/2)}H^2\big) \quad , \tag{7.30}$$

where the geometrical factor b has been absorbed into the scaling function $\mathcal{G}$. Comparison with the previous, more classical relation, Eq. (7.17), displays the simplicity and power of our approach to scaling the nonlinear magnetization in the vicinity of T_g.

7.5.2 Experimental nonlinear magnetization

We extract the effective waiting time $t_H^{\rm eff}$ in Eq. (7.3) from the time at which $S(t, t_{\rm w}; H)$ is a maximum as before. Our results for all four conditions in Table 7.1 are exhibited as a function of magnetic field in Fig. 7.6. The slope of the data in Fig. 7.6 at small

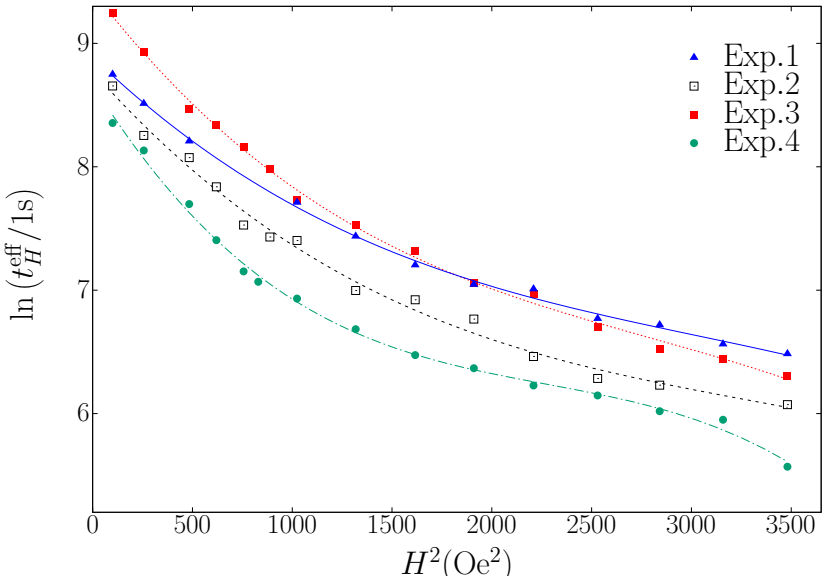

Figure 7.6: A plot of the peak times, $t_H^{\rm eff}$, for the crystal CuMn 6 at.% *vs* H^2 for the four values of T_m and $t_{\rm w}$ listed in Table 7.1. The slope for small H^2 is used to extract $\xi(t_{\rm w})$ in Table 7.1, and the lines drawn are from fitting to the scaling law introduced in Sec. 7.5.1.

values of the magnetic field H generates the spin-glass correlation length $\xi(t_{\rm w}, T_m)$ from Eqs. (7.4) and (**??**), using values for the replicon exponent $\theta(\tilde{x})$ from Table 7.1. The four values for $\xi(t_{\rm w}, T_m)$ from our experiments are exhibited in Table 7.1 . These results will allow us to express the non-linear susceptibility in terms of $\xi(t_{\rm w})$.

An example of the measured relaxation function, $S(t, t_{\rm w}; H)$, is plotted for $T = 28.5K$ and $t_{\rm w} = 10000$ s in Fig. 7.2 for five different magnetic fields, while the effective response times, $\ln t_H^{\rm eff}$, are plotted in Fig. 7.6 for all four experiments listed in Table 7.1. Note the remarkable similarity in shape of the original experimental results for $\ln t_H^{\rm eff}$ in Fig. 7.1 with our results in Fig. 7.6. Also, note the fit of all four of our results for $\ln t_H^{\rm eff}$ in Fig. 7.6 to the scaling relationship for the nonlinear magnetization, Eq. (7.27), as will be described in more detail below.

Because the scaling relationship, Eq. (7.30), depends upon the magnitude of the waiting time in $\xi(t_{\rm w}, t, T)$, two different values of $t_{\rm w}$ were used at the same intermediate temperature $T = 28.75$ K, among the three temperatures (28.5 K, 28.75 K, and 29.0 K) listed in Sec. 7.2 and in Table 7.1, to test the scaling relation Eq. (7.30) at a given temperature. This allow us to discriminate between the influence of temperature and waiting time on $\xi(t_{\rm w}, t, T)$. In this way, we are able to demonstrate explicitly that $\xi(t_{\rm w}, t, T)$ is the parameter of control.

It is useful to display $t_H^{\rm eff}$ *vs* H^2 individually for each of the four values of T and $t_{\rm w}$. They are exhibited below in Fig. 7.7. The fitting technique is performed through the function:

$$f(x) = c_0 + c_2\, x + c_4\, x^2 + c_6\, x^3 + \mathcal{O}(x^4)\ , \tag{7.31}$$

where $x \equiv H^2$ and the coefficients c_n, according to Eq. (7.27), correspond to:

$$c_0 = \ln\left(t^{\rm eff}_{H\to 0^+}\right) \tag{7.32}$$

$$c_2 = \left[\frac{\hat{S}}{2\,T_{\rm m}}\right]\xi^{D-\theta/2} \tag{7.33}$$

$$c_4 = a_3(T_{\rm m})\xi^{2D-3\theta/2} \tag{7.34}$$

$$c_6 = a_5(T_{\rm m})\xi^{3D-2\theta}\ . \tag{7.35}$$

We have absorbed the geometrical prefactor b of Eq. (7.27), in the non-linear coefficients $a_n(T_{\rm m})$ and in the linear coefficient $\hat{S}$, and we neglect the sub-leading coefficient $a_1(T_{\rm m})/\xi^{\theta(x)/2}$.

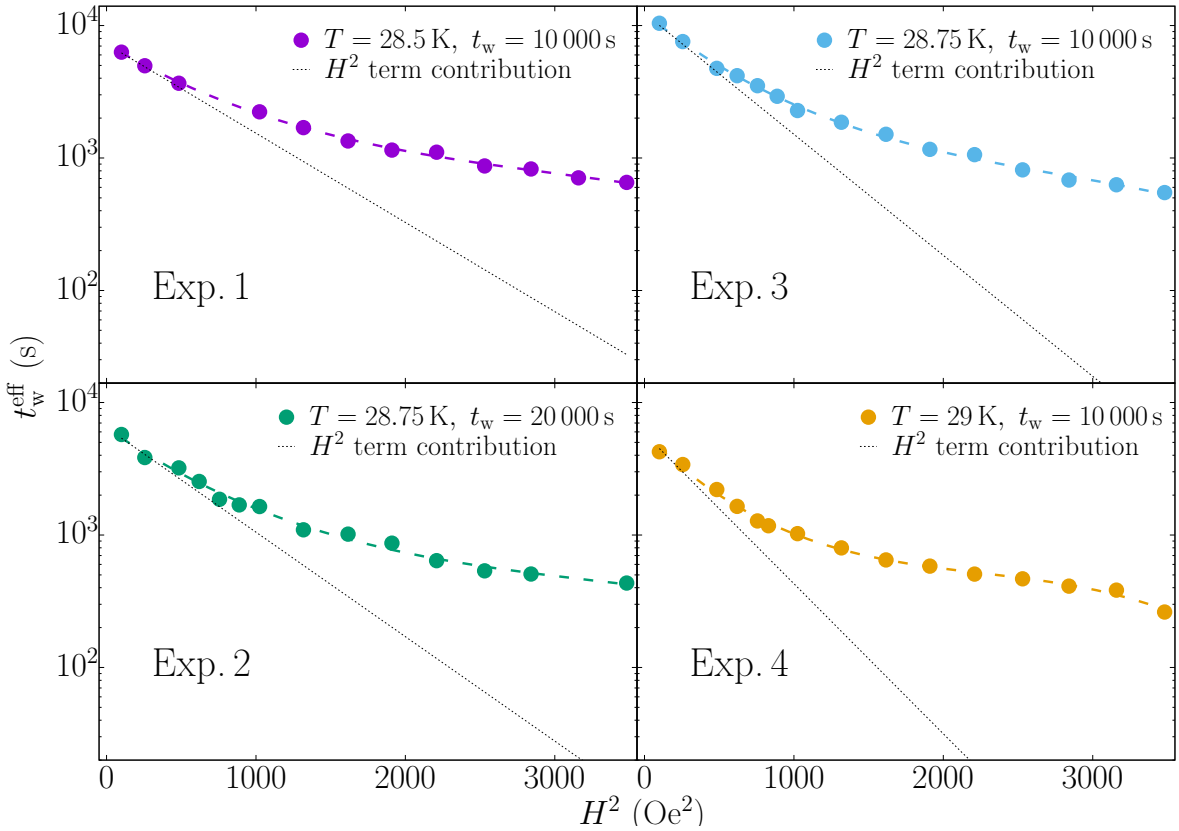

Figure 7.7: **Plots of the peak time**, $t_H^{\rm eff}$, for the crystal CuMn 6 at.% vs H^2. The straight line is an extrapolation of the linear term in the magnetization, and the dashed line is a fit to the data from Eq. (7.27)

Table 7.3: Parameters from our fits to Eq. (7.31) of our experimental data for $\ln t_H^{\rm eff}$, as a function of T and $t_{\rm w}$. The uninteresting fit parameter, c_0, is not included in the Table.

T (K)	$t_{\rm w}$(s)	coefficient	numerical value
		c_2	-1.5509 $\times 10^{-3}$ $\pm$ 1.0336 $\times 10^{-4}$
28.5	10000	c_4	3.9804 $\times 10^{-7}$ $\pm$6.9927 $\times 10^{-8}$
		c_6	-4.3631$\times 10^{-11}$ $\pm$1.2940 $\times 10^{-11}$
		c_2	-1.8157 $\times 10^{-3}$ $\pm$ 2.0032 $\times 10^{-4}$
28.75	10000	c_4	4.5651 $\times 10^{-7}$ $\pm$1.32 $\times 10^{-7}$
		c_6	-4.5844$\times 10^{-11}$ $\pm$2.45$\times 10^{-11}$
		c_2	-2.1035 $\times 10^{-3}$ $\pm$ 1.1934 $\times 10^{-4}$
28.75	20000	c_4	5.8888 $\times 10^{-7}$ $\pm$7.88 $\times 10^{-8}$
		c_6	-7.013$\times 10^{-11}$ $\pm$1.47$\times 10^{-11}$
		c_2	-2.6086 $\times 10^{-3}$ $\pm$ 1.28 $\times 10^{-4}$
29	10000	c_4	1.016 $\times 10^{-6}$ $\pm$8.45$\times 10^{-8}$
		c_6	-1.4913$\times 10^{-10}$ $\pm$1.57$\times 10^{-11}$

The effect of increasing the temperature with waiting time held constant can be seen in the difference between the measured $t_H^{\rm eff}$ and the extrapolated value of the linear magnetization term (quadratic in H^2) for the largest magnetic field ($H = 143$ Oe) in Exps. 1,2 and 4 in Fig. 7.7. Non-linear effects grow for larger $t_{\rm w}$, hence larger $\xi(t, t_{\rm w}; T_{\rm m})$ at the same temperature, which can be seen by comparing Exps. 2 and 3. The linear and nonlinear coefficients of Eq. (7.27) can be extracted from the fit to the data in Fig. 7.7 (dashed lines), whose resulting coefficients are listed in Table 7.3.

To test the scaling relationship, Eq. (7.30), we first consider the fit to the data at $T = 28.75$ K for the two waiting times, $t_{\rm w} = 2 \times 10^4$ s and $t_{\rm w} = 10^4$ s. The linear term is proportional to $\xi^{D-(\theta/2)}$. The ratio of the two correlation lengths from Table 7.3 is, hence,

$$\begin{aligned} \frac{\xi(t_{\rm w} = 20\,000)}{\xi(t_{\rm w} = 10\,000)} &= \left[\frac{c_2(t_{\rm w} = 20\,000)}{c_2(t_{\rm w} = 10\,000)}\right]^{1/[D-(\theta/2)]} \\ &= 1.0535 \quad . \end{aligned} \tag{7.36}$$

Should scaling hold according to Eq. (7.30), then consistency requires that the ratios of the correlation lengths from the nonlinear terms should be the same as that for the linear term. They are:

$$\begin{aligned} \frac{\xi(t_{\rm w} = 20\,000)}{\xi(t_{\rm w} = 10\,000)} &= \left[\frac{c_4(t_{\rm w} = 20\,000)}{c_4(t_{\rm w} = 10\,000)}\right]^{1/[2D-(3\theta/2)]} \\ &= 1.0476 \quad , \end{aligned} \tag{7.37}$$

and

$$\frac{\xi(t_{\rm w}=20\,000)}{\xi(t_{\rm w}=10\,000)} = \left[\frac{c_6(t_{\rm w}=20\,000)}{c_6(t_{\rm w}=10\,000)}\right]^{1/[3D-2\theta]} = 1.0526 \quad . \tag{7.38}$$

The equality of the values that come out from Eqs.(7.36) - (7.38) is an impressive experimental verification of the scaling relationship Eq. (7.30).

Another check is the growth of the correlation length itself. At the temperature $T_m = 28.75$ K and for the two waiting times, it is possible to calculate directly the ratio of the two values of the correlation length by using the power law growth rate expression [Joh99, Kis96],

$$\xi(t_{\rm w}, T_{\rm m}) = a_0\,\hat{C}_1 \left(\frac{t_{\rm w}}{\tau_0}\right)^{\hat{C}_2(T_{\rm m}/T_g)} \equiv a_0\,\hat{C}_1 \left(\frac{t_{\rm w}}{\tau_0}\right)^{T_{\rm m}/(z_c T_g)} \quad , \tag{7.39}$$

where $\hat{C}_1$ and $\hat{C}_2$ are constants, by definition $\hat{C}_2 \equiv 1/z_c$, and τ_0 is a characteristic *exchange time*, here taken as $\hbar/k_B T_g$.

Using the growth rate parameter $z_c = 12.37$ [BJ18, Zha19], one finds,

$$\frac{\xi(t_{\rm w}=20\,000)}{\xi(t_{\rm w}=10\,000)} = \left(\frac{2\times10^4}{10^4}\right)^{T_{\rm m}/(12.37\,T_g)} = 2^{28.75/(12.37\times31.5)} = 1.0525 \quad . \tag{7.40}$$

Comparing the ratio of $\xi(t_{\rm w}, T_{\rm m})$ for the two different waiting times, Eq. (7.40), from the growth law, Eq. (7.39), with the ratios from fitting to the scaling relationship, Eqs. (7.36) - (7.38), is remarkable evidence for the consistency of our physical picture. It demonstrates explicitly the power of using the spin-glass correlation length as the primary factor for evaluating the spin-glass nonlinear magnetization in the vicinity of the transition temperature T_g.

The lingering issue from Eqs. (7.5) and (7.30), according to Zhai *et al.* [Zha19], "is that the replicon exponent $[\theta(\tilde{x})]$...depends upon both the temperature and ξ through the crossover variable $[\tilde{x}]$,with

$$\tilde{x} = \frac{\ell_J}{\xi(t_{\rm w}, T)} \quad ." \tag{7.41}$$

From the notation of Table 7.3, and Eq. (7.5), the number of correlated spins is,

$$N_{\rm corr} = \frac{k_B T_{\rm m}\, c_2}{\chi_{\rm FC}} = \xi^{D-[\theta(x)/2]} = \xi^{D-[\theta(\ell_J/\xi)/2]}. \tag{7.42}$$

The left-hand side is a number, the right hand side is an implicit function of ξ and θ. Using the definition of the Josephson length $\ell_J(\tilde{x})$ and of the replicon $\theta(\tilde{x})$, [3] one can solve for ξ and θ at each of the four values of $T_{\rm m}$ and $t_{\rm w}$ explored experimentally. The results are displayed in Table 7.1.

[3] The reader will find all the necessary details in Appendix D.2.

The aging rate z_c varies as a function of ξ. Using the data at $T_{\rm m} = 28.75$, the approximate aging rate factor is $z_c = 12.37 \pm 1.07$ at $\xi \sim 200$ lattice spacings a_0 [Zha19]. Although the correlation length extracted at 28.75 K is larger than that at 28.5 K, the higher temperature sets the crossover variable $x = \ell_J(T)/\xi = 0.11$ for $t_{\rm w} = 20000$ s and 0.12 for $t_{\rm w} = 10000$ s, in the range of the crossover variable obtained by us previously at $T_{\rm m} = 28.5$ K [Zha20a]. Both measurements have witnessed the slowing down of the spin-glass correlation growth rate near the critical temperature at large correlation lengths.

Using the average value of θ from Table 7.1, $\theta = 0.343$, and setting $z_c = 12.73$, the values exhibited in Eqs. (7.36)- (7.40) are altered to 1.053, 1.048, 1.052, and 1.051, respectively. Using the values from Table 7.1, the temperature dependent coefficients $a_3(T_{\rm m})$ and $a_5(T_{\rm m})$ of Eq. (7.27) can be calculated for each of the four values of $T_{\rm m}$ and $t_{\rm w}$. They are displayed in Fig. 7.8.

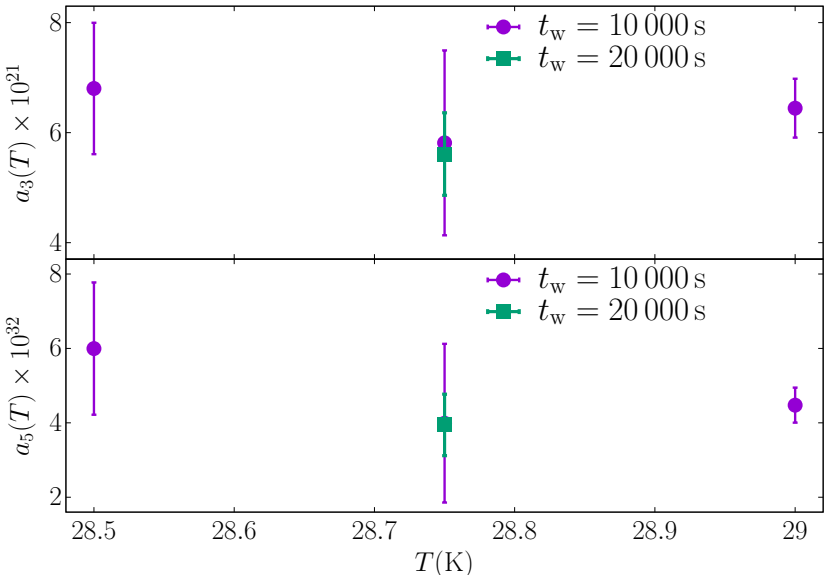

Figure 7.8: Plots shows the temperature dependence of nonlinear coefficients a_3 and a_5 as defined in Eq. (7.27) calculated using the extracted values of ξ and θ for the different temperatures $T_{\rm m}$ and waiting time $t_{\rm w}$.

From Fig. 7.8, one sees that the hope expressed after Eq. (7.25), that the temperature dependence of the coefficients $a_n(T_{\rm m})$ be weak, is realized in this set of experiments. For $a_3(T_{\rm m})$, within the experimental error bars, there is little or no change with temperature. The situation for $a_5(T_{\rm m})$ is not as nice, but there appears to be little change with temperature at the two highest temperatures.

It is interesting to test the scaling relationship [Zha20b]

$$\chi_{2n-1}(t_{\rm w}, T_{\rm m}) \propto a_{2n-1} \left[\xi(t_{\rm w}, T_{\rm m})\right]^{(n-1)D - n\theta(\hat{x})/2} \ . \tag{7.43}$$

Thus,

$$\begin{aligned} \chi_3 &\propto \xi^{D-\theta}\, a_3, \\ \chi_5 &\propto \xi^{2D-\frac{3\theta}{2}}\, a_5. \end{aligned} \tag{7.44}$$

The measured non-linear susceptibilities are exhibited below for the three temperatures $28.5K$, $28.74K$ and $29.0K$. One can test the scaling relationships Eqs. (7.43) and (7.44)

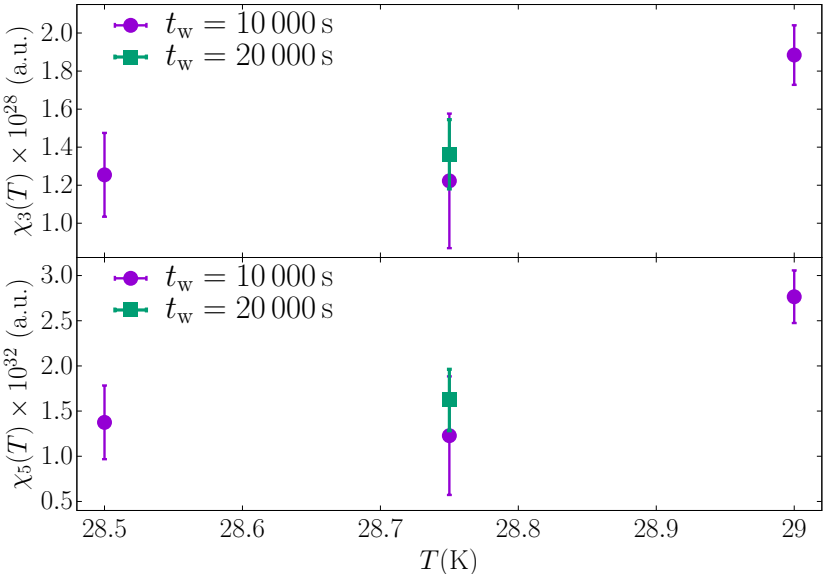

Figure 7.9: Plots show the nonlinear susceptibility $\chi_3(t_w, T_m)$ and $\chi_5(t_w, T_m)$, from Eq. (7.42), plotted as a function of temperature for the four experimental regimes of Tab. 7.1.

by using the measured values for the spin glass correlation length ξ and the replicon exponent θ from Table 7.1 and the values of c_2 and c_4 from Table 7.3. Consider $\chi_3(T, t_w)$ as an example for the temperatures 28.5 K and 29 K and $t_w = 10000$ s. For $T = 28.5$ K, we have $\xi = 320.36\, a_0$, $\theta = 0.337$ (from Table 7.1), and $c_4 = 3.9804 \times 10^{-7}$ (from Table 7.3, note that we have ignored the error bars). Similarly, for $T = 29.0$ K and $t_w = 10000$ we have $\xi = 391.27\, a_0$, $\theta(T = 29.0) = 0.349$, and $c_4 = 10.16 \times 10^{-7}$. Using Eqs. (7.31) and (7.34) and the just quoted values of $c_4(t_w; T_m)$ one finds

$$\frac{\chi_3(t_w = 10000, T_m = 28.5K)}{\chi_3(t_w = 10000, T_m = 29.0)} = 0.666\ . \tag{7.45}$$

This ratio is well within the error bars of the measured non-linear susceptibilities in Fig. 7.9. A similar result is also found for χ_5.

With these scaling observations in hand, it is interesting to ask about using them to estimate the condensation temperature T_g. In principle, determination of T_g would require an infinite t_w because $\xi(T_g)$ would be infinite. One expects that any experiment at finite t_w would yield a maximum for the non-linear susceptibility at a temperature we shall call $T_g(t_w)$ because t_w is finite.

In principle, then, by measuring $T_g(t_w)$ for ever larger t_w, one could extrapolate to the true $\xi(t_w \to \infty)$ condensation temperature T_g. If nothing else, measurements at large values of t_w on laboratory time scales could establish a lower bound for T_g.

The non-linear susceptibility χ_3 diverges as,

$$\chi_3(t_{\rm w} \to \infty, T_{\rm m}) = \chi_0 \, \frac{T_g(t_{\rm w} \to \infty)}{|T_g(t_{\rm w} \to \infty) - T_{\rm m}|^\gamma} \quad , \tag{7.46}$$

where χ_0 is a constant independent of temperature, and $\gamma = 6.13(11)$ [BJ13]. For *finite* $t_{\rm w}$, $\chi_3(t_{\rm w}, T)$ only has a maximum as a function of temperature. A way of arriving at this maximum would be to fit the data to the function

$$\chi_3(t_{\rm w}, T_{\rm m}) = \chi_0 \, \frac{T_g(t_{\rm w})}{|T_g(t_{\rm w}) - T_{\rm m}|^\gamma} \quad , \tag{7.47}$$

and then use the data points from just two or three temperatures to extract $T_g(t_{\rm w})$. For larger and larger $t_{\rm w}$, one could in principle extrapolate to the true T_g. We emphasize that though Eq. (7.47) suggests $\chi_3(t_{\rm w}, T_{\rm m})$ diverges at $T = T_g(t_{\rm w})$, it does not, arriving only at a maximum value for finite $t_{\rm w}$. Nevertheless, Eq. (7.47) is a way of estimating $T_g(t_{\rm w})$ for use in an extrapolation procedure.

To test whether this trick has any validity, one can consider the data exhibited in Fig. 7.9. Here, $t_{\rm w} = 10\ 000$ sec and, taking $\chi_3(t_{\rm w}, T_{\rm m})$ at the center of the error bars for the two temperatures 28.5K and 29. K, one finds $T_g(t_{\rm w} = 10\ 000) = 32$ K. This value is too high as magnetization measurements suggest $T_g(t_{\rm w} \to \infty) = 31.5$ K. More accurate determination of the parameters in Table 7.3 would diminish the error in $T_g(t_{\rm w})$, but it does suggest a feasible process for taking laboratory data for finite $t_{\rm w}$, and extrapolating to find $T_g(t_{\rm w} \to \infty)$.

7.5.3 Reanalysis of older data

Given the above analysis of our recent data, it is convenient to revisit the work of Joh *et al.* [Joh99] and Bert *et al.* [Ber04], to examine whether the Zeeman energy is proportional to H^2 or H; or, respectively, to the number of correlated spins or to the square root of the total number of spins. We have already alluded to their results as displaying the effect of magnetization nonlinearity. We now explore this assertion in detail using the analysis contained above in subsection 7.5.2.

Fig. 1 of Joh *et al.*, reproduced as Fig. 7.1 in this chapter, and Fig. 3 of Bert *et al.*, reproduced as Fig. 7.10. Both exhibit significant deviations away from an H^2 dependence of the ln $t_H^{\rm eff}$ with increasing values of H. Bert *et al.* [Ber04] go on to assert a linear dependence, as exhibited in their Fig. 3, reproduced here in Fig. 7.10 . Their magnetic fields are quite large, and the scale of their plot does not cover the dependence on H^2 for small H. Nevertheless, they claim their data fits a linear dependence of ln $t_H^{\rm eff}$ on H. A glance at the left panel of Fig. 7.10, suggests how they could rationalize their conclusion.

Yet, as noted by the authors of experiments in Fig. 7.1 [Joh99], a linear dependence upon H is a poor fit to the data at small H. Further, the argument behind the magnetization varying as $\sqrt{N_c}$ is supposedly valid at small H [Bou01], where the dependence on the number of correlated spins, N_c is argued to be proportional to $\sqrt{N_c}$, rather than

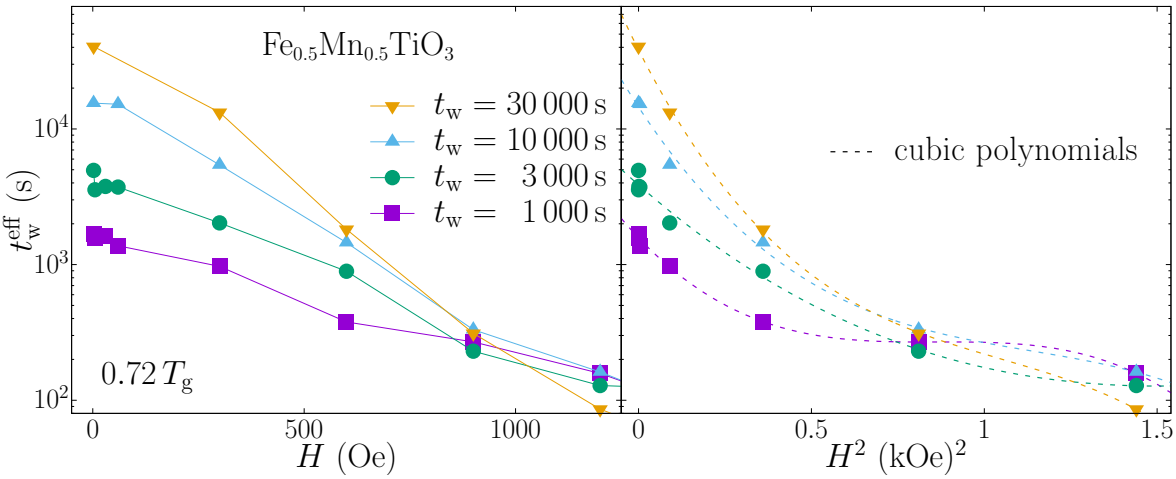

Figure 7.10: *Left*: Effective waiting times (in log scale) derived from the field-change experiments on Ising sample ($Fe_{0.5}Mn_{0.5}TiO_3$) as a function of the magnetic field H. The plot reproduces from Fig. 3 of Bert *et al.* [Ber04] (solid lines are linear interpolations to data with the same t_w). *Right*: Same data plotted against H^2. The dashed lines are fits to Eq. (7.31), with fit parameters listed in Tab. 7.4.

as N_c, as from Eq. (7.4). On the other hand, the data exhibited in their Fig. 3 (Fig. 7.10) uses magnetic fields substantially larger than used in this study.

We assert that their observed departure from linearity in H^2 as H increases is simply the effect of nonlinearity. To prove this, we apply the scaling relation, Eq. (7.30), to their Fig. 3 data [Ber04] reproduced in our Fig. 7.10, doing our best to extract their measured values from their printed figure. Our fit to Eq. (7.31) is shown in the right panel of Fig. 7.10, with the parameters c_n listed in Table 7.4.

Although only 1-2 digits are significant in Table 7.4, we write more digits, for the sake of reproducibility. The fitting quality for $t_w = 10\,000$ s and $t_w = 30\,000$ s is better than for the other two waiting times. Note that the coefficients c_n listed in Table 7.4 are considerably smaller than in our Table 7.3 for our current experiments on a CuMn 6 at. % single crystal. We believe this is because our measurements are for $T_m \approx 0.9\,T_g$ whereas Bert *et al.* [Ber04] worked at $0.72\,T_g$, where non-linear terms are expected to be much smaller.

Using the fitting coefficients from Table 7.4 and $\theta(\tilde{x}) = 0.3$, we obtain

$$\frac{\xi(t_w = 30\,000\text{ s})}{\xi(t_w = 10\,000\text{ s})} = \left[\frac{c_2(30\,000\text{ s})}{c_2(10\,000\text{ s})}\right]^{1/[D-\theta(\tilde{x})/2]} \approx 1.094, \tag{7.48}$$

$$\frac{\xi(t_w = 30\,000\text{ s})}{\xi(t_w = 10\,000\text{ s})} = \left[\frac{c_4(30\,000\text{ s})}{c_4(10\,000\text{ s})}\right]^{1/[2D-3\theta(\tilde{x})/2]} \approx 1.054, \tag{7.49}$$

$$\frac{\xi(t_w = 30\,000\text{ s})}{\xi(t_w = 10\,000\text{ s})} = \left[\frac{c_6(30\,000\text{ s})}{c_6(10\,000\text{ s})}\right]^{1/[3D-2\theta(\tilde{x})]} \approx 1.045. \tag{7.50}$$

The three ratios, Eq. (7.48)–(7.50) do not agree with one another perfectly, but

Table 7.4: We report, as a function of $t_{\rm w}$, the parameters from fits to Eq. (7.31) of the data obtained by Bert *et al.* [Ber04] for $\ln t_{\rm H}^{\rm eff}$. Their data correspond to $Fe_{0.5}Mn_{0.5}TiO_3$ at $T = 0.72\ T_g$ (see Fig. 3 of Ref. [Ber04]). The fits are shown in our Fig. 7.10. The uninteresting fit parameter, c_0, is not included in the Table.

$t_{\rm w}$ (s)	coefficient	value
1 000	c_2	-6.23×10^{-6}
	c_4	7.23×10^{-12}
	c_6	-2.78×10^{-18}
3 000	c_2	-4.57×10^{-6}
	c_4	1.40×10^{-12}
	c_6	1.26×10^{-19}
10 000	c_2	-8.74×10^{-6}
	c_4	6.81×10^{-12}
	c_6	-1.99×10^{-18}
30 000	c_2	-1.15×10^{-5}
	c_4	9.32×10^{-12}
	c_6	-2.95×10^{-18}

again, considering the rawness of the analysis, they are certainly suggestive. In summary, we believe that the assessment of Ref. [Ber04] that their data is evidence for $E_{\rm Z} \propto H$ is in error. Rather, we believe the departure they observe from linearity in H^2 arises from non-linear terms in the magnetization as a result of the large magnetic fields utilized in their study.

7.5.4 Numerical study of the ratio of the effective time at H and $H = 0^+$.

We have extracted the effective times $t_H^{\rm eff}$ exploiting our proposed relation Eq. (7.15), as explained in Appendix D.1.3. Our results are displayed in Fig. 7.11. In the subsequent analysis in Sec. 7.5.5, we shall need the derivative of $\ln\left(t_H^{\rm eff}/t_{H\to 0+}^{\rm eff}\right)$ with respect to H^2, evaluated numerically at $H^2 = 0$. Our main scope here will be evaluating this derivative.

An obvious strategy is fitting the numerical data for $\ln\left(t_H^{\rm eff}/t_{H\to 0+}^{\rm eff}\right)$ as we did for the experimental data in Eq. (7.31). Note that our sought derivative at $H^2 = 0$ is just the coefficient c_2 in the fit. A welcome simplification in the analysis of the numerical data is that we can explicitly put $c_0 = 0$ in the fit to Eq. (7.31) [indeed, we are able to carry out the fit for $\ln\left(t_H^{\rm eff}/t_{H\to 0+}^{\rm eff}\right)$ thanks to Eq. (7.15)]. Our fitting parameters are reported in Table 7.5. Unfortunately, as the reader will note from Fig. 7.11, these fits predict unphysically wild oscillations that are not observed in the numerical data. A plausible explanation for these oscillations relies on the very large magnetic fields used (recall that $H = 1$ for the IEA model roughly corresponds to 5×10^4 Oe in physical units). These huge magnetic fields probably exceed the radius of convergence of the Taylor expansion of Eq. (7.30). At any rate, the oscillations cast some doubts on the determination of the derivative at $H^2 = 0$. This is why we have turned to a different

	coefficient	value	H^2-range
Run1	$c_2(t_w;T)$	-6.01(6) $\times 10^2$	[0 : 0.025]
	$c_4(t_w;T)$	3.45(13) $\times 10^4$	
	$c_6(t_w;T)$	-1.305(90) $\times 10^6$	
	$c_8(t_w;T)$	1.998(19)$\times 10^7$	
Run2	$c_2(t_w;T)$	-1.589(19) $\times 10^3$	[0 : 0.01]
	$c_4(t_w;T)$	1.976(55) $\times 10^5$	
	$c_6(t_w;T)$	-1.4135(569)$\times 10^7$	
	$c_8(t_w;T)$	3.86(18)$\times 10^8$	
Run3	$c_2(t_w;T)$	-4.380(15) $\times 10^3$	[0 : 0.008]
	$c_4(t_w;T)$	1.338(79) $\times 10^6$	
	$c_6(t_w;T)$	-1.3328(966)$\times 10^8$	
Run4	$c_2(t_w;T)$	-1.385(58) $\times 10^3$	[0 : 0.008]
	$c_4(t_w;T)$	2.24(41) $\times 10^5$	
	$c_6(t_w;T)$	-1.75(50)$\times 10^7$	
Run5	$c_2(t_w;T)$	-3.355(90) $\times 10^3$	[0 : 0.008]
	$c_4(t_w;T)$	9.41(63) $\times 10^5$	
	$c_6(t_w;T)$	-9.12(77)$\times 10^7$	
Run6	$c_2(t_w;T)$	-7.910(153)$\times 10^3$	[0 : 0.008]
	$c_4(t_w;T)$	3.276(106)$\times 10^6$	
	$c_6(t_w;T)$	-3.56(13)$\times 10^8$	

Table 7.5: The outcome of the fits to Eq. (7.31) of the numerical data for the time ratio $\ln(t_H^{\rm eff}/t_{H\to 0^+}^{\rm eff})$. In order to stabilize the fits we needed to include terms on r.h.s of Eq. (7.31) for two cases.

strategy in order to validate our computation.

Our starting point, see Ref. [BJ18] and Eq. (7.27), is the expected scaling behavior for the coefficient $c_2(t_w,T)$ listed in Table 7.5. The nonlinear coefficient $c_2(t_w,T)$ reported in Tab. 7.5 behaves as [Zha20b]

$$c_2(t_w,T) = \xi^{D-\theta(\tilde{x})/2}\left(\frac{\hat{S}}{2T} + \frac{a_1(T)}{\xi^{\theta(\tilde{x})/2}}\right) , \tag{7.51}$$

using the scaling of the susceptibility χ_1 from Eq. (7.23). Here, $\hat{S}$ is the function appearing in the Fluctuation-Dissipation relation [BJ17b] and $a_1(T)$ is a smooth function of temperature, and we have absorbed the geometrical prefactor b of Eq. (7.27) in $a_1(T)$ and $\hat{S}(T)$. Notice that the term $a_1(T)\xi^{-\theta(x)/2}$ is sub-leading compared to $\hat{S}/(2T)$ and it was neglected in the previous analysis.

We rewrite Eq. (7.51) as:

$$\frac{c_2(T,t_w)T}{\xi^{D-\theta(\tilde{x})/2}} = \frac{\hat{S}}{2} + Ta_1(T)\xi^{-\theta(\tilde{x})/2} . \tag{7.52}$$

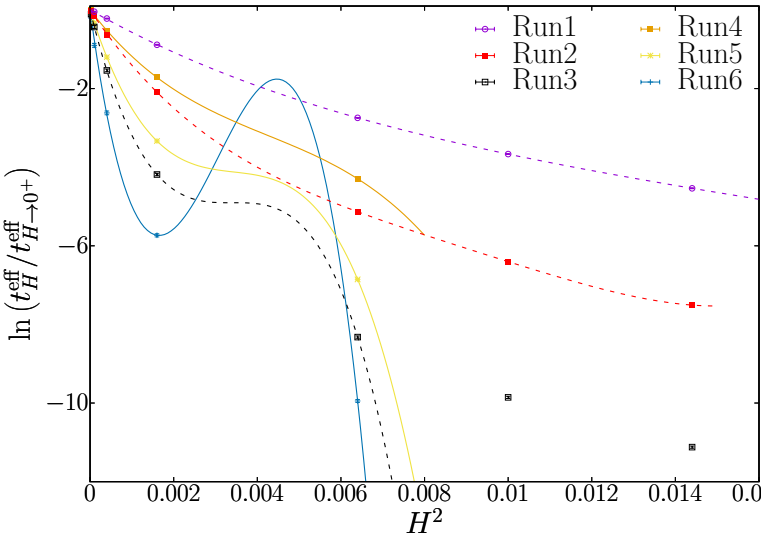

Figure 7.11: **The numerical time ratio** $\ln(t_H^{\rm eff}/t_{H\to 0^+}^{\rm eff})$.
The data were fitted as a polynomial of H^2 as reported in Table 7.5 in order to exhibit the non-linear terms.
The continuous lines are fits for data at $T = 1.0$; the dashed lines correspond to the data at $T = 0.9$.

and we study this quantity as a function of $[\xi(t_{\rm w})]^{-\theta(\tilde{x})/2}$ in Fig. 7.12. Note that, in the above expression ξ was *not* obtained from the response to the magnetic field. Instead, we computed ξ from the correlation functions at $H = 0$ (see Appendix C and Ref. [Bel08b]). The data exhibit a constant value, $a_1(T) = 0$, except for the point correspondent to $t_{\rm w} = 2^{31.75}$ at $T = 1.0$ (Run 6). Therefore, we shall accept the numerical estimation of the derivative at $H^2 = 0$ through the coefficient c_2 for all cases but for our Run 6. In order to clarify what is going on with Run 6, we report in the right panel of Fig. 7.12 an enlargement of Fig. 7.11 in the small magnetic field regime for this case. As it could be guessed from the left panel, the fitting procedure clearly underestimates the slope of the curve at $H^2 = 0$. Therefore, in order to estimate the derivative for Run 6, we have rather relied on Eq. (7.52) by averaging the constant value found in Fig. 7.12 over all Runs (excluding Run 6). We estimated the derivative for Run 6 by multiplying this averaged constant value by $[\xi(t_{\rm w})]^{D-\theta(\tilde{x})/2}$ [see Eq. (7.52)].

7.5.5 Nonlinear scaling

In order to test the scaling form, Eq. (7.30), the data for all of the nonlinear contributions to the magnetization, experimental and numerical, are plotted according to the functional form,

$$\xi^{-\frac{\theta}{2}}\mathcal{G}(T, \xi^{D-\frac{\theta}{2}}H^2) \tag{7.53}$$

in Fig. 7.13–7.14. The fit to our form for the scaling relationship, Eq. (7.30), is remarkable, and testimony to the agreement for both the experimental and numerical data.

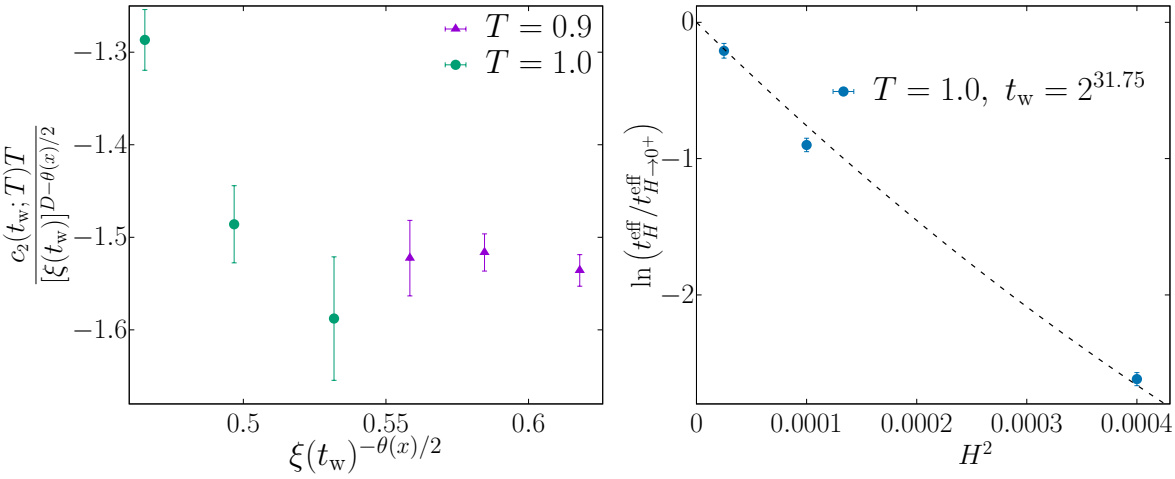

Figure 7.12: *Left:* Behavior of the rescaled quantity $c_2(t_w;T)T/[\xi(t_w)]^{D-\theta(x)/2}$ as a function of $\xi(t_w)^{-\theta(x)/2}$, see Eq. (7.52).
Right: An enlargement of Fig. 7.11 in the small-magnetic field regime, for the case $t_w = 2^{31.75}$ at $T = 1.0$ (Run 6 of Tab. 7.2) and its fit reported in Table 7.5.

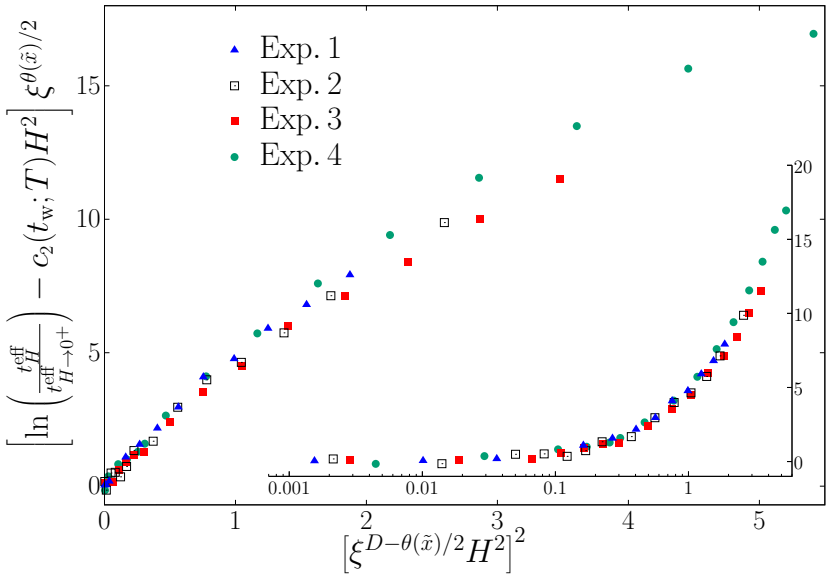

Figure 7.13: The nonlinear parts from the experimental response time data, $[\ln t_H^{\rm eff} - c_2(t_w;T)H^2]\xi^{\theta(\tilde{x})/2}$, plotted against $(\xi^{D-\theta(\tilde{x})/2}H^2)^2$. The deviations of the data at $T =$ 29 K may be caused by a shift in T_g as the temperature begins to approach $T_g(H)$. The **inset** is a magnification of the small x-range.

Comparison between different nonlinear scaling laws

In order to underline the step forward introduced by Eq. (7.30), we show here that the data do not collapse equally well if we use two different scaling laws, one from Ref. [BJ17a] and the other a simple rational modification of Ref. [BJ17a]. Specifically, we

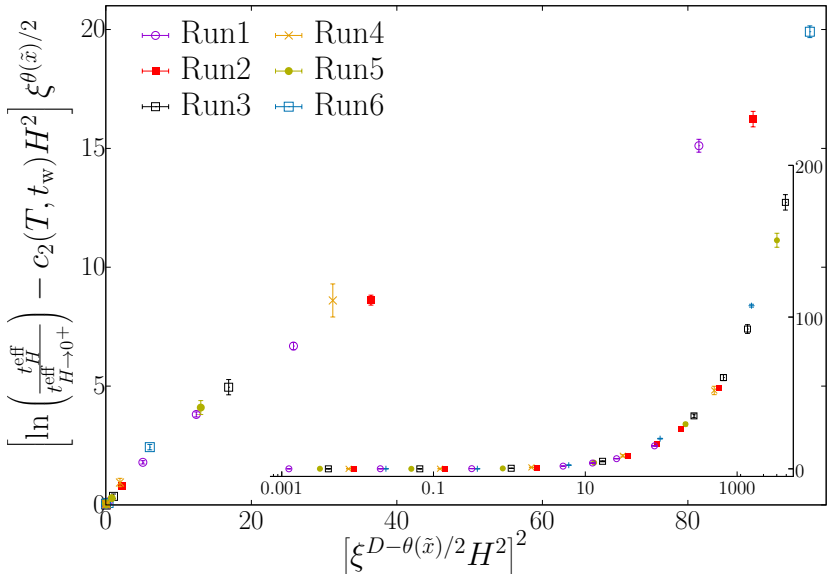

Figure 7.14: The nonlinear parts from the numerical response time data, $[\ln(t_H^{\rm eff}/t_{H\to 0^+}^{\rm eff}) - c_2(t_{\rm w};T)H^2]\xi^{\theta(\tilde{x}/2)}$, plotted against $(\xi^{D-\theta(\tilde{x})/2}H^2)^2$. The abscissa of the **main panel** is a linear scale and shows a closeup for small values of $(\xi^{D-\theta(\tilde{x})/2}H^2)^2$. The abscissa of the **inset** is log scale in order to report all our numerical data.

reanalyze our data both through the scaling equation proposed in Ref. [BJ17a],

$$\ln\left(\frac{t_H^{\rm eff}}{t_{H\to 0^+}^{\rm eff}}\right) = \mathcal{F}\left[\xi^{D-\frac{\theta(\tilde{x})}{2}}H^2\right] , \tag{7·54}$$

or by postulating that the data can be rationalized through a single scaling term,

$$\left[\ln\left(\frac{t_H^{\rm eff}}{t_{H\to 0^+}^{\rm eff}}\right)\right]\xi^{\theta(\tilde{x})/2} = \mathcal{F}\left(\xi^{D-\frac{\theta(\tilde{x})}{2}}H^2\right) . \tag{7·55}$$

We report the non-linear scaling behaviors using Eqs. (7·54) and (7·55) in Figs. 7.15 (experimental data) and Fig. 7.16 (numerical data). To ease comparisons, we use the same scaling variable and x-axis scale that we used in Fig. 7.13, where we collapsed the data using Eq. (7·53). However, because the scalings are easier to interpret with a linear y-axis scale, we also provide the same plots in a semi-log scale (Figs. 7.17 and 7.18).

The collapse of the experimental data with Eqs. (7·54) and (7·55) (Figs. 7.15 and 7.17) works well only at most $x = (H^2\xi^{D-\theta/2})^2 = 6\times 10^{20}$ Oe, which is about half of the validity range of the collapses in Fig. 7.13, which are accurate at least up to $x = 2\times 10^{21}$ Oe.

The collapse of the numerical data with Eqs. (7·54) and (7·55) (Figs. 7.16 and 7.18) is less accurate throughout the whole range of x.

We believe, therefore, that the scaling relationship represented by Eq. 7·53 is far superior.

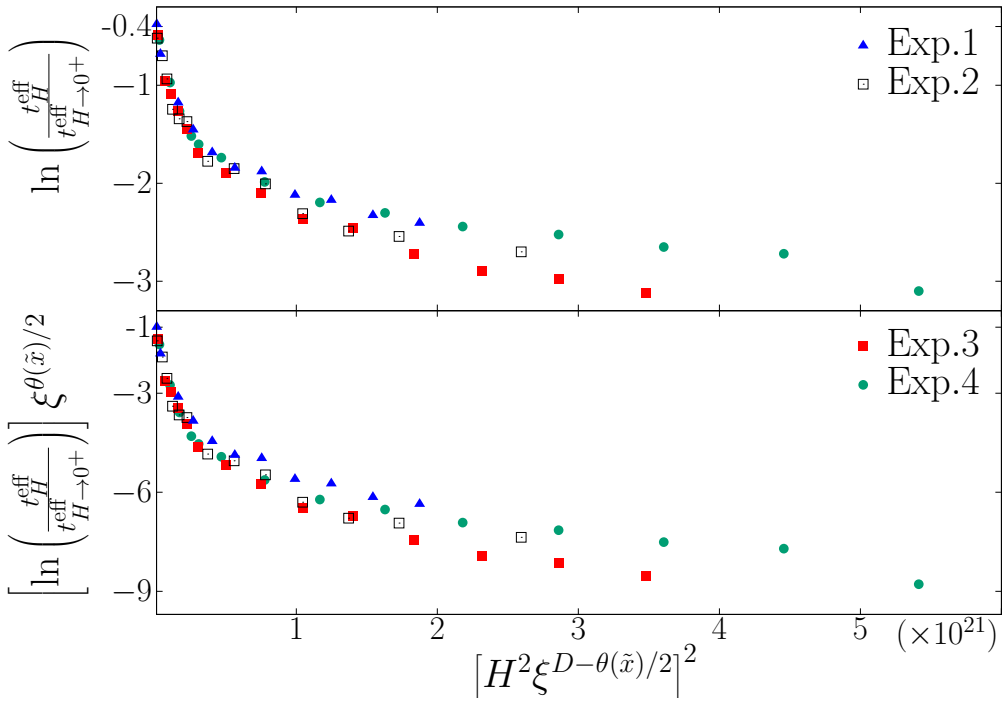

Figure 7.15: **Top** The nonlinear part of the experimental response time data: $[\ln(t_H^{\rm eff}/t_{H\to 0^+}^{\rm eff})$ plotted against the scaling variable $[H^2\xi^{D-\theta(\tilde{x})/2}]^2$, according to Ref. [BJ17a], see Eq. (7.54). The plot is in linear scale. **Bottom** The non-linear part of the response time data:$[\ln(t_H^{\rm eff}/t_{H\to 0^+}^{\rm eff})\xi^{\theta(\tilde{x})/2}$ plotted against the scaling variable $[H^2\xi^{D-\theta(\tilde{x})/2}]^2$, according to Eq. (7.55). The plot is in linear scale.

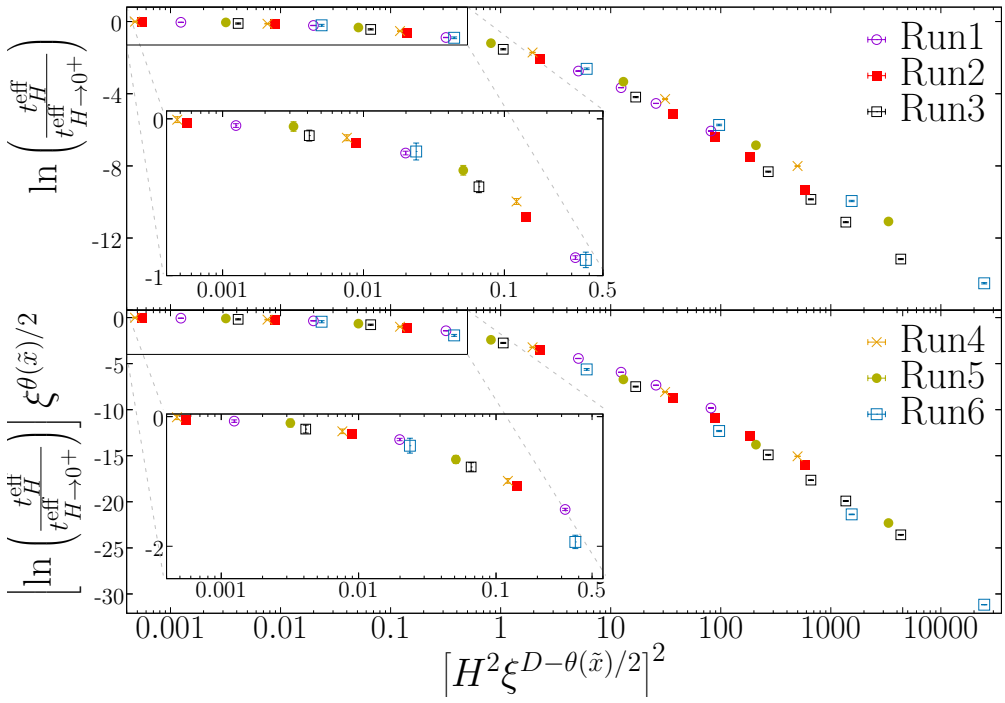

Figure 7.18: **Top** The non-linear part of the numerical response time data: $[\ln(t_H^{\rm eff}/t_{H\to 0^+}^{\rm eff})$ plotted against the scaling variable $[H^2\xi^{D-\theta(\tilde{x})/2}]^2$, according to Ref. [BJ17a], see Eq. (7.54). Its **main** panel is in semi-log scale and its **inset** is a zoom in the small x region. **Bottom** The non-linear part of the response time data:$[\ln(t_H^{\rm eff}/t_{H\to 0^+}^{\rm eff})\xi^{\theta(\tilde{x})/2}$ plotted against the scaling variable $[H^2\xi^{D-\theta(\tilde{x})/2}]^2$, according to Eq. (7.55). Its **main** panel is in semi-log scale and its **inset** is a zoom in the small x range.

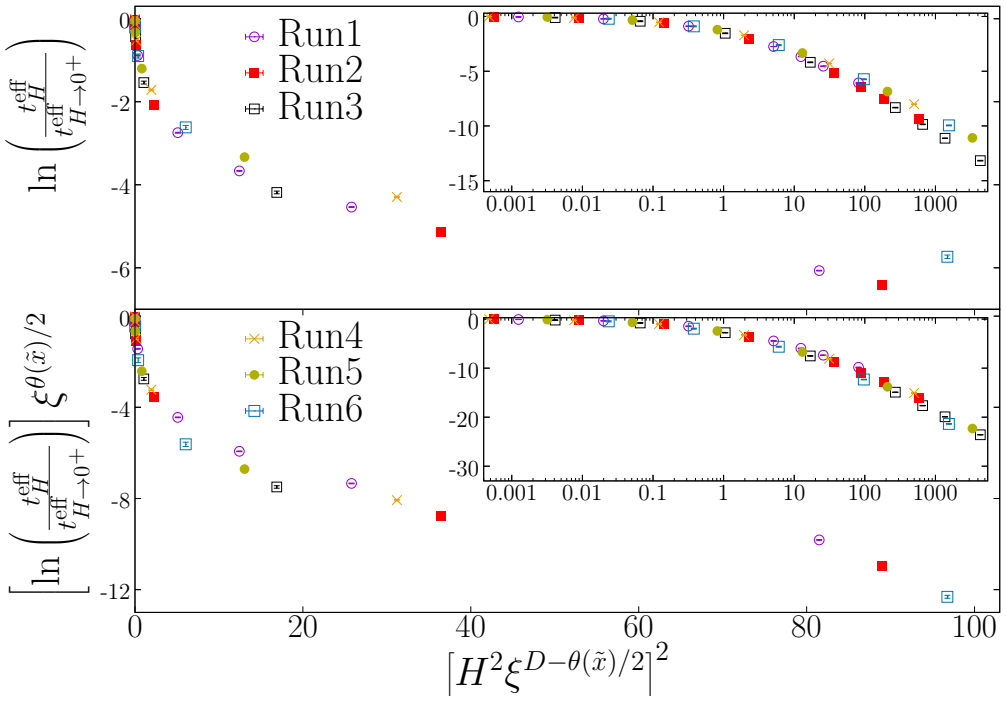

Figure 7.16: **Top** The non-linear part of the numerical response time data: $[\ln(t_H^{\rm eff}/t_{H\to 0^+}^{\rm eff})$ plotted against the scaling variable $[H^2\xi^{D-\theta(\tilde{x})/2}]^2$, according to Ref. [BJ17a], see Eq. (7.54). Its **main** panel is in linear scale, instead its **inset** is in semi-log scale. **Bottom** The non-linear part of the response time data:$[\ln(t_H^{\rm eff}/t_{H\to 0^+}^{\rm eff})\xi^{\theta(\tilde{x})/2}$ plotted against the scaling variable $[H^2\xi^{D-\theta(\tilde{x})/2}]^2$, according to Eq. (7.55). Its **main** panel is in linear scale, instead its **inset** is in semi-log scale.

7.6

The connection between the Hamming Distance and barrier heights

The analysis explained in Sec. 7.4.2 introduces the possibility to associate the peak of the response function $S(t, t_{\rm w}; H)$ to a Hamming distance (HD). This enables us to relate $t_H^{\rm eff}$ to the maximum barrier height, $\Delta_{\rm max}$, encountered at that time, thus connecting explicitly the Hamming distance with its barrier height. This was first computed by Vertechi and Virasoro [Ver89] and is directly relevant to experiments [Led91].
Let us define our *numerical* Hamming distance as:

$$\mathrm{HD}(t, t_{\rm w}, H) = \frac{1}{2}[1 - C(t, t_{\rm w}, H)] \,. \tag{7.56}$$

From the definition of $C(t, t_{\rm w}, H)$, see Eq. (7.8), this can be interpreted as a measure of the loss of the single site amplitude after t when the magnetic field H is turned on at $t_{\rm w}$.
In order to treat the dynamics of the spin system, we shall transition to, in a completely

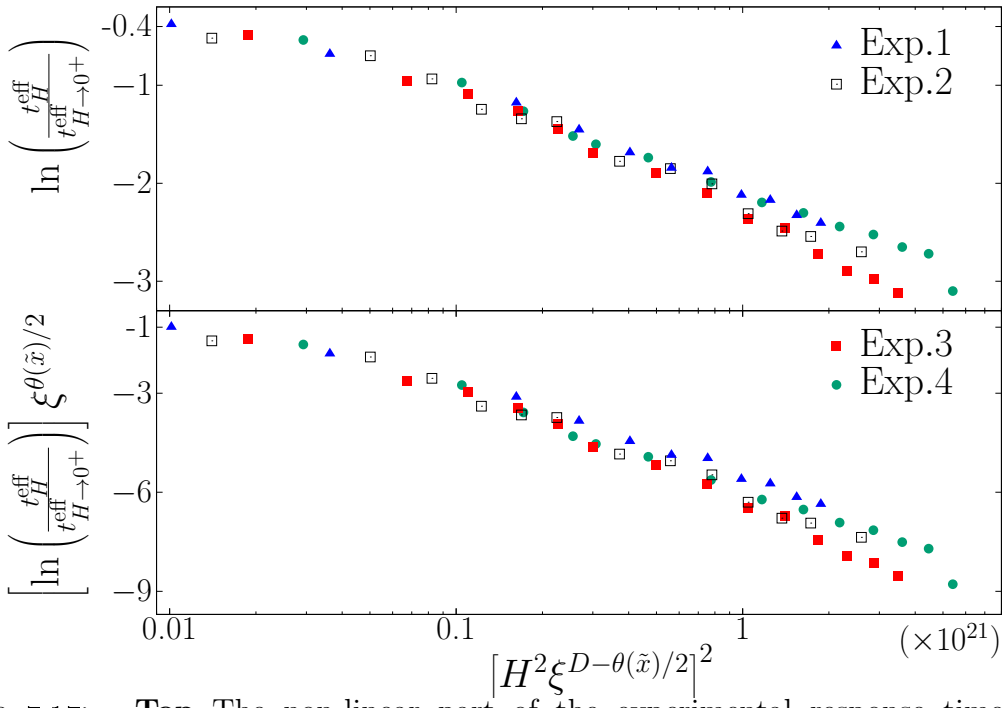

Figure 7.17: **Top** The non-linear part of the experimental response time data: $[\ln(t_H^{\rm eff}/t_{H\to 0^+}^{\rm eff})$ plotted against the scaling variable $[H^2\xi^{D-\theta(\tilde{x})/2}]^2$, according to Ref. [BJ17a], see Eq. (7.54). The plot is in semi-log scale. **Bottom** The non-linear part of the response time data: $[\ln(t_H^{\rm eff}/t_{H\to 0^+}^{\rm eff})\xi^{\theta(\tilde{x})/2}$ plotted against the scaling variable $[H^2\xi^{D-\theta(\tilde{x})/2}]^2$, according to Eq. (7.55). The plot is in semi-log scale.

complementary fashion, the states of the spin system in overlap space. This can be visualized according to an ultrametric distribution of metastable states [Méz84b].
The overlap between two states of spin-glass system α and β is defined by,

$$q_{\alpha\beta} = \frac{1}{N}\sum_i s_i^\alpha s_i^\beta \ . \tag{7.57}$$

In this space, when the system is quenched to temperature T_1 and the magnetic field H is turned on after the waiting time $t_{\rm w}$, the spin system initially finds itself in the state α, as displayed in Fig. 7.19. The state belongs to the lowest level of the tree appropriate to the temperature T_1. All these states are degenerate in energy and posses the same magnetization $M(t, t_{\rm w}, H)$ [Méz85a].

The occupancy of the initial spin state diminishes in amplitude with increasing time t as the system diffuses along the tree, occupying successive states of diminishing overlap.
This diffusion overcomes barriers whose heights increase as $q_{\alpha\gamma}$ diminishes. Physically, one can think of this as being related to the number of pairs of spins that flip as the diffusion process develops, preserving the magnetization.
The point of this analysis will be to associate the height of the barriers with the magnitude of the minimum overlap achieved within the time interval t.

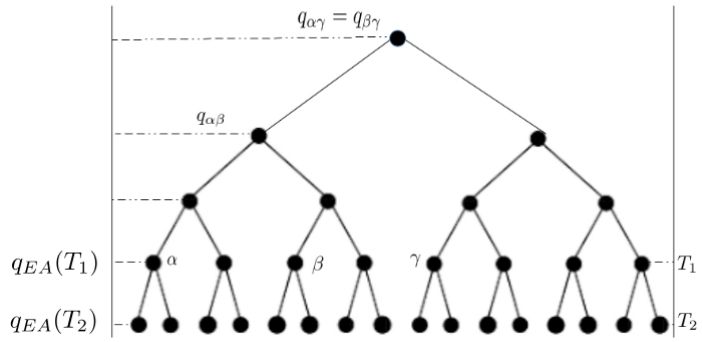

Figure 7.19: Ultrametric organization of metastable states at two temperatures T_1 and T_2, ($T_1 > T_2$). At T_1 ,α ,β and γ are metastable states (relative minima of the free energy in configuration space). The mutual overlaps $q_{\alpha\beta}$, $q_{\alpha\gamma}$, and $q_{\beta\gamma}$ are such that $q_{\alpha\gamma} = q_{\beta\gamma} < q_{\alpha\beta}$.
As the temperature is lowered from T_1 to T_2 , state α gives *birth* to N α states which are the new metastable states at T_2. $q_{\rm EA}(T)$ denotes the maximum value of the overlap function at temperature T .
Note how the number of degenerate states increases as the overlap with the initial state, $q_{\alpha\gamma}$, diminishes. Though this picture is highly idealized, it does give a rationale to the exponential increase of the number of states as the overlap $q_{\alpha\beta}$ diminishes. Figure from Ref. [Ver89]

In this context, one can define the Hamming distance as:

$$(HD)_{\alpha\beta}(t, t_{\rm w}, h) = \frac{1}{4N}\sum_i [s_i^\alpha - s_i^\beta]^2 = \frac{1}{2}[q_{\rm EA} - q_{\alpha\beta}]\,. \tag{7.58}$$

Let us try to find a connection between the two definitions of HD, Eqs. (7.56) and (7.58).
A glance at Fig. 7.19 shows the exponential increase of state occupancies as the overlap $q_{\alpha\beta}$ diminishes. This is a simplified picture, but it is representative of what we assume to be the (random) nature of the ultrametric tree representing spin-glass dynamics. Hence, the two definitions are equal. That is, as the single site Hamming distance represents the diminishing amplitude of occupancy, the final state with the exponentially largest density is the one at $q_{\rm min}$, and concomitantly with the largest barrier height. In this context, that means the dominant decay path for the single site occupancy can be projected onto the ultrametric tree (going from physical space to overlap space) as transitioning from the initial spin-glass state upon a temperature quench, with self overlap $q_{\rm EA}$, predominantly to the state *with minimum overlap* , $q_{\rm min}$.

This is precisely the reverse of the argument for the decay of the spin-glass magnetization upon a change of magnetic field. The decay is governed by the largest barrier height. Hence, the decay of the magnetization is associated with the diminishing of the occupancy of the state at $q_{\rm min}$ through $q_{\rm EA}$ to the lower Zeeman energy manifold. This is, because of the dominance of the number of states separated at $q_{\rm min}$. If the

decay works in this direction because of exponential occupancy, this is assumed to be true in the reverse direction.

Let try to establish a relationship between the height of the largest barrier and the HD. This idea was anticipated thirty years ago by Vertecchi and Virasoro [Ver89]. They calculated the "*mean value of energy barriers versus normalized [Hamming] distance*", exhibited in Fig. 7.20.

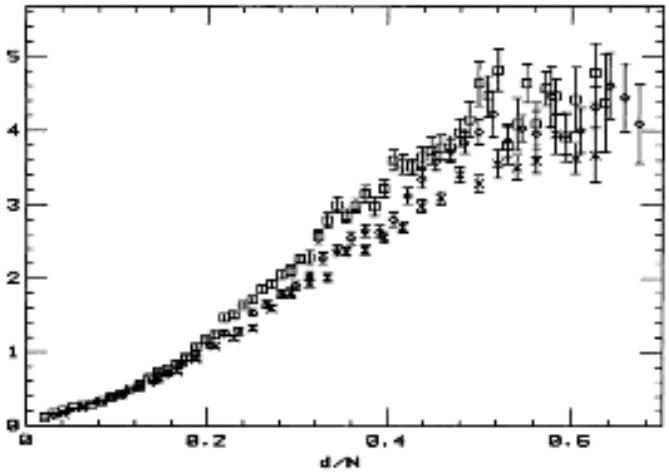

Figure 7.20: From Fig. 1 of Vertechi and Virasoro [Ver89].
Mean value of energy barriers *versus* normalized distance d/N for $N = 48$ (crosses), $N = 64$ (diamonds),$N = 96$ (squares).

In Fig. 7.21 we show the $\ln(t/t_H^{\rm eff})$ as a function of the Hamming distance, where we use the Hamming distance associated to the $C_{\rm peak}(t_{\rm w})$, see Tab. 7.2. A scaling scenario emerges from Fig. 7.21 and the numerical data suggest that:

- The determination of $C_{\rm peak}(t_{\rm w})$ is not crucial since the value $C_{\rm peak}(t_{\rm w})$ changes $\ln t_H^{\rm eff}(C_{\rm peak})$ only by a constant. This implies that $\ln t_H^{\rm eff}(C_{\rm peak})$ does not depends on H^2, but it is sensible only to the zero-limit $H^2 \to 0^+$.

$$\ln\left[t/t_H^{\rm eff}(C_{\rm peak})\right] = \mathcal{F}\left(C(t, t_{\rm w}; H)\right) \ . \tag{7.59}$$

- The free energy barriers for spin glass dynamics are not fixed chemical barriers. Rather, they are created by the growth of the correlation length, mirrored through the growth of the HD.

- The hierarchical nature of overlap space is proven because the free energy barrier heights increase in proportion to the HD.

- There is a quantitative relationship between the number of spin flip pairs and the free energy barriers to get there from the initial state.

- The above relationships do not change with temperature.

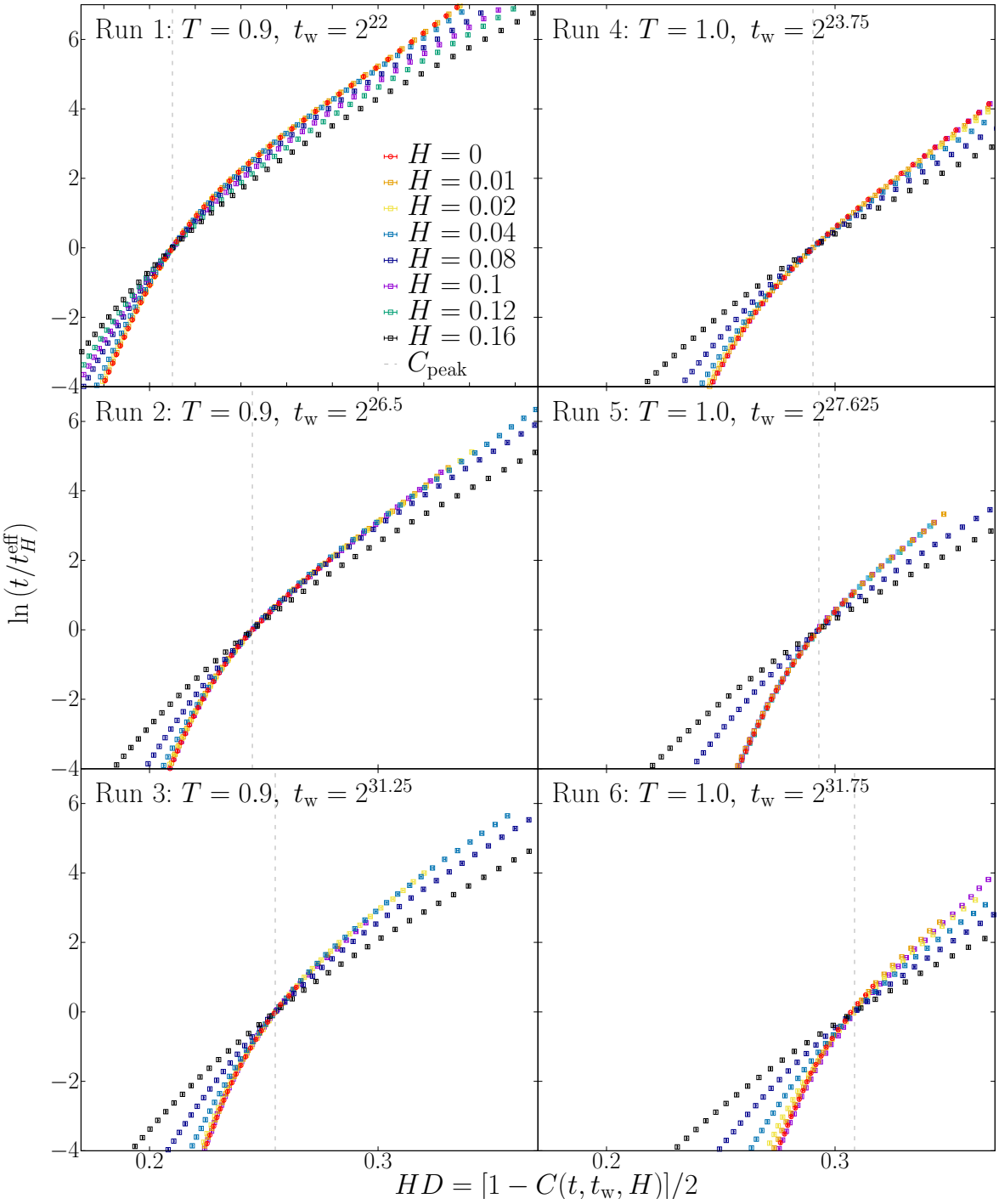

Figure 7.21: Behavior of the rescaled time $\ln(t/t_H^{\text{eff}})$ vs the Hamming distance. The dashed lines are the value of the Hamming distance associated to $C_{\text{peak}}(t_w)$.

7.7

Overshoot phenomena

In this Sec. 7.7.0.1, we first address the dynamical scaling law for a system in presence of a magnetic field at temperature close to the critical temperature T_g. Then, we analyze, dynamical scaling for ferromagnetic systems, either Ising or Heisenberg, in the presence of an external magnetic field.

Dynamical scaling close to T_g

We evaluate the growth of the correlation length $\xi(t, t_{\rm w}; H)$ in simulations that mimic the experimental field cooling protocol cooling (FC), where the temperature is lowered from above to below T_g in the presence of a constant magnetic field, H.

We performed two independent simulations on Janus II at the critical temperature $T_g = 1.102(3)$ (in *Janus units*) [BJ13] and at $T = 1.05$ for several external magnetic fields and 16 samples. An equivalent protocol to FC, but convenient for simulations, is to place a random spin configuration instantaneously at the working temperature T, while the external magnetic field is turned on at the same instant, so that $t_{\rm w} = 0$.

According to Eq. (7.19) at the critical temperature T_g, and for small external magnetic fields H, there exists a scaling behavior that connects $\xi(t, t_{\rm w}; H)$ with the external magnetic field H:

$$[\xi(t_{\rm w}, t; H)\ H^{2/y_H}] \quad \propto const\,. \tag{7.60}$$

The correlation length $\xi(t, t_{\rm w}; H)$ grows as:

$$\xi(t, t_{\rm w}; H) \propto t^{1/z(T)}\,, \tag{7.61}$$

with an exponent that, in first approximation, is expected to behave near the critical temperature as [BJ18]:

$$z(T) \simeq z_c \frac{T_g}{T}\,, \quad \text{where} \quad z_c = z(T_g) = 6.69(6)\,. \tag{7.62}$$

Hence, using Eqs. (7.61) and Eq. (7.62) in the scaling argument of Eq. (7.60), we have equivalently,

$$[t\ \times H^{2z(T)/y_H}] \quad \propto const\,. \tag{7.63}$$

In Tab. 7.6 we list the aging rate factor $z(T)$ used in our analysis. We plot our rescaled data in Fig. 7.22.

The agreement with the scaling prediction, exhibited in the collapsed data, is striking. They also exhibit an overshoot as evidence for the paramagnetic phase when the magnetic field is turn on.

The reader could wonder why we have used Eq. (7.60) for the scaling analysis at the cold temperature $T = 1.05$, and if this implies evidence of the absence of the de Almeida-Thouless (dAT) line in finite dimension. We address these questions in the next Section 7.8.

T	$z(T)$
1.1	6.60
1.05	7.00
1.0	7.30
0.9	8.12

Table 7.6: The aging rate factors $z(T)$ used in Figs. 7.22.

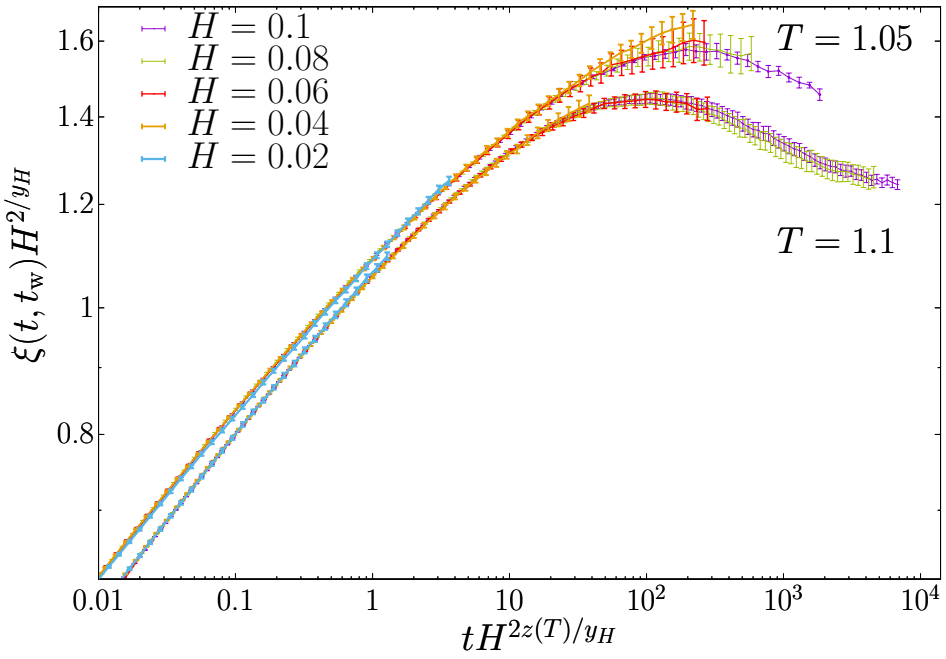

Figure 7.22: **Critical dynamical scaling.** The log-log plots show the behavior of the two dimensionless quantities $[\xi(t)H^{2/y_H}]$ and $[tH^{2z/y_H}]$ defined in Eq. (7.60) and (7.63).

Overshoot in a ferromagnetic system

By studying two ordered systems we can show that the overshoot phenomenon is, in fact, general. To demonstrate generality, we have simulated the three-dimensional Ising and Heisenberg model in a cubic lattice with periodic boundary conditions and size L at the critical point T_c. The $N = L^D$ Heisenberg spins interact with their lattice nearest neighbors through the Hamiltonian

$$\mathcal{H} = -\sum_{<\mathbf{r},\mathbf{r}'>} \mathbf{S}_\mathbf{r} \cdot \mathbf{S}_{\mathbf{r}'} + \mathbf{H} \cdot \sum_{\mathbf{r}} \mathbf{S}_\mathbf{r} \,. \tag{7.64}$$

	L	H	Number of runs
Ising	256	0	2200
		0.001	2600
		0.003	1700
		0.005	1200
Heisenberg	200	0	2660
		0.003	1000
		0.004	1600
		0.005	2400

Table 7.7: Information about the Ising and Heisenberg simulations for ferromagnetic system.

where $\mathbf{S_r}$ are unit vector spins and $\mathbf{H}$ is an external magnetic field. The connected correlation function is

$$C(r,t) = \frac{1}{L^3}\sum_{\mathbf{x}} \mathbf{S_x}(t)\cdot\mathbf{S_{r+x}}(t) - [\mathbf{m}(t)]^2\,, \tag{7.65}$$

with

$$\mathbf{m}(t) = \frac{1}{L^3}\sum_{\mathbf{x}} \mathbf{S_x}(t)\,. \tag{7.66}$$

We only write equations for the Heisenberg model, Eqs. (7.64)-(7.66), but the Ising analogues can be obtained trivially by just dropping the vector symbol in the spins. Furthermore, the correlation function $C(r,t)$ will be averaged over different initial conditions (runs). We report the simulation details in Table 7.7.

The Ising and Heisenberg model have different symmetry properties, so they belong to two distinct universal classes. In other words, each model expresses a distinct value for the critical temperature and exponents. The Ising model has $\eta = 0.0362978(20)$[SD17], $z = 2.0245(15)$[Has20] and $\beta_c = 0.221654626(5)$[Fer18b]. Instead, for the Heisenberg's one $\eta = 0.378(3)$[Cam02, Has11], $z = 2.033(5)$[Ast19] and $\beta_c = 0.693001(10)$[Bal96a] ($\beta_c \equiv 1/T_c$).

As explained in section 2.3, the correlation function, $\xi(t, t_w; H)$ can be calculated exploiting the integral estimators [Bel08a, Bel09a],

$$I_k(T,t_w) = \int_0^\infty \mathrm{d}r\, r^k C(T,r,t_w) \quad , \quad \xi_{k,k+1}(T,t_w) = \frac{I_{k+1}(T,t_w)}{I_k(T,t_w)}\,. \tag{7.67}$$

In this Section, we evaluate the correlation length $\xi_{23}(t, t_w; H)$. As the reader can notice, the growth of $\xi_{23}(t)$ exhibits an overshoot before to reach equilibrium for any external magnetic field for both the ferromagnetic models, see Fig. 7.23.

According to Eq. (7.19) at the critical temperature T_c, and for small external magnetic fields H, there exists a scaling behavior that connects $\xi(t, t_w; H)$ with the external magnetic field H in ferromagnetic system:

$$[\xi(t_w, t, H)\ H^{1/y_H}] \quad \propto const\,. \tag{7.68}$$

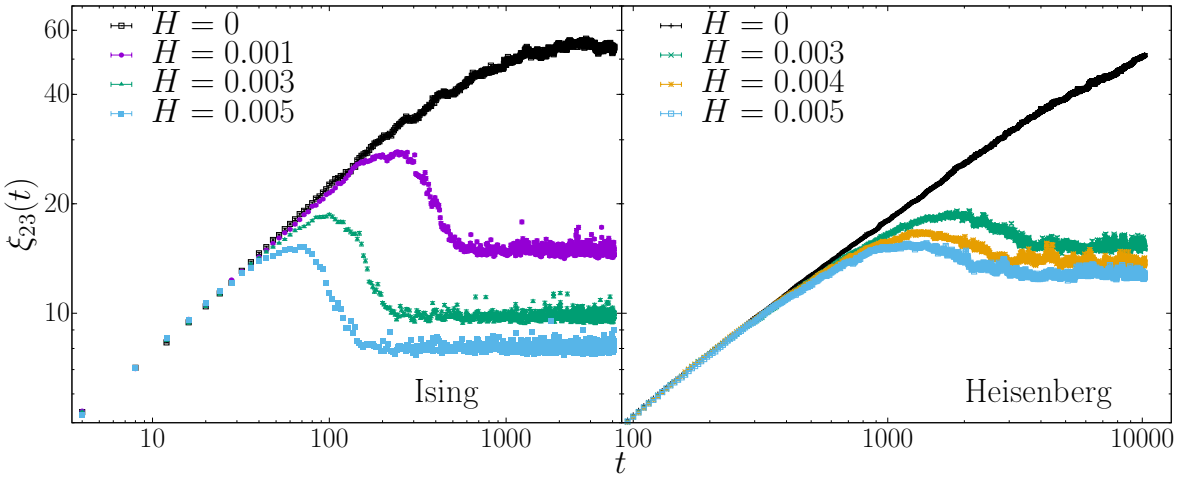

Figure 7.23: The log-log plots show the behavior of ξ_{23} versus time for the Ising (*left*) and Heisenberg models (*right*) for three magnetic fields. All the simulations were performed at the critical temperature T_c proper of each model. The saturation of long times exhibited by the Ising model is a finite size effect

As the reader can notice Eq. (7.68) differs from Eq. (7.60) in the power of the magnetic field. In the ferromagnetic system, the relevant external variable is H and not H^2 as it would be for spin-glasses [Par88, Ami05]. Analogously to Eq. (7.63), we can rescale the time as

$$[t \times H^{z(T)/y_H}] \quad \propto const\,. \tag{7.69}$$

We plot our rescaled data in Fig. 7.24. The agreement with the scaling prediction,

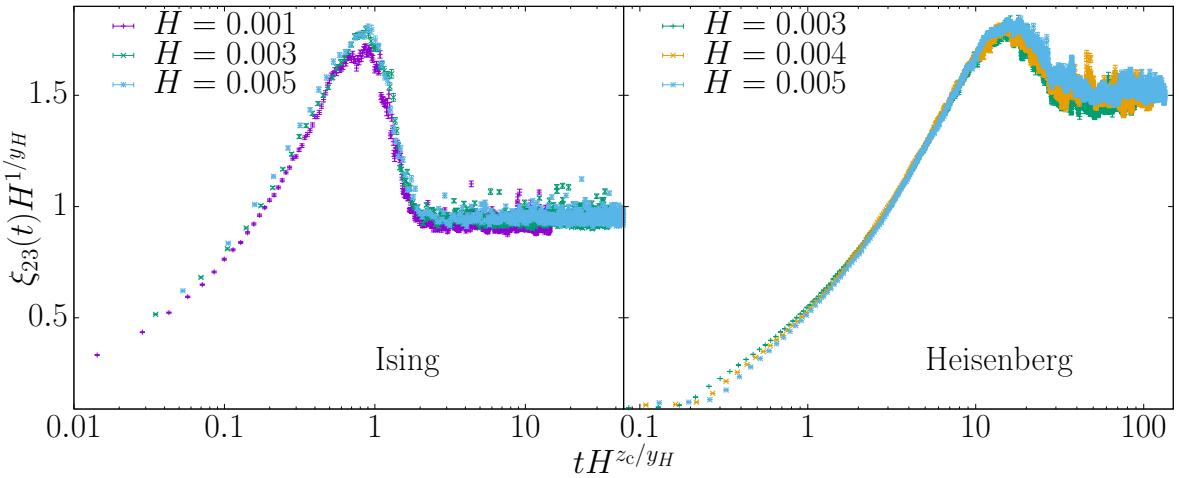

Figure 7.24: **Critical dynamical scaling.**
The data from Fig. 7.23 for the Ising (*left*) and Heisenberg model (*right*) for three magnetic fields are rescaled following the predictions of the renormalization group [see Eqs. (7.68)-(7.69)]. In this case the relevant variables are $\xi H^{1/y_H}$ and tH^{z_c/y_H}, with $y_H = (D + 2 - \eta)/2$ with $D = 3$.

both for the Heisenberg and the Ising model, is remarkable.

In conclusion, the overshoot phenomenon is general and we have observed it both in ferromagnetic systems, Figs. 7.23-7.24, and in disordered ones, Fig. 7.22.

7.8

Investigation of the dAT line in finite dimension D = 3.

The existence (or not) of the spin-glass condensation in the presence of a magnetic field remains the subject of some controversy. In a mean field treatment, de Almeida and Thouless [Alm78b] showed that, for the Sherrington-Kirkpatrick infinite range mean field model [She78], there would be a phase transition according to the following relationship for Ising spin-glasses,

$$\left(1 - \frac{T_g(H)}{T_g(0)}\right)^3 = \frac{3}{4}\, h^2 \quad , \tag{7.70}$$

with,

$$h = \frac{\mu H}{k_B T_g(0)} \quad , \tag{7.71}$$

where μ is the spin magnetic moment. Conversely, the so-called "droplet model" [Fis86, Bra86] would predict no phase transition except exactly at $H = 0$. This dispute was addressed by Lefloch et al. [Lef94]. Their final conclusion bears repetition: "Thus, even if the spin-glass does not exist in a magnetic field, *at least it looks the same as in zero field*, as far as we experimentalists can see."

In finite dimension and for T very close to the critical temperature $T_g(H = 0)$, the de Almeida-Thouless (dAT) line, provided it exists, should be governed by the Fisher-Sompolinsky [Fis85] relation:

$$\left(1 - \frac{T_g(H)}{T_g(0)}\right) \propto H^{4/\nu(5-\eta)} \tag{7.72}$$

where we have specialized to $D = 3$ [4]. Rather than through $T_g(H)$, we are interested in describing geometrically the dAT line by the inverse function of $T_g(H)$, namely $H_c(T)$. Hence, we rewrite Eqs. (7.70) and (7.72) as

$$\text{Mean} - \text{Field}: \qquad H_c(T) \propto \left(1 - \frac{T}{T_g}\right)^{a_{\rm MF}} \qquad a_{\rm MF} = 1.5\,, \tag{7.73}$$

$$\text{3D}: \qquad H_c(T) \propto \left(1 - \frac{T}{T_g}\right)^{a_{\rm 3D}} \qquad a_{\rm 3D} = \frac{\nu(5-\eta)}{4} \quad \rightarrow a_{\rm 3D} = 3.45(5)\,, \tag{7.74}$$

where we have taken the $3D$ critical exponents ν and η from Ref. [BJ13]. The following considerations, based on Eqs. (7.73)- (7.74), will be useful:

[4] Notice this is the same relation used for matching the numerical and experimental scales in Sec. 7.3

- $H_c(T)$ is a decreasing function of the temperature T (remember $T \leq T_g$) and $H_c(T_g) = 0$. This means that, upon approaching T_g from below, one eventually crosses the dAT line for any $H > 0$, no matter how small H is.

- When $H > H_c(T)$ the system is above the dAT line, in its paramagnetic phase: the correlation length, $\xi(t, t_w; H)$, reaches asymptotically its equilibrium value $\xi_{eq}(H)$ for very large time t.

- When $H < H_c(T)$ we are in the spin-glass phase and one expects to observe a power-law growth of the correlation length, see Eq. (7.61).

- The a_{3D} exponent is much larger than the mean-field (MF) one, $a_{3D} \backsimeq 2.3 \times a_{MF}$. This implies that, in $D = 3$, the dAT line is *very* flat when one approaches the critical temperature, $T \backsimeq T_g$.

In particular, our last item above suggests an interpretation of the somewhat surprising results in Fig. 7.22, where data for $T = 1.05$ were successfully scaled with the scaling law appropriated for T_g [recall that $1.05 < T_g = 1.102(3)$ and that at $T = T_g$ we are in the paramagnetic phase for any $H > 0$]. Let us estimate the critical magnetic field at $T = 1.05$ exploiting Eq. (7.74):

$$H_c(T = 1.05) \sim 3 \times 10^{-5} \,. \tag{7.75}$$

Considering, now, that the smallest magnetic field in Fig. 7.22, namely $H = 0.02$, is larger than $H_c(T = 1.05)$ by a factor of 1000 or so, there is little surprise in that an scaling law assuming $H_c(T = 1.05) = 0$ works with our data.

Our focus in this section will be an exploration of growth of the spin-glass correlation length, $\xi(t, t_w; H)$, under conditions that mimic the experimental protocol for measurement of the zero-field cooled magnetization, $M_{ZFC}(t, t_w; H)$ for $t_w \neq 0$, recall Sec. 7.3.

In Fig. 7.25 we display the behavior of $\xi(t, t_w \neq 0; H)$ as a function of time for different magnetic fields H. We compute ξ from the microscopic correlation function $C_4(r)$ (see section 4.2), which requires that we compute error bars from the sample-to-sample fluctuations. We have simulated different samples only for some values of H and t_w because of the enormous computational effort involved. Only in those cases where they can be computed, we represent error bars in Fig. 7.25.

The time evolution of the spin-glass correlation time, $\xi(t, t_w; H)$, depends markedly on the interplay between the waiting time t_w and the value of the magnetic field H, see Fig. 7.25. The system needs several time steps before responding to the switching on of the magnetic field. Different scenarios appear.

For the largest magnetic fields, namely $H > 0.04$ both at $T = 0.9$ and $T = 1.0$, the correlation length displays a non-monotonic time behavior, just as we found in Sect. 7.7.0.1 for the dynamics in the paramagnetic phase (recall that $t_w = 0$ in Sect. 7.7.0.1). In particular, for those cases when the starting correlation length, $\xi(t = 0, t_w; H)$, is *larger* than the equilibrium value $\xi_{eq}(H)$, the correlation length

decays. Otherwise, we observe an overshooting phenomenon reminiscent of our findings in Sect. 7.7.0.1, see Fig. 7.25.

Here we must distinguish between the mean field $H_c^{\rm MF}(T)$ and the Fisher-Sompolinsky scaling $H_c^{\rm 3D}(T)$, *i.e.* between Eqs. (7.73) and (7.74). Using Eq. (7.70) for the former, one finds,

$$H_c^{\rm MF}(T=0.9) \sim 0.0675 \quad \text{and} \quad H_c^{\rm MF}(T=1.0) \sim 0.02421 \quad . \tag{7.76}$$

Interestingly, the scaling result, Eq. (7.74), yields,

$$H_c^{\rm 3D}(T=0.9) \sim 0.003 \quad \text{and} \quad H_c^{\rm 3D}(T=1.0) \sim 0.0003 \quad . \tag{7.77}$$

Thus, for the magnetic fields used in our simulations, one is presumably in the condensed state for $0.005 \leq H < 0.08$ from the perspective of the mean field solution of the Sherrington Kirkpatrick model [She78], while from the perspective of the Fisher-Sompolinsky scaling [Fis85], one is always in the paramagnetic state as $H > H_c^{\rm 3D}(T = 0.9, 1.0)$. Though this latter region is not accessible experimentally through magnetic measurements, one can argue that the simulation results should be symmetric around $T_c(H)$. This is the basis for our comparison between experiment and simulations contained in Sec. 7.5 of this work.

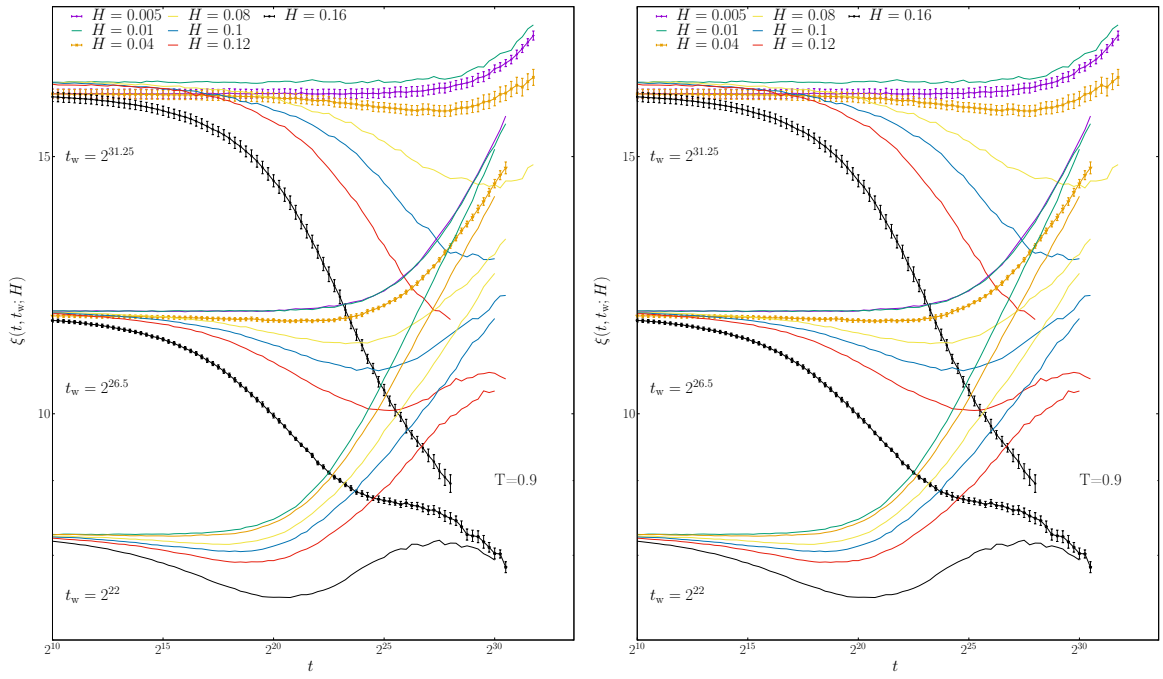

(a) Data at $T = 1.0$ (b) Data at $T = 0.9$.

Figure 7.25: **Growth of** $\xi(t, t_{\rm w} \neq 0; H)$ in simulations that mimic the experimental protocol of the zero-field cooling (ZFC). Plots are in log-log scale.

Let us now attempt a scaling analysis similar to the one in Sect. 7.7.0.1 for those magnetic field values for which the asymptotic $\xi_{\rm eq}(H)$ can be at least guessed from

Fig. 7.25. We start by modifying the scaling relationship Eq. (7.60) to,

$$\xi(t, t_{\rm w}; H)|H^2 - H_c^2(T)|^{1/y_H} \propto \text{const.} \tag{7.78}$$

Next, using Eqs. (7.61) in the scaling argument of Eq. (7.78), we have equivalently,

$$\left(t \times |H^2 - H_c^2(T)|^{z(T)/y_H}\right) \propto \text{const.} \tag{7.79}$$

We replot our rescaled data in Fig. 7.26 for the mean field values of $H_c^{\rm MF}(T)$, see Eq. (7.76). As seen in Fig. 7.26b, there is nearly perfect scaling for $H \geq 0.08$ but not for $H = 0.04$, though the curves do seem to coalesce for the three different waiting times.

It is tempting to suggest that, for this value of magnetic field, one is in the condensed phase. However, glancing at Fig. 7.25b, the growth of $\xi(t, t_w; H)$ for $H = 0.04$ breaks away from the growth for the smaller values of magnetic field, so that it is very possible that it would join the equilibrium curves (*i.e.* the paramagnetic regime) at times longer than are accessible in our simulations. This ambiguity softens an interpretation that we have broached the dAT line in our simulations as would be predicted from a mean field approach.

However, if we replot our data using the scaling result, Eq. (7.77), as exhibited in Fig. 7.27, for the values of $H_c^{\rm 3D}(T)$ for $T = 0.9$, the data appear to collapse for *all* of the magnetic fields, including $H = 0.04$ [$H_c^{\rm 3D}(T = 0.9) \ll 0.04$]. This supports the above conjecture that, at $T = 0.9$, our simulation results for $H = 0.04$ are in the paramagnetic regime.

The rescaled data of Fig. 7.25a , appropriate to $T = 1.0$, are plotted in Figs. 7.26a and 7.27a, for the mean field and 3D scaling, respectively. The data are of low quality, limiting the magnetic fields to only relatively large values. For the three values ($H = 0.04,\ 0.08,\ 0.16$) for which it is feasible to rescale, all are above the $H_c^{\rm MF,\ 3D}(T = 1.0)$ values given by Eqs. (7.76) and (7.77). Hence, all are in the paramagnetic regime, as can seen from the shape of the curves in both figures.

Thus, though the data of Fig. 7.25b suggests that, for the lowest magnetic fields and $T = 0.9$, $\xi(t, t_w, T)$ may be growing as a power law, and thus be in the condensed phase, our limited time scale for the simulations is unable to conclude that we have, in fact, straddled the dAT line. If one assumes Fisher-Sompolinsky scaling, Eq. (7.77), all of our simulation results would be in the paramagnetic region. Until much longer times scales became reachable (either at lower temperatures, or smaller magnetic field), even our powerful Janus II simulations are unable to arrive at a definitive conclusion regarding the existence, or non-existence of the dAT line for Ising spin-glasses.

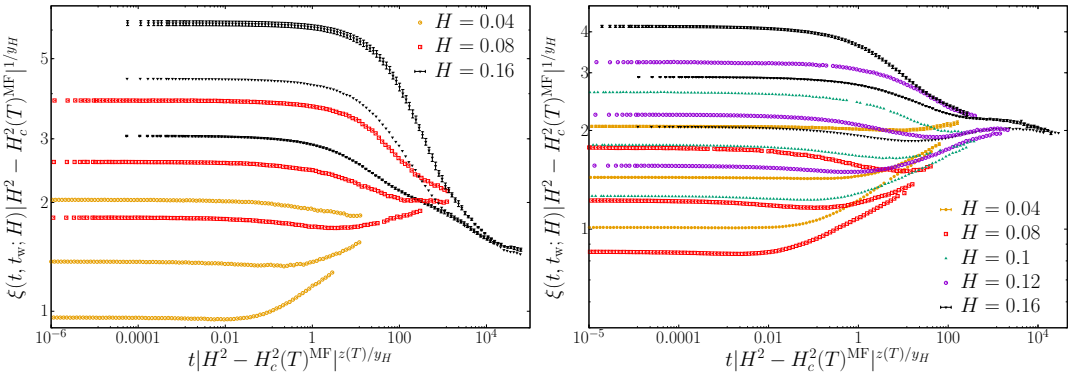

(a) Data at $T = 1.0$ (b) Data at $T = 0.9$.

Figure 7.26: **Evidence of the dAT line in finite dimension**
Plots are in log-log scale and show the behavior of the rescaled quantities defined in Eqs. (7.78)-(7.79) for the mean-field estimators $H_c(T)^{MF}$ (see Eq. (7.76).
We report the aging rate $z(T)$ used in this scaling in Tab. 7.6 to be found in Sec. 7.7.

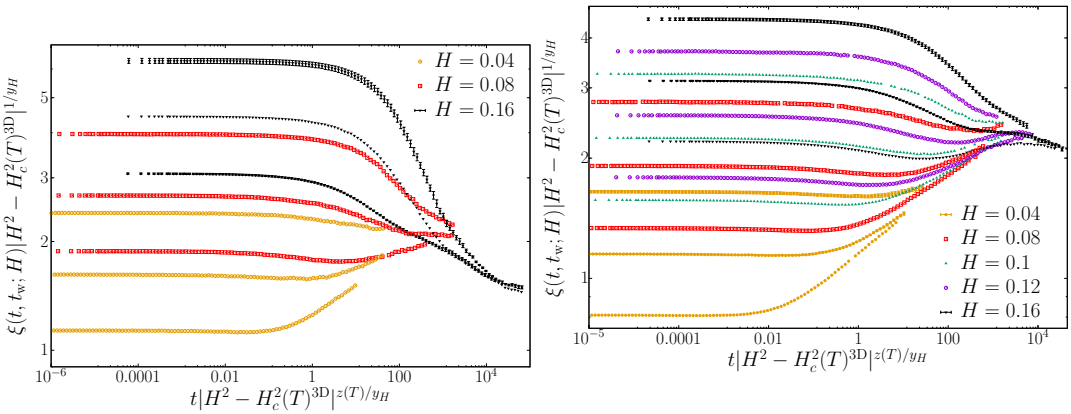

(a) Data at $T = 1.0$ (b) Data at $T = 0.9$.

Figure 7.27: **Evidence of the dAT line in finite dimension**
Plots are in log-log scale and show the behavior of the rescaled quantities defined in Eqs. (7.78)-(7.79) for the Fisher-Sompolinsky estimators $H_c(T)^{3D}$ (see Eq. (7.77).
We report the aging rate $z(T)$ used in this scaling in Tab. 7.6 to be found in Sec. 7.7.

7.9

Remark

This work displays the unique and powerful combination of experiment, theory, and simulations addressing complex dynamics. The use of single crystals enables experiments to exhibit the consequences of very large spin-glass correlation length. The power of a special purpose computer, Janus II, in combination with theory, is sufficient to extend simulation times and length scales to values explored experimentally. To-

gether, these approaches unite to develop new and important insights into spin-glass dynamics.

Previous work [Joh99, BJ17a] explored the reduction of the free energy barrier heights responsible for aging in spin-glasses by the Zeeman (magnetic field H) energy. The observations for small magnetic fields, proportional to H^2, have been used to extract a quantitative value for the spin-glass correlation length and its growth rate with time. However, as the magnetic field was increased, departures from the proportionality to H^2 were observed. This work presents detailed experimental observations of this behavior, and, together with theory [Zha20b], is able to demonstrate the applicability of a new non-linear scaling law for the magnetization in the vicinity of the spin-glass condensation temperature T_g. Remarkably, Janus II simulations were able to generate comparable values for the magnetization dynamics, with the added value of direct measurement of the characteristic response time.

The combination of these two approaches has put to rest a decades old controversy concerning the nature of the Zeeman energy. It was shown that the departures from proportionality to H^2 was caused by non-linear terms in the magnetization, and not by fluctuations of the magnetization that lead to a Zeeman energy proportional to H. Further, the departure from an H^2 behavior that was used to justify the proportionality to H was shown to be a consequence of non-linear behavior of the magnetization in H, and fully accounted for using the new scaling law. This is an important finding because otherwise the extraction of the spin-glass correlation length from the Zeeman energy reduction in the barrier height would have been in error.

One of the most interesting findings in this work was the extraction of the characteristic response time for spin-glasses, t_H^{eff}, from simulations. This was made possible by noting that the spin-glass correlation function reaches a peak *at the response time*. That is,

$$C(t_H^{\text{eff}}, t_{\text{w}}; H) = C_{\text{peak}}(t_{\text{w}}) \tag{7.80}$$

Thus, by extracting $C_{\text{peak}}(t_{\text{w}})$ one can determine the characteristic response time t_H^{eff}. It was this observation that enabled the simulations to give quantitative values for the non-linear magnetic susceptibility that could be compared with the new scaling law.

In addition, we have explored the microscopic behavior of the magnetic states through the growth of the correlation lengths under two experimental protocols: zero-field cooling (ZFC) and field cooling (FC). We proved that in a system close enough to the condensation temperature T_g, the Fisher-Sompolinsky scaling relation holds under out-of-equilibrium conditions (see Sec. 7.5.5.) This will enable us in future simulations to compare the magnitude and growth of the spin-glass correlation length under the two dynamical protocols: zero-field cooled magnetization, and thermoremanent magnetization dynamics. The important point here is that this work displays that our analysis will be valid under these non-equilibrium conditions.

We discovered an overshoot phenomenon that we showed to be general for both ordered and disordered magnetic systems. And finally, we explored the nature of the spin-glass condensation at T_g as a function of the external magnetic field, the so-called de Almeida-Thouless line. Though our results are preliminary, we displayed evidence for its existence as a true condensation transition, but this conclusion should

be regarded as provisional.

In conclusion, this work has explored the nature of the spin-glass state in the vicinity of its condensation temperature T_g. We displayed the power of combining insights from both experiment and simulations, coupled together by theory. We look forward to continued development of spin-glass dynamics using this relationship as we examine the microscopic nature of such phenomena as rejuvenation and memory. Finally, because spin-glass dynamics have applications is many diverse fields (ecology, biology, optimization, and even social science), our work demonstrates that modeling of complex systems is feasible in finite dimensions.

Part IV

Conclusions

CHAPTER VIII

Conclusion

8.1 General considerations

Spin glasses provide a toy model extensively used since the 1950s by both theorists and experimentalists to research the glass transition. Unfortunately, in spite of continued and significant efforts, we are still far from a full understanding of our toy model. This is particularly true for spin glasses in a small spatial dimension ($D = 3$ is *small* in this context).

One can make an amusing parallelism between the scientific endeavor and spin-glass dynamics. In both cases we find sluggish dynamics, frustration and a hierarchical organization of the states. Indeed, scientific progress is built on many small advancements that (at some happy but rare moments) combine together to make a big step forward. The analogue of scientific discovery in the world of a glassy system would be equilibration, which is achieved only after many small barriers are overcome. Just to make an example of this *glassy* evolution of scientific research, we can mention the discovery of gravitational waves by the LIGO and VIRGO collaborations. Indeed, this fantastic discovery was possible only after more than a century of continued efforts after Einstein conjectured that gravitational waves could propagate.

Although my dissertation has not revolutionized our understanding of spin-glasses, it can be hoped that this thesis provides a milestone for the combined study of spin glasses through experimental, theoretical and computational means. This combined strategy has been very rarely followed in the past but we have shown that it can solve some difficult problems that have challenged physicists for decades.

In the following sections we briefly outline the main results in this thesis. The interested reader will find a more extended exposition in the concluding paragraphs for each chapter.

8.2

The importance of state-of-the-art computation in spin-glasses research

The core of this dissertation was the investigation of the glassy transition combining experimental and numerical results. Without special hardware or sophisticated computational technique, [the synchronous multispin packing], we could not achieve realistic time and length scale, and, so the synergy between theory, experiment, and simulations could be impossible.

The data in part II were obtained on standard CPUs employing synchronous multispin coding. At the moment of the publication of [Fer19b], despite the experimental success achieved in the investigation of film systems, no numerical works were present. We posed the basis for further explorations of spin glass systems in a film geometry.

In part III we performed remarkable simulations on the dedicated super-computer Janus II, an FPGA-based computer designed specifically for Ising spin glass simulations. The success of an FPGA-based computer is remarked by the results obtained since the 2008s.

8.3

The Ising spin glass in film geometry

We have unveiled the complex landscape of a thin glassy film at the bulk temperature.

In addition, we have studied in detail, for the first time, the dimensional crossover in the aging dynamics of spin glasses in film geometry, uncovering rich and composed dynamics. Several very different regimes and scaling laws emerge, and we have succeeded to clarify with good precision the behavior of all of them. Our analysis starts from the intuition about the presence of a dimensional crossover, linking $2D$ and $3D$ physics through films: we find that the intuition is correct but oversimplifies a reality that turns out to be more complex. Film physics is becoming very relevant from an experimental point of view, but it is also becoming clear that it can also become a powerful computational tool.

8.4

The Ising Edward-Anderson model in presence of an external magnetic field

We conduct a parallel study of non-equilibrium spin-glass dynamics both in an experiment in a CuMn single crystal and in a large-scale simulation of the Ising-Edwards-Anderson (IEA) model carried out on the Janus II custom-built supercomputer [BJ14b].

We introduced a scaling law that describes the system's response over its entire natural range of variation. The observations for small magnetic fields, proportional to H^2, have been used to extract a quantitative value for the spin-glass correlation length and its growth rate with time. However, as the magnetic field was increased, departures from the proportionality to H^2 were observed. This work presents detailed experimental observations of this behavior, and, together with theory [Zha20b], is able to demonstrate the applicability of a new non-linear scaling law for the magnetization in the vicinity of the spin-glass condensation temperature T_g.

The combination of these two approaches has put to rest a decades-old controversy concerning the nature of the Zeeman energy. It was shown that the departures from proportionality to H^2 were caused by non-linear terms in the magnetization, and not by fluctuations of the magnetization that lead to a Zeeman energy proportional to H. Further, the departure from an H^2 behavior that was used to justify the proportionality to H was shown to be a consequence of non-linear behavior of the magnetization in H, and fully accounted for using the new scaling law.

In addition, we have explored the microscopic behavior of the magnetic states through the growth of the correlation lengths under two experimental protocols: zero-field cooling (ZFC) and field cooling (FC). We proved that in a system close enough to the condensation temperature T_g, the Fisher-Sompolinsky scaling relation holds under out-of-equilibrium conditions (see Sec. 7.5.5.)

We discovered an overshoot phenomenon that we showed to be general for both ordered and disordered magnetic systems. And finally, we explored the nature of the spin-glass condensation at T_g as a function of the external magnetic field, the so-called de Almeida-Thouless line.

8.5

Future challenges and opportunities

The advances exposed in this dissertation will represent a small step forward in the full comprehension of the glass transition and its modeling. On the other hand, new research opportunities have been unveiled in this thesis.

From a computational point of view, we implemented several packing techniques to speed-up both simulations and analysis. This numerical approach allowed us to simulate very large systems and to thermalize them even at cold temperatures. In this dissertation, we have proven that the film geometry is a powerful tool for the investigation of the spin-glass:

- the dimensional crossover that happens as soon as the correlation length, ξ, is compatible with the thickness, speeds up the dynamics; so, the system can easily achieve the equilibrium.
- The equilibrium is characterized by a finite correlation length;
- we can compare the numerical results to the experiments of the last generation.

In addition, being part of the *Janus Collaboration* was a unique opportunity. A breakthrough for the comprehension of a spin-glass system in the presence of a magnetic field is given by the range of the correlation lengths that we were able to achieve both experimentally and numerically. The results obtained through the super-computer Janus II represented a step forward by a factor three in the length scales than previous works. On the experimental side, our co-workers reached a correlation length four times larger. The synergy between these two approaches allowed us to solve a three-decade-old controversy concerning the nature of the magnetic state. As we have explained in Part III, it was a tough task the calculation of the numerical relaxation rate which represents the main quantity evaluated in the experiments. However, the discovery of a coherent structure in the spin-glass response to a magnetic field arises new prospects. The most direct ones are:

- the investigation of the microscopical nature of spin-glass dynamics as rejuvenation and memory;
- the microscopical equivalence between the experimental protocols of the Thermoremanent and the zero-field cooling;
- the microscopical features of the Hamming distance.

Part V

Appendices

APPENDIX A

Multispin coding

A.1 Synchronous Multispin coding

Modern CPUs, both Intel and AMD, support 256-bit words in their streaming extensions and perform synchronously independent Boolean operations for all the bits in a computer word.

This means that one can exploit basic Boolean operations (AND, XOR, etc) in parallel for all the bits in a computer word. Hence, the Metropolis algorithm is perfect for a straightforward implementation since a single spin-flip is possible using only Boolean operations if the couplings are binary $J_{\mathbf{xy}} = \pm 1$.
Starting from the innovative idea of Ref. [Fan14], we implement our algorithm to speed-up the simulation of a single system. In their parallel tempering simulation, each bit represents an independent system copy and all of them evolve under the same couplings, but at different temperatures.
The multispin coding is fruitful for the reduction of step operations, but the real problem in the simulation speed-up is in the manager of the random number generator. Each bit of the computer word obtained thanks to the SEE2 extensions, need an independent random number. However, it has been realized several times that most of the effort in generating (pseudo) random numbers is wasted when simulating discrete models at low temperatures [Gil77, Bor75].
At a given time the simulation may try to overcome an energy barrier ΔE. The associated probability in this *energy jump* is $e^{-\Delta E/T}$. In other words, this means that for each time we are wasting $e^{\Delta E/T}$ random numbers, which are associated to deny overcoming the barrier until we generate one random number that really allows us to walk uphill in energy.
In our model, the energy barrier could only be $\Delta E = 4, 8$, or 12. So, at the critical temperature T_c, in the best cases we use only one random number out of $e^{4/1.1} \approx 38$.
Hence, one can *recycle* the random numbers that are associated with a deny spin-flip

changing the perspective of the probability associated with each spin-flip. Let us regard the random-number generator as a collection of flags: red for denying us the right to increase the energy and green ones for allowing us to increase the energy. Now, most of the flags are red and a diluted set is green. The trick is setting all flags to red by default, and then caring only about placing green flags with the correct probability.

Let us assume that all the flags are red, for all the sites and all barriers $\Delta E = 4, 8$, and 12. Now, for each site in the physical lattice, we draw one 64-bits uniformly distributed random numbers:

$$0 \leq R_4 < 1\,. \tag{A.1}$$

If $R_4 < e^{-4/T}$ then we put a green flag for $\Delta E = 4$ and draw a second uniform random number:

$$0 \leq R_8 < 1\,. \tag{A.2}$$

Now, if $R_8 < e^{-4/T}$ we put a green flag for $\Delta E = 8$, and draw a *third* uniform random number:

$$0 \leq R_{12} < 1\,. \tag{A.3}$$

Finally, if $R_{12} < e^{-12/T}$ we put a green flag for $\Delta E = 12$.
Of course ours is just an instance among many valid generators. This particular random number generator was chosen because it is fairly easy to simulate.
Let us describe how we simulate the generator R_i. We generate an integer $n_4 \geq 0$, with the following meaning: one performs n_i unfruitful calls to the generator, but on call $1 + n_i$ we should put a green flag. The cumulative probability for n_i is:

$$F(n_i \geq k) \equiv \mathrm{Prob}(n_i \geq k) = 1 - (1 - e^{-4/T})^{k+1}\,. \tag{A.4}$$

Hence, we just need to draw an uniform random number $0 < R \leq 1$ and select $n_4 = k$, where k is the non-negative integer that verifies

$$F(k-1) \leq R < F(k) \qquad [F(-1) \equiv -1]\,. \tag{A.5}$$

Combining these ideas with the use of look-up tables, we have found that overall cost of generating random numbers can be made quite bearable.
Let us now explain the geometry of the multispin coding.

A.1.1 MUlti SIte (MUSI) multispin coding implementation

We have simulated Metropolis dynamics through two different multispin codings:MUlti SAmple multispin coding (MUSA) and MUlti SIte multispin coding (MUSI). The MUSA algorithm is based on the representation of many samples in a single computer word (128 in our implementation). In other words, each bit corresponds to a different sample. This implementation does not have any computational constraints. One can simulate a system with any lattice value and with any kind of boundary conditions. Otherwise, the MUSI implementation, which has a better performance in the

computational speed-up of a single sample, is more complex and needs some geometrical constraints. The MUSI technique is efficient because it packs the physical spins in a new computational lattice that exploits the memory access architecture of the last generation chips.
Hence, the MUSI implementation can be used only for simulating a system with periodic boundary conditions and with lattice values that are multiples of 2^m with $m \in \mathbb{N}$. This technique is well-known in the $3D$ spin-glass simulation [Fer15].
Here, we shall explain the MUSI implementation for a spin-glass system with a film geometry.
Let take an Ising glassy system in a cubic lattice with film geometry, which has two long sides of lengths $L_x = L_y = 256$ and thickness $L_z << L_x$.
Physically, spins are sitting on the nodes of a lattice with periodic boundary conditions. Euclidean coordinates then run as:

$$\begin{aligned} 0 \leq x < L_x \ , \\ 0 \leq y < L_y \ , \\ 0 \leq z < L_z \ . \end{aligned}$$

Each physical spin is a binary variable to be coded in a single bit $s_{(x,y,z)} = \pm 1$.
We pack 256 physical spins into one *superspins*. Our superspins sit in the nodes of a different lattice.
The major requirement is that nearest-neighbors in the physical lattice should be as well nearest neighbors in the superspin lattice.
Let us consider the system as L_z bidimensional layers with dimensions $L_x = L_y = L/16$. Hence, let us place at the nodes of the layer surface for any given z value.
The relation between physical coordinates (x, y) and the coordinates in the superspin lattice (i_x, i_y) is:

$$\begin{aligned} x = b_x L_x + i_x \ , \quad 0 \leq i_x < L_x \, , \quad 0 \leq b_x < 16 \, , \\ y = b_y L_y + i_y \ , \quad 0 \leq i_y < L_y \, , \quad 0 \leq b_y < 16 \, , \end{aligned} \tag{A.6}$$

In this way, exactly 256 sites in the physical lattice are given the same superspin coordinates (i_x, i_y).
We differentiate between them by means of the bit index:

$$i_b = 16 b_y + b_x \, , \quad 0 \leq i_b \leq 255 \, . \tag{A.7}$$

This *layer-superspin* construction does not preserve the parity of the original site. Hence, we give at each layer-superspin a parity depending on the z value. In this way, we can recover the parity of the physical system $x + y + z$ and exploit the bipartite representation.
It can be regarded as a two interleaved face-centered cubic lattice. A given site is said to belong to the *even* or the *odd* sublattice according to the parity $x + y + z$.
For a model with only first neighbors interactions, sites belonging to (say) the even

sublattice interact only with the odd sites.
As consequence, the even-odd decomposition introduces a high parallelism level. Indeed, we define the full lattice Metropolis sweep as the update of all the $L^2L_z/2$ even sites, followed by the update of all the $L^2L_z/2$ odd sites. The bipartite nature of the lattice makes irrelevant the updating order of sites of a given parity. Hence, several updating threads may legitimately concur on the same lattice, provided that all of them simultaneously access only sites of the same parity.

A.2

The Janus Super computer

Most of our Monte Carlo simulations have been carried out on the Janus special-purpose machine[1]. Information about Janus' hardware as well as some details of low-level programming can be found in [Bel09b, BJ12, BJ14b]. Janus is built out of 256 computing cores rocessors (Xilinx Virtex-7 XC7VX485T FPGA) arranged on 16 boards. The 16 FPGAs on a board communicate with a host PC via a 17th on-board control FPGA. An exhaustive explanation is given in Ref. [BJ14b, BJ12].

A.3

Parallel Tempering

The Parallel Tempering (PT) algorithm is a global algorithm [Mar92, Gey91] and it is commonly used for the equilibrium investigation of large systems or of very low temperatures. For each sample we simulate N_T different copies of the system, each of them at one of the temperatures $T_1 < T_2 < \cdots < T_{N_T}$. The PT update consists of proposing a swap between configurations at neighboring temperatures.
The exchange is accepted with the Metropolis probability

$$P = min\left[1, e^{-\beta\Delta E}\right] \ , \tag{A.8}$$

where ΔE is the energy difference between the two configurations and β is the inverse temperature. One of the two systems involved in the swap will decrease its energy, so that change will be automatically accepted. On the other hand, the PT swap is possible if both the configuration changes are accepted.
One can generalize that the swap is accepted with probability $e^{-\beta|\Delta E|}$. To have an acceptance rate reasonable, where the system copies N_T are not stuck at a given temperature, we carefully determinate the temperature range, ΔT.

[1] We carried on massive simulation of Janus II for the investigation of the Ising EA model in presence of an external magnetic field, see Part III

The temperature ranges of the N_T are chosen for having an acceptance ratio of approximately $\in [20 : 30]\%$. Notice that exchanging configurations is equivalent to exchange temperatures, so instead of swapping configurations, one can swap directly temperatures, reducing the data transfer to a single number.

APPENDIX B

Managing the statistical errors

The numerical observables $\mathcal{O}$ shown in this dissertation suffer at least from two noises, one due to thermal fluctuations during a single run, and a second one deriving from the disorder. In the MUSA implementation, there is a third error given by the no complete independence of the samples, but we have checked that this error is sub-leading to the other two.
In any case, we treat the measurements of our observable as independent identically distributed (i.i.d) random variables with two independent noises.

Given a set of $\mathcal{N}$ measurements $\mathcal{O}_i$, their expected value $\mathrm{E}(\mathcal{O})$ can be evaluated through an estimator

$$\tilde{\mathrm{E}}(\mathcal{O}) = \frac{1}{\mathcal{N}} \sum_{i=1}^{N} \mathcal{O}_i \tag{B.1}$$

that for the central limit theorem is at $o(\mathcal{N}^{-1/2})$ distance from $\mathrm{E}(\mathcal{O})$.

Nonlinear functions of the observables, $f(\mathcal{O})$, can be estimated by evaluating them over the estimator. For notation' simplicity, we write a nonlinear function of a single observable, but our statements are valid for functions of many observables.
This estimation give us an estimator $f(\tilde{\mathrm{E}}(\mathcal{O}))$ which is a distance $o(\mathcal{N}^{-1})$ from the actual expected value $f(\mathrm{E}(\mathcal{O}))$. However, we can neglect this bias because it is smaller than the statistical errors.

We present in this appendix the jackknife method.

B.1 The Jackknife Method

The jackknife technique is a powerful resampling method that was used to calculate error bars throughout this dissertation. It is a well-known technique, and it has extended literature, for example, [You12]. Hence, we will limit ourselves to a brief description of it.

The main idea of the Jackknife (JK) method is of packing the data in blocks that suppress fluctuations and time correlations.
Let take a set $\mathcal{A}$ of measurements $\mathcal{O}_i$ ($i = 1, ..., \mathcal{N}$) and let group them in n blocks a_j ($j = 0, ..., n-1$) of size l, so $nl = \mathcal{N}$. Hence, we get n per-block estimators

$$\tilde{\mathrm{E}}_j(\mathcal{O}) = \frac{1}{l} \sum_{i \in a_j}^{l} \mathcal{O}_i \tag{B.2}$$

of the expectation value $\mathrm{E}(\mathcal{O})$.
From those we construct JK estimators by creating new JK bins.
Each JK bins $a_j^{\mathbf{JK}}$ contains the full data except that regarding precisely a_j, so $a_j = \mathcal{A}/a_j$. The JK estimators are

$$\tilde{\mathrm{E}}_j^{\mathbb{JK}}(\mathcal{O}) = \frac{1}{\mathcal{N}-l} \sum_{i \notin a_j}^{\mathcal{N}-l} = \frac{1}{\mathcal{N}-l} \sum_{i \in a^{\mathbf{JK}_j}} \mathcal{O}_i \ , \tag{B.3}$$

and over each of them, we evaluate the nonlinear function $f_j^{\mathbf{JK}} = f\left(\tilde{\mathrm{E}}^{(\mathbf{JK})}(\mathcal{O})\right)$.
The JK error estimate σ_f is then

$$\sigma_f = \sqrt{(n-1)\left[\frac{1}{n}\sum_{j=0}^{n-1}(f_j^{\mathbf{JK}})^2 - \left(\frac{1}{n}\sum_{j=0}^{n-1} f_j^{\mathbf{JK}}\right)^2\right]} \ . \tag{B.4}$$

APPENDIX C

Four-Replica Correlators

In this Appendix, we give some details about the 4-replica correlators used in Part III. We explain how to find the replicon and the longitudinal connected correlation functions G_R and G_L. Then, we show how to implement the Fast-Fourier Transformation (FTT) with the multispin coding technique.
In the presence of an external magnetic field, a spin-glass system, even in the paramagnetic phase, has a no-zero overlap and a residual magnetization $m \neq 0$. Hence, the correlation function $C_4(r, t_{\rm w} + t)$ does not go to zero for large distance.
We need therefore to explicitly construct correlators that go to zero, as these two quantities that can be measured directly:

$$\Gamma_1(\mathbf{x}, \mathbf{y}) = \overline{\left[\langle s_{\mathbf{x}} s_{\mathbf{y}} \rangle - \langle s_{\mathbf{x}} \rangle \langle s_{\mathbf{y}} \rangle\right]^2} \,, \tag{C.1}$$

$$\Gamma_2(\mathbf{x}, \mathbf{y}) = \overline{\left[\langle s_{\mathbf{x}} s_{\mathbf{y}} \rangle^2 - \langle s_{\mathbf{x}} \rangle^2 \langle s_{\mathbf{y}} \rangle^2\right]} \,. \tag{C.2}$$

C.0.1 The Replicon and/or Longitudinal correlation functions construction

For simplicity, we shall explain the equilibrium formulation, but the out-equilibrium one is straightforward just by inserting the time dependence. Having at least 4 replica we can construct three different correlators [1]

$$G_1(\mathbf{x}, \mathbf{y}) = \overline{\langle s_{\mathbf{x}} s_{\mathbf{y}} \rangle^2} \,, \tag{C.3}$$

$$G_2(\mathbf{x}, \mathbf{y}) = \overline{\langle s_{\mathbf{x}} s_{\mathbf{y}} \rangle \langle s_{\mathbf{x}} \rangle \langle s_{\mathbf{y}} \rangle} \,, \tag{C.4}$$

$$G_3(\mathbf{x}, \mathbf{y}) = \overline{\langle s_{\mathbf{x}} \rangle^2 \langle s_{\mathbf{y}} \rangle^2} \,. \tag{C.5}$$

These quantities doe not go to zero for large distances $\| \mathbf{x} - \mathbf{y} \|$, but in the paramagnetic phase, they all tend to the same value, $q_{\rm EA}$, when $\| \mathbf{x} - \mathbf{y} \| \to \infty$. Hence, one can obtain the basic connected propagators of the replicated field theory, namely the replicon $G_{\rm R}$ and the longitudinal $G_{\rm L}$ one, [Dom98, Dom06] by a linear combinations of the previous

[1] In Part III we utilized this method.

quantities:

$$G_{\mathrm{R}} = G_1 - 2G_2 + G_3 \,, \tag{C.6}$$
$$G_{\mathrm{L}} = G_1 - 4G_2 + 3G_3 \,. \tag{C.7}$$

Now, let us manipulate the Γ_i expressions for showing their connection to the G_{R} and G_{L} expressions.

$$\begin{aligned}\Gamma_1(\mathbf{x},\mathbf{y}) &= \overline{[\langle s_{\mathbf{x}} s_{\mathbf{y}}\rangle - \langle s_{\mathbf{x}}\rangle\langle s_{\mathbf{y}}\rangle]^2} \\ &= \overline{\langle s_{\mathbf{x}} s_{\mathbf{y}}\rangle^2 - 2\langle s_{\mathbf{x}} s_{\mathbf{y}}\rangle + \langle s_{\mathbf{x}}\rangle\langle s_{\mathbf{y}}\rangle} \,.\end{aligned} \tag{C.8}$$

As the reader can observe, this is exactly the expression of the replicon G_{R}

$$\Gamma_1(\mathbf{x},\mathbf{y}) = G_{\mathrm{R}}(\mathbf{x},\mathbf{y}) \,. \tag{C.9}$$

To expand Γ_2 we complete a square

$$\begin{aligned}\Gamma_2(\mathbf{x},\mathbf{y}) &= \overline{[\langle s_{\mathbf{x}} s_{\mathbf{y}}\rangle^2 - \langle s_{\mathbf{x}}\rangle^2\langle s_{\mathbf{y}}\rangle^2]} \\ &= \overline{(\langle s_{\mathbf{x}} s_{\mathbf{y}}\rangle^2 - 2\langle s_{\mathbf{x}} s_{\mathbf{y}}\rangle\langle s_{\mathbf{x}}\rangle\langle s_{\mathbf{y}}\rangle + \langle s_{\mathbf{x}}\rangle^2\langle s_{\mathbf{y}}\rangle^2)} + \\ &+ 2\left(\overline{\langle s_{\mathbf{x}} s_{\mathbf{y}}\rangle\langle s_{\mathbf{x}}\rangle\langle s_{\mathbf{y}}\rangle - \langle s_{\mathbf{x}}\rangle^2\langle s_{\mathbf{y}}\rangle^2}\right) \\ &= G_{\mathrm{R}}(\mathbf{x},\mathbf{y}) + 2\left[G_2(\mathbf{x},\mathbf{y}) - G_3(\mathbf{x},\mathbf{y})\right] \,.\end{aligned} \tag{C.10}$$

Let us rewrite Eq. (C.10) in the convenient form $\Gamma_2 - \Gamma_1 = 2(G_2 - G_3)$ and with a bit of algebra we find:

$$G_{\mathrm{L}}(\mathbf{x},\mathbf{y}) = 2\Gamma_1(\mathbf{x},\mathbf{y}) - \Gamma_2(\mathbf{x},\mathbf{y}) \,. \tag{C.11}$$

The definition of the two connected propagators, Eq. (C.6) and (C.7), are valid at the equilibrium, but they were successfully used in the out-equilibrium context [BJ14b].

C.1 Measuring the propagators with MultiSpin Coding

Let us express the replicon correlator G_{R} in a useful way for MSC implementation and, then, we will show the clue for the analysis.

C.1.1 Correlators as simple functions of simple fields

Let us write the physical correlation functions in terms of *field of differences* that is a simple way of constructing unbiased quantities in Monte Carlo computations.
With four replicas we can define

$$\begin{aligned}X_1(\mathbf{x}) &= (s^{\mathrm{a}}_{\mathbf{x}} - s^{\mathrm{b}}_{\mathbf{x}})(s^{\mathrm{c}}_{\mathbf{x}} - s^{\mathrm{d}}_{\mathbf{x}}) \,, \\ X_2(\mathbf{x}) &= s^{\mathrm{a}}_{\mathbf{x}} s^{\mathrm{b}}_{\mathbf{x}} - s^{\mathrm{c}}_{\mathbf{x}} s^{\mathrm{d}}_{\mathbf{x}} \,.\end{aligned} \tag{C.12}$$

Actually, these are the quantities we measure. We want to relate them with the correlation functions G_{R} and G_{L} (Eqs. (C.6)-(C.7)).

Expanding the X_1 field correlator, we get

$$\langle X_1(\mathbf{x})X_1(\mathbf{y})\rangle = 4\langle s^{\mathrm{a}}_{\mathbf{x}} s^{\mathrm{c}}_{\mathbf{x}} s^{\mathrm{a}}_{\mathbf{y}} s^{\mathrm{c}}_{\mathbf{y}}\rangle - 8\langle s^{\mathrm{a}}_{\mathbf{x}} s^{\mathrm{c}}_{\mathbf{x}} s^{\mathrm{a}}_{\mathbf{y}} s^{\mathrm{d}}_{\mathbf{y}}\rangle + 4\langle s^{\mathrm{a}}_{\mathbf{x}} s^{\mathrm{c}}_{\mathbf{x}} s^{\mathrm{b}}_{\mathbf{y}} s^{\mathrm{d}}_{\mathbf{y}}\rangle\,. \tag{C.13}$$

On the other side rewriting the replicon propagator G_{R} as a function of four replica yields

$$G_{\mathrm{R}}(\mathbf{x},\mathbf{y}) = \overline{\langle s^{\mathrm{a}}_{\mathbf{x}} s^{\mathrm{a}}_{\mathbf{y}} s^{\mathrm{b}}_{\mathbf{x}} s^{\mathrm{b}}_{\mathbf{y}}\rangle - 2\langle s^{\mathrm{a}}_{\mathbf{x}} s^{\mathrm{a}}_{\mathbf{y}} s^{\mathrm{b}}_{\mathbf{x}} s^{\mathrm{c}}_{\mathbf{y}}\rangle + \langle s^{\mathrm{a}}_{\mathbf{x}} s^{\mathrm{a}}_{\mathbf{y}} s^{\mathrm{c}}_{\mathbf{x}} s^{\mathrm{d}}_{\mathbf{y}}\rangle}\,, \tag{C.14}$$

so

$$G_{\mathrm{R}}(\mathbf{x},\mathbf{y}) = \frac{1}{4}\overline{\langle X_1(\mathbf{x})X_1(\mathbf{y})\rangle}\,. \tag{C.15}$$

Equivalently, an expansion of the X_2 field correlator returns

$$\begin{aligned}\langle X_2(\mathbf{x})X_2(\mathbf{y})\rangle &= \langle s^{\mathrm{a}}_{\mathbf{x}} s^{\mathrm{b}}_{\mathbf{x}} s^{\mathrm{a}}_{\mathbf{y}} s^{\mathrm{b}}_{\mathbf{y}}\rangle - \langle s^{\mathrm{a}}_{\mathbf{x}} s^{\mathrm{b}}_{\mathbf{x}} s^{\mathrm{c}}_{\mathbf{y}} s^{\mathrm{d}}_{\mathbf{y}}\rangle - \langle s^{\mathrm{c}}_{\mathbf{x}} s^{\mathrm{d}}_{\mathbf{x}} s^{\mathrm{a}}_{\mathbf{y}} s^{\mathrm{b}}_{\mathbf{y}}\rangle + \langle s^{\mathrm{c}}_{\mathbf{x}} s^{\mathrm{d}}_{\mathbf{x}} s^{\mathrm{c}}_{\mathbf{y}} s^{\mathrm{d}}_{\mathbf{y}}\rangle = \\ &= 2\left(\langle s_{\mathbf{x}} s_{\mathbf{y}}\rangle^2 - \langle s_{\mathbf{x}}\rangle^2\langle s_{\mathbf{y}}\rangle^2\right)\,.\end{aligned} \tag{C.16}$$

By averaging it over the disorder we can relate it to the non-connected correlators of Eq. (C.3)-(C.5),

$$\frac{1}{2}\overline{\langle X_2(\mathbf{x})X_2(\mathbf{y})\rangle} = G_1(\mathbf{x},\mathbf{y}) - G_3(\mathbf{x},\mathbf{y}) = \tag{C.17}$$

$$= 2G_{\mathrm{R}}(\mathbf{x},\mathbf{y}) - G_{\mathrm{L}}(\mathbf{x},\mathbf{y})\,, \tag{C.18}$$

where for the second relation we used Eqs. (C.6)-(C.7). The expression of G_{L} in terms of the fields X_i becomes

$$G_{\mathrm{L}}(\mathbf{x},\mathbf{y}) = \frac{1}{2}\overline{\langle X_1(\mathbf{x})X_1(\mathbf{y})\rangle} - \frac{1}{2}\overline{\langle X_2(\mathbf{x})X_2(\mathbf{y})\rangle}\,. \tag{C.19}$$

Since it is possible to construct the fields X_i with three independent permutations of the replicas ($X_i^{\mathrm{abcd}}, X_i^{\mathrm{acbd}}$ and X_i^{adbc}), we compute correlators starting from each of those permutations and then average to reduce fluctuations.

C.1.2 Fourier transformation for managing the correlator distance r

The correlator functions G_{R} and G_{L} are averaged over the disorder, J_{ij}, and one can rewrite them as a function of the vector distance $\mathbf{r}$.
In the following, we focused only on the calculation of the $G_{\mathrm{R}}(\mathbf{r})$ because it carries the most signal [BJ14a].
It is expressed as:

$$G_{\mathrm{R}}(\mathbf{r}) = \frac{1}{4}\sum_{\mathrm{x}} \overline{\langle X_1(\mathbf{x})X_2(\mathbf{x}+\mathbf{r})\rangle} \tag{C.20}$$

where we averaged over the different replica, see below for details.

For the convolution theorem, one can express it in the Fourier space:

$$\hat{G_{\mathrm{R}}}(\mathbf{r}) = \frac{N}{4}\overline{\langle \hat{X}_1(\mathbf{k})\hat{X}_1(-\mathbf{k})\rangle}\ , \tag{C.21}$$

where, for $\mathbf{k} = (k, 0, 0)$,

$$\hat{X}_1(\mathbf{k}) = \frac{1}{N}\sum_{n}^{L} e^{ikn} P(n)\,. \tag{C.22}$$

The quantity $P(n)$ is the field averaged over a plane with $x_1 = n$

$$P(n) = \sum_{y,z} X_1(n, y, z)\,. \tag{C.23}$$

There are infinite plane orientations, but we only focused on the ones that have the easiest code implementation. In our analysis, we chose planes orthogonal to the vectors of the euclidean basis and the diagonals of the lattice. These geometric operations are fast, as they are of order L. The computational effort is in the replica permutations that we need to perform to gain statistic.
In the next section, we show how to build a smart code variable to speed up the analysis.

C.1.3 Multispin coding

We will present a smart way to code our spin variables and, so, to calculate the elementary bricks through which we can construct our correlators.

Let us take the directions (x, y, z) and the single planes are the L possible planes one can construct along each direction.
According to Eq. (C.14), we need four distinct replicas to calculate G_{R} for a given distance $\mathbf{r}$ and, then, we can average over all the replica combinations.
Let rewrite Eq. (C.14) in a more convenient way:

$$G_{\mathrm{R}}(\mathbf{r}) = \frac{1}{N^4}\sum_{\{a\neq b\neq c\neq d\}} (s^{\mathrm{a}}_{\mathbf{x}} - s^{\mathrm{b}}_{\mathbf{x}})(s^{\mathrm{a}}_{\mathbf{y}} - s^{\mathrm{b}}_{\mathbf{y}})(s^{\mathrm{c}}_{\mathbf{x}} - s^{\mathrm{d}}_{\mathbf{x}})(s^{\mathrm{c}}_{\mathbf{y}} - s^{\mathrm{d}}_{\mathbf{y}}) \tag{C.24}$$

$$= \left[\frac{1}{N^4}\sum_{\{a\neq b\neq c\neq d\}} (s^{\mathrm{a}}_{\mathbf{x}} - s^{\mathrm{b}}_{\mathbf{x}})(s^{\mathrm{a}}_{\mathbf{y}} - s^{\mathrm{b}}_{\mathbf{y}})\right]\left[\frac{1}{N^4}\sum_{\{a\neq b\neq c\neq d\}} (s^{\mathrm{c}}_{\mathbf{x}} - s^{\mathrm{d}}_{\mathbf{x}})(s^{\mathrm{c}}_{\mathbf{y}} - s^{\mathrm{d}}_{\mathbf{y}})\right] \tag{C.25}$$

$$= \left[N(q^{\mathrm{a}}_{\mathbf{xy}} + q^{\mathrm{b}}_{\mathbf{xy}}) - (M^{\mathrm{a}}_{\mathbf{x}}M^{\mathrm{b}}_{\mathbf{y}} + M^{\mathrm{a}}_{\mathbf{y}}M^{\mathrm{b}}_{\mathbf{x}})\right]\left[N(q^{\mathrm{c}}_{\mathbf{xy}} + q^{\mathrm{d}}_{\mathbf{xy}}) - (M^{\mathrm{c}}_{\mathbf{x}}M^{\mathrm{d}}_{\mathbf{y}} + M^{\mathrm{c}}_{\mathbf{y}}M^{\mathrm{d}}_{\mathbf{x}})\right] \tag{C.26}$$

where

$$q^{\alpha}_{\mathbf{xy}} = \frac{1}{N}\sum_{\alpha} s^{\alpha}_{\mathbf{x}} s^{\alpha}_{\mathbf{y}} \tag{C.27}$$

$$M^{\alpha}_{\mathbf{x}} = \frac{1}{N}\sum_{\alpha} s^{\alpha}_{\mathbf{x}}\,. \tag{C.28}$$

Let us remark all the sum are over different replica (a $\neq$ b $\neq$ c $\neq$ d).
Hence, we can use the computer extension SEE2 to build large computer word and parallelize the bitwise operations that we need for calculating the quantities in Eq. (C.26).

In an Ising spin-glass, each spin has only two possible values, $\sigma = \pm 1$, and one can store it in a single bit through the well-known transformation:

$$s_x = \frac{(1 - \sigma_x)}{2} \,. \tag{C.29}$$

Hence, we can store in a single computer word the spin at a given lattice position x for all the replica:

```
typedef __m256i MY_WORD;
MY_WORD replicas[2][V] // we have 512 replicas
```

This operation aligns 256 bits, exploiting SEE2 computer extension.
Now, we divided the $N_{\rm R}$ replica in four sub-groups, which one corresponds to different replica.

```
VectorUnion64 wx,wx1,wy,wy1;
NewVectorUnion64 ax,ay,bx,by,cx,cy,dx,dy;

  wx.sse=replicas[0][x];
  wx1.sse=replicas[1][x];
  wy.sse=replicas[0][y];
  wy1.sse=replicas[1][y];

//This cicle gives us access to the bits of the macro-computer word
    _m256i
  for(iw=0;iw<2;iw++){
     ax.vec[iw]=wx.vec[iw];
     bx.vec[iw]=wx.vec[iw+2];
     cx.vec[iw]=wx1.vec[iw];
     dx.vec[iw]=wx1.vec[iw+2];

     ay.vec[iw]=wy.vec[iw];
     by.vec[iw]=wy.vec[iw+2];
     cy.vec[iw]=wy1.vec[iw];
     dy.vec[iw]=wy1.vec[iw+2];
     }
//We built new computer words which have exactly 128 distinct
   replicas at the position x,y
//(x,y) are arbitrary position points
   SigmaAx=ax.sse;
   SigmaBx=bx.sse;
   SigmaCx=cx.sse;
   SigmaDx=dx.sse;
   SigmaAy=ay.sse;
   SigmaBy=by.sse;
   SigmaCy=cy.sse;
   SigmaDy=dy.sse;
```

where the variable definitions are:

```
typedef __m128i MY_WORD128;

typedef union {
    __m256i sse;
    unsigned long long vec[4];
} VectorUnion64; // This struct Union aligns 256 bits, divided into
    four long long variables

typedef union {
    __m256i sse;
    unsigned vec[8];
} VectorUnion32; // This struct Union aligns 256 bits, divided in
   eight unsigned variables

typedef union {
    __m128i sse;
    unsigned long long vec[2];
} NewVectorUnion64; // This struct Union aligns 128 bits, divided
   into two long long variables.


VectorUnion64 wx,wx1,wy,wy1;
NewVectorUnion64 ax,ay,bx,by,cx,cy,dx,dy;

MY_WORD128 SigmaAx,SigmaAy,SigmaBx,SigmaBy,mi_QxyA,mi_QxyB;
MY_WORD128 SigmaCx,SigmaCy,SigmaDx,SigmaDy,mi_QxyC,mi_QxyD;
```

These computer words **Sigma** correspond to the spins of 128 replicas at the lattice position x or y, which are completely arbitrary till now.
Hence, we directly calculate the overlap $q^{\alpha}_{\mathbf{xy}}$ and the magnetization $M^{\alpha}_{\mathbf{x}}$ in Eq. (C.26) using bitwise operations.

```
mi_QxyA= SigmaAx ^ SigmaAy; //they are all variables of type
    MY_WORD128
mi_QxyB= SigmaBx ^ SigmaBy;
mi_QxyC= SigmaCx ^ SigmaCy;
mi_QxyD= SigmaDx ^ SigmaDy;
```

Then, we used the popcount128() function[2] to calculate how many zero and ones we have in our *super-overlap* miQxyA and in the magnetization $M^{\alpha}_{\mathbf{x}}$ associated to the *super-spin* SigmaAx:

```
qa=128 -2*popcount128(&mi_QxyA);
qb=128-2*popcount128(&mi_QxyB);
qc=128-2*popcount128(&mi_QxyC);
qd=128-2*popcount128(&mi_QxyD);

Mxa=128-2*popcount128(&SigmaAx);
Mya=128-2*popcount128(&SigmaAy);
Mxb=128-2*popcount128(&SigmaBx);
Myb=128-2*popcount128(&SigmaBy);
Mxc=128-2*popcount128(&SigmaCx);
```

[2]It is a simple implementation of the popcount() function for variable of 128 bits

```
Myc=128-2*popcount128(&SigmaCy);
Mxd=128-2*popcount128(&SigmaDx);
Myd=128-2*popcount128(&SigmaDy);
```

The final contribution to the replicon correlator is:

```
g1_popAB= (qa+qb) - (Mxa*Myb + Mya*Mxb);
g1_popCD= (qc+qd) - (Mxc*Myd + Myc*Mxd);

g1_popAC= (qa+qc) - (Mxa*Myc + Mya*Mxc);
g1_popBD= (qb+qd) - (Mxb*Myd + Myb*Mxd);

g1_popAD= (qa+qd) - (Mxa*Myd + Mya*Mxd);
g1_popBC= (qb+qc) - (Mxb*Myc + Myb*Mxc);
Gamma1+= g1_popAB*g1_popCD + g1_popAC*g1_popBD + g1_popAD*g1_popBC
    ;
```

where we did three replica combinations, see Eq. (C.14).
We performed this code construction for all the Cartesian direction (x, y, z) and the L possible planes that one can build along each direction

```
for (r=0;r<L/2+1;r++){
    Gamma1=0;
    for (z=0,i=0;z<L;z++){
        zz=mod160[z+r];   //where,  for (i=0;i<=160+80;i++)
           mod160[i]=i%160;
        for (y=0;y<L;y++){
            yy=mod160[y+r];
            nx=z*L*L+y*L;
            ny=z*L*L+yy*L;
            nz=zz*L*L+y*L;
            for (x=0;x<L;x++,i++){
                    xx=mod160[x+r];
                    gamma1(i,xx+nx); //gamma1(int,int) is the
                       function that includes all the previous
                       code
                    gamma1(i,ny+x);
                    gamma1(i,nz+x);
                    }
             }
        }
    GR[r]= (double)Gamma1/N4/(V*18LL*4); //where N4= pow(128,4)
```

This analysis was performed over the configurations generated by Janus II, and we had $N_R = 512$. Of course, we could not calculate all the possible replica permutations $3 \times 512!/(508!4!)$, but we were able to calculate a third of these enormous numbers in a very fast way.

APPENDIX D

The Ising spin-glass in presence of an external magnetic field H

D.1

Technical details

D.1.1 Smoothing and interpolating the data

Our numerical data for the magnetization at small magnetic fields are rather noisy, which complicates the process of taking its derivative with respect to $\log t$. This derivative is the response function $S(t, t_{\rm w}; H)$ [recall Eq. (7.10)]. This is why, before computing the derivative, we have used a denoising method first proposed in Ref. [BJ17b]. However, because we work at larger correlation lengths (and closer to T_g) than it was done in Ref. [BJ17b], we have found it preferable to change some technical details. We explain below the precise denoising method that we have followed in this work.

Our starting observation is that the derivative of both $M_{\rm ZFC}(t, t_{\rm w}; H)$ and $TM_{\rm ZFC}(t, t_{\rm w}; H)/H$ peak at exactly the same time $t_H^{\rm eff}$. However, $TM_{\rm ZFC}(t, t_{\rm w}; H)/H$ enjoys the advantage of being a very smooth function of the correlation $C(t, t_{\rm w}; H)$. This smooth function is named the Fluctuation-Dissipation relation [Cug93, Cru03, Fra94, Fra98, Fra99]. The key point is that, at variance with the magnetization, $C(t, t_{\rm w}; H)$, can be computed with high accuracy for any field value H, including $H = 0$. Thus, we follow a simple two-steps denoising algorithm:

1. We fit our data for $TM_{\rm ZFC}(t, t_{\rm w}; H)/H$ as a function of $C(t, t_{\rm w}; H)$, see Eq. (D.1).

2. We *replace* our data for $TM_{\rm ZFC}(t, t_{\rm w}; H)/H$ by the just mentioned fitted function, which is evaluated at $C(t, t_{\rm w}; H)$.

Our chosen functional form is as follows. Let the quantity $TM_{\rm ZFC}(t, t_{\rm w}, H)/H$ be approximated by $f(\hat{x})$, where for notation simplicity we do not write its explicit

dependence on $t, t_{\rm w}$ and H,

$$f(\hat{x}) = f_{\rm L}(\hat{x})\frac{1+\tanh[\mathcal{Q}(\hat{x})]}{2} + f_{\rm s}(\hat{x})\frac{1-\tanh[\mathcal{Q}(\hat{x})]}{2} \tag{D.1}$$

with $\mathcal{Q}(\hat{x}) = (\hat{x} - x^*)/w$. The function $f(\hat{x})$ has two distinct behaviors for large and small $\hat{x}$. The crossover between the two functional forms is smoothed by the $\tanh[\mathcal{Q}(\hat{x})]$ functional term, where x^* is the crossover point and w is the crossover rate. The functional form for small $\hat{x}$ is:

$$f_{\rm s}(\hat{x}) = a_0 + \sum_{k=1}^{N} a_k \frac{(\hat{x} - \hat{x}_{min})^k}{k!} \tag{D.2}$$

For the large $\hat{x}$ region, we choose a polynomial expansion in terms of $(1-\hat{x})$:

$$f_{\rm L}(\hat{x}) = (1-\hat{x}) + \sum_{k=2}^{N'+1} b_k \frac{(1-\hat{x})^k}{k!} \tag{D.3}$$

The polynomial expansion in $(1-\hat{x})$ is quite natural in the large $\hat{x}$ region [BJ17b], as a deviation from the Fluctuation-Dissipation Theorem. This Theorem, that holds only under equilibrium conditions, predicts $N' = 0$ for Eq. (D.3) and $x^* = w = 0$ for Eq. (D.1) [so that, in equilibrium, one would have $f(\hat{x}) = (1-\hat{x})$ in Eq. (D.1)]. In the small $\hat{x}$ region, there is not any theoretical justification for this functional form for $f_{\rm s}(\hat{x})$. The quantity $TM_{\rm ZFC}(t, t_{\rm w}, H)/H$ is affected by strong nonlinear effects that increase with increasing external magnetic field H and upon approaching the temperature, (see Fig. D.1).

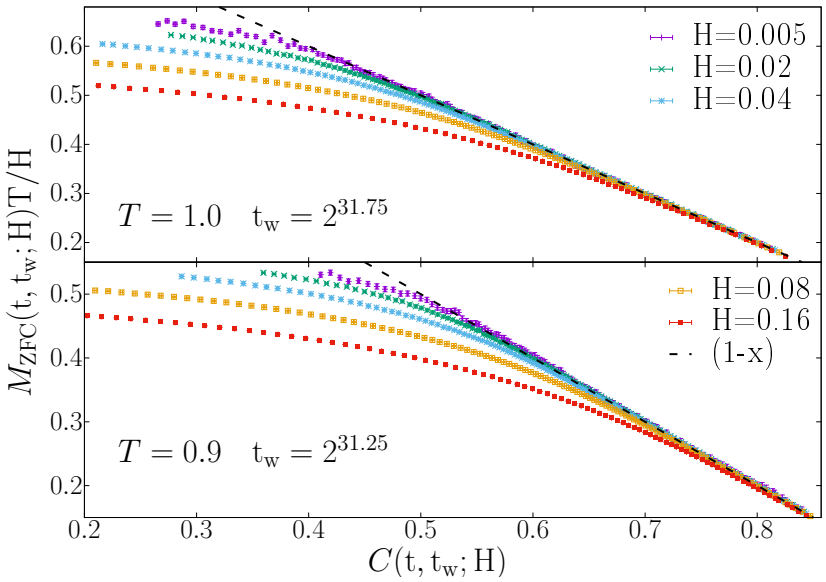

Figure D.1: The behavior of the quantity $TM_{\rm ZFC}(t, t_{\rm w}, H)/H$ is exhibited as a function of $C(t, t_{\rm w}; H)$. **The upper** plot is for the case of $T = 1.0$ $t_{\rm w} = 2^{31.75}$. **The bottom** pot is for the case of $T = 0.9$ $t_{\rm w} = 2^{31.25}$. We do not report all the magnetic values for simplicity.

As we will discuss in Appendix D.1.2, selecting the appropriate order for the polynomials in Eqs. (D.1) and (D.3) and (D.2). Our preferred choices are given in Table D.1.

Errors are computed using a jackknife procedure. We perform an independent fit for each jack-knife block, and compute errors from the jack-knife fluctuations of the fitted $f(\hat{x})$. In Fig. D.2 we show a comparison between the original and smoothed data for the case $T = 1.0$ and $t_w = 2^{31.75}$. As expected, the de-noising technique is most important for the smallest magnetic fields.

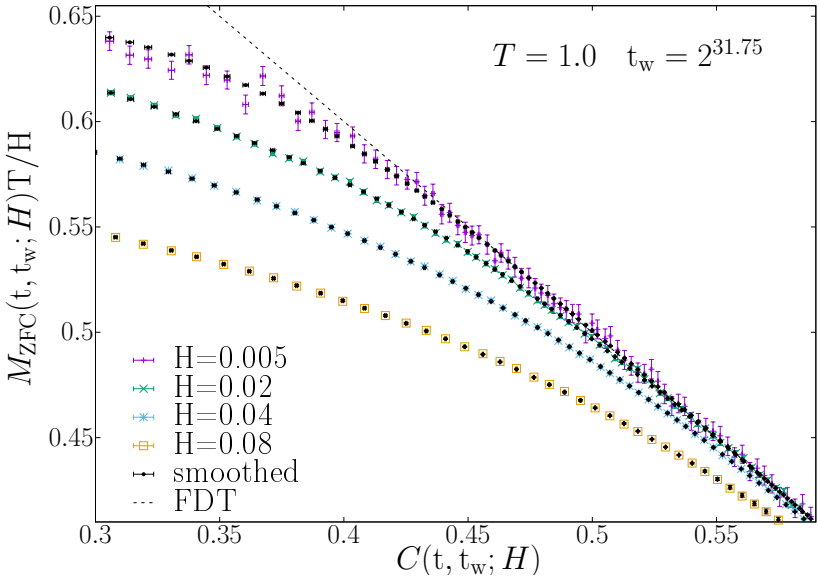

Figure D.2: Comparison between the original and smoothed data at $T = 1.0$ and waiting time $t_w = 2^{31.75}$. One can clearly see the advantage of the de-noising method for the lowest magnetic field.

D.1.2 Over-fitting problem

A difficulty in our fits to Eq. (D.1) is that we can use only the diagonal part of the covariance matrix in the computation of the goodness-of-fit indicator χ^2. This is the reason underlying the very small values for χ^2 that we show in Tab. D.1. As a consequence, we cannot trust the χ^2 test for selecting the appropriate order for the polynomial expansions in Eqs. (D.2) and (D.3). Hence, we followed a different strategy.

Fortunately, we can also compare the statistical errors that we find for the denoised $TM_{ZFC}(t, t_w; H)/H$ with different choices of the polynomial expansion (remember that these errors are not computed from χ^2, but from the jack-knife fluctuations). As an example, take the case at $T = 0.9$ for a waiting time $t_w = 2^{31.75}$ and $H = 0.002$, which is considered in Fig. D.3. The figure compares the statistical errors of the original, not-denoised data with the errors found with two possible choices for the polynomial fits in Eqs. (D.2) and (D.3). Although both fits are indistinguishable from the point

	$\mathbf{t_w}$	**H**	**N**	**N′**	$\mathbf{x^*}$	**w**	$\boldsymbol{\chi^2}$**/DOF**
$\mathbf{T} = 0.9$	2^{22}	0.01	1	1	0.583(11)	0.128(1)	45.7206/110
		0.02	1	1	0.604(6)	0.1264(6)	49.8735/110
		0.04	3	2	0.589(4)	0.099(4)	27.9909/107
		0.08	3	2	0.576(7)	0.164(11)	64.3442/107
		0.1	3	2	0.681(12)	0.187(4)	33.1334/99
		0.12	3	3	0.665(18)	0.0725(5)	31.7093/98
		0.16	4	4	0.617(36)	0.052(1)	65.326/104
	$2^{26.5}$	0.005	2	0	0.530(17)	0.100(7)	28.518/112
		0.01	1	1	0.520(10)	0.115(4)	37.3434/112
		0.02	2	0	0.535(3)	0.091(3)	35.5349/112
		0.04	2	0	0.653(2)	0.033(2)	59.3249/112
		0.08	3	2	0.585(7)	0.161(11)	55.0056/109
		0.1	3	2	0.674(12)	0.176(4)	32.874/103
		0.12	3	3	0.683(64)	0.078(11)	42.7819/102
		0.16	4	4	0.623(15)	0.0336(84)	77.2971/106
	$2^{31.25}$	0.005	1	0	0.503(8)	0.074(7)	35.145/123
		0.01	1	1	0.520(12)	0.139(2)	32.3306/118
		0.02	1	2	0.550(7)	0.0335(3)	31.2191/121
		0.04	2	0	0.554(16)	0.080(2)	75.7904/116
		0.08	3	2	0.598(6)	0.152(8)	38.4391/115
		0.10	3	2	0.688(10)	0.170(4)	29.9037/107
		0.12	3	3	0.655(14)	0.062(4)	32.3955/98
		0.16	4	4	0.549(22)	0.077(6)	67.2957/112
$\mathbf{T} = 1.0$	$2^{23.75}$	0.005	1	0	0.371(18)	0.178(12)	60.7092/103
		0.01	1	0	0.411(4)	0.129(4)	46.7089/103
		0.02	1	0	0.397(2)	0.138(2)	76.0089/103
		0.04	2	0	0.457(2)	0.146(2)	49.4012/102
		0.08	4	0	0.589(6)	0.066(1)	36.3845/100
		0.16	4	3	0.639(12)	0.061(6)	48.3379/98
	$2^{27.625}$	0.005	1	0	0.37(2)	0.157(1)	34.6242/101
		0.01	1	0	0.400(8)	0.128(5)	45.1691/111
		0.02	1	0	0.389(2)	0.132(2)	53.1209/111
		0.04	3	0	0.559(11)	0.049(4)	32.7385/109
		0.08	3	1	0.638(8)	0.023(11)	491.701/108
		0.16	3	1	0.667(2)	0.023(3)	140.853/108
	$2^{31.75}$	0.005	2	0	0.357(9)	0.170(12)	41.854/127
		0.01	1	0	0.114(10)	0.114(10)	39.2024/123
		0.02	2	0	0.488(8)	0.116(7)	40.968/118
		0.04	3	0	0.534(12)	0.070(4)	33.5791/109
		0.08	3	1	0.631(4)	0.023(5)	271.914/108
		0.16	4	0	0.686(9)	0.080(3)	160.49/108

Table D.1: For each of our fits to Eq. (D.1) we report: the order of the polynomial in Eq. (D.2) N, the number of fitted parameters in Eq. (D.3) N', [$N' = 0$ means $f_L(\hat{x}) = (1 - \hat{x})$], the crossover parameters x^* and w, and the fit's figure of merit χ^2**/DOF**. Mind that we can only compute the so-called diagonal χ^2, which takes into account only the diagonal elements of the covariance matrix. Due to this limitation, for many of our fits we find a value of χ^2 significantly smaller than the number of degrees of freedom.

case	**N**	**N′**	**x***	**w**	χ^2**/DOF**
over-fitted	1	1	0.547(6)	0.132(1)	28.0591/122
our choice	2	0	0.550(7)	0.0335(3)	31.2191/121

Table D.2: Information about the two fits shown in Fig. D.3. We follow the same notational conventions of Table D.1.

of view of the χ^2 test, see Tab. D.2, the resulting errors are very different. In one case, we find statistical errors that evolve rather smoothly with t. For the second choice, we find wild oscillations in the size of errors as t varies. When in doubt, we have always taken the choice providing the smoother t evolution for the errors. As we said above, our final choices are reported in Tab. D.1.

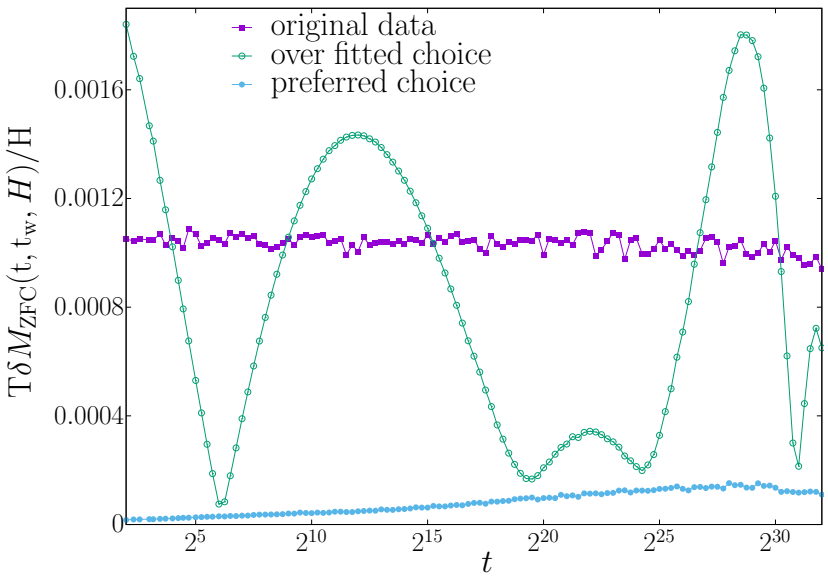

Figure D.3: Comparison between the original and the smoothed relative errors, $T\delta M_{\rm ZFC}(t, t_{\rm w}, H)/H$ (with $T = 0.9$, $t_{\rm w} = 2^{31.75}$, and $H = 0.002$), for two different fitting functions $f(\hat{x})$ reported in Table D.2.

D.1.3 Time discretization and the calculation of the relaxation function $S(t_{\rm w}, t; H)$

As it was explained in the main text, the quantity used in experiment [Joh99] to extract $t^{\rm eff}(H)$ is the relaxation function $S(t, t_{\rm w}; H)$ of Eq. (7.10). We calculate $S(t, t_{\rm w}; H)$ as a finite time difference:

$$S(t, t_{\rm w}, t'; H) = \frac{M_{\rm ZFC}(t', t_{\rm w}; H) - M_{\rm ZFC}(t, t_{\rm w}; H)}{\log\left(\frac{t'}{t}\right)} \,. \tag{D.4}$$

In simulations, the time is discrete and we have stored configurations at times $t_n =$ integerpartof $2^{n/4}$, with n an integer. Let us write explicitly the integer dependence of the time t and t' as:

$$t \equiv t_n \qquad t' \equiv t_{n+k}$$

where k is an integer time parameter. Hence, we rescaled the time as:

$$t_{\rm new} = \frac{1}{2}\log\left(\frac{t_{n+k}}{t_n}\right) \tag{D.5}$$

and, we expressed our observables as functions of the time $t_{\rm new}$:

$$S(t, t_{\rm w}, t'; H) \quad \to \quad S(t_{\rm new}, t_{\rm w}; H) \tag{D.6}$$
$$C(t, t_{\rm w}; H) \quad \to \quad C(t_{\rm new}, t_{\rm w}; H)\,. \tag{D.7}$$

The relaxation function $S(t_{\rm new}, t_{\rm w}; H)$ is trivial to construct, see Eq. (D.4). However, the correlation function $C(t_{\rm new}, t_{\rm w}; H)$ needs to be calculated using a linear interpolation. For any given value of $t_{\rm new}$, we looked for our *original discrete* time t_n such that:

$$\log(t_n) < \log(t_{\rm new}) \leq \log(t_{n+1})\,. \tag{D.8}$$

Using a linear interpolation, we obtain:

$$C(t_{\rm new}) = \frac{\log(t_{\rm new}) - \log(t_{n+1})}{\log(t_n) - \log(t_{n+1})} C(t_n) - \frac{\log(t_{\rm new}) - \log(t_n)}{\log(t_n) - \log(t_{n+1})} C(t_{n+1})\,. \tag{D.9}$$

Finally, one can express the relaxation function, $S(t_{\rm new}, t_{\rm w}; H)$, as a function of the correlation function, $\mathcal{S}(C, H)$, in much the same manner as Eq. (D.9)

D.1.4 The $t_H^{\rm eff}$ calculation

As explained in the main text, the extraction of the $t_H^{\rm eff}$ from Eq. (7.15) is delicate because the $C_{\rm peak}(t_{\rm w})$ are implicit functions of the rescaled time $t_{\rm new}$. In order to solve Eq. (7.15), we calculate the $t_H^{\rm eff}$ values through a quadratic interpolation. First, we calculate the *original* discrete time t_n such that:

$$C(t + t_{n+1}; t_{\rm w}; H) < C_{\rm peak} \leq C(t + t_n, t_{\rm w}; H)\,. \tag{D.10}$$

Then, we solve the three equation system:

$$\begin{aligned} C(t + t_{n-1}) &= \alpha_0 + \alpha_1 x_{n-1} + \alpha_2 x_{n-1}^2 \\ C(t + t_n) &= \alpha_0 + \alpha_1 x_n + \alpha_2 x_n^2 \\ C(t + t_{n+1}) &= \alpha_0 + \alpha_1 x_{n+1} + \alpha_2 x_{n+1}^2\,, \end{aligned}$$

where $x_n = \log t_n$ and, for brevity' sake, we omit the arguments t_w and H. The solution generates the coefficients α_i:

$$\begin{aligned}
\alpha_2 &= \frac{C(t_\mathrm{w}, t_\mathrm{w}+t_{n-1}) - C(t_\mathrm{w}, t_\mathrm{w}+t_n)}{x_{n-1}-x_n} - \frac{C(t_\mathrm{w}, t_\mathrm{w}+t_{n+1}) - C(t_\mathrm{w}, t_\mathrm{w}+t_n)}{(x_{n-1}-x_{n+1})(x_{n+1}-x_n)}\,,\\
\alpha_1 &= \frac{C(t_\mathrm{w}, t_\mathrm{w}+t_{n+1}) - C(t_\mathrm{w}, t_\mathrm{w}+t_n)}{x_{n+1}-x_n} - \alpha_2(x_n + x_{n+1})\,,\\
\alpha_0 &= C(t_\mathrm{w}, t_\mathrm{w}+t_n) - \alpha_1 x_n - \alpha_2 x_n^2\,.
\end{aligned}$$

We can then calculate the t_H^{eff} solving the equation:

$$C_{\mathrm{peak}} = \alpha_0 + \alpha_1 \log\left(t_H^{\mathrm{eff}}\right) + \alpha_2 \left[\log\left(t_H^{\mathrm{eff}}\right)\right]^2\,, \tag{D.11}$$

where only the solution verifying $t_n \le t_H^{\mathrm{eff}} < t_{n+1}$ is physical.

D.2

The Josephson length

For the readers convenience, we reproduce here the interpolation proposed in Ref. [Zha19] of the data obtained in Ref. [BJ18] for the replicon exponent as a function of the Josephson length and the correlation length.

The Josephson length, $\ell_J(T^{(J)})$, scales as

$$\ell_J\big(T^{(J)}\big) = \frac{b_0 + b_1\big(T_c^{(J)} - T^{(J)}\big)^\nu + b_2\big(T_c^{(J)} - T^{(J)}\big)^{\omega\nu}}{\big(T_c^{(J)} - T^{(J)}\big)^\nu}, \tag{D.12}$$

where the $T^{(J)}$ is the temperature in *Janus units*,

$$T^{(J)} = \frac{T}{T_c} T_c^{(J)} \quad T_c^{(J)} = 1.102 \tag{D.13}$$

and we have included analytic (b_1) and confluent (b_2) scaling corrections with $\omega = 1.12(10)$ and $\nu = 2.56(4)$ [BJ13]. The numerical coefficients are:

$$\begin{aligned}
\omega &= 1.12(10),\\
\nu &= 2.56(4),\\
b_0 &= 0.1015,\\
b_1 &= 0.3725,\\
b_2 &= 0.1997.
\end{aligned} \tag{D.14}$$

From Ref. [BJ13], the replicon exponent $\theta\big(x(\xi,T)\big)$ can be well interpolated as,

$$\theta(x) = \theta_0 + d_1\left(\frac{x}{1+e_1 x}\right)^{2-\theta_0} + d_2\left(\frac{x}{1+e_2 x}\right)^{3-\theta_0}, \tag{D.15}$$

where,

$$\begin{aligned} \theta_0 &= 0.303980, \\ e_1 &= 1.38179, \\ d_1 &= 2.72489, \\ e_2 &= 2.12634, \\ d_2 &= -9.98389. \end{aligned} \tag{D.16}$$

Note, that the replicon exponent $\theta(\tilde{x}(\xi, T))$ depends on both the temperature and the correlation length ξ through the crossover variable

$$\tilde{x} = \frac{\ell_J(T)}{\xi(t_{\rm w}; T)}\,. \tag{D.17}$$

D.3

Sample-dependence of the nonlinear scaling results.

We demonstrate that the nonlinear scaling results are sample-independent for the case $H = 0.005$, $t_{\rm w} = 2^{31.25}$, at $T = 0.9$. We simulate four independent samples and, for each one, we build the relaxation function $\mathcal{S}(C, H)$, see Sec. 7.4.2 and Appendix D.1.3. We exhibit them in Fig. D.4 where we report only the case for $k = 8$. To compare peak regions of the relaxation function, $\mathcal{S}(C, H)$, we shift the lowest curves, namely S_0 and S_2, vertically. An amplification of the peak region is shown in Fig. D.4.
As one can observe from Fig. D.4, there is a sample dependence of the peak position. We report the estimates of $C_{\rm peak}(t_{\rm w})$ for each sample in Tab. D.3. Note that the sample S_0 is the one analyzed in the main text. We extract the effective time $t_H^{\rm eff}$ for each sample, according to Eq. (7.15). They are listed in Tab. D.3. The sample dependence found for the $C_{\rm peak}(t_{\rm w}, S_i)$ values is seen in the $t_H^{\rm eff}$ values too. Accordingly, we repeat the analysis addressed in Sec. 7.5.4 using, as input parameter for extracting the $t_H^{\rm eff}$, the $C_{\rm peak}(t_{\rm w}, S_2)$ value exhibithed in Tab. D.3. We analyze the effective time ratio $\ell n \frac{t_H^{\rm eff}}{t_{H\to 0^+}^{\rm eff}}$ according to Eq. (7.30). We then compare the scaling behavior for the two values of $C_{\rm peak}(t_{\rm w}, S_i)$. The two sets of data are statistically compatible, see Fig. D.5. This implies that the physical scenario is not affected by the small uncertain in the determination of $C_{\rm peak}(t_{\rm w})$. We therefore assert that the scaling results are sample-independent.

Sample	$\log_2\left(t_H^{\text{eff}}\right)$	$C_{\text{peak}}(t_{\text{w}})$
S_0	30.434(21)	0.493
S_1	30.196(23)	0.493
S_2	30.546(24)	0.505
S_3	30.327(21)	0.505

Table D.3: Information about the t_H^{eff} and $C_{\text{peak}}(t_{\text{w}}, S_i)$ evaluations in the case $H = 0.005$, $t_{\text{w}} = 2^{31.25}$ and $T = 0.9$.

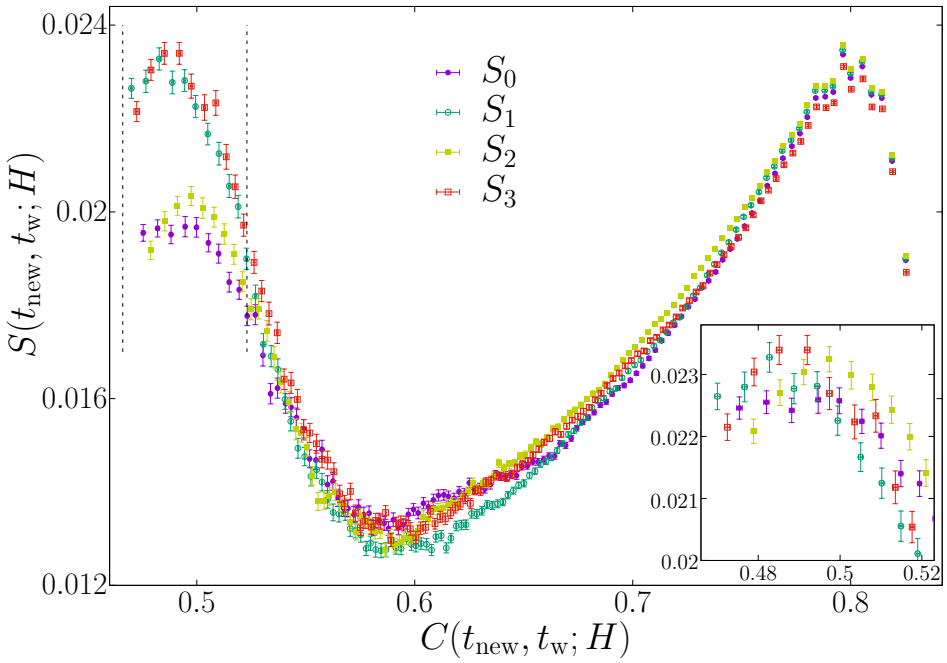

Figure D.4: Plots show the behavior of $\mathcal{S}(C, H)$ for four independent samples for $H = 0.005$, $t_{\text{w}} = 2^{31.25}$ at $T = 0.9$. The peak area is enlarged in the *insert* after a vertical shift.

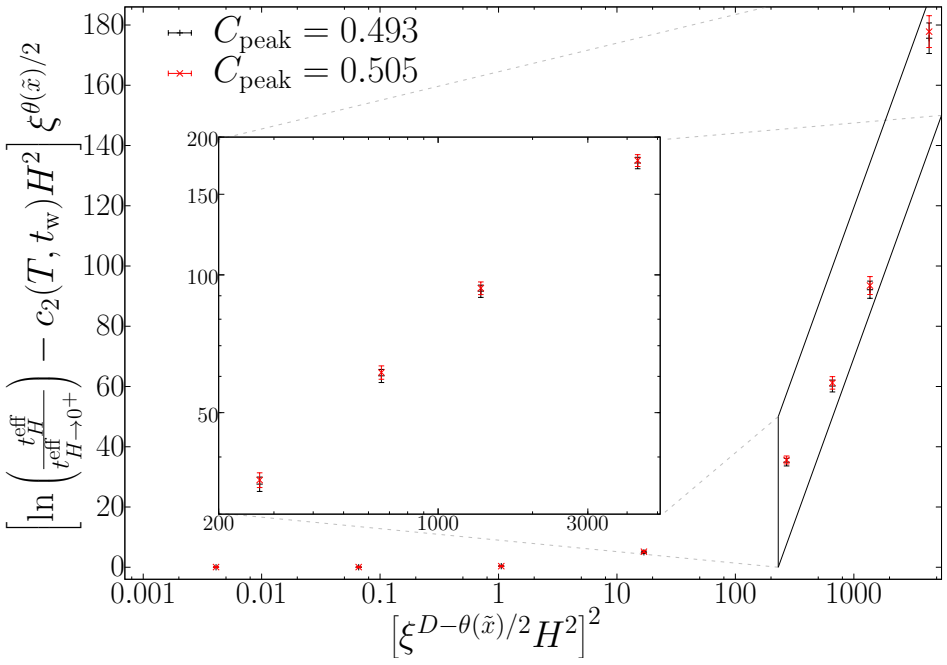

Figure D.5: The behavior of the scaling law for the case $t_{\rm w} = 2^{31.25}$ at $T = 0.9$ for the two different $C_{\rm peak}$ values in Tab. D.3. The **main** figure is in semi-logscale; whereas, the **insert** is amplified in a log-log scale. It can be seen that the data points for the two cases of $C_{\rm peak}$ are equivalent within their respective error bars.

Bibliography

[AB10a] R. Alvarez Baños, A. Cruz, L. A. Fernandez, J. M. Gil-Narvion, A. Gordillo-Guerrero, M. Guidetti, A. Maiorano, F. Mantovani, E. Marinari, V. Martín-Mayor, J. Monforte-Garcia, A. Muñoz Sudupe, D. Navarro, G. Parisi, S. Perez-Gaviro, J. J. Ruiz-Lorenzo, S. F. Schifano, B. Seoane, A. Tarancon, R. Tripiccione and D. Yllanes (Janus Collaboration): *J. Stat. Mech.* **2010**, P06026 (2010). doi:10.1088/1742-5468/2010/06/P06026. arXiv:1003.2569.

[AB10b] R. Alvarez Baños, A. Cruz, L. A. Fernandez, J. M. Gil-Narvion, A. Gordillo-Guerrero, M. Guidetti, A. Maiorano, F. Mantovani, E. Marinari, V. Martín-Mayor, J. Monforte-Garcia, A. Muñoz Sudupe, D. Navarro, G. Parisi, S. Perez-Gaviro, J. J. Ruiz-Lorenzo, S. F. Schifano, B. Seoane, A. Tarancon, R. Tripiccione and D. Yllanes (Janus Collaboration): *Phys. Rev. Lett.* **105**, 177202 (2010). doi:10.1103/PhysRevLett.105.177202. arXiv:1003.2943.

[AK94] H. Aruga Katori and A. Ito: *Journal of the Physical Society of Japan* **63**, 3122–3128 (1994). doi:10.1143/JPSJ.63.3122. http://dx.doi.org/10.1143/JPSJ.63.3122, URL http://dx.doi.org/10.1143/JPSJ.63.3122.

[Alm78a] J. de Almeida, R. Jones, J. Kosterlitz and D. Thouless: *Journal of Physics C: Solid State Physics* **11**, L871 (1978). doi:10.1088/0022-3719/11/21/005. URL http://stacks.iop.org/0022-3719/11/i=21/a=005.

[Alm78b] J. R. L. de Almeida and D. J. Thouless: *J. Phys. A: Math. Gen.* **11**, 983 (1978). doi:10.1088/0305-4470/11/5/028. URL http://stacks.iop.org/0305-4470/11/i=5/a=028.

[Ami05] D. J. Amit and V. Martín-Mayor: *Field Theory, the Renormalization Group and Critical Phenomena*. third edition (World Scientific, Singapore, 2005). doi:10.1142/9789812775313_bmatter. URL http://www.worldscientific.com/worldscibooks/10.1142/5715.

[Amo03] C. Amoruso, E. Marinari, O. C. Martin and A. Pagnani: *Phys. Rev. Lett.* **91**, 087201 (Aug 2003). doi:10.1103/PhysRevLett.91.087201. URL http://link.aps.org/doi/10.1103/PhysRevLett.91.087201.

[And70] P. Anderson: *Materials Research Bulletin* **5**, 549 (1970). ISSN 0025-5408. doi:10.1016/0025-5408(70)90096-6.

[And78] P. W. Anderson and C. M. Pond: *Phys. Rev. Lett.* **40**, 903–906 (Mar 1978). doi:10.1103/PhysRevLett.40.903. URL http://link.aps.org/doi/10.1103/PhysRevLett.40.903.

[Ang13] M. Angelini and F. Parisi, G. Ricci-Tersenghi: *Phy. Rev. B* **87**, 134201 (2013). doi:10.1103/PhysRevB.87.134201. arXiv:1111.6869.

[Asp04] T. Aspelmeier and M. A. Moore: *Phys. Rev. Lett.* **92**, 077201 (2004).

[Ast19] A. Astillero and J. J. Ruiz-Lorenzo: *Phys. Rev. E* **100**, 062117 (Dec 2019). doi:10.1103/PhysRevE.100.062117. URL https://link.aps.org/doi/10.1103/PhysRevE.100.062117.

[Bal96a] H. G. Ballesteros, L. A. Fernandez, V. Martín-Mayor and A. Muñoz Sudupe: *Phys. Lett. B* **387**, 125 (1996).

[Bal96b] H. G. Ballesteros, L. A. Fernandez, V. Martín-Mayor and A. Muñoz Sudupe: *Phys. Lett. B* **378**, 207 (1996). doi:10.1016/0370-2693(96)00358-9. arXiv:hep-lat/9511003.

[Bal98] H. G. Ballesteros, L. A. Fernandez, V. Martín-Mayor, A. Muñoz Sudupe, G. Parisi and J. J. Ruiz-Lorenzo: *Nucl. Phys. B* **512**, 681 (1998). doi:http://dx.doi.org/10.1016/S0550-3213(97)00797-9.

[Bal00] H. G. Ballesteros, A. Cruz, L. A. Fernandez, V. Martín-Mayor, J. Pech, J. J. Ruiz-Lorenzo, A. Tarancon, P. Tellez, C. L. Ullod and C. Ungil: *Phys. Rev. B* **62**, 14237–14245 (2000). doi:10.1103/PhysRevB.62.14237. arXiv:cond-mat/0006211.

[Ban87] J. R. Banavar and A. J. Bray: *Phys. Rev. B* **35**, 8888 (1987). doi:10.1103/PhysRevB.35.8888.

[Bar82] F. Barahona: *Journal of Physics A: Mathematical and General* **15**, 3241 (1982). doi:10.1088/0305-4470/15/10/028. URL http://stacks.iop.org/0305-4470/15/i=10/a=028.

[Bar01] A. Barrat and L. Berthier: *Phys. Rev. Lett.* **87**, 087204 (Aug 2001). doi:10.1103/PhysRevLett.87.087204. URL http://link.aps.org/doi/10.1103/PhysRevLett.87.087204.

[Bel06] F. Belletti, F. Mantovani, G. Poli, S. F. Schifano, R. Tripiccione, I. Campos, A. Cruz, D. Navarro, S. Perez-Gaviro, D. Sciretti, A. Tarancon, J. L. Velasco, P. Tellez, L. A. Fernandez, V. Martín-Mayor, A. Muñoz Sudupe, S. Jimenez, A. Maiorano, E. Marinari and J. J. Ruiz-Lorenzo (Janus Collaboration): *Computing in Science and Engineering* **8**, 41 (2006).

[Bel08a] F. Belletti, M. Cotallo, A. Cruz, L. A. Fernandez, A. Gordillo, A. Maiorano, F. Mantovani, E. Marinari, V. Martín-Mayor, A. Muñoz Sudupe, D. Navarro, S. Perez-Gaviro, J. J. Ruiz-Lorenzo, S. F. Schifano, D. Sciretti, A. Tarancon, R. Tripiccione and J. L. Velasco (Janus Collaboration): *Comp. Phys. Comm.* **178**, 208–216 (2008). doi:10.1016/j.cpc.2007.09.006. arXiv:0704.3573.

[Bel08b] F. Belletti, M. Cotallo, A. Cruz, L. A. Fernandez, A. Gordillo-Guerrero, M. Guidetti, A. Maiorano, F. Mantovani, E. Marinari, V. Martín-Mayor, A. M. Sudupe, D. Navarro, G. Parisi, S. Perez-Gaviro, J. J. Ruiz-Lorenzo, S. F. Schifano, D. Sciretti, A. Tarancon, R. Tripiccione, J. L. Velasco and D. Yllanes (Janus Collaboration): *Phys. Rev. Lett.* **101**, 157201 (2008). doi:10.1103/PhysRevLett.101.157201. arXiv:0804.1471.

[Bel09a] F. Belletti, A. Cruz, L. A. Fernandez, A. Gordillo-Guerrero, M. Guidetti, A. Maiorano, F. Mantovani, E. Marinari, V. Martín-Mayor, J. Monforte, A. Muñoz Sudupe, D. Navarro, G. Parisi, S. Perez-Gaviro, J. J. Ruiz-Lorenzo, S. F. Schifano, D. Sciretti, A. Tarancon, R. Tripiccione and D. Yllanes (Janus Collaboration): *J. Stat. Phys.* **135**, 1121 (2009). doi:10.1007/s10955-009-9727-z. arXiv:0811.2864.

[Bel09b] F. Belletti, M. Guidetti, A. Maiorano, F. Mantovani, S. F. Schifano, R. Tripiccione, M. Cotallo, S. Perez-Gaviro, D. Sciretti, J. L. Velasco, A. Cruz, D. Navarro, A. Tarancon, L. A. Fernandez, V. Martín-Mayor, A. Muñoz-Sudupe, D. Yllanes, A. Gordillo-Guerrero, J. J. Ruiz-Lorenzo, E. Marinari, G. Parisi, M. Rossi and G. Zanier (Janus Collaboration): *Computing in Science and Engineering* **11**, 48 (2009). doi:10.1109/MCSE.2009.11.

[Ber04] F. Bert, V. Dupuis, E. Vincent, J. Hammann and J.-P. Bouchaud: *Phys. Rev. Lett.* **92**, 167203 (Apr 2004). doi:10.1103/PhysRevLett.92.167203. URL http://link.aps.org/doi/10.1103/PhysRevLett.92.167203.

[Bia12] I. Biazzo, A. Braunstein and R. Zecchina: *Phys. Rev. E* **86**, 026706 (Aug 2012). doi:10.1103/PhysRevE.86.026706. URL http://link.aps.org/doi/10.1103/PhysRevE.86.026706.

[Bin82] K. Binder: *Phys. Rev. A* **25**, 1699 (1982).

[Bin86] K. Binder and A. P. Young: *Rev. Mod. Phys.* **58**, 801–976 (Oct 1986). doi:10.1103/RevModPhys.58.801. URL http://link.aps.org/doi/10.1103/RevModPhys.58.801.

[Bin11] K. Binder and W. Kob: *Glassy Materials and Disordered Solids. An Introduction to Their Statistical Mechanics* (World Scientific, Singapore, 2011).

[BJ12] M. Baity-Jesi, R. A. Baños, A. Cruz, L. A. Fernandez, J. M. Gil-Narvion, A. Gordillo-Guerrero, M. Guidetti, D. Iniguez, A. Maiorano, F. Mantovani, E. Marinari, V. Martín-Mayor, J. Monforte-Garcia, A. Munoz Sudupe, D. Navarro, G. Parisi, M. Pivanti, S. Perez-Gaviro, F. Ricci-Tersenghi, J. J. Ruiz-Lorenzo, S. F. Schifano, B. Seoane, A. Tarancon, P. Tellez, R. Tripiccione and D. Yllanes: *Eur. Phys. J. Special Topics* **210**, 33 (AUG 2012). doi:10.1140/epjst/e2012-01636-9. arXiv:1204.4134.

[BJ13] M. Baity-Jesi, R. A. Baños, A. Cruz, L. A. Fernandez, J. M. Gil-Narvion, A. Gordillo-Guerrero, D. Iniguez, A. Maiorano, F. Mantovani, E. Marinari, V. Martín-Mayor, J. Monforte-Garcia, A. Muñoz Sudupe, D. Navarro, G. Parisi,

S. Perez-Gaviro, M. Pivanti, F. Ricci-Tersenghi, J. J. Ruiz-Lorenzo, S. F. Schifano, B. Seoane, A. Tarancon, R. Tripiccione and D. Yllanes (Janus Collaboration): *Phys. Rev. B* **88**, 224416 (2013). doi:10.1103/PhysRevB.88.224416. arXiv:1310.2910.

[BJ14a] M. Baity-Jesi, R. A. Baños, A. Cruz, L. A. Fernandez, J. M. Gil-Narvion, A. Gordillo-Guerrero, D. Iniguez, A. Maiorano, M. F., E. Marinari, V. Martín-Mayor, J. Monforte-Garcia, A. Muñoz Sudupe, D. Navarro, G. Parisi, S. Perez-Gaviro, M. Pivanti, F. Ricci-Tersenghi, J. J. Ruiz-Lorenzo, S. F. Schifano, B. Seoane, A. Tarancon, R. Tripiccione and D. Yllanes: *J. Stat. Mech.* **2014**, P05014 (2014). doi:10.1088/1742-5468/2014/05/P05014. arXiv:1403.2622.

[BJ14b] M. Baity-Jesi, R. A. Baños, A. Cruz, L. A. Fernandez, J. M. Gil-Narvion, A. Gordillo-Guerrero, D. Iniguez, A. Maiorano, F. Mantovani, E. Marinari, V. Martín-Mayor, J. Monforte-Garcia, A. Muñoz Sudupe, D. Navarro, G. Parisi, S. Perez-Gaviro, M. Pivanti, F. Ricci-Tersenghi, J. J. Ruiz-Lorenzo, S. F. Schifano, B. Seoane, A. Tarancon, R. Tripiccione and D. Yllanes (Janus Collaboration): *Comp. Phys. Comm* **185**, 550–559 (2014). doi:10.1016/j.cpc.2013.10.019. arXiv:1310.1032.

[BJ14c] M. Baity-Jesi, L. A. Fernandez, V. Martín-Mayor and J. M. Sanz: *Phys. Rev.* **89**, 014202 (2014). doi:10.1103/PhysRevB.89.014202. arXiv:1309.1599.

[BJ15] M. Baity-Jesi: *Criticality and Energy Landscapes in Spin Glasses*. Ph.D. thesis, Universidad Complutense de Madrid (October 2015). arXiv:1602.08239.

[BJ17a] M. Baity-Jesi, E. Calore, A. Cruz, L. A. Fernandez, J. M. Gil-Narvion, A. Gordillo-Guerrero, D. Iñiguez, A. Maiorano, E. Marinari, V. Martin-Mayor, J. Monforte-Garcia, A. Muñoz Sudupe, D. Navarro, G. Parisi, S. Perez-Gaviro, F. Ricci-Tersenghi, J. J. Ruiz-Lorenzo, S. F. Schifano, B. Seoane, A. Tarancon, R. Tripiccione and D. Yllanes (Janus Collaboration): *Phys. Rev. Lett.* **118**, 157202 (Apr 2017). doi:10.1103/PhysRevLett.118.157202. URL https://link.aps.org/doi/10.1103/PhysRevLett.118.157202.

[BJ17b] M. Baity-Jesi, E. Calore, A. Cruz, L. A. Fernandez, J. M. Gil-Narvión, A. Gordillo-Guerrero, D. Iiguez, A. Maiorano, E. Marinari, V. Martin-Mayor, J. Monforte-Garcia, A. Muoz Sudupe, D. Navarro, G. Parisi, S. Perez-Gaviro, F. Ricci-Tersenghi, J. J. Ruiz-Lorenzo, S. F. Schifano, B. Seoane, A. Tarancón, R. Tripiccione and D. Yllanes: *Proceedings of the National Academy of Sciences* **114**, 1838–1843 (2017). doi:10.1073/pnas.1621242114. URL http://www.pnas.org/content/114/8/1838.abstract.

[BJ18] M. Baity-Jesi, E. Calore, A. Cruz, L. A. Fernandez, J. M. Gil-Narvion, A. Gordillo-Guerrero, D. Iñiguez, A. Maiorano, E. Marinari, V. Martin-Mayor, J. Moreno-Gordo, A. Muñoz Sudupe, D. Navarro, G. Parisi, S. Perez-Gaviro, F. Ricci-Tersenghi, J. J. Ruiz-Lorenzo, S. F. Schifano, B. Seoane, A. Tarancon, R. Tripiccione and D. Yllanes (Janus Collaboration): *Phys. Rev. Lett.* **120**, 267203 (Jun 2018). doi:10.1103/PhysRevLett.120.267203. URL https://link.aps.org/doi/10.1103/PhysRevLett.120.267203.

[BJ20] M. Baity-Jesi, E. Calore, A. Cruz, L. A. Fernandez, J. M. Gil-Narvion, I. Gonzalez-Adalid Pemartin, A. Gordillo-Guerrero, D. Iñiguez, A. Maiorano, E. Marinari, V. Martin-Mayor, J. Moreno-Gordo, A. Muñoz Sudupe, D. Navarro, I. Paga, G. Parisi, S. Perez-Gaviro, F. Ricci-Tersenghi, J. J. Ruiz-Lorenzo, S. F. Schifano, B. Seoane, A. Tarancon, R. Tripiccione and D. Yllanes: Temperature chaos is present in off-equilibrium spin-glass dynamics (2020). arXiv:2011.09419.

[Bn11] R. A. Baños, A. Cruz, L. A. Fernandez, J. M. Gil-Narvion, A. Gordillo-Guerrero, M. Guidetti, D. Iñiguez, A. Maiorano, F. Mantovani, E. Marinari, V. Martín-Mayor, J. Monforte-Garcia, A. Muñoz Sudupe, D. Navarro, G. Parisi, S. Perez-Gaviro, F. Ricci-Tersenghi, J. J. Ruiz-Lorenzo, S. F. Schifano, B. Seoane, A. Tarancón, R. Tripiccione and D. Yllanes: *Phys. Rev. B* **84**, 174209 (Nov 2011). doi:10.1103/PhysRevB.84.174209. arXiv:1107.5772, URL http://link.aps.org/doi/10.1103/PhysRevB.84.174209.

[Bn12a] R. A. Baños, A. Cruz, L. A. Fernandez, J. M. Gil-Narvion, A. Gordillo-Guerrero, M. Guidetti, D. Iniguez, A. Maiorano, E. Marinari, V. Martín-Mayor, J. Monforte-Garcia, A. Muñoz Sudupe, D. Navarro, G. Parisi, S. Perez-Gaviro, J. J. Ruiz-Lorenzo, S. F. Schifano, B. Seoane, A. Tarancon, P. Tellez, R. Tripiccione and D. Yllanes: *Proc. Natl. Acad. Sci. USA* **109**, 6452 (2012). doi:10.1073/pnas.1203295109.

[Bn12b] R. A. Baños, L. A. Fernandez, V. Martin-Mayor and A. P. Young: *Phys. Rev. B* **86**, 134416 (Oct 2012). doi:10.1103/PhysRevB.86.134416. arXiv:1207.7014, URL http://link.aps.org/doi/10.1103/PhysRevB.86.134416.

[Boe05] S. Boettcher: *Phys. Rev. Lett.* **95**, 197205 (Nov 2005). doi:10.1103/PhysRevLett.95.197205. arXiv:cond-mat/0508061, URL http://link.aps.org/doi/10.1103/PhysRevLett.95.197205.

[Bor75] A. B. Bortz, M. H. Kalos and J. L. Lebowitz: *J. Comp. Phys.* **17**, 10–18 (1975). doi:doi:10.1016/0021-9991(75)90060-1.

[Bou92] J. Bouchaud: *Journal de Physique I* **2**, 1705–1713 (1992). doi:10.1051/jp1:1992238. URL https://hal.archives-ouvertes.fr/jpa-00246652.

[Bou01] J.-P. Bouchaud, P. Doussineau, T. de Lacerda-Arôso and A. Levelut: *Eur. Phys. J. B* **21**, 335 (2001).

[Bra78] A. J. Bray and M. A. Moore: *Phys. Rev. Lett.* **41**, 1068–1072 (Oct 1978). doi:10.1103/PhysRevLett.41.1068. URL http://link.aps.org/doi/10.1103/PhysRevLett.41.1068.

[Bra79] A. Bray and M. Moore: *Journal of Physics C: Solid State Physics* **12**, 79 (1979). doi:10.1088/0022-3719/12/1/020. URL http://stacks.iop.org/0022-3719/12/i=1/a=020.

[Bra80] A. Bray and M. Moore: *Journal of Physics C: Solid State Physics* **13**, L469 (1980). doi:10.1088/0022-3719/13/19/002. URL http://stacks.iop.org/0022-3719/13/i=19/a=002.

[Bra86] A. J. Bray, M. A. Moore and A. P. Young: *Phys. Rev. Lett.* **56**, 2641–2644 (Jun 1986). doi:10.1103/PhysRevLett.56.2641. URL http://link.aps.org/doi/10.1103/PhysRevLett.56.2641.

[Bra87] A. J. Bray and M. A. Moore: *Phys. Rev. Lett.* **58**, 57–60 (Jan 1987). doi:10.1103/PhysRevLett.58.57. URL https://link.aps.org/doi/10.1103/PhysRevLett.58.57.

[Bro59] R. Brout: *Phys. Rev.* **115**, 824–835 (Aug 1959). doi:10.1103/PhysRev.115.824. URL http://link.aps.org/doi/10.1103/PhysRev.115.824.

[Cam02] M. Campostrini, A. Pelissetto, P. Rossi and E. Vicari: *Phys. Rev. E* **65**, 066127 (2002). doi:10.1103/PhysRevE.65.066127.

[Cam06] I. Campos, M. Cotallo-Aban, V. Martín-Mayor, S. Perez-Gaviro and A. Tarancon: *Phys. Rev. Lett.* **97**, 217204 (2006). doi:10.1103/PhysRevLett.97.217204.

[Car96] J. Cardy: *Scaling and Renormalization in Statistical Field Theory*, volume 5 of *Lecture notes in physics* (P. Goddard and J. Yeomans, Cambridge University Press, Cambridge, 1996). ISBN 0521499593.

[Cas05] T. Castellani and A. Cavagna: *J. Stat. Mech.* **2005**, P05012 (2005). doi:10.1088/1742-5468/2005/05/P05012.

[Cha93] P. Chandra, P. Coleman and I. Ritchey: *Journal de Physique I* **3**, 591–610 (1993). doi:https://doi.org/10.1051/jp1:1993104.

[Cha14] P. Charbonneau, J. Kurchan, G. Parisi, P. Urbani and F. Zamponi: *Nature Communications* **5**, 3725 (2014). doi:10.1038/ncomms4725. arXiv:1404.6809.

[Che77] J.-H. Chen and T. C. Lubensky: *Phys. Rev. B* **16**, 2106–2114 (Sep 1977). doi:10.1103/PhysRevB.16.2106. URL http://link.aps.org/doi/10.1103/PhysRevB.16.2106.

[Con09] P. Contucci, C. Giardinà, C. Giberti, G. Parisi and C. Vernia: *Phys. Rev. Lett* **103**, 017201 (2009). doi:10.1103/PhysRevLett.103.017201. arXiv:0902.0594.

[Cro98] J. Crowe, J. Carpenter and L. Crowe: *Annu. Rev. Physiol.* **60**, 73–103 (March 1998). doi:10.1146/annurev.physiol.60.1.73. PMID: 9558455, URL http://dx.doi.org/10.1146/annurev.physiol.60.1.73.

[Cru03] A. Cruz, L. A. Fernández, S. Jiménez, J. J. Ruiz-Lorenzo and A. Tarancón: *Phys. Rev. B* **67**, 214425 (Jun 2003). doi:10.1103/PhysRevB.67.214425. URL http://link.aps.org/doi/10.1103/PhysRevB.67.214425.

[Cug93] L. F. Cugliandolo and J. Kurchan: *Phys. Rev. Lett.* **71**, 173–176 (Jul 1993). doi:10.1103/PhysRevLett.71.173. URL http://link.aps.org/doi/10.1103/PhysRevLett.71.173.

[Dom80] C. de Dominicis, Gabay, M., Garel, T. and Orland, H.: *J. Phys. France* **41**, 923–930 (1980). doi:10.1051/jphys:01980004109092300. URL http://dx.doi.org/10.1051/jphys:01980004109092300.

[Dom98] C. de Dominicis, I. Kondor and T. Temesvári: In *Spin Glasses and Random Fields*, edited by A. P. Young (World Scientific, Singapore, 1998). arXiv:cond-mat/9705215.

[Dom06] C. de Dominicis and I. Giardina: *Random Fields and Spin Glasses: a field theory approach* (Cambridge University Press, Cambridge, England, 2006).

[Dot87] V. Dotsenko: *Journal of Physics C: Solid State Physics* **20**, 5473 (1987). doi:10.1088/0022-3719/20/33/005. URL http://stacks.iop.org/0022-3719/20/i=33/a=005.

[Dot01] V. Dotsenko: *Introduction to the Replica Theory of Disordered Statistical Systems* (Cambridge University Press, Cambridge, England, 2001).

[Dru07] D. Drung, C. Assmann, J. Beyer, A. Kirste, M. Peters, F. Ruede and T. Schurig: *Applied Superconductivity, IEEE Transactions on* **17**, 699–704 (June 2007). ISSN 1051-8223. doi:10.1109/TASC.2007.897403.

[Edw75] S. F. Edwards and P. W. Anderson: *Journal of Physics F: Metal Physics* **5**, 965 (1975). doi:10.1088/0305-4608/5/5/017. URL http://stacks.iop.org/0305-4608/5/i=5/a=017.

[Edw76] S. F. Edwards and P. W. Anderson: *J. Phys. F* **6**, 1927 (1976). doi:10.1088/0305-4608/6/10/022. URL http://stacks.iop.org/0305-4608/6/i=10/a=022.

[Fan14] Y. Fang, S. Feng, K.-M. Tam, Z. Yun, J. Moreno, J. Ramanujam and M. Jarrell: *Comp. Phys. Comm.* **185**, 2467–2478 (2014). doi:doi:10.1016/j.cpc.2014.05.020. arXiv:1311.5582.

[Fer09] L. A. Fernandez, V. Martín-Mayor and D. Yllanes: *Nucl. Phys. B* **807**, 424–454 (2009).

[Fer15] L. A. Fernández and V. Martín-Mayor: *Phys. Rev. B* **91**, 174202 (May 2015). doi:10.1103/PhysRevB.91.174202. URL http://link.aps.org/doi/10.1103/PhysRevB.91.174202.

[Fer16a] L. A. Fernandez, E. Marinari, V. Martin-Mayor, G. Parisi and J. J. Ruiz-Lorenzo: *Phys. Rev. B* **94**, 024402 (Jul 2016). doi:10.1103/PhysRevB.94.024402. URL https://link.aps.org/doi/10.1103/PhysRevB.94.024402.

[Fer16b] L. A. Fernández, E. Marinari, V. Martín-Mayor, G. Parisi and D. Yllanes: *Journal of Statistical Mechanics: Theory and Experiment* **2016**, 123301 (2016). doi:10.1088/1742-5468/2016/12/123301. arXiv:1605.03025, URL http://stacks.iop.org/1742-5468/2016/i=12/a=123301.

[Fer18a] L. A. Fernández, E. Marinari, V. Martín-Mayor, G. Parisi and J. Ruiz-Lorenzo: *Journal of Statistical Mechanics: Theory and Experiment* **2018**, 103301 (2018). doi:10.1088/1742-5468/aae2e1. arXiv:1805.08504, URL http://stacks.iop.org/1742-5468/2018/i=10/a=103301.

[Fer18b] A. M. Ferrenberg, J. Xu and D. P. Landau: *Phys. Rev. E* **97**, 043301 (Apr 2018). doi:10.1103/PhysRevE.97.043301. URL https://link.aps.org/doi/10.1103/PhysRevE.97.043301.

[Fer19a] L. A. Fernandez, E. Marinari, V. Martin-Mayor, I. Paga and J. J. Ruiz-Lorenzo: *Phys. Rev. B* **100**, 184412 (Nov 2019). doi:10.1103/PhysRevB.100.184412. URL https://link.aps.org/doi/10.1103/PhysRevB.100.184412.

[Fer19b] L. A. Fernández, E. Marinari, V. Martín-Mayor, G. Parisi and J. Ruiz-Lorenzo: *Journal of Physics A: Mathematical and Theoretical* **52**, 224002 (2019). doi:10.1088/1751-8121/ab1364. URL https://doi.org/10.1088%2F1751-8121%2Fab1364.

[Fis85] D. S. Fisher and H. Sompolinsky: *Phys. Rev. Lett.* **54**, 1063 (1985). doi:10.1103/PhysRevLett.54.1063.

[Fis86] D. S. Fisher and D. A. Huse: *Phys. Rev. Lett.* **56**, 1601 (Apr 1986). doi:10.1103/PhysRevLett.56.1601. URL http://link.aps.org/doi/10.1103/PhysRevLett.56.1601.

[Fis87] D. S. Fisher and D. A. Huse: *J. Phys. A: Math. Gen.* **20**, L1005 (1987). doi:10.1088/0305-4470/20/15/013.

[Fis88a] D. S. Fisher and D. A. Huse: *Phys. Rev. B* **38**, 386 (1988). doi:10.1103/PhysRevB.38.386.

[Fis88b] D. S. Fisher and D. A. Huse: *Phys. Rev. B* **38**, 373–385 (Jul 1988). doi:10.1103/PhysRevB.38.373. URL https://link.aps.org/doi/10.1103/PhysRevB.38.373.

[Fra94] S. Franz, G. Parisi and M. Virasoro: *J. Phys. (France)* **4**, 1657 (1994). doi:10.1051/jp1:1994213.

[Fra98] S. Franz, M. Mézard, G. Parisi and L. Peliti: *Phys. Rev. Lett.* **81**, 1758–1761 (Aug 1998). doi:10.1103/PhysRevLett.81.1758. URL http://link.aps.org/doi/10.1103/PhysRevLett.81.1758.

[Fra99] S. Franz, M. Mézard, G. Parisi and L. Peliti: *Journal of Statistical Physics* **97**, 459–488 (1999). ISSN 1572-9613. doi:10.1023/A:1004602906332. URL http://dx.doi.org/10.1023/A:1004602906332.

[Gey91] C. J. Geyer: In *Computing Science and Statistics: Proceedings of the 23rd Symposium on the Interface*, edited by E. M. Keramigas (Interface Foundations, Fairfax, 1991).

[Gil77] D. T. Gillespie: *J. Phys. Chem.* **81**, 2340–2361 (1977). doi:10.1021/j100540a008.

[Gre95] A. L. Greer: *Science* **267**, 1947–1953 (March 1995). doi:10.1126/science.267.5206.1947. URL http://www.sciencemag.org/content/267/5206/1947.

[Guc14] S. Guchhait and R. Orbach: *Phys. Rev. Lett.* **112**, 126401 (Mar 2014). doi:10.1103/PhysRevLett.112.126401. URL http://link.aps.org/doi/10.1103/PhysRevLett.112.126401.

[Guc17] S. Guchhait and R. L. Orbach: *Phys. Rev. Lett.* **118**, 157203 (Apr 2017). doi:10.1103/PhysRevLett.118.157203. URL https://link.aps.org/doi/10.1103/PhysRevLett.118.157203.

[Gue02] F. Guerra and F. L. Toninelli: *Communications in Mathematical Physics* **230**, 71–79 (2002). ISSN 0010-3616. doi:10.1007/s00220-002-0699-y. URL http://dx.doi.org/10.1007/s00220-002-0699-y.

[Gue03] F. Guerra: *Comm. Math. Phys.* **233**, 1–12 (2003). doi:10.1007/s00220-002-0773-5. arXiv:cond-mat/0205123.

[Gun91] K. Gunnarsson, P. Svedlindh, P. Nordblad, L. Lundgren, H. Aruga and A. Ito: *Phys. Rev. B* **43**, 8199–8203 (1991). doi:10.1103/PhysRevB.43.8199.

[Ham92] J. Hammann, M. Ocio, R. Orbach and E. Vincent: *Physica (Amsterdam)* **185A**, 278 (1992).

[Har76] A. B. Harris, T. C. Lubensky and J.-H. Chen: *Phys. Rev. Lett.* **36**, 415–418 (Feb 1976). doi:10.1103/PhysRevLett.36.415. URL http://link.aps.org/doi/10.1103/PhysRevLett.36.415.

[Har99a] A. K. Hartmann: *Phys. Rev. E.* **59**, 84 (1999). arXiv:cond-mat/9806114.

[Har99b] A. K. Hartmann and U. Nowak: *Eur. Phys. J. B* **7**, 105–109 (1999). doi:10.1007/s100510050593. URL http://dx.doi.org/10.1007/s100510050593.

[Har01] A. K. Hartmann and A. P. Young: *Phys. Rev. B* **64**, 214419 (Nov 2001). doi:10.1103/PhysRevB.64.214419. URL http://link.aps.org/doi/10.1103/PhysRevB.64.214419.

[Har03] A. K. Hartmann and M. A. Moore: *Phys. Rev. Lett.* **90**, 127201 (Mar 2003). doi:10.1103/PhysRevLett.90.127201. URL https://link.aps.org/doi/10.1103/PhysRevLett.90.127201.

[Har06] A. K. Hartmann and M. Weigt: *Phase transitions in combinatorial optimization problems: basics, Algorithms and Statistical Mechanics* (John Wiley and Sons, 2006). ISBN 9783527606733. doi:10.1002/3527606734.

[Has08] M. Hasenbusch, A. Pelissetto and E. Vicari: *J. Stat. Mech.* **2008**, L02001 (2008). doi:10.1088/1742-5468/2008/02/L02001.

[Has11] M. Hasenbusch and E. Vicari: *Phys. Rev. B* **84**, 125136 (Sep 2011). doi:10.1103/PhysRevB.84.125136. URL https://link.aps.org/doi/10.1103/PhysRevB.84.125136.

[Has20] M. Hasenbusch: *Phys. Rev. E* **101**, 022126 (Feb 2020). doi:10.1103/PhysRevE.101.022126. URL https://link.aps.org/doi/10.1103/PhysRevE.101.022126.

[Hem79] J. van Hemmen and R. Palmer: *Journal of Physics A: Mathematical and General* **12**, 563 (1979). URL http://stacks.iop.org/0305-4470/12/i=4/a=016.

[Hér02] D. Hérisson and M. Ocio: *Phys. Rev. Lett.* **88**, 257202 (2002). doi:10.1103/PhysRevLett.88.257202. arXiv:cond-mat/0112378.

[Hua87] K. Huang: *Statistical Mechanics*. second edition (John Wiley and Sons, Hoboken, NJ, 1987). ISBN 0471815187.

[Hus87] D. A. Huse and D. S. Fisher: *Phys. Rev. B* **35**, 6841–6846 (May 1987). doi:10.1103/PhysRevB.35.6841. URL http://link.aps.org/doi/10.1103/PhysRevB.35.6841.

[JÖ6] T. Jörg, J. Lukic, E. Marinari and O. C. Martin: *Phys. Rev. Lett.* **96**, 237205 (Jun 2006). doi:10.1103/PhysRevLett.96.237205. URL http://link.aps.org/doi/10.1103/PhysRevLett.96.237205.

[Joh99] Y. G. Joh, R. Orbach, G. G. Wood, J. Hammann and E. Vincent: *Phys. Rev. Lett.* **82**, 438–441 (Jan 1999). doi:10.1103/PhysRevLett.82.438. URL http://link.aps.org/doi/10.1103/PhysRevLett.82.438.

[Jon98] K. Jonason, E. Vincent, J. Hammann, J. P. Bouchaud and P. Nordblad: *Phys. Rev. Lett.* **81**, 3243–3246 (Oct 1998). doi:10.1103/PhysRevLett.81.3243. URL http://link.aps.org/doi/10.1103/PhysRevLett.81.3243.

[Jör06] T. Jörg: *Phys. Rev. B* **73**, 224431 (2006). doi:10.1103/PhysRevB.73.224431.

[Jör08] T. Jörg, H. G. Katzgraber and F. Krzakala: *Phys. Rev. Lett.* **100**, 197202 (2008). doi:10.1103/PhysRevLett.100.197202. arXiv:0712.2009.

[Kad76] L. Kadanoff: *Annals of Physics* **100**, 359–394 (1976). ISSN 0003-4916. doi:10.1016/0003-4916(76)90066-X.

[Kas56] T. Kasuya: *Prog. Theor. Phys.* **16**, 45 (1956).

[Kat03a] H. Katzgraber and A. P. Young: *Phys. Rev. B* **67**, 134410 (2003). doi:10.1103/PhysRevB.67.134410.

[Kat03b] H. G. Katzgraber and A. P. Young: *Phys. Rev. B* **68**, 224408 (Dec 2003). doi:10.1103/PhysRevB.68.224408. URL https://link.aps.org/doi/10.1103/PhysRevB.68.224408.

[Kat05a] H. G. Katzgraber, M. Körner, F. Liers, M. Jünger and A. K. Hartmann: *Phys. Rev. B* **72**, 094421 (Sep 2005). doi:10.1103/PhysRevB.72.094421. URL https://link.aps.org/doi/10.1103/PhysRevB.72.094421.

[Kat05b] H. G. Katzgraber and L. W. Lee: *Phys. Rev. B* **71**, 134404 (Apr 2005). doi:10.1103/PhysRevB.71.134404. URL https://link.aps.org/doi/10.1103/PhysRevB.71.134404.

[Kat05c] H. G. Katzgraber and A. P. Young: *Phys. Rev. B* **72**, 184416 (Nov 2005). doi:10.1103/PhysRevB.72.184416. URL https://link.aps.org/doi/10.1103/PhysRevB.72.184416.

[Kat08] H. G. Katzgraber: *Journal of Physics: Conference Series* **95**, 012004 (jan 2008). doi:10.1088/1742-6596/95/1/012004. URL https://doi.org/10.1088/1742-6596/95/1/012004.

[Ken18] G. G. Kenning, D. M. Tennant, C. M. Rost, F. G. da Silva, B. J. Walters, Q. Zhai, D. C. Harrison, E. D. Dahlberg and R. L. Orbach: *Phys. Rev. B* **98**, 104436 (Sep 2018). doi:10.1103/PhysRevB.98.104436. URL `https://link.aps.org/doi/10.1103/PhysRevB.98.104436`.

[Kho18] H. Khoshbakht and M. Weigel: *Phys. Rev. B* **97**, 064410 (Feb 2018). doi:10.1103/PhysRevB.97.064410. URL `https://link.aps.org/doi/10.1103/PhysRevB.97.064410`.

[Kir78] S. Kirkpatrick and D. Sherrington: *Phys. Rev. B* **17**, 4384–4403 (Jun 1978). doi:10.1103/PhysRevB.17.4384. URL `http://link.aps.org/doi/10.1103/PhysRevB.17.4384`.

[Kis96] J. Kisker, L. Santen, M. Schreckenberg and H. Rieger: *Phys. Rev. B* **53**, 6418–6428 (Mar 1996). doi:10.1103/PhysRevB.53.6418. URL `http://link.aps.org/doi/10.1103/PhysRevB.53.6418`.

[Kot83] G. Kotliar, P. W. Anderson and D. L. Stein: *Phys. Rev. B* **27**, 602 (1983). doi:10.1103/PhysRevB.27.602.

[Kum14] P. A. Kumar, R. Mathieu, P. Nordblad, S. Ray, O. Karis, G. Andersson and D. D. Sarma: *Phys. Rev. X* **4**, 011037 (Mar 2014). doi:10.1103/PhysRevX.4.011037. URL `http://link.aps.org/doi/10.1103/PhysRevX.4.011037`.

[Lś86] L. P. Lévy and A. T. Ogielski: *Phys. Rev. Lett.* **57**, 3288–3291 (Dec 1986). doi:10.1103/PhysRevLett.57.3288. URL `https://link.aps.org/doi/10.1103/PhysRevLett.57.3288`.

[Led91] M. Lederman, R. Orbach, J. M. Hammann, M. Ocio and E. Vincent: *Phys. Rev. B* **44**, 7403–7412 (Oct 1991). doi:10.1103/PhysRevB.44.7403. URL `https://link.aps.org/doi/10.1103/PhysRevB.44.7403`.

[Lee03] L. W. Lee and A. P. Young: *Phys. Rev. Lett.* **90**, 227203 (2003). doi:10.1103/PhysRevLett.90.227203.

[Lef94] F. Lefloch, J. Hammann, M. Ocio and E. Vincent: *Physica B: Condensed Matter* **203**, 63 – 74 (1994). ISSN 0921-4526. doi:https://doi.org/10.1016/0921-4526(94)90278-X. URL `http://www.sciencedirect.com/science/article/pii/092145269490278X`.

[Leu08] L. Leuzzi, G. Parisi, F. Ricci-Tersenghi and J. J. Ruiz-Lorenzo: *Phys. Rev. Lett.* **101**, 107203 (Sep 2008). doi:10.1103/PhysRevLett.101.107203. URL `http://link.aps.org/doi/10.1103/PhysRevLett.101.107203`.

[Leu09] L. Leuzzi, G. Parisi, F. Ricci-Tersenghi and J. J. Ruiz-Lorenzo: *Phys. Rev. Lett.* **103**, 267201 (2009). doi:10.1103/PhysRevLett.103.267201. `arXiv:0811.3435`.

[Lév88] L. P. Lévy: *Phys. Rev. B* **38**, 4963–4973 (Sep 1988). doi:10.1103/PhysRevB.38.4963. URL `http://link.aps.org/doi/10.1103/PhysRevB.38.4963`.

[Luk04] J. Lukic, A. Galluccio, E. Marinari, O. C. Martin and G. Rinaldi: *Phys. Rev. Lett.* **92**, 117202 (Mar 2004). doi:10.1103/PhysRevLett.92.117202. URL http://link.aps.org/doi/10.1103/PhysRevLett.92.117202.

[Luk06] J. Lukic, E. Marinari, O. C. Martin and S. Sabatini: *Journal of Statistical Mechanics: Theory and Experiment* **2006**, L10001 (2006). URL http://stacks.iop.org/1742-5468/2006/i=10/a=L10001.

[Lul16] M. Lulli, G. Parisi and A. Pelissetto: *Phys. Rev. E* **93**, 032126 (Mar 2016). doi:10.1103/PhysRevE.93.032126. URL http://link.aps.org/doi/10.1103/PhysRevE.93.032126.

[Ma76] S.-k. Ma: *Modern Theory of Critical Phenomena* (Westview Press, New York, 1976). ISBN 0-7382-0301-7.

[Mac82] N. D. Mackenzie and A. P. Young: *Phys. Rev. Lett.* **49**, 301–304 (Aug 1982). doi:10.1103/PhysRevLett.49.301. URL http://link.aps.org/doi/10.1103/PhysRevLett.49.301.

[Mai18] A. Maiorano and G. Parisi: *Proceedings of the National Academy of Sciences* **115**, 5129–5134 (2018). ISSN 0027-8424. doi:10.1073/pnas.1720832115. https://www.pnas.org/content/115/20/5129.full.pdf, URL https://www.pnas.org/content/115/20/5129.

[Mal82a] A. P. Malozemoff, B. Barbara and Y. Imry: *Journal of Applied Physics* **53**, 2205 (1982). doi:https://doi.org/10.1063/1.330818.

[Mal82b] A. P. Malozemoff and Y. Imry: *Journal of Applied Physics* **53**, 7672 (1982). doi:https://doi.org/10.1063/1.330179.

[Man15a] M. Manssen and A. K. Hartmann: *Phys. Rev. B* **91**, 174433 (May 2015). doi:10.1103/PhysRevB.91.174433. arXiv:1411.5512, URL http://link.aps.org/doi/10.1103/PhysRevB.91.174433.

[Man15b] M. Manssen, A. K. Hartmann and A. P. Young: *Phys. Rev. B* **91**, 104430 (Mar 2015). doi:10.1103/PhysRevB.91.104430. arXiv:1501.06760, URL http://link.aps.org/doi/10.1103/PhysRevB.91.104430.

[Mar60] W. Marshall: *Phys. Rev.* **118**, 1519–1523 (Jun 1960). doi:10.1103/PhysRev.118.1519. URL http://link.aps.org/doi/10.1103/PhysRev.118.1519.

[Mar92] E. Marinari and G. Parisi: *Europhys. Lett.* **19**, 451–458 (1992). doi:10.1209/0295-5075/19/6/002.

[Mar01] L.-M. Martinez and C. A. Angell: *Nature* **410**, 663–667 (2001). doi:10.1038/35070517.

[Mar06] G. Marsh: 50 years of reinforced plastic boats (October 8 2006). URL http://www.materialstoday.com/composite-applications/features/50-years-of-reinforced-plastic-boats/.

[Mat81] D. Mattis: *Theory of Magnetism I: statics and dynamics.* first edition (Springer-Verlag, Berlin Heidelberg, 1981). doi:10.1007/978-3-642-83238-3.

[May93] R. Mayer: *Design with Reinforced Plastics: A Guide for Engineers and Designers.* First edition (Springer Science & Business Media, Netherlands, 1993). ISBN 978-0-85072-294-9, 978-94-011-2210-8.

[Méz84a] M. Mézard, G. Parisi, N. Sourlas, G. Toulouse and M. Virasoro: *Phys. Rev. Lett.* **52**, 1156 (1984). doi:10.1103/PhysRevLett.52.1156.

[Méz84b] M. Mézard, G. Parisi, N. Sourlas, G. Toulouse and M. Virasoro: *J. Phys. France* **45**, 843–854 (1984). doi:10.1051/jphys:01984004505084300.

[Méz85a] M. Mézard, G. Parisi and M. Virasoro: *J. Physique Lett.* **46**, 217–222 (1985). doi:10.1051/jphyslet:01985004606021700.

[Méz85b] M. Mézard and M. Virasoro: *J. Physique* **46**, 1293–1307 (1985). doi:10.1051/jphys:019850046080129300.

[Méz87] M. Mézard, G. Parisi and M. Virasoro: *Spin-Glass Theory and Beyond* (World Scientific, Singapore, 1987). doi:10.1142/0271.

[Méz09] M. Mézard and A. Montanari: *Information, Physics, and Computation* (OUP Oxford, Oxford, UK, 2009).

[Mig75] A. Migdal: *Zhurnal Eksperimentalnoi i teoreticheskoi fiziki* (1975). ISSN 0044-4510.

[Myd93] J. A. Mydosh: *Spin Glasses: an Experimental Introduction* (Taylor and Francis, London, 1993).

[Nag79] S. Nagata, P. H. Keesom and H. R. Harrison: *Phys. Rev. B* **19**, 1633–1638 (Feb 1979). doi:10.1103/PhysRevB.19.1633. URL `http://link.aps.org/doi/10.1103/PhysRevB.19.1633`.

[Nig76] M. Nightingale: *Physica A: Statistical Mechanics and its Applications* **83**, 561 – 572 (1976). ISSN 0378-4371. doi:http://dx.doi.org/10.1016/0378-4371(75)90021-7. URL `http://www.sciencedirect.com/science/article/pii/0378437175900217`.

[Nis01] H. Nishimori: In *Statistical Physics of Spin Glasses and Information Processing* (Oxford University Press, Oxford, 2001). URL `http://oxfordindex.oup.com/view/10.1093/acprof:oso/9780198509417.003.0004`.

[Nob59] J. de Nobel and F. Chatenier: *Physica* **25**, 969–979 (January 1959). ISSN 0031-8914. doi:10.1016/0031-8914(59)90018-7. URL `http://www.sciencedirect.com/science/article/pii/0031891459900187`.

[Nor86] P. Nordblad, P. Svedlindh, L. Lundgren and L. Sandlund: *Phys. Rev. B* **33**, 645–648 (Jan 1986). doi:10.1103/PhysRevB.33.645. URL `https://link.aps.org/doi/10.1103/PhysRevB.33.645`.

[Nor97] P. Nordblad and P. Svedlindh: *Experiments on Spin Glasses* (World Scientific, Singapore, 1997). Spin Glasses and Random Fields edited by A.P. Young, Directions in Condensed Matter Physics Vol. 12, p. 1, URL https://doi.org/10.1142/3517.

[Olv10] F. W. J. Olver, D. W. Lozier, R. Boisvert and C. W. Clark: *NIST Handbook of Mathematical Functions* (Cambridge University Press, Cambridge, 2010). URL http://dlmf.nist.gov/.

[Owe56] J. Owen, M. Browne, W. D. Knight and C. Kittel: *Phys. Rev.* **102**, 1501–1507 (Jun 1956). doi:10.1103/PhysRev.102.1501. URL http://link.aps.org/doi/10.1103/PhysRev.102.1501.

[Pag21] I. Paga, Q. Zhai, M. Baity-Jesi, E. Calore, A. Cruz, L. A. Fernandez, J. M. Gil-Narvion, I. G.-A. Pemartin, A. Gordillo-Guerrero, D. Iñiguez, A. Maiorano, E. Marinari, V. Martin-Mayor, J. Moreno-Gordo, A. Muñoz-Sudupe, D. Navarro, R. L. Orbach, G. Parisi, S. Perez-Gaviro, F. Ricci-Tersenghi, J. J. Ruiz-Lorenzo, S. F. Schifano, D. L. Schlagel, B. Seoane, A. Tarancon, R. Tripiccione and D. Yllanes: *Journal of Statistical Mechanics: Theory and Experiment* **2021**, 033301 (mar 2021). doi:10.1088/1742-5468/abdfca. URL https://doi.org/10.1088/1742-5468/abdfca.

[Pal99] M. Palassini and S. Caracciolo: *Phys. Rev. Lett.* **82**, 5128–5131 (1999). doi:10.1103/PhysRevLett.82.5128. arXiv:cond-mat/9904246.

[Par79a] G. Parisi: *Phys. Rev. Lett.* **43**, 1754–1756 (Dec 1979). doi:10.1103/PhysRevLett.43.1754. URL http://link.aps.org/doi/10.1103/PhysRevLett.43.1754.

[Par79b] G. Parisi: *Phys. Lett.* **73A**, 203 (1979). doi:10.1016/0375-9601(79)90708-4.

[Par80a] G. Parisi: *Journal of Physics A: Mathematical and General* **13**, 1887 (1980). doi:10.1088/0305-4470/13/5/047. URL http://stacks.iop.org/0305-4470/13/i=5/a=047.

[Par80b] G. Parisi: *J. Phys. A: Math. Gen.* **13**, 1101 (1980). doi:10.1088/0305-4470/13/3/042.

[Par80c] G. Parisi: *J. Phys. A: Math. Gen.* **13**, L115–L121 (1980). ISSN 0305-4470. doi:10.1088/0305-4470/13/4/009.

[Par83] G. Parisi: *Phys. Rev. Lett.* **50**, 1946 (1983). doi:10.1103/PhysRevLett.50.1946. URL http://journals.aps.org/prl/abstract/10.1103/PhysRevLett.50.1946.

[Par88] G. Parisi: *Statistical Field Theory* (Addison-Wesley, 1988).

[Ram86] R. Rammal, G. Toulouse and M. A. Virasoro: *Rev. Mod. Phys.* **58**, 765–788 (Jul 1986). doi:10.1103/RevModPhys.58.765. URL http://link.aps.org/doi/10.1103/RevModPhys.58.765.

[Rie94] H. Rieger, B. Steckemetz and M. Schreckenberg: *EPL (Europhysics Letters)* **27**, 485 (1994). doi:10.1209/0295-5075/27/6/013.

[Rod03] G. F. Rodriguez, G. G. Kenning and R. Orbach: *Phys. Rev. Lett.* **91**, 037203 (Jul 2003). doi:10.1103/PhysRevLett.91.037203. URL http://link.aps.org/doi/10.1103/PhysRevLett.91.037203.

[Rod04] G. F. Rodriguez: *Ph.D. dissertation* (2004). URL https://www.researchgate.net/publication/252531893_Initial_conditions_and_long_time_dynamics_for_a_complex_system_Hierarchical_properties_of_the_spin_glass_decay.

[Rod13] G. Rodriguez, G. Kenning and R. Orbach: *Phys. Rev. B* **88**, 054302 (Aug 2013). doi:10.1103/PhysRevB.88.054302. URL http://link.aps.org/doi/10.1103/PhysRevB.88.054302.

[Rud54] M. Ruderman and C. Kittel: *Phys. Rev.* **96**, 99 (1954).

[Sch93] A. G. Schins, A. F. M. Arts and H. W. de Wijn: *Phys. Rev. Lett.* **70**, 2340–2343 (Apr 1993). doi:10.1103/PhysRevLett.70.2340. URL https://link.aps.org/doi/10.1103/PhysRevLett.70.2340.

[SD17] D. Simmons-Duffin: *J. High Energ. Phys.* **86**, 88 (2017). doi:10.1007/JHEP03(2017)086.

[She75] D. Sherrington and S. Kirkpatrick: *Phys. Rev. Lett.* **35**, 1792–1796 (Dec 1975). doi:10.1103/PhysRevLett.35.1792. URL http://link.aps.org/doi/10.1103/PhysRevLett.35.1792.

[She78] D. Sherrington: *Journal of Physics A: Mathematical and General* **11**, L185 (1978). doi:10.1088/0305-4470/11/8/004. URL http://stacks.iop.org/0305-4470/11/i=8/a=004.

[She07] D. Sherrington: In *Spin Glasses*, edited by E. Bolthausen and A. Bovier, volume 1900 of *Lecture Notes in Mathematics*, pages 45–62 (Springer Berlin Heidelberg, 2007). ISBN 978-3-540-40902-1. doi:10.1007/978-3-540-40908-3_2. arXiv:cond-mat/0512425, URL http://dx.doi.org/10.1007/978-3-540-40908-3_2.

[Sou77] B. W. Southern and A. P. Young: *Journal of Physics C: Solid State Physics* **10**, 2179 (1977). doi:10.1088/0022-3719/10/12/023. URL http://stacks.iop.org/0022-3719/10/i=12/a=023.

[Tal06] M. Talagrand: *Ann. of Math.* **163**, 221 (2006).

[Tho77] D. J. Thouless, P. W. Anderson and R. G. Palmer: *Phil. Mag.* **35**, 593–601 (1977). doi:10.1080/14786437708235992. http://dx.doi.org/10.1080/14786437708235992, URL http://dx.doi.org/10.1080/14786437708235992.

[Tou77] G. Toulouse: *Communications on Physics* **2**, 115 (1977).

[Ver89] M. A. Vertechi, D.and Virasoro: *Journal de physique Paris* **50**, 2325–2332 (1989). ISSN 0302-0738. doi:https://doi.org/10.1051/jphys:0198900500170232500.

[Vin95] E. Vincent, J. P. Bouchaud, D. S. Dean and J. Hammann: *Phys. Rev. B* **52**, 1050–1060 (Jul 1995). doi:10.1103/PhysRevB.52.1050. URL https://link.aps.org/doi/10.1103/PhysRevB.52.1050.

[Vin97] E. Vincent, J. Hammann, M. Ocio, J.-P. Bouchaud and L. F. Cugliandolo: In *Complex Behavior of Glassy Systems*, edited by M. Rubí and C. Pérez-Vicente, number 492 in Lecture Notes in Physics (Springer, 1997). doi:10.1007/BFb0104827.

[Vin07] E. Vincent: In *Ageing and the Glass Transition*, edited by M. Henkel, M. Pleimling and R. Sanctuary, number 716 in Lecture Notes in Physics (Springer, 2007). doi:10.1007/BFb0104827.

[Web13] J. Weber, R. Jack and V. Pande: *Journal of the American Chemical Society* **135**, 5501–5504 (2013). doi:10.1021/ja4002663.

[Wid65] B. Widom: *Journal of Chemical Physics* **43**, 3898 (1965).

[Yos57] K. Yosida: *Phys. Rev.* **106**, 893–898 (Jun 1957). doi:10.1103/PhysRev.106.893. URL `http://link.aps.org/doi/10.1103/PhysRev.106.893`.

[You76] A. P. Young and R. B. Stinchcombe: *Journal of Physics C: Solid State Physics* **9**, 4419 (1976). doi:10.1088/0022-3719/9/24/012. URL `http://stacks.iop.org/0022-3719/9/i=24/a=012`.

[You81] A. Young: *Journal of Physics C: Solid State Physics* **14**, L1085 (1981). doi:10.1088/0022-3719/14/34/004. URL `http://stacks.iop.org/0022-3719/14/i=34/a=004`.

[You98] A. P. Young: *Spin Glasses and Random Fields* (World Scientific, Singapore, 1998). doi:10.1142/3517.

[You12] A. P. Young: Everything you wanted to know about data analysis and fitting but were afraid to ask. School on "Efficient Algorithms in Computational Physics", Bad Honnef (September 2012). `arXiv:1210.3781v3`.

[Zen51a] C. Zener: *Phys. Rev.* **81**, 440–444 (Feb 1951). doi:10.1103/PhysRev.81.440. URL `http://link.aps.org/doi/10.1103/PhysRev.81.440`.

[Zen51b] C. Zener: *Phys. Rev.* **82**, 403–405 (May 1951). doi:10.1103/PhysRev.82.403. URL `http://link.aps.org/doi/10.1103/PhysRev.82.403`.

[Zen51c] C. Zener: *Phys. Rev.* **83**, 299–301 (Jul 1951). doi:10.1103/PhysRev.83.299. URL `http://link.aps.org/doi/10.1103/PhysRev.83.299`.

[Zha17a] Q. Zhai, D. C. Harrison and R. L. Orbach: *Phys. Rev. B* **96**, 054408 (Aug 2017). doi:10.1103/PhysRevB.96.054408. URL `https://link.aps.org/doi/10.1103/PhysRevB.96.054408`.

[Zha17b] Q. Zhai, D. C. Harrison, D. Tennant, E. D. Dahlberg, G. G. Kenning and R. L. Orbach: *Phys. Rev. B* **95**, 054304 (Feb 2017). doi:10.1103/PhysRevB.95.054304. URL `https://link.aps.org/doi/10.1103/PhysRevB.95.054304`.

[Zha19] Q. Zhai, V. Martin-Mayor, D. L. Schlagel, G. G. Kenning and R. L. Orbach: *Phys. Rev. B* **100**, 094202 (Sep 2019). doi:10.1103/PhysRevB.100.094202. URL `https://link.aps.org/doi/10.1103/PhysRevB.100.094202`.

[Zha20a] Q. Zhai, R. L. Orbach and D. Schlagel: (2020). 2010.01214.

[Zha20b] Q. Zhai, I. Paga, M. Baity-Jesi, E. Calore, A. Cruz, L. A. Fernandez, J. M. Gil-Narvion, I. Gonzalez-Adalid Pemartin, A. Gordillo-Guerrero, D. Iñiguez, A. Maiorano, E. Marinari, V. Martin-Mayor, J. Moreno-Gordo, A. Muñoz Sudupe, D. Navarro, R. L. Orbach, G. Parisi, S. Perez-Gaviro, F. Ricci-Tersenghi, J. J. Ruiz-Lorenzo, S. F. Schifano, D. L. Schlagel, B. Seoane, A. Tarancon, R. Tripiccione and D. Yllanes: *Phys. Rev. Lett.* **125**, 237202 (Nov 2020). doi: 10.1103/PhysRevLett.125.237202. URL https://link.aps.org/doi/10.1103/PhysRevLett.125.237202.

[Zim60] J. Zimmerman: *J. Phys. Chem. Solids* **17**, 52–56 (December 1960). An additional author, F.E. Hoare, appears in Edwards' citation of this article., URL http://www.sciencedirect.com/science/article/pii/0022369760901748.

List of Figures

List of Tables